Preface

This dissertation is submitted for the Degree of Doctor of Philosophy in Natural Sciences at the University of Cambridge. The work reported here was carried out between October 1999 and October 2002 under the supervisions of Pr. H. K. D. H. Bhadeshia at Department of Materials Science and Metallurgy and Dr. P. Woollin at TWI. To the best of my knowledge, this work is original, except where suitable references are made to previous work. Neither this, nor any substantially similar dissertation has been submitted for any degree, diploma or qualification at any other university or institution. This dissertation contains less than 60,000 words.

Part of this work has been presented in the following publications :

D. Carrouge, H. K. D. H. Bhadeshia and P. Woollin, *Microstructural change in high temperature heat-affected zone of low carbon weldable 13 %Cr martensitic stainless steels*, Proceedings of the Stainless Steel World conference 2002 (Houston, Texas, USA), 61-67.

P. Woollin and D. Carrouge, *Heat-affected zone microstructures in supermartensitic stainless steels*, Proceedings of the Supermartensitic Stainless Steels conference 2002 (Brussels, belgium), 199-204.

Dominique Carrouge
October 2002

Acknowledgments

I am indebted to TWI ltd, the DTI and the EPSRC for co-funding this project which was carried out in the frame of the Postgraduate Training Partnership (PTP) scheme.

I would like to thanks Professors D. J. Fray and A. H. Windle for the provision of laboratory facilities in the Department of Materials Science and Metallurgy at the University of Cambridge. I am also very grateful to my supervisors Pr. Harry Bhadeshia, Dr. Paul Woollin and the recently deceased Dr. Trevor Gooch for their advice and encouragement.

Special thanks are due to Dr. Toshihiro Tsuchiyama and Dr. Yann de Carlan for sharing with me their experiences and practical knowledge of martensitic stainless steels. I am especially grateful to Doctors Peter Hart, Lee Smith, Andrew Leonard and Andrea Gregori for their assistance and useful discussions at TWI.

I am also grateful to the present and past members of the Phase Transformations group; in particular, Franck Tancret, Miguel Yescas-Gonzalez, Pedro Rivera, Dorothy Elder, Victoria Yardley, Daniel Gaude Fugarolas, Harsha Lalam, Gareth Hopkins, Philippe Opdenacker, Carlos Garcia Mateo, Hiroshi Matsuda, Shingo Yamasaki, Matthew Peet and Thomas Sourmail.

Finally, I would like to thank my wife Angelique and my parents for their constant love and support throughout the project.

Abstract

Supermartensitic stainless steels have recently been introduced in the oil and gas industries to substitute more expensive duplex stainless steels for onshore and offshore tubing applications. Although easily joined by arc welding processes, the service life of the supermartensitic welded joint in corrosive environments relies to a large extent on the behaviour of the heat-affected zone (HAZ). The microstructure of the HAZ in these new materials has, until now, received little attention.

The work presented in this thesis is concerned with the experimental study of the microstructure developing in the HAZ of a range of supermartensitic stainless steels, with particular attention to the retention of the potentially detrimental δ-ferrite phase, and the development of a model to facilitate the choice of a suitable post-weld heat-treatment temperature.

The microstructural examination of a variety of welds revealed the presence of retained δ-ferrite in dual-phase and grain-coarsened HAZ regions. Under normal welding conditions, δ-ferrite retention was more pronounced in dual-phase HAZ and in molybdenum containing alloys. However, in multipass welds, δ-ferrite distribution was non-uniform as a result of reheating effects.

A number of methods of estimating δ-ferrite retention have been employed. The most corrosion-resistant alloys were successfully predicted to be more prone to δ-ferrite retention.

Charpy impact toughness tests performed on simulated heat-affected zones revealed a weak effect of δ-ferrite on the HAZ ductile to brittle transition temperature. In fact, due to its larger grain size, the coarse-grained HAZ determined the impact properties of the tested HAZ.

Finally, a neural network in a Bayesian framework has been created to estimate the temperature of the onset of austenite formation as a function of the employed heating rate. The model helps the determination of the appropriate tempering temperature of welded joints to avoid partial austenitisation and can be applied to martensitic stainless steels and low-alloy steels.

Contents

Nomenclature and Abbreviations

a	thermal diffusivity
Ac_1 and Ac_3	temperature of the onset and completion (respectively) of austenite formation on heating
Ae_1 and Ae_3	equilibrium temperature of the onset and completion (respectively) of austenite formation
Ac_4 and Ac_5	temperature of the onset and completion (respectively) of δ-ferrite formation on heating
Ae_4 and Ae_5	equilibrium temperature of the onset and completion (respectively) of δ-ferrite formation
d_{hkl}	interplanar spacing for plans (hkl)
h_j	expression of the tanh function for a neural network with j hidden units
I_γ and $I_{\alpha'}$	integrated intensity from a given plane from austenite and martensite respectively
k	the boltzman constant
M_S	martensite-start temperature
M_F	martensite-finish temperature
q	intensity of the heat source
R	the gas constant
r	radial distance from the weld center line
T	the temperature
T_p and T_0	peak and preheat temperatures of a weld thermal cycle
T_q	quenching temperature
t	time
V_γ and $V_{\alpha'}$	volume fraction of austenite and martensite
v	arc velocity
w_{ij}	weight attributed to the input i in a model of j hidden units
y	general expression of the function modelled in a neural network

α	alpha-ferrite
δ	delta-ferrite
γ	austenite
γ_r	retained austenite
σ_y	yield stress
η	arc efficiency
λ	thermal conductivity
b.c.c.	body-centred cubic
b.c.t.	body-centred tetragonal
f.c.c.	face-centred cubic
DBTT	Ductile to Brittle Transition Temperature
EDX	Energy Dispersive X-ray analysis
FF	Ferrite Factor
FN	Ferrite Number
FP	Ferrite percentage
HAZ	Heat-Affected Zone
HVN	Hardness Vickers Number
LVDT	Linear Velocity Displacement Transducer
MAP	Materials Algorithms Project library
MT-DATA	Metallurgical and Thermochemical Databank
PRE	Pitting Resistance Equivalent
PWHT	Post-Weld Heat-Treatment
SEM	Scanning Electron Microscopy
SGTE	Scientific Group Thermodata Europe
SSC	Sulfide Stress Cracking
TEM	Transmission Electron Microscopy
TWI	The Welding Institute, Cambridge UK
UNS	Unified Numbering System
WRC	Welding Research Council

Chapter 1

Introduction to supermartensitic stainless steels

The purpose of this chapter is to present the metallurgy and properties of recently developed supermartensitic stainless steels.

1.1 Introduction

1.1.a Materials selection

During the past ten years, the oil and gas production industries have encouraged steel manufacturers to develop corrosion-resistant and economically-viable alloys for onshore and offshore pipeline applications. The materials must have [1, 2] :

1. Adequate corrosion resistance to a range of species found in water that may be produced together with oil and gas, including CO_2, Cl^- and H_2S, at temperatures up to 150 °C and at pH values as low as 3.

2. High yield strength (about 550 MPa) to allow the use of thinner pipes with a saving in weight and cost.

3. Good low temperature impact toughness in case of emergency closure of the well-head.

4. The capacity to be easily and reliably joined by welding (good weldability) with short or no post-weld heat-treatment (PWHT).

A comparison of the costs of typical materials used in the manufacture of pipelines is reported in table 1.1. Although at the bottom of the price scale, the use of carbon steels for transportation of corrosive media may not be a financially good choice due to the need for corrosion protection, inspection, maintenance and early replacement of corroded parts. Stainless steels on the other hand, are more expensive, due mainly to their high nickel and chromium concentrations. However, their inherent corrosion resistance precludes the need for frequent inspection and maintenance and therefore are increasingly employed as pipeline materials [3, 4].

Amongst the different families of stainless steels, ferritic/austenitic (duplex) stainless steels match all the design criteria but their high nickel and chromium concentrations still render them uneconomic. On the other hand, cheaper martensitic alloys such as AISI 410 or 420 (table 1.2) possess high yield strength but lower corrosion resistance, toughness and weldability. However, these properties can be enhanced by adding nickel and molybdenum in suitable amounts and by reducing the carbon content. These latter modifications led to the introduction of the so-called *supermartensitic* stainless steels.

	C	**Cr**	**Ni**	**Mo**	**Price**
Carbon steel	0.26	0	0	0	1000
Duplex stainless steel 2205	≤ 0.03	22	5	3	4300
Supermartensitic stainless steel	~ 0.01	12	6	2.5	3200

Table 1.1: Comparison of prices (in $ per tonne) of alloys used for flowlines applications. All compositions given in wt% [5].

Compared with their ancestors, supermartensitic stainless steels have enhanced resistance to general and localised corrosion and improved sulfide stress-corrosion cracking resistance at ambient temperature (figure 1.1). In addition, they possess higher yield and tensile strength than duplex stainless steels (table 1.4) and are about 25 % cheaper (table 1.1). This combination of factors renders the new steels extremely attractive and further market growth is expected.

Grade	C	Mn	Si	Cr	Ni	Mo
403	0.15 max	1.00	0.5	11.5 - 13.0	0	0
410	0.15 max	1.00	1.00	11.5 - 13.5	0	0
414	0.15 max	1.00	1.00	11.5 - 13.5	1.25 - 2.50	0
420	0.15 min	1.00	1.00	12.0 - 14.0	0	0

Table 1.2: Part of the AISI 400 series. All chemical compositions given in wt% [6].

Table 1.3 lists some typical compositions developed to cover a range of corrosion resistance and price. The best corrosion resistance is achieved with the richly alloyed grades (*i.e.* 12 Cr 6.5 Ni 2.5 Mo wt%).

Alloy	C	N	Si	Mn	Cr	Ni	Mo	Cu	Ti
11Cr 2.5Ni	0.011	0.006	0.10	1.77	10.6	2.4	0.06	0.48	0.006
12Cr 4.5Ni 1.5Mo	0.017	0.011	0.20	1.77	11.7	4.9	1.39	0.51	0.007
12Cr 6.5Ni 2.5Mo	0.018	0.011	0.09	1.72	12.6	6.5	2.32	0.49	0.008

Table 1.3: Typical compositions (in wt%) of supermartensitic stainless steels developed by CLIFAFER [8].

1.1.b Constituents of supermartensitic stainless steels

Supermartensitic stainless steels are essentially alloys based on iron but containing chromium, nickel and molybdenum. They owe their name to their room temperature martensitic microstructure. To understand the metallurgy of this family of steels, attention is paid to the effects that the key alloying elements have on phase stability and properties.

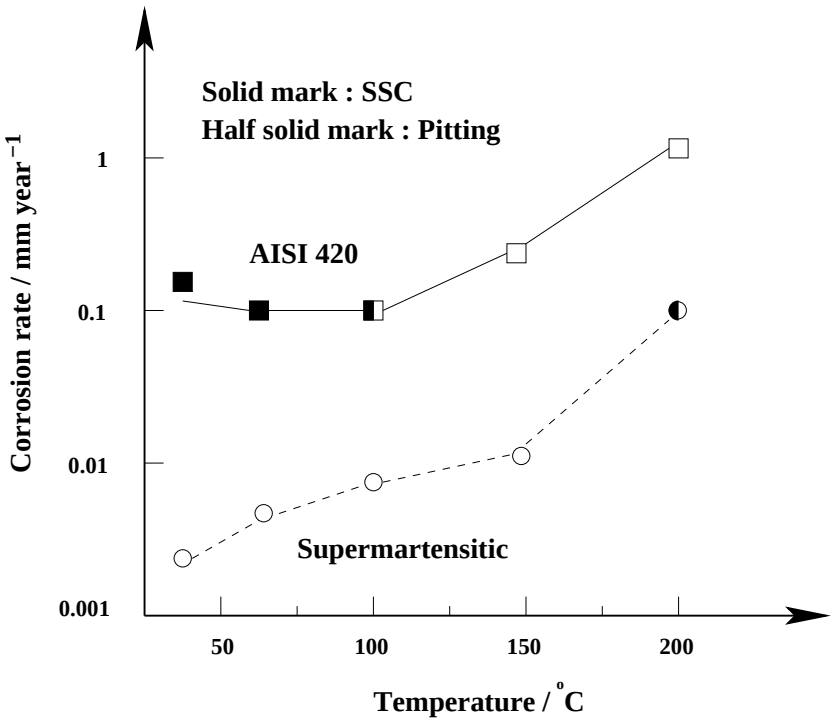

Figure 1.1: Effect of temperature on corrosion rate, localised corrosion and sulfide stress-cracking (SSC) of a conventional AISI 420 and a supermartensitic stainless steel (0.02 C 12 Cr 5.5 Ni 2 Mo wt%) [7]. Experimental conditions : 0.001 MPa H_2S, 3 MPa CO_2, 5 % NaCl, 100 % yield stress, immersed for 336 h.

i Chromium

Chromium is a ferrite stabiliser which has the property of being able to protect itself with a passive oxide film and to contribute this property to other metals with which it is alloyed. Stainless steels owe therefore their corrosion resistance to chromium and a minimum of 10.5 wt% of this element is required to generate a thin, adherent, continuous oxide film on the surface of the alloy. The exact composition of such oxide films is difficult to determine, but they all contain chromium in (III), (IV) and (VI) oxidation states in varying proportions [9]. Paradoxically, the oxide film itself is formed by rapid corrosion of the steel surface. However, once established it dramatically stifles the rate of further oxidation by acting as an insulating barrier between the metal and the corrosive environment. The steel is thus said to be in a state of passivity [10, 11].

Alloy	Y.S. (MPa)	T.S. (MPa)
11Cr 2.5Ni	598	753
12Cr 4.5Ni 1.5Mo	769	918
12Cr 6.5Ni 2.5Mo	733	931
22Cr 5Ni 3Mo	480	680
25Cr 7Ni 3.5Mo	550	760

Table 1.4: Yield strength (Y.S.) and tensile strength (T.S.) at room temperature of steels presented in table 1.3 and two typical duplex stainless steels [8].

Figure 1.2 shows part of the Fe-Cr constitution diagram according to Bungardt [12]. By analogy with iron and ordinary steels, the body-centered cubic (figure 1.3) ferrite precipitated from the melt is known as δ-ferrite, while ferrite resulting from transformation of austenite during cooling is called α-ferrite. The two types of ferrite show differing grain structures. δ-ferrite is often coarse when compared with α-ferrite and its morphology retains features of the solidification microstructure.

Low carbon Fe-Cr stainless steels have either a ferritic or martensitic, possibly semi-ferritic, microstructure depending on composition :

- When the chromium content is below approximately 12 wt% it is possible to obtain a martensitic microstructure since the steel can be made fully austenitic at elevated temperatures. Such steels solidify as δ-ferrite and are completely transformed to austenite (γ) at high temperature, followed by relatively rapid cooling to transformation into non-equilibrium martensite.

- A chromium content greater than approximately 14 wt% gives a completely ferritic stainless steel over the whole temperature range corresponding to the solid state and hence cannot be hardened on quenching.

- Between the austenite phase field and the fully ferritic domain, there is a narrow range of compositions which defines the semi-ferritic alloys, with a

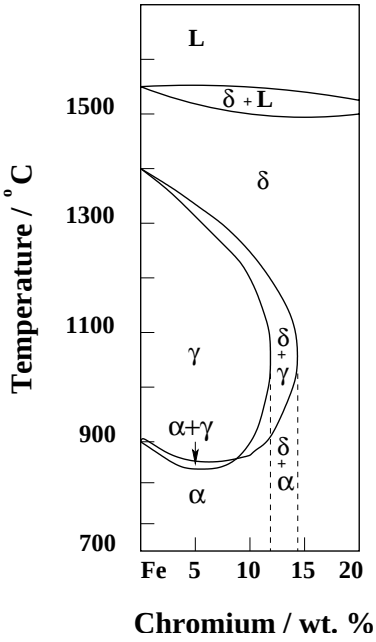

Figure 1.2: Range of liquid, austenite and ferrite (α and δ) phase in the iron-chromium constitution diagram with a carbon content below 0.01 wt%.

microstructure consisting partly of δ-ferrite which remains unchanged following solidification, the remainder being martensite.

Considering that a minimum of 10.5 wt% Cr is required to obtain passivity and that a chromium content above 12 wt% produces semi-ferritic microstructures, martensitic stainless steels have their chromium content in the range 10.5-12 wt%. At this concentration, hardenability is considerably improved making the steels air hardenable.

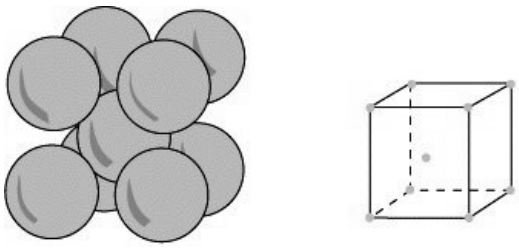

Figure 1.3: Schematic view of the body centered cubic (b.c.c.) structure of ferrite.

ii Molybdenum

To increase corrosion resistance for transportation of oil and gas, the addition of molybdenum is essential. Alloying with molybdenum reduces the general corrosion rate, improves the resistance to localised corrosion at elevated temperatures and also reduces sulfide stress-corrosion cracking susceptibility (figure 1.4) [12-16]. However, being a strong ferrite stabilising element (figure 1.5), it must be balanced by the addition of austenite stabilising elements such as carbon, nitrogen or nickel. Depending on the corrosivity of the environment the amount of molybdenum used ranges between 0-3 wt%.

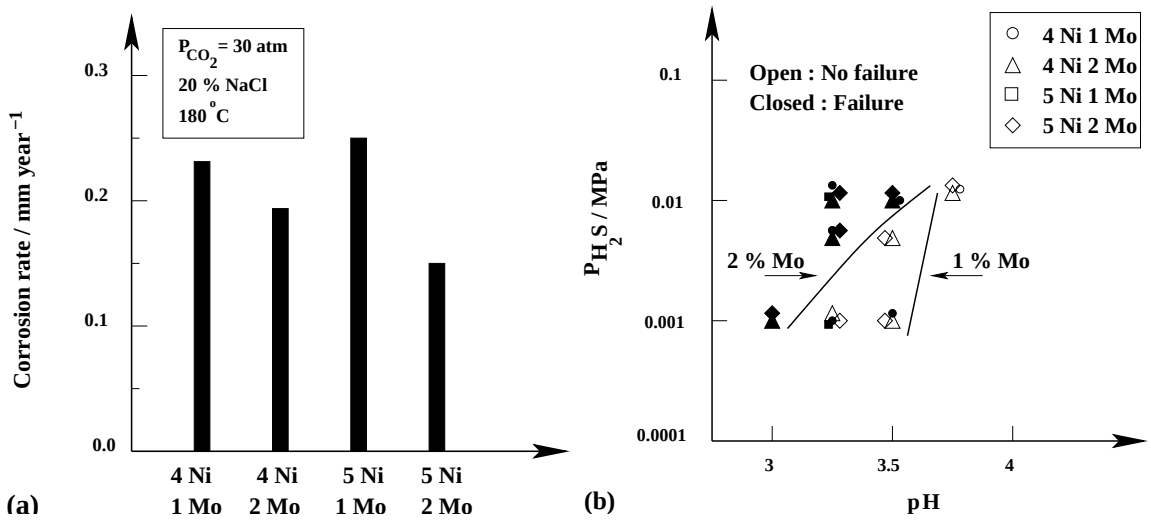

Figure 1.4: (a) Effect of molybdenum on CO_2 corrosion resistance at 180 °C for two different nickel concentrations (specimens immersed for 7 days). (b) Effect of molybdenum on the resistance to sulfide stress-corrosion cracking (applied stress: 100 % yield strength). Base composition 0.025 C 13 Cr 0.45 Mn wt% [13].

iii Carbon and nitrogen

It is necessary to expand the austenitic field to maintain the completely martensitic microstructure in the presence of molybdenum. In this respect, carbon and nitrogen are strong austenite stabilisers in Fe-Cr alloys (figure 1.6). However, in supermartensitic stainless steels, both the carbon and nitrogen contents have to be kept as low as possible, about 0.01 wt%. This is because martensite hardness increases sharply with carbon concentration and therefore raises the probability of sulfide stress corrosion-cracking and hydrogen-induced cold-cracking. On the other

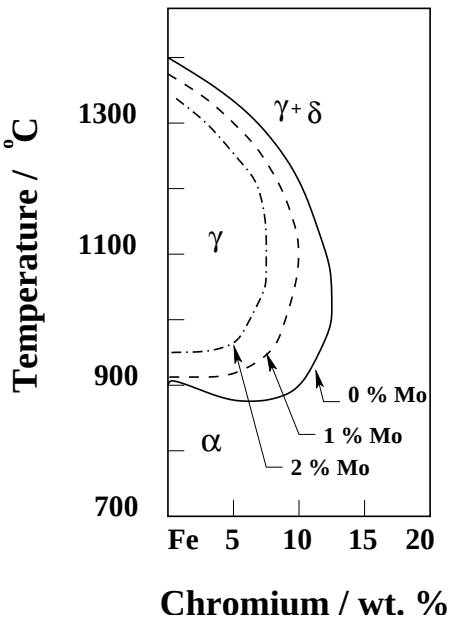

Figure 1.5: Effect of molybdenum on the austenite phase stability field in the Fe-Cr phase diagram [10].

hand, carbon and nitrogen in the presence of 11-13 wt% chromium and 0-3 wt% molybdenum, can lead to the formation of a range of precipitates such as $M_{23}C_6$ and M_2X, which diminish the effective chromium and molybdenum concentrations in solid solution and therefore decrease corrosion resistance [11, 14, 15, 16].

iv Nickel

As both the carbon and nitrogen concentrations must be kept low, austenite can be stabilised using substitutional solutes. Nickel has the strongest effect in this respect (figure 1.7) and also a tendency to improve toughness.

v Phase balance in 0.01 C wt% Fe-Cr-Ni-Mo system

Based on microstructural observations, Kondo *et al.* have produced a diagram (figure 1.8) representing the boundaries of martensite, δ-ferrite and austenite regions obtained at room temperature in 0.01 wt% C Fe-Cr-Ni-Mo system [14]. They showed that as the Mo concentration was increased from 0 to 2 wt%, the area corresponding to the fully martensitic structure was considerably reduced. According to their

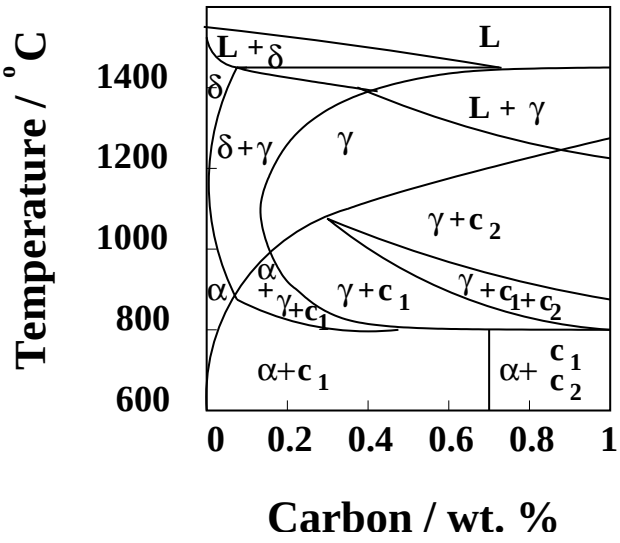

Figure 1.6: Phase fields in the ternary iron-chromium-carbon at 13 wt% Cr, L, c_1 and c_2 refer to liquid, $M_{23}C_6$ and M_7C_3 respectively [10].

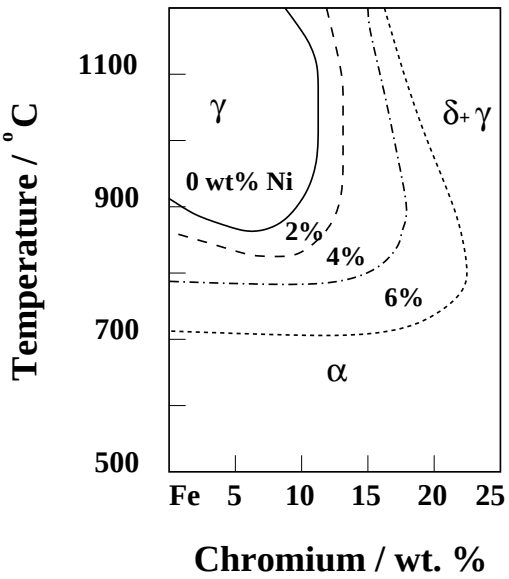

Figure 1.7: Influence of nickel on the range of the austenite phase field in the iron-chromium system [10].

diagram a 13 Cr, 2 Mo wt% steel, should have nickel concentration in the range 4 to 8 wt%. Above 8 wt%, increasing amount of austenite are retained in the microstructure. This is because the martensite-start temperature (M_S, equation 1.1, [17]) is depressed below room temperature and consequently the diffusionless transformation of austenite into martensite cannot be completed unless cryogenic treatments are employed.

$$M_S(^\circ\mathrm{C}) = 540 - 497\mathrm{C} - 6.3\mathrm{Mn} - 36.3\mathrm{Ni} - 10.8\mathrm{Cr} - 46.6\mathrm{Mo}\ \mathrm{wt}\% \qquad (1.1)$$

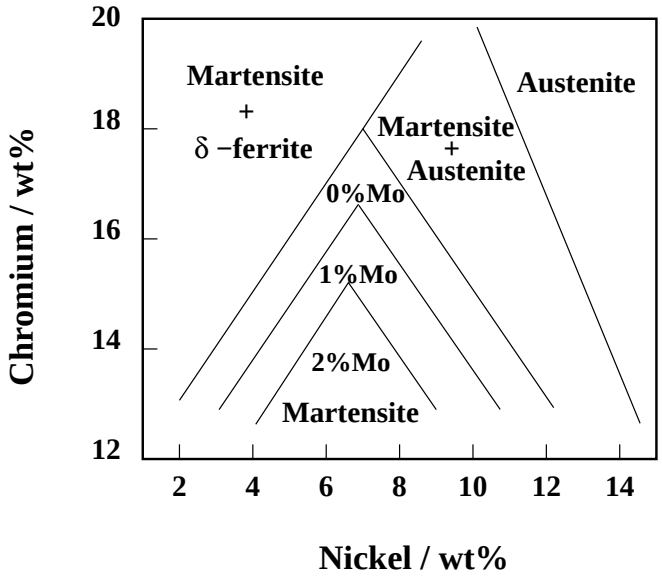

Figure 1.8: Experimental diagram showing the boundaries of the austenite, ferrite and martensite phases as a function of Cr, Ni and Mo concentration for 0.01 wt% C after austenitisation at 1050 °C and air cooling [14].

vi Other elements

Some other alloying elements are added to supermartensitic stainless steels to facilitate their processing and modify their properties in one direction or another. The effects are summarised below :

Austenite stabilising elements

- **Manganese**, is added in concentrations up to 2 wt % to substitute some of the more expensive nickel. It is also used as a deoxidiser [18].

- **Copper**, is believed to improve corrosion resistance in CO_2 or CO_2/H_2S environments. However, different investigators disagree on the extent of its effect on corrosion resistance [13, 16]. Copper is also reported to increase yield strength and reduce toughness if added in concentrations greater than 1-2 wt% [16, 19, 20].

Ferrite stabilising elements

- **Silicon**, is a strong ferrite former, essential as a deoxidiser during refining of the steel. However, to maintain a fully austenitic microstructure at elevated temperatures its concentration does not generally exceed 0.7 wt% [18].

- **Titanium**. By forming very stable carbo-nitrides, Ti(C,N), titanium has an effect comparable with that of a decrease in the carbon and nitrogen content. It limits the precipitation of chromium, molybdenum or vanadium carbonitrides such as M_2X and MX which may reduce corrosion resistance and cause secondary hardening during tempering [14]. The minimum titanium content required to prevent these effects is four times the carbon plus nitrogen concentration (wt %) due to the stoichiometry of Ti(C,N). However, excessive additions lead to the precipitation of intermetallic compounds such as TiNi instead of Ti(C,N) [14, 18]. Titanium is also effective in maintaining a finer microstructure in the weld heat-affected zones due to the pinning effect of stable TiN precipitates [14].

Impurity elements such has sulfur and phosphorus are always kept as low as possible, typically below 50 ppm and 200 ppm respectively, to maintain good hot workability and reduce the susceptibility to sulfide stress-corrosion cracking [18].

1.2 Types of corrosion

The types of corrosion and stress-corrosion encountered in oil and gas wells can be divided into three classes; corrosion by CO_2 (so-called sweet-corrosion), cracking in sour H_2S containing media (so-called sulfide stress-cracking or SSC, typically in association with CO_2 and Cl^-), and an intermediate regime of cracking in moderately sour media (so-called mildly sour region). The tolerable concentration of hydrogen sulfide in the corrosive fluid has yet to be clarified for safe use of supermartensitic stainless steels but partial pressures as low as 0.1 bar (compared with possibly 30 bar for CO_2) lead to rapid failure. The most serious CO_2 corrosion problems are encountered in deep wells ($\geq$ 5000 m), where the increase in pressure and temperature make the environment more aggressive. The causes and mechanism of the most common forms of corrosion encountered in pipelines are introduced below.

1.2.a Uniform attack

Uniform attack is a form of electrochemical corrosion that occurs all over the exposed surface and often leaves behind a scale or a deposit. In oil and gas flowlines, CO_2 is generally responsible for such attacks. Carbon dioxide is a weak acidic gas which must hydrate to carbonic acid (H_2CO_2) to become corrosive. The latter process is slow but accelerates with an increase in temperature and CO_2 partial pressure [2]. General corrosion behaviour is usually measured by weight loss.

1.2.b Pitting

Pitting is an insidious type of localised corrosion, often going undetected and with very little material loss until failure occurs. Pits may be initiated at localised inner-surface defects such as scratches or slight variations in composition [4]. They ordinarily appear inside the linepipes and penetrate towards the outer surface. The mechanism for pitting is probably due to oxidation within the pit itself, with complementary reduction at the surface. The solution at the pit becomes more concentrated, acidic and dense as pit growth progresses.

The pitting resistance equivalent number (PRE) has been introduced to estimate

the relative pitting corrosion resistance in terms of the chromium, molybdenum and nitrogen concentrations [21]. Although, originally derived for austenitic stainless steels, the use of the PRE formula (equation 1.2) is commonly extended to duplex and occasionally to martensitic stainless steels. Supermartensitic and duplex stainless steels have PRE numbers in the range 12 to 20 and 20 to 40 respectively. Table 1.5 lists the range of chemical composition over which the formula has been derived.

$$PRE = \mathrm{Cr} + 3.3\mathrm{Mo} + 16\mathrm{N}\ \mathrm{wt}\% \tag{1.2}$$

Element	Composition range (wt %)
Cr	18.6 - 25.3
Mo	2.2 - 4.4
N	0.048 - 0.22

Table 1.5: Composition range of confidence for the pitting resistance equivalent formula [21].

1.2.c Stress-corrosion cracking

Stress-corrosion cracking results from the combined action of an applied tensile stress and a corrosive environment. Small cracks form and then propagate in a direction perpendicular to the applied stress, with the result that brittle failure may eventually occur. Cracks may form at relatively low stress levels, significantly below the tensile strength. The stress that produces stress-corrosion cracking need not be externally applied; it may be residual stress resulting from rapid temperature change and uneven contraction, or difference in expansion coefficients in two-phase alloys [4].

1.2.d Hydrogen embrittlement

Hydrogen-induced cracking and hydrogen stress-cracking are two manifestations of hydrogen embrittlement. Macroscopically speaking, hydrogen embrittlement is

similar to stress-corrosion in that a normally ductile metal experiences brittle fracture when exposed to both a tensile stress and hydrogen resulting from metal dissolution in a corrosive atmosphere. Hydrogen-induced cracks are most often transgranular, although intergranular fracture is observed for some alloy systems. Hydrogen in its atomic form diffuses interstitially through the crystal lattice, and concentrations as low as a few parts per million can lead to cracking [4]. A number of mechanisms have been proposed to explain hydrogen embrittlement: most of them are based on the interference of dislocations with dissolved hydrogen.

1.2.e Sulfide stress cracking

Sulfide stress-corrosion cracking is a special case of hydrogen embrittlement commonly associated with high strength steels. As shown in figure 1.9 this type of cracking arises from corrosion reactions with subsequent absorption of hydrogen in the metal.

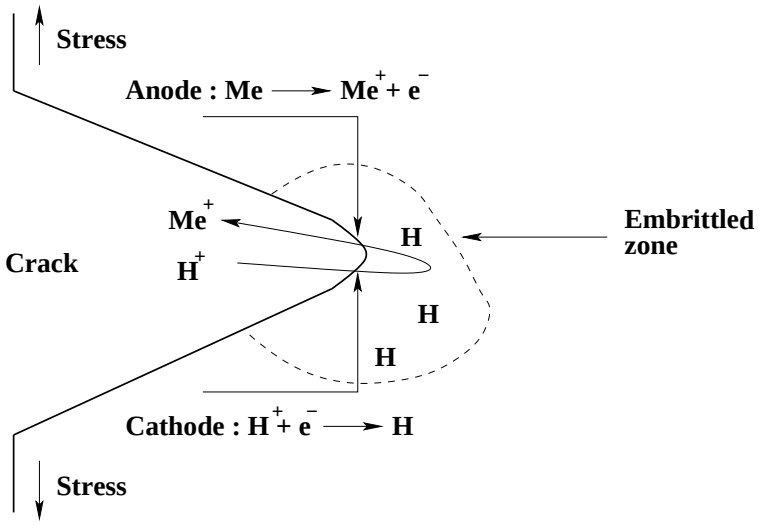

Figure 1.9: Mechanism of hydrogen absorption in sulfide stress-corrosion cracking [22].

The presence of sulfur from H_2S accelerates embrittlement by retarding the formation of molecular hydrogen and thereby increasing the residence time of atomic hydrogen on the metal surface and hence its absorption. Kondo *et al.* found that

the most favourable solution to improve sulfide stress cracking resistance consisted of decreasing the steel hydrogen content by reducing the general corrosion rate. Indeed, decreasing the corrosion rate results in a decrease of hydrogen generated on the steel surface, which in turns reduces the hydrogen permeation rate and hence decreases the steel hydrogen content [14].

Hardness criteria are generally used for ranking of steels with regard to sulfide stress-corrosion cracking resistance. The maximum hardness limit to avoid the potential for sulfide stress cracking in martensitic stainless steels in CO_2 and H_2S is 23 HRC (about 240 HV) according to the requirement of the National Association Corrosion Engineers (NACE) standard MR0175 [23].

1.3 Phases present and mechanical properties

1.3.a Martensite

Martensite is the desired predominant phase in martensitic stainless steels. Its presence is a consequence of the diffusionless transformation of austenite during cooling to room temperature. The carbon which was in solid solution in the octahedral interstices in the austenite phase, becomes trapped in the martensite which contains three times as many octahedral interstices arranged in three sublattices. If the carbon atoms order into one of these sublattices then the martensite adopts a body-centered tetragonal crystal system.

Martensitic transformation in supermartensitic steels is *athermal*, meaning that the amount of martensite formed depends only on the undercooling below the M_s temperature and not on the time at temperature. This behaviour is expressed in the Koistinen and Marburger equation [24] :

$$V_m = \exp(-0.011 \times (M_s - T_q)) \tag{1.3}$$

where V_m is the fraction of martensite and T_q is the quenching temperature below M_s.

The displacement associated with martensite formation is an invariant-plane strain, in which the shear is accompanied by a volume change normal to the invariant plane (habit plane). The shear strain is approximately 0.22 and the dilatational strain about 0.03 [25]. These strains are large and force the martensite to adopt a thin-plate shape in order to better accommodate the shape deformation. In alloys containing less than about 0.6 wt% C, the martensite forms as laths which are aligned parallel to one another. The laths are grouped into larger structural entities, called blocks and packets (figure 1.10) [26]. The microstructure of lath martensite is generally too fine to be revealed using optical microscopy, necessitating the use of electron microscopy [4].

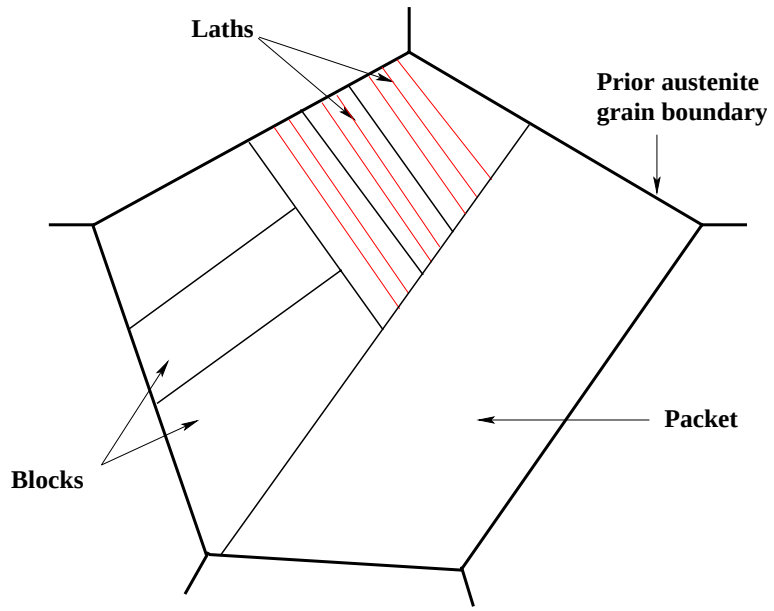

Figure 1.10: Schematic illustration of the microstructural features of lath martensite.

i Martensite hardness and toughness

The tetragonal strain caused by carbon trapped in the structure renders dislocation motion difficult and therefore martensite is harder than austenite. Martensite hardness increases dramatically with the carbon content (table 1.6), but with only 0.01 wt% C, supermartensitic stainless steel martensite is relatively soft. Martensite hardness is also claimed to be affected by the presence of nitrogen. In this respect,

nitrogen has been found to be 2.5 times less effective than carbon, but this effect is not widely recognised [27].

Carbon content / wt%	0.068	0.133	0.206	0.450	0.600
Hardness HV_{10kg}	364	462	480	580	620

Table 1.6: Effect of carbon content on martensite hardness in 12 Cr 0.25 Si 0.02 N (wt%) steels, after quenching from 1050 °C [11].

Richly alloyed supermartensitic stainless steels possess low M_s temperatures (typically 200 °C) and consequently little or no auto-tempering of the martensite occurs during cooling to room temperature. The quenched and tempered condition helps to optimise both strength and toughness. In industrial practice, the tempering treatment is generally carried out few degrees above Ac_1 to accelerate martensite recovery and to precipitate some carbo-nitrides [28]. Due to the small carbon and nitrogen concentrations, precipitation is limited and thus the loss of corrosion resistance due to tempering is minimal.

All body-centered cubic metals, including supermartensitic stainless steels, show a marked temperature dependence of the fracture toughness, as indicated in figure 1.11. At high temperatures fracture occurs normally by ductile rupture, whereas cleavage is the dominating fracture mode at low temperatures. The low carbon content of supermartensitic steels and appropriate tempering treatment ensure reduced transition temperatures so that satisfactory toughness can be achieved even at low temperatures, as shown on figure 1.12.

1.3.b Retained austenite

Austenite (f.c.c. structure figure 1.13) might be present in supermartensitic stainless steels as a result of two different processes. As mentioned before the addition of substitutional elements depresses M_S temperature and consequently cooling from the austenitic field might lead to uncomplete martensitic transformation. On the other hand, austenite can be retained in the microstructure as a result of an

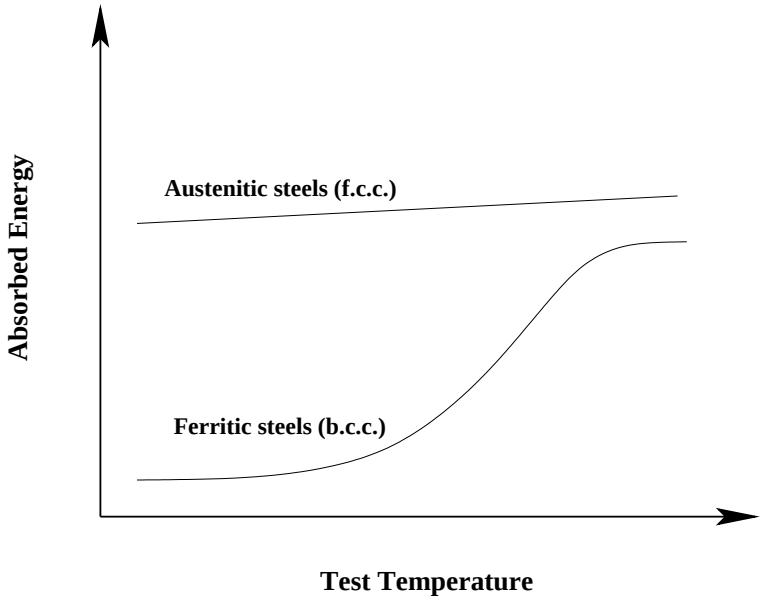

Figure 1.11: Effect of temperature on notch toughness for face-centered and body-centered cubic structures [22].

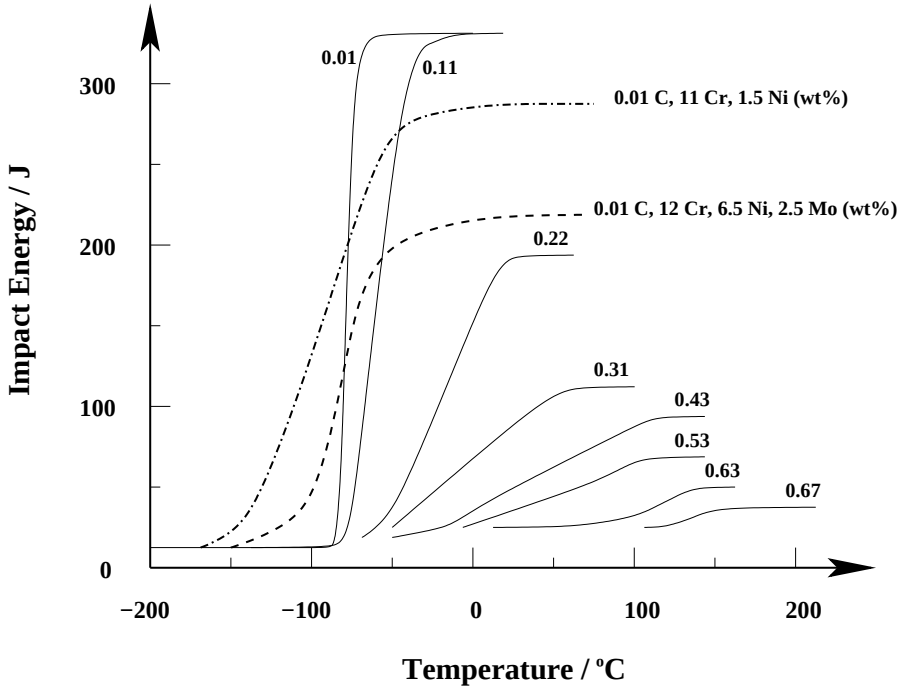

Figure 1.12: Influence of carbon content on the Charpy V-notch energy versus temperature behaviour in steels and comparison with supermartensitic stainless steels [29, 30].

intercritical annealing treatment *i.e.* carried out above the temperature of the onset of austenite formation on heating (Ac_1). In this case the stability of the reverted austenite is dependent upon the heat-treatment duration and temperature. If Ac_1 is exceeded by say 40 °C, only a small quantity of austenite is formed. Because the transformation is diffusional the austenite is enriched in elements such as nickel, carbon and nitrogen. The latter enrichment strongly depresses M_S temperature and consequently austenite remains stable after cooling. At temperatures where the equilibrium austenite content is large, the relative enrichment is reduced, and cooling to room temperature leads to complete martensitic transformation [31].

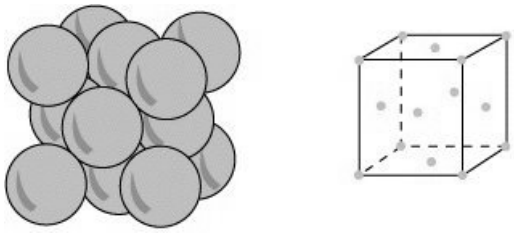

Figure 1.13: Schematic view of the face-centered cubic (f.c.c.) structure of austenite.

Diagrams giving quantitative estimates of the room temperature austenite contents have been developed on a range of low carbon nickel-containing martensitic stainless steels after various reheating treatments (figure 1.14). Austenite reversion usually commences when the Larson Miller parameter, P, exceeds $\sim$ 16 equating to tempering for 16 min at 550 °C or 75 s at 600 °C. Most of the reverted austenite formed between $P \sim 16$ and 17.5 remains stable on cooling. Above $P \sim 18$ reverted austenite becomes increasingly unstable and transforms to untempered martensite on cooling. The maximum volume percentage of reverted austenite that remains stable after isothermal treatments and cooling to room temperature does not generally exceed 30-35 % [1,32-37]

i Hardness and toughness in the presence of retained austenite

Figure 1.15 relates the hardness of the microstructures obtained after various heat-treatments, to the tempering parameter P. Below a tempering parameter of $\sim$ 18, the presence of austenite reduces hardness, but once this parameter is exceeded,

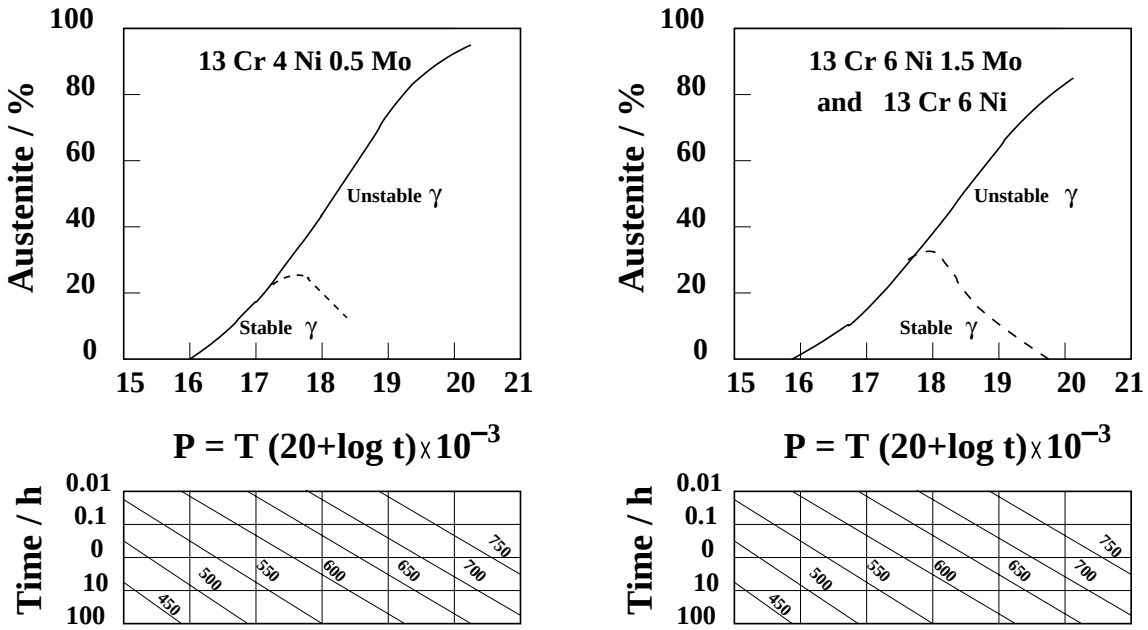

Figure 1.14: Effect of various tempering conditions on austenite reformation and stability in low carbon martensitic stainless steels [1]. P is the Larson Miller parameter. Temperature (T) and time (t) are expressed in Kelvin and hours respectively.

hardness increases sharply due to the formation of fresh, untempered martensite.

The toughness improves in the presence of stable finely dispersed films of austenite in low carbon martensitic stainless steels [39, 40, 41]. It has been argued that when retained austenite is present near a propagating crack, the concentrated strain field at the crack tip induces transformation into martensite. This mechanically-induced transformation would absorb energy and thus increase the toughness. The associated volumetric expansion of the martensitic transformation would tend to close the crack and relieve stresses at its tip. The latter mechanism absorbs strain energy during fracture and therefore limits crack extension [42].

ii Corrosion resistance in the presence of retained austenite

In titanium free supermartensitic alloys containing 0.02 wt% C, the retention of austenite formed during intercritical annealing was found beneficial to corrosion resistance [33]. The latter was attributed to the dissolution of chromium and molyb-

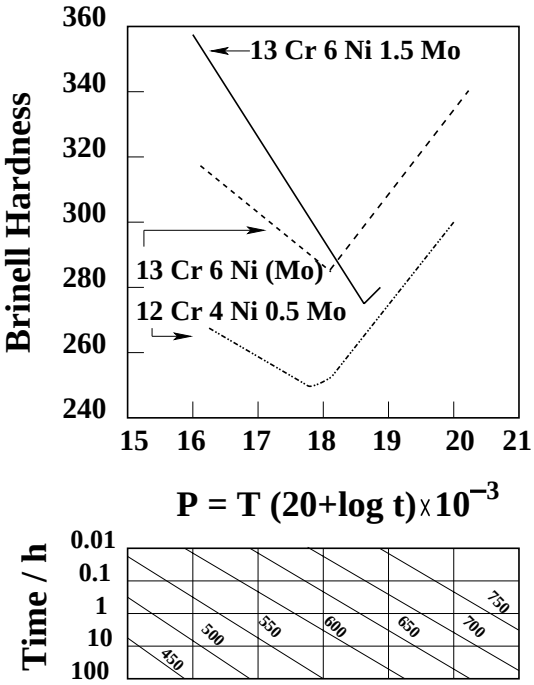

Figure 1.15: Effect of various tempering conditions on hardness of low carbon martensitic stainless steels [38].

denum carbo-nitrides in the favour of austenite. Since there was no chromium and molybdenum loss in the matrix the corrosion resistance was improved.

Similarly, sulfide stress-corrosion cracking improvements were reported in a titanium stabilised supermartensitic steel containing austenite. It is believed that austenite[1] absorbs hydrogen from martensite and thus contributes to lower its concentration [32, 33]. The hardness reduction caused by austenite presence may, however, be another explanation. Consequently, austenite in supermartensitic stainless steels does not have harmful effects on corrosion resistance.

[1]Austenite has a higher solubility for hydrogen than martensite.

1.3.c Ferrite

In general the presence of δ-ferrite in the microstructure of martensitic stainless steels is undesirable. The effects of its presence on the properties are presented below.

i Hardness

The hardness of ferrite in low carbon semi-ferritic and martensitic stainless steels ranges between 150 and 200 HVN [43]. These values are typically 100-150 Vickers lower than low carbon fresh martensite and therefore low carbon semi-ferritic stainless steels exhibit reduced yield and tensile strength compared with fully martensitic steels [38, 44].

ii Impact toughness

Ferrite at low temperatures is notch sensitive and fails in a brittle manner. In martensitic stainless steels, ferrite presence in excess of 10 % can result in an approximate 50 % reduction in impact values [11, 45].

iii Corrosion resistance

In early AISI type 410 and 420 grades, ferrite was found in the microstructure as a result of variations in balance between ferrite and austenite stabilising elements within the specification. Sulfide stress-corrosion cracking tests showed cracking to occur in martensite rather than in ferrite. The reduction of ferrite volume fraction by the addition of nickel to AISI type 410 steel did not lead to any improvement of the sulfide stress-corrosion cracking resistance. Rather than acting to initiate cracks, ferrite was reported to obstruct crack propagation and fail in a ductile mode. This behaviour was attributed to the lower hardness of ferrite [46].

The effect that δ-ferrite has on the sulfide stress cracking resistance of tempered unstabilised supermartensitic stainless steel parent materials was also recently reported. Cracking occurred at the δ-ferrite/martensite interface due to the chromium depletion associated with the precipitation of chromium carbo-nitrides during tempering [47].

1.4 Summary

The metallurgy of martensitic stainless steels has been improved to respond to the need for more cost-effective corrosion-resistant alloys for applications in oil and gas transportation. The constituents and phases present in the microstructure of the new alloys as well as the mechanical and corrosion resistance properties have been reviewed. The tempered martensitic microstructure of the parent materials is highly desirable to ensure corrosion resistance, high strength and good low temperature toughness.

The next chapter concentrates on the welding of supermartensitic stainless steels and on the properties of the welded joint.

Chapter 2

Welding and heat-affected zone microstructures and properties

The ability to weld supermartensitic stainless steels, both in land based and in offshore constructions, is critical to their successful exploitation. However, welding significantly affects the optimised microstructure in the region next to the weld metal, the so-called heat-affected zone (HAZ). As a result, the HAZ is the critical part of the weldment.

In this chapter, the welding processes employed to weld supermartensitic stainless steel pipes are first introduced, the different HAZ regions and their properties are then presented and finally the methods to estimate δ-ferrite retention in welded joints are reviewed.

2.1 Introduction to fusion welding

Welding in one of the most popular joining methods for steels. Fusion welding involves the application of a heat source to melt the edges of two surfaces, with or without the help of a filler wire. The mixing of molten material from the workpiece and molten drops of filler material creates a weld pool, which when solidified forms the joint between the two components. The method by which heat is generated in order to fuse the base metal and filler wire defines the nature of the welding process. The fusion welds of concern to this study are formed by arc welding which is now described in some more detail.

2.1.a Arc welding processes

Although there are numerous arc welding systems, their general configuration remains the same. A power source generates an arc between an electrode and the workpiece, creating a temperature which in some regions is in excess of 10,000 °C. All arc welding processes use a shielding system to protect the molten weld metal from the air.

Gas Tungsten Arc (GTA) Welding

This process, also called tungsten inert gas (TIG), uses non-consumable electrodes made from tungsten alloys because of their extremely high melting temperatures ($\sim$ 3000 °C). Nevertheless, the electrode tip is usually cooled to ensure it remains solid. Filler material is supplied by a rod or wire, which melts as it is fed close to the electrode tip. The weld pool is shielded by an inert gas, typically argon or helium, piped in around the electrode. The TIG process usually generates clean welds with high standards of weld metal quality in all welding positions and can be mechanised. A schematic diagram of the arc area and components of the TIG process is shown in figure 2.1.

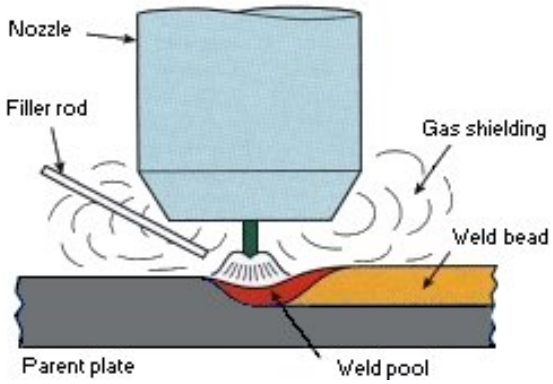

Figure 2.1: Schematic view of gas tungsten arc welding [48].

Metal Inert Gas (MIG) Welding

This process also called gas metal arc welding (GMAW) uses a continuous wire which is fed through the weld torch (figure 2.2). The mode of liquid metal transfer from the electrode to the base metal can be varied by choosing different types of gases. All metals can be welded using gas mixtures based on argon or carbon dioxide. This process gives high metal deposition rates and can be automated, but offers less control than TIG.

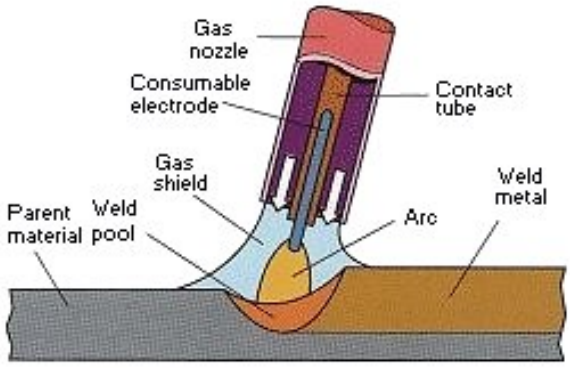

Figure 2.2: Schematic view of manual gas metal arc welding [48].

Manual Metal Arc (MMA) Welding

A consumable coated electrode is employed (figure 2.3). The coating provides elements, which act as arc stabilizers, generate gases and a slag cover to protect the weld pool from the environment. The coating sometimes contains alloying elements, which help determine the weld composition. The simplicity of the process makes it popular, but the lack of control over the weld bead and possibly high inclusion levels might not be satisfactory for critical applications.

2.1.b Variables associated with welding

The most important variables are the process, chemical composition of the weld deposit, heat input, the initial temperature of the parent material (pre-heat), temperature of the weld deposit during multirun welding (interpass temperature), and

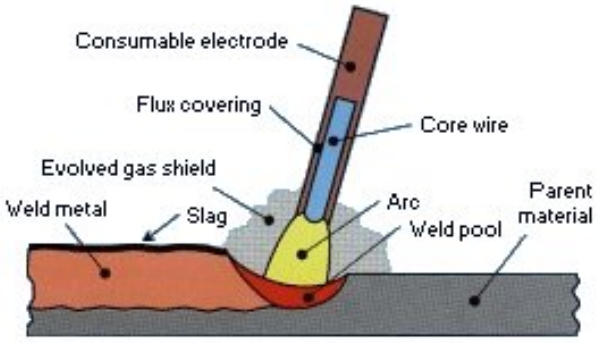

Figure 2.3: Schematic view of manual metal arc welding [48].

heat-treatment given after welding (post-weld heat-treatment). The type of joint and the material thickness are also important parameters.

In any welding process, the weld thermal cycle is composed of rapid heating to a high temperature followed by rapid cooling. The heating and cooling rate are both governed by the amount of heat input, defined as :

$$\text{Net heat input (J m}^{-1}) = \frac{\eta I V}{\upsilon} \tag{2.1}$$

where I is the current in Amperes, V is the voltage applied between the power source terminal and electrode expressed in volts, υ is the travel speed of the heat source in m s^{-1} and η the arc transfer efficiency. In most of arc welding processes the efficiency is between 0.6 and 0.99 [49].

2.2 Welding of supermartensitic stainless steels

2.2.a Hydrogen-induced cold cracking

Due to the hardness and brittleness of martensite, early martensitic steels are considered to be the most difficult family of stainless steels to weld. During welding, the transformation of austenite into martensite is accompanied by an abrupt decrease in the solubility of hydrogen. The latter may result in supersaturation and

cause the liberation of molecular hydrogen at micro-defects in the HAZ or the weld metal. This liberation in molecular form introduces high stresses that are liable to initiate cracks at room temperature in hard and brittle structures [50].

The reduced carbon concentration of supermartensitic stainless produces a soft and ductile martensite, which when welded with a low hydrogen-generating process, renders the risk of cold cracking virtually to nil. This represents a considerable improvement compared with the earlier higher carbon martensitic stainless steels. Supermartensitic alloys are therefore said to have improved weldability.

2.2.b Welding consumables

In general, supermartensitic stainless steels are welded using either matching electrodes or superduplex stainless steel weld metal (typical composition 25 Cr, 10 Ni, 3.5 Mo, 0.25 N wt%). Matching composition consumables, now commercially available, may be selected when the weld metal has to be stronger than the parent materials *e.g.* when installation is by reeling. On the other hand, superduplex welding alloys are employed when the weld metal must have a better corrosion resistance and toughness [51].

2.2.c The welded joint

As illustrated in figure 2.4, a welded joint can be divided into two major regions, the fusion zone and the heat-affected zone. The fusion zone experiences temperatures above the melting point of the material and represents both the deposited metal and the parts of the base metal melted during welding. The heat-affected zone on the other hand, represents the portion of the base metal where all microstructural changes induced by welding occur in the solid state.

i HAZ regions

Ideally, the heat-affected zone should have the same homogeneous tempered martensitic structure as the parent material. However the gradient of temperature in the HAZ leads to a corresponding gradient of microstructure and therefore different HAZ regions can be identified. The regions due to a single-pass root weld in a supermartensitic stainless steel have recently been characterised using optical

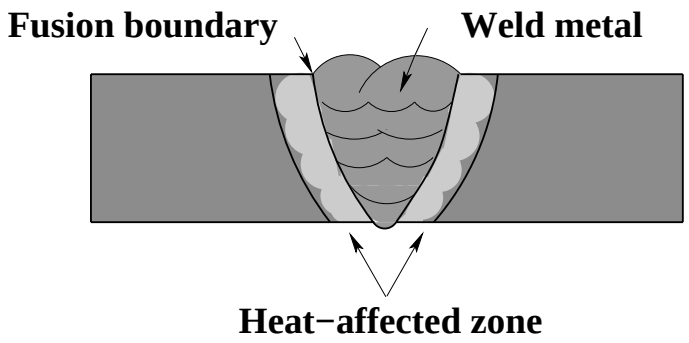

Figure 2.4: A fusion weld [52].

microscopy by Enerhaug *et al.* as follows (figure 2.5) [53] :

(i) Partially melted region, located adjacent to the fusion boundary. This is where incipient melting of the newly formed δ-ferrite occurs on heating.

(ii) Region which transforms completely to δ-ferrite on heating with significant grain growth, also called the coarse-grained HAZ (CG-HAZ).

(iii) High-temperature two-phase region characterised by partial transformation of austenite to δ-ferrite on heating.

(iv) Region which completely transforms to austenite during heating.

(v) A low peak temperature two-phase region, characterised by partial transformation of the tempered martensite to austenite during heating.

However, as mentioned before, the HAZ represents the area where all phase transformations occur in the solid state and therefore the partially melted region should not be regarded as belonging to the HAZ. The other regions can be artificially classified into two categories depending on the maximum temperature they experienced before cooling, the high temperature and the low temperature HAZ. The high temperature HAZ (HT-HAZ) includes the prior δ-ferrite region and the high temperature two-phase region while the low temperature HAZ (LT-HAZ) refers

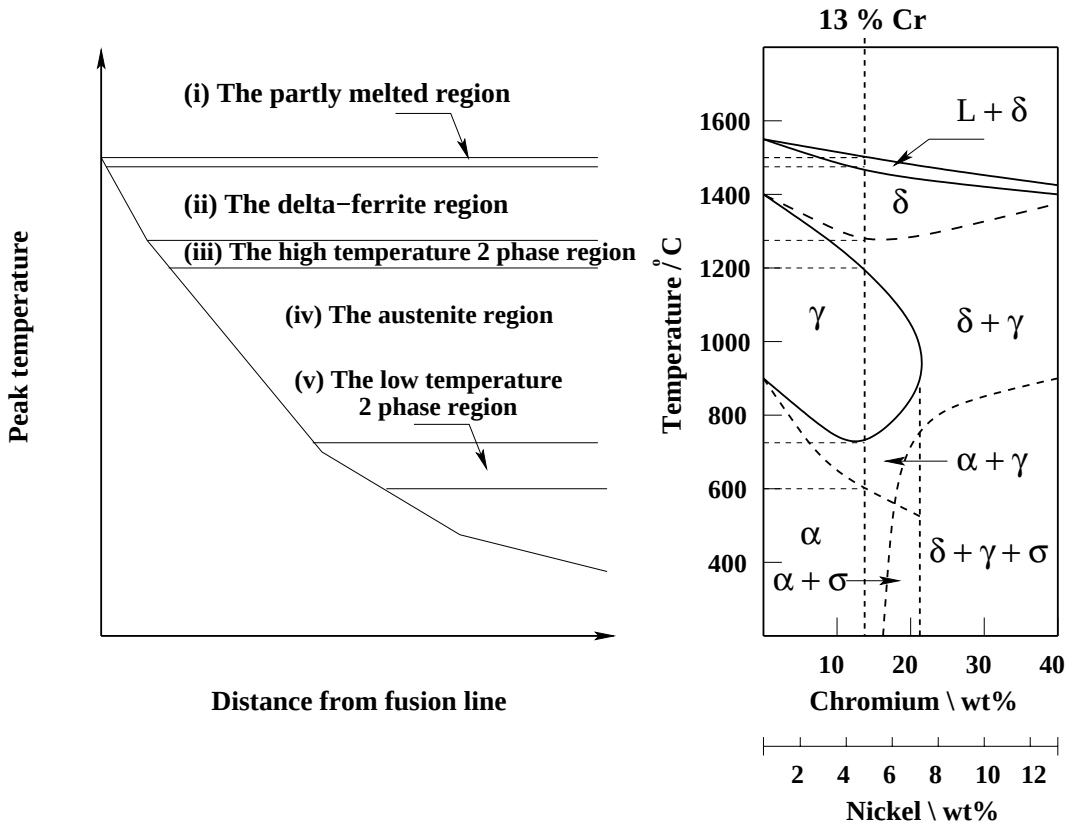

Figure 2.5: Schematic diagram illustrating structural changes that occur within heat-affected zone of single-pass supermartensitic stainless steel weld [53].

to the remainder of the HAZ.

The work by Enerhaug *et al.* was published during the time scale of the present project and is the only study where the presence of δ-ferrite is clearly shown in the high temperature HAZ. Although the different HAZ regions were presented, confusions were made between the partially melted and prior fully ferritic regions in the discussion.

2.3 HAZ properties

The welded joint service behaviour relies to a large extent on the response of the HAZ to the external environment and stresses. Recently, catastrophic fractures

or cracks have been reported in HAZ of supermartensitic stainless steels tested in conditions representative of field environment [54, 55].

2.3.a Hardness

There exists a hardness profile in HAZ caused by the different microstructures that develop during welding [53]. As figure 2.6 illustrates, from the parent material the hardness first increases to reach a maximum level of typically 350-375 HV and then tends to slightly decrease as the high temperature regions of the HAZ are reached. The initial hardness increase is attributed to the formation of fresh martensite in regions heated up above Ac_1, while the reasons for the decrease are not documented but might be caused by grain size effect or the presence of δ-ferrite.

The hardness level of 350 HV is not suitable for optimum sulfide stress cracking resistance but can be reduced by the use of expensive and often unpractical post-weld heat-treatment (PWHT).

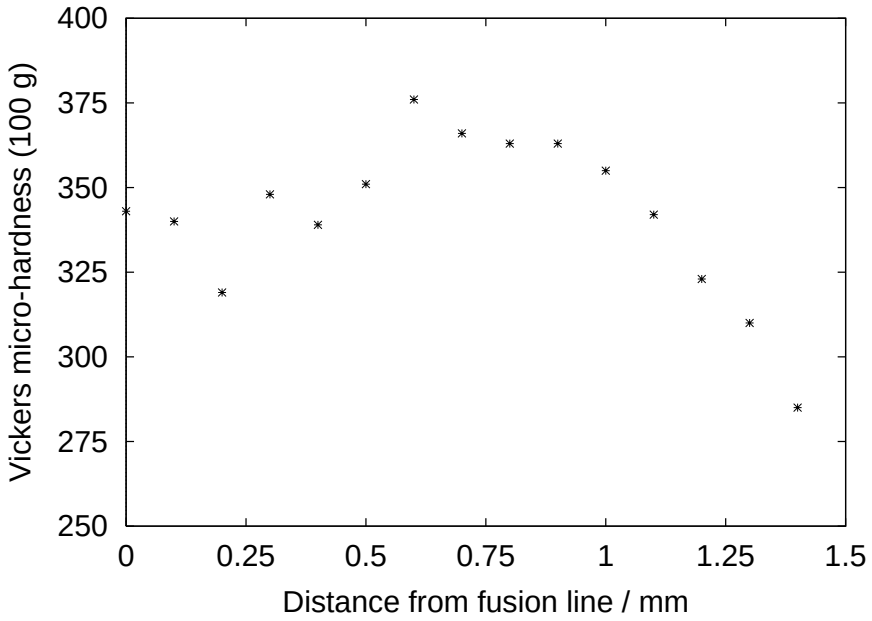

Figure 2.6: Micro-hardness distribution in single-pass TIG bead-in-groove weld HAZ in an unstabilised 12 Cr 6 Ni 2 Mo (wt%) alloy. Arc energy 0.35 kJ mm^{-1} [56].

When employed, PWHT are usually carried out at temperatures of the order of

650 - 700 °C for 5 to 10 minutes [44]. At those temperatures there is a risk of partial austenitisation and subsequent transformation to hard martensite in some regions of the HAZ. To avoid this problem, it is advisable to perform PWHT at temperatures just below Ac_1.

2.3.b Charpy toughness

In general, supermartensitic steels are capable of giving high HAZ toughness values, although in most of the published work the quoted HAZ results probably include some parent material and/or weld metal. Typical results for a 12 Cr 5 Ni 2 Mo (wt%) alloy indicate values well in excess of 200 J at -60 °C.

i Effect of δ-ferrite

Since the presence of δ-ferrite in HAZ of supermartensitic stainless steels is not established, its effect on impact toughness has never been published. However, the reduced impact toughness of the HAZ of martensitic stainless steels containing substantial amount of δ-ferrite (semi-ferritic stainless steels) such as the one illustrated in figure 2.7, is well documented.

The HAZ of semi-ferritic stainless steels can either be mainly ferritic with some martensite or conversely mainly martensitic with some ferrite. When ferrite is the major phase in HAZ, the presence of grain boundary martensite lowers the ductile to brittle transition temperature. This is because austenite has higher solubility for carbon than ferrite and transforms to hard martensite during cooling. The martensite then acts as an internal stress raiser and thus increases the probability of cleavage of the surrounding ferrite [57, 58]. On the other hand, predominantly martensitic HAZ have reduced toughness when ferrite is present even in small quantities [59].

ii Effect of austenite

The effect of the presence of austenite in HAZ of supermartensitic alloys on impact properties is not yet established. However, in supermartensitic weld metals the presence of finely dispersed films of austenite was shown to yield higher impact values at subzero temperatures [60].

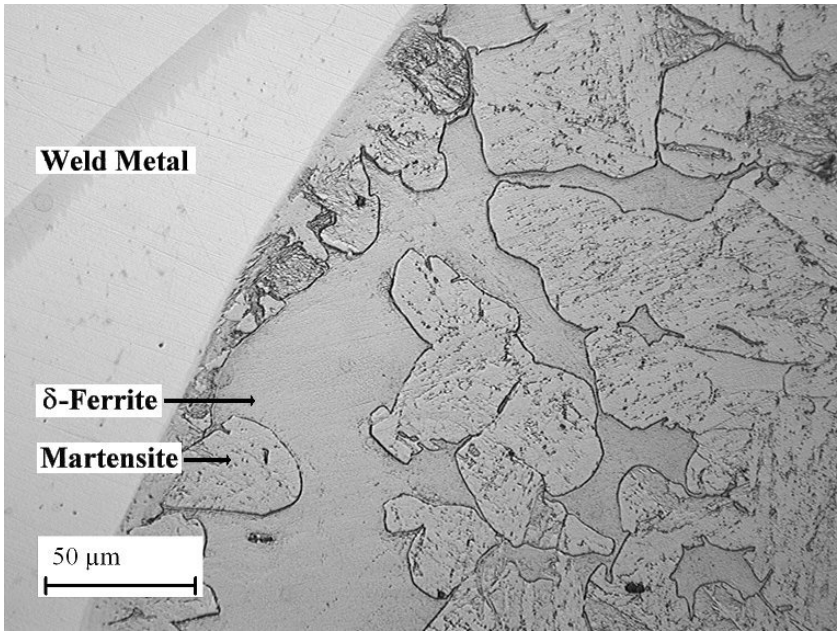

Figure 2.7: Optical macrograph showing large amount of δ-ferrite in high temperature heat-affected zone of a multipass weld performed on a semi-ferritic stainless steel (0.01 C 12 Cr 0.5 Ni in wt%). Picture from this work.

A study of thermally simulated HAZ carried out on a range of supermartensitic stainless steels revealed that austenite was no longer present in HAZ regions cooled from temperatures exceeding 1200 °C [30]. Consequently, unless a specific intercritical post-weld heat-treatment is carried out, no retained austenite is to be expected in the high temperature HAZ of single-pass welds.

2.3.c Grain size

A small grain size in HAZ is important for strength and toughness. The dependence of the yield strength on grain size is given by the Hall-Petch relationship [61]:

$$\sigma_y = \sigma_i + k_y d^{-1/2} \tag{2.2}$$

where d is the grain diameter, σ_y is the yield stress, σ_i is the friction stress opposing the movement of dislocations in the grains and k_y is a constant.

The derivation of the Hall-Petch equation relies on the formation of a dislocation pile-up at a grain boundary, one which is large enough to trigger dislocation activity in an adjacent grain. Yield in a polycrystalline material is in this context defined as the transfer of slip across grains. A larger grain is able to accommodate more dislocations in a pile-up, enabling a larger stress concentration at the boundary, thereby making it easier to promote slip in the nearby grain [62]. For martensitic structures, however, dislocation sources are found at grain boundaries, which is different from Hall-Petch approach, which considers dislocation sources within individual grains. In this case the increase in strength due to martensite lath size is given by :

$$\sigma_G \simeq 115(\bar{L})^{-1} \tag{2.3}$$

where $\bar{L}$ is the mean linear intercept taken on random sections and at random angles to the length of any lath section.

There is no general mechanism by, which grain refinement improves toughness. The argument for steels is that carbide particles are finer when the grain size is small. Fine particles are more difficult to crack and any resulting small cracks are difficult to propagate, thus leading to an improvement in toughness.

2.3.d Corrosion resistance

The corrosion performance of supermartensitic stainless steels HAZ is claimed to match that of the parent material both with respect to general corrosion and sulfide stress-corrosion cracking [44]. In practice, however, the HAZ suffers preferential pitting corrosion compared to weld metal and parent material. Enerhaug *et al.* found that the HAZ microstructure was not the major factor affecting the pitting corrosion resistance but rather the nature and the thickness of the oxide film on the steel surface [53]. Pitting was observed at a distance of about 5 to 7 mm from the fusion line (low temperature HAZ) and it could be concluded that the presence of δ-ferrite in HAZ did not necessarily reduce pitting corrosion resistance. However, it should be noted that no PWHT was applied and as mentioned in chapter 1, δ-ferrite was found to lower sulfide stress-corrosion cracking resistance in the tempered condition. Therefore, at present it is not clear whether the presence of δ-ferrite affects the HAZ corrosion resistance.

2.4 Ferrite prediction

Since little work has been performed on δ-ferrite retention in supermartensitic stainless steels HAZ, and as this phase is apparently undesirable, it is interesting to know where and when it forms and to be able to estimate its content. This section reviews some of the work that has been performed on δ-ferrite formation and decomposition in martensitic stainless steels and then introduces the methods available to predict δ-ferrite retention in weld metals and HAZ of a range of stainless steels.

2.4.a Formation and decomposition of δ-ferrite

Ferrite forms in the HAZ of martensitic stainless steels during continuous heating after the Ac_4 temperature has been exceeded. Like, Ac_1 and Ac_3, Ac_4 temperature increases with the employed heating rate but to a lower extent (*i.e.* 30 °C difference between heating rates of 8 and 300 °C s^{-1}) [63]. If the alloy has the capacity to become fully ferritic, as is the case in the micrograph shown in figure 2.7, then the ferritisation is finished at the Ac_5 temperature. Above this temperature, grain growth occurs until melting starts at the solidus temperature.

However, not all martensitic stainless steels have the capacity to become fully ferritic. Indeed, a detailed study of δ-ferrite formation and dissolution has been performed by Fenn on a relatively high carbon containing martensitic stainless steel called HT9 (table 2.1) [63]. The microstructures of quenched thermally simulated HAZ of this alloy were never found completely ferritic. Indeed, optical micrographs showed prior austenite grain boundaries decorated with δ-ferrite in HAZ regions close to the fusion line. The uncomplete ferritisation was apparently not due to δ-ferrite dissolution since cooling rates slower than 2 °C s^{-1} were required for ferrite to decompose. As ferritisation is expected to be fast at elevated temperatures, steel HT9 should have been fully ferritic before cooling. To check the latter point, thermodynamic calculations have been performed using MT-DATA.

According to MT-DATA (figure 2.8), at temperatures above 1230 °C δ-ferrite nucleates and grows at the expense of austenite. At temperatures above 1410 °C,

the liquid phase appears and reacts with austenite to produce δ-ferrite (peritectic reaction) and shortly after δ-ferrite dissolves in favour of the liquid phase. Consequently, consistent with Fenn's observations steel HT9 could never be fully ferritised.

Material	C	Si	Mn	Cr	Mo	Ni	Nb	V	W
Sandvik HT9	0.21	0.37	0.48	11.20	1.00	0.52	0.01	0.30	0.02

Table 2.1: Chemical composition of steel HT9 (wt %) [63].

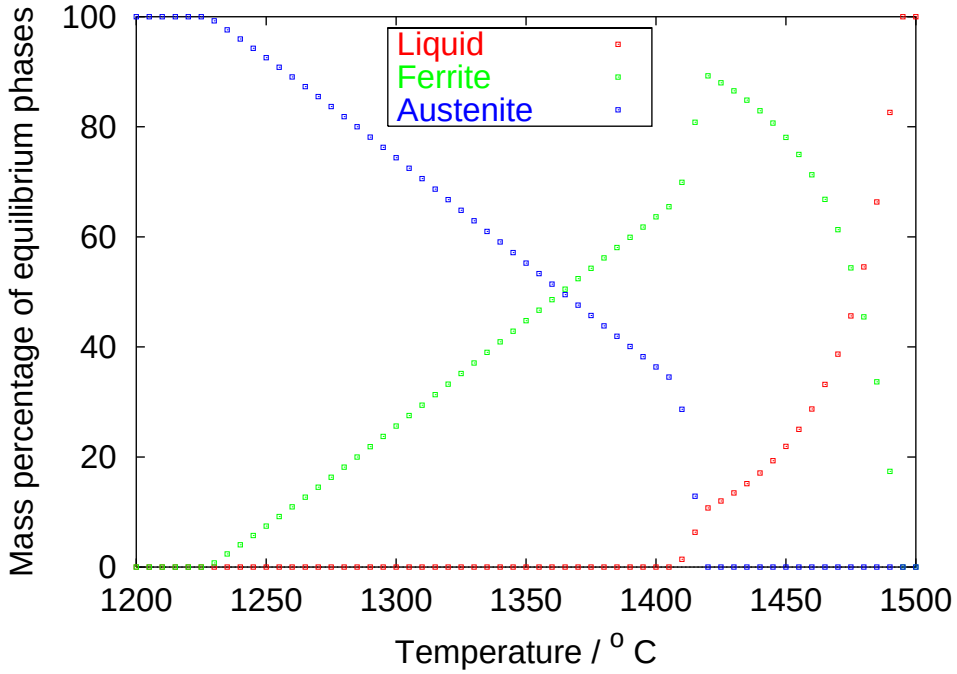

Figure 2.8: Results of MT-DATA equilibrium calculations performed on steel HT9. The calculations were performed using *plus* and $sub-sgte$ databases and by allowing austenite, ferrite and liquid phases.

According to the recent description of the different heat-affected zone regions of supermartensitic stainless steels by Enerhaug *et al.* (figure 2.5), supermartensitic alloys have the capacity to become fully ferritic before melting [53].

In stainless steels, it is well known that the decomposition of δ-ferrite is cooling rate dependent. Mundt and Hoffmeister and Singh *et al.* have studied the effect of cooling rate on the temperature of the onset of austenite reformation from δ-ferrite (Ar_4) on initially fully ferritised duplex and austenitic stainless steels [64, 65]. As the cooling rate was increased from 20 to 100 °C s^{-1}, the Ar_4 temperatures were depressed by about 60 °C. The reverse transformation therefore starts at temperatures where substitutional elements diffusivity is reduced and consequently contribute to uncomplete dissolution of δ-ferrite.

2.4.b Prediction of δ-ferrite retention in HAZ

i Physical modelling

A fundamental way of predicting δ-ferrite volume fractions consists of developing kinetic models. Hemmer compiled such a model for δ-ferrite retention in HAZ of electron beam welded duplex stainless steels [66]. The model accounts for both the effects of chemical composition and weld thermal cycle on δ-ferrite retention and grain size. The model was constituted of three parts. First, dissolution of austenite during heating at temperatures above Ac_4 (in the dual-phase regime), followed by δ-ferrite grain growth, and eventually, δ-ferrite dissolution during cooling to room temperature.

Due to the fast heating and cooling rates experienced during electron beam welding, paraequilibrium[1] was assumed in each part of the model. Thanks to the large amount of literature published on the studied materials, the validity of the model could be assessed and shown to compare well with experimental data. The following conclusions could be drawn. Increasing nitrogen concentration raised the temperature at which the microstructure was fully ferritic (Ac_5) and thus led to slower ferrite coarsening behaviour in HAZ. High Ac_5 temperature combined with smaller δ-ferrite grain size favoured austenite reformation during cooling.

[1]Carbon and nitrogen diffuse more rapidly than substitutional elements hence under rapid heating conditions, the latter elements are unable to partition during the time scale related to the welding operation.

2.4.c Prediction of δ-ferrite retention in weld metals

Most of the work dealing with prediction of δ-ferrite retention in stainless steels has been performed on weld metals. The following sections summarise the work of practical relevance.

i Measuring ferrite content

A problem encountered with the empirical determination of δ-ferrite is the considerable scattering of δ-ferrite values measured by different methods and in different laboratories. In austenitic and duplex stainless steels, that problem has been remedied by the introduction of a magnetic method based on the measurement of the force required to tear off a defined permanent magnet from the surface of the specimen. As the content of the ferro-magnetic δ-ferrite increases, the tearing force increases, while other not ferro-magnetic constituent such as austenite, carbides, sigma phase and inclusions have no influence at all. Thus the tearing force is an indirect measurement of δ-ferrite content. To indicate the difference compared to other existing methods, the measured ferrite value was designated as ferrite number (FN) rather than ferrite percentage (FP) [67]. Several relationships have been proposed to relate ferrite numbers to ferrite volume fractions as for example equation 2.4 which has been derived in the 0 - 15 FP range [68, 69, 70].

$$FN = 1.7 \times FP \tag{2.4}$$

Generally, the various correlations agree that the FN overstates the ferrite percent but they do not agree on the amount of overstatement.

The magnetic method of measuring ferrite content is, unfortunately not applicable to martensitic stainless steels since both martensite and ferrite are ferromagnetic. Therefore ferrite measurement in martensitic stainless steels is quantified using standard point counting methods as in ASTM E562-99 or image analysis.

ii Ferrite factor

The Kaltenhauser Ferrite Factor (FF) is a compositional relationship which is commonly employed to assess the tendency of stainless steels base metal to retain ferrite [71] :

$$FF = \mathrm{Cr} + 6\mathrm{Si} + 8\mathrm{Ti} + 4\mathrm{Mo} + 2\mathrm{Al} + 4\mathrm{Nb} - 2\mathrm{Mn} - 4\mathrm{Ni} - 40(\mathrm{C} + \mathrm{N})\ \mathrm{wt}\%$$

The relationship advanced in the late sixties was initially developed to yield a measure of the residual austenite content in ferritic stainless steel welds. The use of this relationship has been extended to martensitic stainless steels. However, Hewitt clearly showed the discrepancy associated with the use of the ferrite factor in the case of low carbon martensitic stainless steels (figure 2.9) [72].

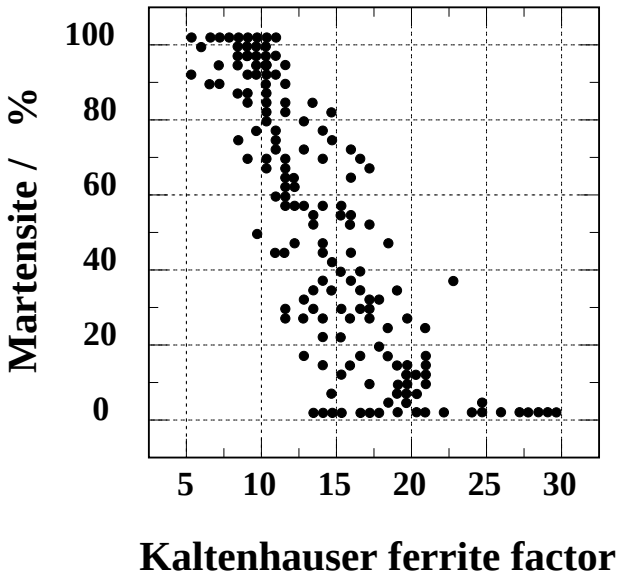

Figure 2.9: Percentage martensite versus ferrite factor [72].

The transition below the fully martensitic ($FF \leq 5$) and the fully ferritic microstructure ($FF \geq 25$) occur over a long ferrite factor range and show considerable scatter. As far as heat-affected zones are concerned, it has been reported that the transition occurs on a shorter ferrite factor range *i.e.* between 8 and 12 [73].

iii Diagrams

The Schaeffler diagram (Figure 2.10) developed in the fifties offers a convenient way of representing the effect of alloy composition on room temperature weld metal microstructure and phase volume fraction [74]. Phase boundaries of austenite, δ-ferrite and martensite are plotted in terms of the chromium and nickel equivalents.

The chromium equivalent has been empirically determined to take into account the effect of the common ferrite forming elements. Similarly, the nickel equivalent does the same for the austenite formers. The ratio between the two thus describes the proportions of each phase present in an alloy.

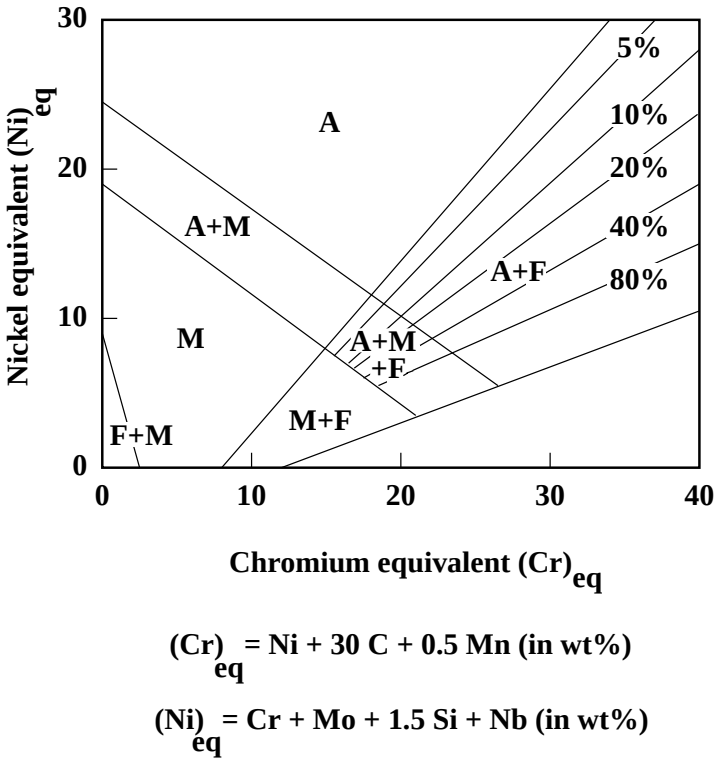

Figure 2.10: The Schaeffler diagram. F, M and A represent ferrite, martensite and austenite, respectively [11].

The Schaeffler diagram was improved upon by addition of a nitrogen contribution in the Delong diagram, which has in turn been further improved for modern steels by the WRC-1988 and WRC-1992 diagrams [67, 76, 77]. Those diagrams made predictions in terms of ferrite number (FN) instead of ferrite percent (FP). Further research devoted to the ferritic/martensitic region led more recently to the Balmforth *et al.* diagram [43, 75]. The latter diagram (figure 2.11) gives iso-ferrite contour maps in volume-percent ferrite and represents a significant improvement for prediction in the ferrite plus martensite region. Table 2.2 lists the modification brought to the Cr and Ni equivalent formulae and table 2.3 gives the composition range of confidence

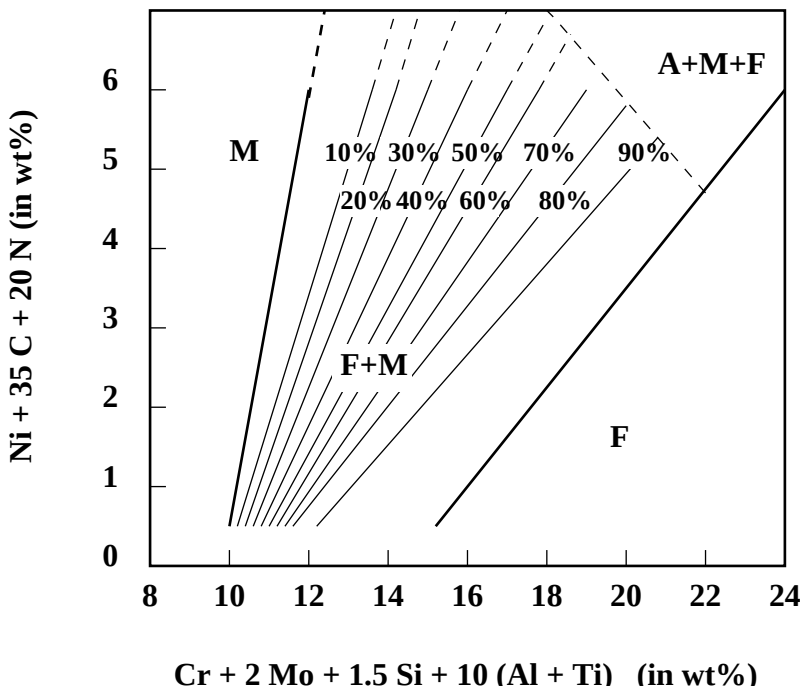

Figure 2.11: The new ferritic-martensitic diagram with iso ferrite lines in volume % [75].

for the Balmforth *et al.* diagram.

All diagrams offer a practical way of quantitatively estimating the room temperature microstructure of weld metals, however the effect that cooling rates can have on the phase balance are not accounted for.

iv Neural networks

Neural network models developed using both the WRC92 database and more recent data are available since 2001. These models can be used to predict more accurately the ferrite number of austenitic weld metals as a function of chemical composition [78, 79, 80]. Although the databases contain information mostly on austenitic steels, the use of the models can in principle be extended to martensitic stainless steels. Chapter 6 will investigate the capacity of one of those models to make predictions and comparisons between different supermartensitic stainless steels alloys.

Source	Year	Cr-Equivalent (wt%)	Ni-Equivalent (wt%)
Schaeffler	1949	Cr+Mo+1.5Si+0.5Nb	Ni+0.5Mn+30C
Delong *et al.*	1956	Cr+Mo+1.5Si+0.5Nb	Ni+0.5Mn+30(C+N)
Kaltenhauser	1971	Cr+6Si+8Ti+4Mo+2Al	4Ni+2Mn+40(C+N)
WRC-1992	1992	Cr+Mo+0.7Nb	Ni+0.25Cu+35C+20N
Balmforth *et al.*	2000	Cr+2Mo+10(Al+Ti)	Ni+35C+20N

Table 2.2: Evolution of the chromium and nickel equivalent formulae [43].

Element	Composition range
Cr	11 - 30
Ni	0.1 - 3.0
Si	0.3 - 1.0
C	0.07 - 0.2
Mn	0.3 - 1.8
Mo	0 - 2.0
Al	0 - 0.3
Ti	0 - 0.5
N	0 - 0.25

Table 2.3: Composition range of confidence for the new ferrite plus martensite diagram [75].

2.5 Summary

Due to their low carbon concentrations, supermartensitic stainless steels can reliably be arc welded. The service behaviour of the welded joint relies to a large extent on the microstructure developing in the HAZ. In this regard, the properties are likely to be altered by the presence of δ-ferrite in any marked extent in the high temperature HAZ. However, limited information is available on the presence of δ-ferrite and on the effects of the welding variables on its stability in the new steels.

On the other hand, fundamental modelling of δ-ferrite retention in HAZ is dependent upon the availability of reliable thermodynamic data and the capacity to predict weld thermal cycles.

Chapter 3

Experimental techniques

In this chapter the different techniques and equipment that have been employed in experiments are introduced.

3.1 Imaging

3.1.a Optical microscopy

To reveal the microstructures, specimens were first mounted in conductive bakelite then the newly formed surfaces were ground on SiC paper to grit 1200 and polished with a 1 μm cloth coated with diamond paste. The samples were finally etched using one of the three etchants listed in table 3.1. The use of different etchants was necessary to highlight specific features and phases and thus obtain complementary information on microstructures. Digital photographs were taken using a Leica DMR digital camera.

3.1.b Scanning Electron Microscopy

The fracture surfaces of Charpy specimens and the HAZ of a variety of welds were observed using a JEOL 5800 scanning electron microscope (SEM). Secondary electron mode was employed in each case and the machine was operated at an accelerating voltage of 15 kV.

Name	Composition	Etching procedure	Specificity
Villela's [81]	1 g $C_6H_3OH(NO_2)_3$ 5 ml HCl 100 ml C_2H_6OH	Immersion of sample for 20 to 30 s	Reveals martensite
Sulfuric [81]	20 ml H_2SO_4 0.01 g NH_4CNS 80 ml H_2O	Immersion of sample and electrolytic etching at 4 V for 20 s	Reveals δ-ferrite but not martensite
Stock [82]	1 g $K_2S_2O_5$ 20 ml HCl 80 ml H_2O	Immersion of sample until specimens becomes red	Reveals δ-ferrite in blue and martensite yellow/brown

Table 3.1: Compositions and conditions of use of etchants.

3.1.c Image analysis

The volume fractions of δ-ferrite in the various specimens have been determined using SigmaScan Pro 5.0 software using the following procedure. A series of digital micrographs obtained using either electron or light microscopy were taken from representative areas of the specimens. The images were first enhanced to use the full intensity spectrum and the total number of pixels in the image was determined. To highlight δ-ferrite, the intensity threshold method was employed and the sum of pixels constituting the selected features was performed. The ratio of the latter sum with the original number of pixels led to the determination of the volume fraction.

For the image analysis technique to be effective, pictures have to be taken under the same conditions of brightness and contrast and the δ-ferrite should have the same range of intensity throughout the image. Every effort was made to keep the lighting condition constant but due to the different etching responses of the materials this was not always achievable.

To estimate the uncertainty associated with this method, three measurements were performed on each image. The most likely intensity range corresponding to δ-ferrite was chosen in the first measurement, while in the two other the apparent minimum and maximum intensity ranges were chosen. This method was applied to two or three pictures of the area of interest and allowed measurement of the volume fraction of δ-ferrite and estimation of the associated error.

3.1.d Transmission Electron Microscopy

Some specimens were observed using transmission electron microscopy (TEM) to identify retained austenite in the parent materials and δ-ferrite in the HAZ. Thin foils were examined using a JEOL 200 CX TEM operated at 200 kV.

Sections were cut to create discs of 3 mm in diameter and approximately 50 μm thickness. The discs were electropolished in a solution of 5 % perchloric acid, 15 % glycerol and 80 % ethanol at an applied voltage of 50 V at room temperature.

Selected area diffraction could be used to distinguish austenite (f.c.c.) from low carbon martensite (b.c.c.). However, δ-ferrite and martensite could not be distinguished using diffraction since they both have the b.c.c. structure. This was however not a problem because δ-ferrite had a characteristic morphology that can be easily identified.

3.2 Chemical analysis

3.2.a EDX microanalysis

To examine potential partitioning of alloying elements some micro-analytical experiments were carried out using an energy dispersive X-ray (EDX) analysis system on a CAMSCAN CS144 scanning electron microscope. ZAF (atomic number, absorption, fluorescence) corrections were employed, the acquisition time was set to 100 s and the dead time was kept below 20 %.

3.2.b X-ray analysis

The volume fractions of retained austenite (V_γ) in the different specimens were measured using X-ray diffraction with Cu K_α radiation at 40 kV and 40 mA. A Phillips diffractometer was used with step scan mode to cover the angular 2θ range from 47.1 to 103 °. The 2θ step size was 0.05 ° with a dwell time of 30 s. Samples were ground and polished using the normal metallographic preparation procedure with two cycles of polishing and etching before the X-ray diffraction test to remove any deformed layer caused by polishing.

The volume fraction of austenite could be estimated from measurements of the integrated intensities of martensite[1] and austenite phases assuming they are the only phases present. The ratio of the intensities of diffraction peaks from two phases of a polycrystalline sample is given by equation 3.1 [83]:

$$\frac{I_{\gamma\ (hkl)}}{I_{\alpha'(hkl)}} = \frac{R_{\gamma\ (hkl)}}{R_{\alpha'(hkl)}} \times \frac{V_\gamma}{V_{\alpha'}} \tag{3.1}$$

where $I_{\gamma\ (hkl)}$ and $I_{\alpha'\ (hkl)}$ are the integrated intensity from a given plane (hkl) from the austenite and martensite (or ferrite) phase respectively. V_γ and $V_{\alpha'}$ are the volume fractions of austenite and martensite respectively, and $R_{\gamma\ (hkl)}$ and $R_{\alpha'(hkl)}$ are given for a specific peak by :

$$R = \frac{1}{v^2}[|F|^2(p)(L_p)]e^{-2m} \tag{3.2}$$

where :
v = volume of unit cell,
F = structure factor,
p = multiplicity factor,
L_p = Lorentz-polarization factor,
e^{-2m} = temperature factor.

Considering that all materials in reality exhibit crystallographic texture, the average integrated intensity for at least three specific reflections for austenite and

[1]Low carbon martensite and ferrite have similar structure.

martensite (table 3.2) were taken into account (equation 3.3 and 3.4).

Phase i	**Diffracting plane** (hkl)
Martensite 1	200
Martensite 2	211
Martensite 3	220
Austenite 1	200
Austenite 2	220
Austenite 3	311

Table 3.2: Diffracting hkl planes used for martensite and austenite.

$$\frac{I_\gamma}{R_\gamma} = \frac{1}{3}\sum_{i=1}^{3}\frac{I_i^\gamma}{R_i^\gamma} \tag{3.3}$$

$$\frac{I_{\alpha'}}{R_{\alpha'}} = \frac{1}{3}\sum_{i=1}^{3}\frac{I_i^{\alpha'}}{R_i^{\alpha'}} \tag{3.4}$$

The value of $V_\gamma/V_{\alpha'}$ in equation 3.1 can be obtained from the measurement of $I_\gamma/I_{\alpha'}$ and the calculation of $R_\gamma/R_{\alpha'}$. Once $V_\gamma/V_{\alpha'}$ is found, the value of V_γ can be obtained from the additional relationship :

$$V_\gamma + V_{\alpha'} = 1 \tag{3.5}$$

The 2θ values for three austenite peaks were used to calculate the d spacings with Bragg's law and then the lattice parameter a. These values were plotted against $\sin^2\,\theta$. An accurate value of a_γ was found by extrapolation to $\sin^2\,\theta = 1$ [83].

3.3 Mechanical properties

3.3.a Hardness

Hardness measurements were made using a Vickers pyramidal hardness-testing machine using a load of 10 kg. The indent had diagonals of typically 200 μm. When the width of the observed region was smaller than the latter figure, micro hardness was employed using a load of 100 g. Indents this time had diagonals of about 25 μm. Ten measurements were taken over the metallographic specimen area regardless of the technique employed to measure the hardness.

3.3.b Charpy impact toughness

The Charpy impact toughness test was used to characterise the ability of different microstructures to absorb energy during the process of fracture. A pre-notched standard sample of 10 mm square section $\times$ 55 mm with a 2 mm deep V-notch positioned through-thickness at the middle of the specimen is fractured using a weighted pendulum hammer [62]. To reveal any ductile-brittle transition the tests were conducted in the range 20 °C to -200 °C and were performed according to British Standard 10045-1 [84].

3.4 Dilatometry

Two dilatometers have been used during this project to attempt to measure phase transformation temperatures over a range of heating rates.

3.4.a Thermomechanical simulator

The "Thermec-mastor" thermomechanical simulator allows the computer-controlled application of heat-treatments and deformation to a specimen of material. The temperature and diametrical dilation of the specimen are measured and thus the progress of phase transformations within the material can be followed.

The experiments were performed in a sealed chamber (figure 3.1) which is evac-

uated (to a vacuum of $\sim 10^2$ Pa) to prevent oxidation effects. The solid cylindrical specimen with an 8 mm diameter and a length of 12 mm seats centrally between two silicon nitride dies. The die holders are insulated from the dies by two mica discs. The temperature is recorded using a platinum / platinum-10 % rhodium thermocouple spot-welded in a central position to the specimen. The accuracy of the temperature reading is ± 3 °C whilst the variation along the specimen length is no more than ± 10 °C.

The heating of the sample is by a water cooled, high frequency induction coil which surrounds the sample. The maximum heating rate that can be achieved is around 50 °C s^{-1} but is also dependent upon the material. The cooling of the sample is controlled via helium jets.

The diametrical dilation of the sample is monitored using a He-Ne laser beam. The beam is positioned at the same height as a thermocouple spot-welded onto the sample to ensure that the temperature and dilation measurements are from the same location. The accuracy of the dilation reading is ± 1 μm. Time, temperature and dilation are recorded and are stored on a computer for subsequent analysis.

3.4.b Netzsch dilatometer

Dilatometric measurements were also carried out using a Netzsch 402C dilatometer capable of operation between 25 and 1600 °C. Details of the instrument are shown in figure 3.2. The heating and cooling of the sample are ensured by a sealed furnace, which surrounds the specimen holder. The temperature of the specimen is measured by a Pt/Pt-Rh thermocouple located about 1 mm above its surface. To limit the temperature difference between the furnace and the specimen, it is essential to use slow heating rates (1 °C s^{-1} maximum). During the experiment, the longitudinal dilation is measured using a pushrod connected to a linear velocity displacement transducer (LVDT). Time, temperature and dilation are recorded and are stored on a computer for subsequent analysis.

To allow rapid transmission of the heat, 12 mm long hollow cylinders of 8 mm

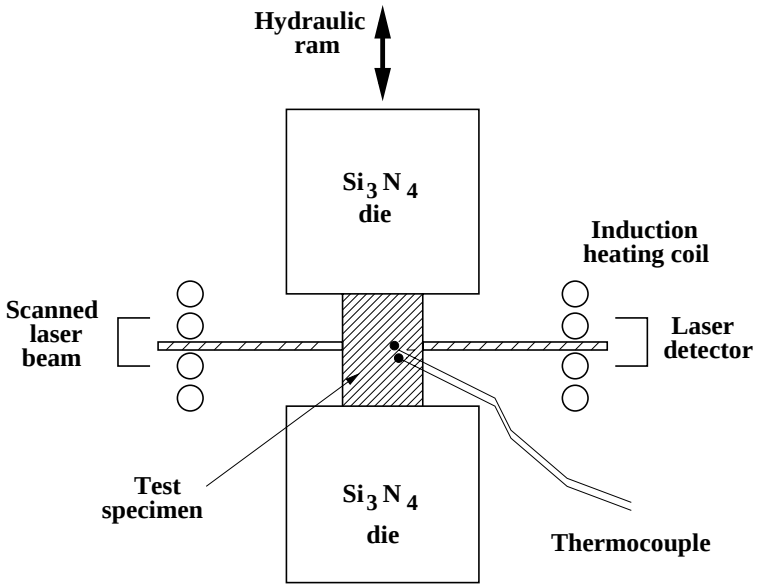

Figure 3.1: The arrangement of equipment within the *Thermec-mastor* thermomechanical simulator.

external diameter and 5 mm internal diameter have been used. Tests were carried out using a static argon atmosphere to prevent oxidation of the specimens.

3.5 Weld heat-affected zone simulator

3.5.a Gleeble

The Gleeble is a thermomechanical testing device that is used in a wide range of applications including simulation and testing of weld heat-affected zones. A major advantage of the Gleeble is that it generates large volumes of microstructure that simulate small, hard to study region in actual weldments. A range of specimen geometries can be used, but by using bars, Charpy specimens can directly be machined after simulation, thus enabling the toughness of any region of the heat-affected zone to be measured.

The machine (figure 3.3), is interfaced to a computer that is readily programmed

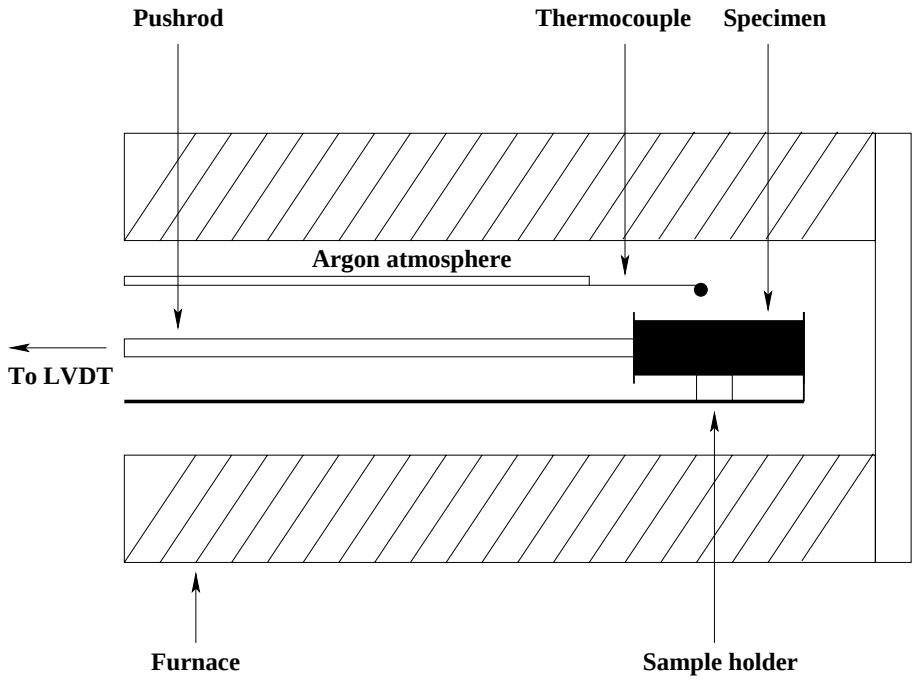

Figure 3.2: The arrangement of equipment within the Netzsch 402C dilatometer. LVDT : linear velocity displacement transducer.

to provide reference signals for close loop control of the applied thermal cycle. Heating is accomplished by the flow of low-frequency alternating current in the specimen. The current distribution is controlled by the cross section of the specimen and the jaws used to mount it. The feedback signal necessary for closed-loop control is obtained from a thermocouple welded to the specimen surface [85].

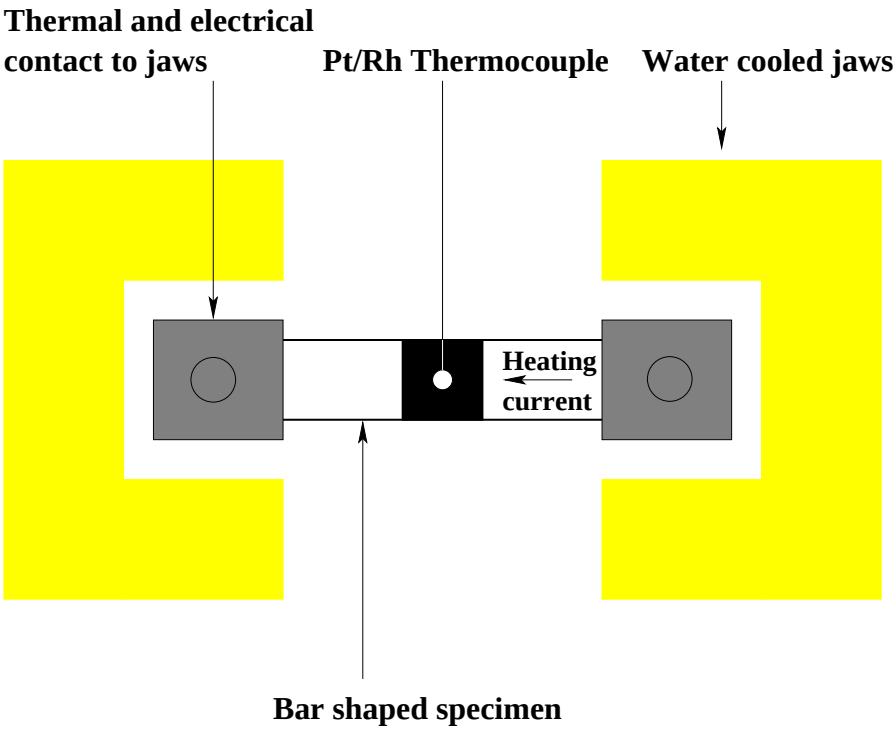

Figure 3.3: The arrangement of equipment within the Gleeble simulator.

Chapter 4

Characterisation and predictions

The aim of the work presented in this chapter was first to characterise the as-received microstructure of the supermartensitic stainless steels studied in this thesis, then determine their phase transformation temperatures and finally compare the latter with equilibrium and paraequilibrium predictions made using MT-DATA software.

4.1 Studied materials

Three supermartensitic stainless steels covering the contemporary range of composition have been studied in this work. Steels A, B and C whose chemical compositions are reported in table 4.1 consisted of seamless pipes of different diameters and wall thicknesses. Steel A is a highly alloyed supermartensitic stainless steels stabilised by the addition of titanium. Steels B and C are lean and medium alloyed compared to steel A and also contain less titanium. The chromium concentration varies between 10.9 and 12.5 wt%, but the most significant differences between the three alloys was their nickel and molybdenum concentrations.

The details of manufacturers, designation and dimensions are listed in table 4.2. No information could be gathered about the production route and the few data obtained about heat-treatments are reported in table 4.3. Unfortunately, in most cases the solution treatment times and temperatures were not specified.

Steel name	C	Si	Mn	Ni	Cr	Mo	Cu	Ti	N
A	0.01	0.26	0.46	6.46	12.20	2.48	0.03	0.09	0.0070
B	0.01	0.18	1.14	1.55	10.90	$\leq$ 0.01	0.49	0.01	0.0060
C	0.01	0.19	0.24	3.12	12.50	0.02	0.06	0.01	0.0120

Table 4.1: Chemical compositions of steels A, B and C in wt%.

Steel name	Manufacturer	Designation	Dimension (mm)
A	Sumitomo	SM 13CRS 80	273.1 (OD) $\times$ 12.0 (WT)
B	Kawasaki	KL 12CR	168.3 (OD) $\times$ 11.0 (WT)
C	NKK	NK 13CRW	273.0 (OD) $\times$ 15.9 (WT)

Table 4.2: Details of steels A, B and C. OD: outer diameter, WT: wall thickness.

4.1.a Initial microstructures

As all materials received different heat and mechanical treatments, it was important to characterise their as-received state before producing any welds. The initial microstructures of the materials, electrolytically etched, are shown in figure 4.1. They all consisted of tempered martensite with no evidence of δ-ferrite and some cube shaped titanium carbo-nitride particles in steel A. The absence of ferrite indicated that all steels could be made completely austenitic at the austenitising temperature. Steels B and C (molybdenum free alloys) showed some corrosion pits on their surfaces after etching. The presence of the latter reflected their reduced corrosion resistance compared with steel A.

4.1.b Retained austenite

The presence of any retained austenite was also investigated. X-ray diffraction tests were carried out according to the procedure described in chapter 3. Those

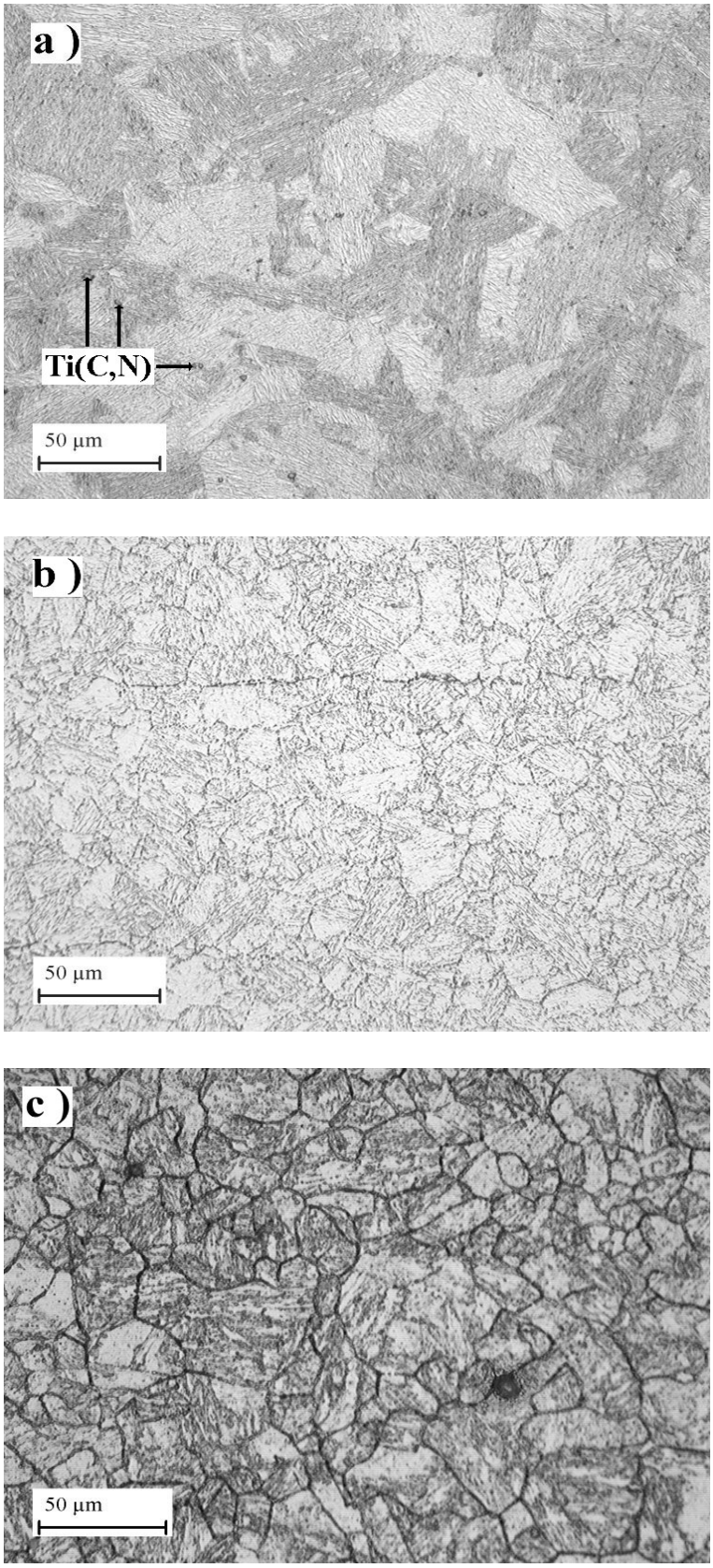

Figure 4.1: Optical micrographs of the initial microstructures of steels A (a), B (b) and C (c), electrolytically etched.

Steel name	Heat-treatment
A	Quenched from 900 °C and tempered at 640 °C
B	Not reported
C	Air cooled and tempered

Table 4.3: Information about heat-treatments provided by steels supplier.

tests revealed that unlike steels B and C (figures 4.2 and 4.3), steel A contained a significant amount of retained austenite (figure 4.4). The volume percentage of the latter was 13 % within an error of ± 0.5 %.

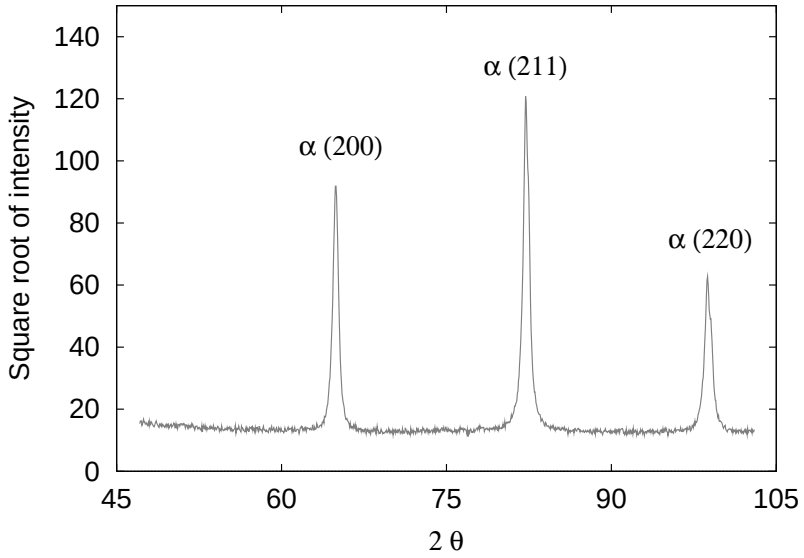

Figure 4.2: X-ray diffraction pattern of steel B in as-received condition.

Figure 4.5 shows that this austenite remained stable after immersion in liquid nitrogen for 30 minutes, but after reaustenitisation at 1000 °C for 30 minutes and water quenching no austenite could be detected. Those results indicated that the presence of retained austenite in the as-received condition of steel A was the consequence of the prior tempering treatment. In fact tempering must have been carried

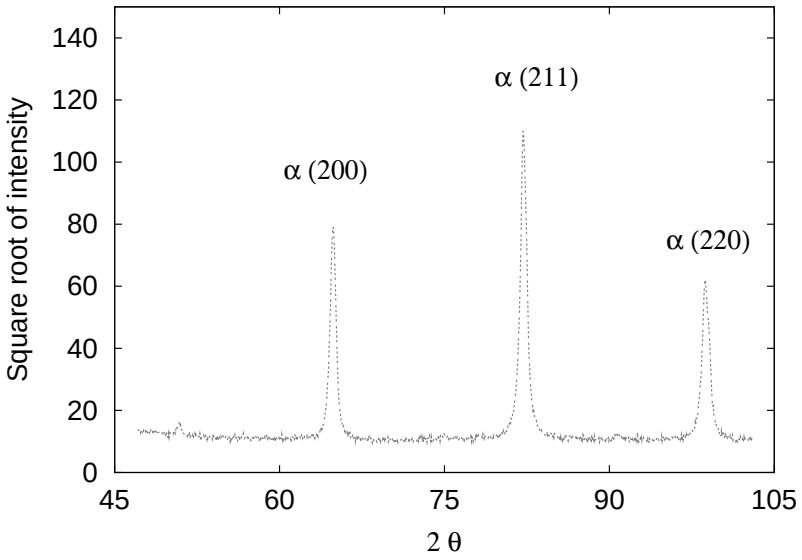

Figure 4.3: X-ray diffraction pattern of steel C in as-received condition.

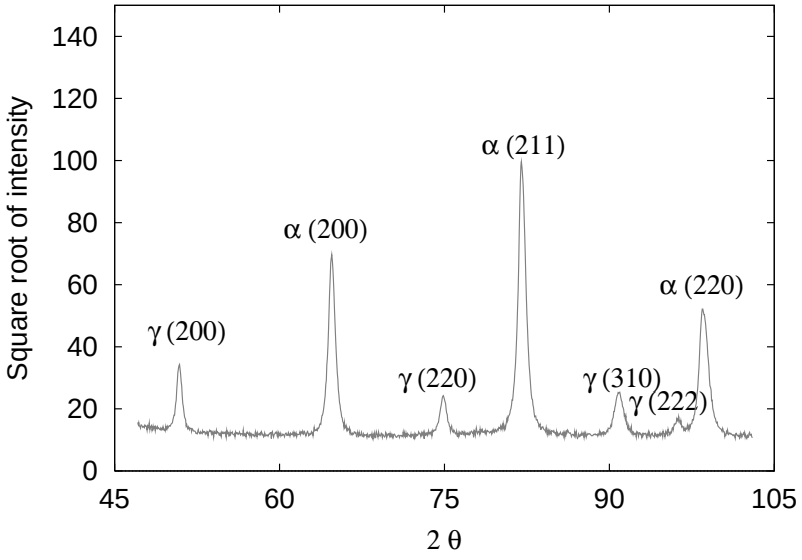

Figure 4.4: X-ray diffraction patterns of steel A in as-received condition.

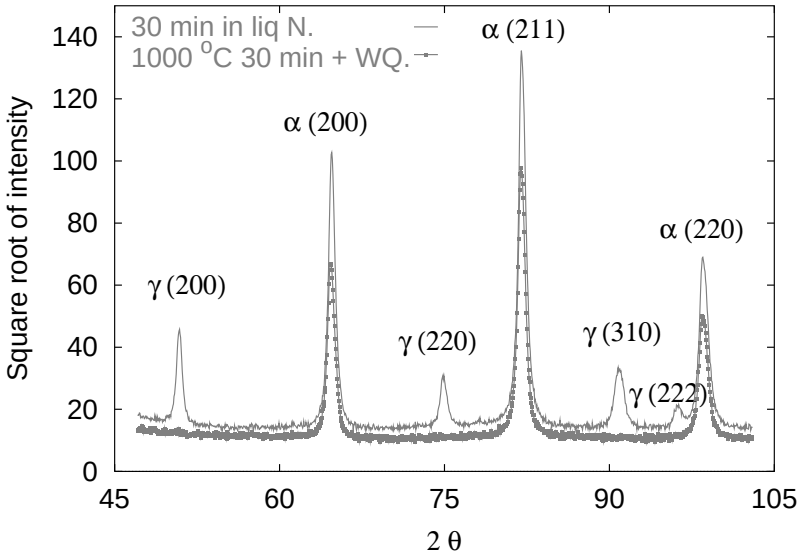

Figure 4.5: X-ray diffraction patterns of steel A after indicated thermal treatment (WQ: water quench).

out few degrees above the steel Ac_1 temperature. In this case, as introduced in chapter 2, the new austenite is significantly enriched in carbon and nickel and remains stable after cooling.

A TEM examination of a thin foil prepared on steel A showed this retained austenite to be present as small elongated grains located at martensite lath boundaries as illustrated on figure 4.6.

Within the limits of experimental error, neither carbides nor nitrides were detected in the three alloys over the angular range investigated in the X-ray diffraction experiments. A part from Ti(C,N) particles no other carbo-nitrides could be observed during the TEM examination of steels A, B and C.

4.1.c Grain size and hardness

The materials had similar initial grain sizes but significantly different hardnesses (table 4.4).

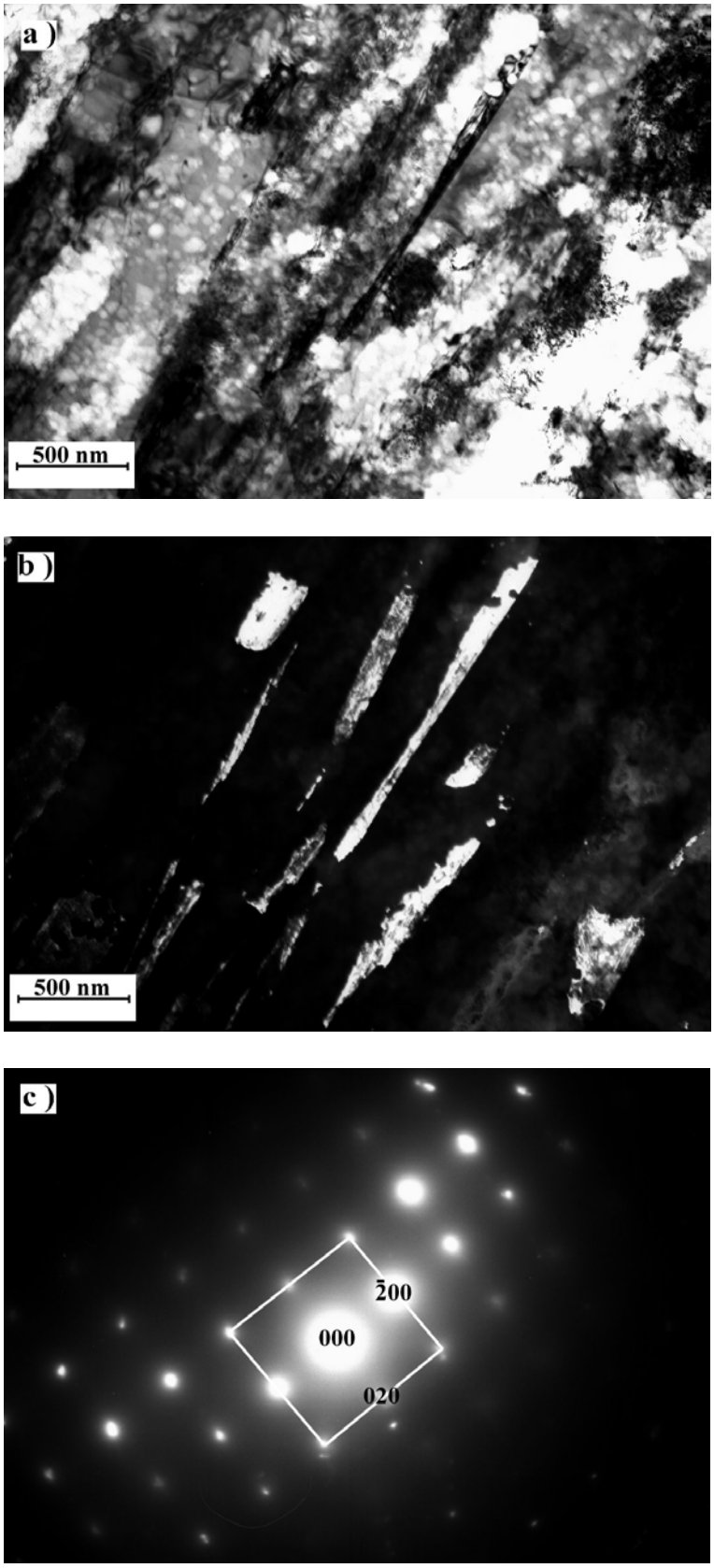

Figure 4.6: (a) Bright field image of a martensite plus retained austenite region. (b) Dark field image of the same region as (a). (c) Selected area diffraction pattern of austenite corresponding to the dark field image.

To measure the materials maximum hardness, samples were austenitised at 1000 °C for 30 minutes and water quenched to obtain fully martensitic microstructures. After heat-treatment all materials had similar hardness levels but the hardness increase of steel A was significantly smaller than that of steels B and C (table 4.5). The latter was due to the virtually carbon free martensite of steel A as a result of the stabilisation by titanium.

Steel name	**Grain size / μm**	**Hardness HV_{10kg}**
A	25 ± 4	296 ± 3
B	13 ± 3	219 ± 1
C	17 ± 4	252 ± 5

Table 4.4: Initial hardnesses and grain sizes of steels A, B and C.

Steel name	**Fresh martensite hardness HV_{10kg}**	**Hardness change**
A	317 ± 8	+ 21
B	323 ± 3	+ 104
C	322 ± 6	+ 70

Table 4.5: Hardness of steels A, B and C after 1000 °C 30 minutes and water quench, and hardness change compared with as-received condition (table 4.4).

4.2 Dilatometric measurements

Very few data have been published on the phase transformation temperatures of supermartensitic stainless steels. In this regard, the temperatures of δ-ferrite formation and completion as well as dissolution have never been measured experimentally. However to understand the microstructures developing in HAZ it is useful to determine those temperatures.

The phase transformation temperatures presented in this section have been obtained using the Netzsch DIL 402 dilatometer presented in chapter 3, employing slow heating and cooling rates of 10 °C min^{-1}.

4.2.a Phase transformations on heating

The detection of phase transformation within the steels using dilatometry relies upon the fact that the phases have different densities. Austenite formation is associated with an overall contraction of the specimen. Conversely δ-ferrite appearance is associated with an overall expansion of the specimen corresponding to the transformation of the f.c.c. lattice into the b.c.c. lattice. In practice, the Ac_1 temperature is the one at which the dilation curves starts to deviate from the straight line in the temperature range 500 - 800 °C while the deviation corresponding to Ac_4 is expected at a higher temperature.

The heating part of the three dilation curves plotted versus temperature is reported in figure 4.7 and the measured Ac_1 and Ac_3 temperatures are listed in table 4.6.

Alloy	**Ac_1**	**Ac_3**	**Ac_1-Ac_3**
A	554	719	165
B	678	792	114
C	650	798	148

Table 4.6: Measured Ac_1, Ac_3 temperatures and Ac_1-Ac_3 temperature intervals in (°C) of steels A, B and C, using a heating rate of 10 °C min^{-1}.

Steel A (6.4 wt% Ni) had the lowest Ac_1 temperature followed by steels C (3.1 wt% Ni) and B (1.5 wt% Ni). Nickel is well known to depress the Ac_1 temperature and this was confirmed experimentally. Steel A also had the largest Ac_1-Ac_3 temperature interval.

An unusual and reproducible contraction could be observed at around 900 °C on the dilation curve of steel A. This phase transformation is believed to be associated with the dissolution of titanium carbides. However, considering the small volume fraction of these particles it would be expected to register anything on the dilation curve. MT-DATA calculations on steel A (showed later in this chapter) are however consistent with this assumption since it predicted TiC dissolution at $\sim$ 900 °C under equilibrium conditions.

A magnified representation of the high temperature part of the dilation curve is shown in figure 4.8. The measured phase transformation temperatures and temperature ranges are reported in table 4.7. The Ac_4 temperatures all exceeded 1300 °C and the temperature intervals of δ-formation (Ac_4-Ac_5) were shorter than 50 °C. On the other hand, steel A combined the highest Ac_4 and Ac_5 temperatures and had its Ac_4-Ac_5 temperature range about twice as long as steels B and C. Finally, as expected, all steels had large fully austenitic range (Ac_3-Ac_4) of about 650-700 °C.

Alloy	**Ac_4**	**Ac_5**	**Ac_4-Ac_5**	**Ac_3-Ac_4**
A	1372	1417	45	653
B	1330	1352	22	652
C	1347	1373	26	697

Table 4.7: Measured phase transformation temperatures and temperature intervals in (°C) of steels A, B and C, using a heating rate of 10 °C min^{-1}.

As Fenn reported, the Ac_4 temperature is less sensitive to heating rate than Ac_1 and Ac_3, therefore the temperatures determined under slow heating condition can be expected to be close to the actual temperatures during welding [63]. As interest is placed on the presence of δ-ferrite in HAZ, the short Ac_4-Ac_5 temperature range indicates that the HAZ region over which δ-ferrite forms is narrow compared with the other HAZ regions.

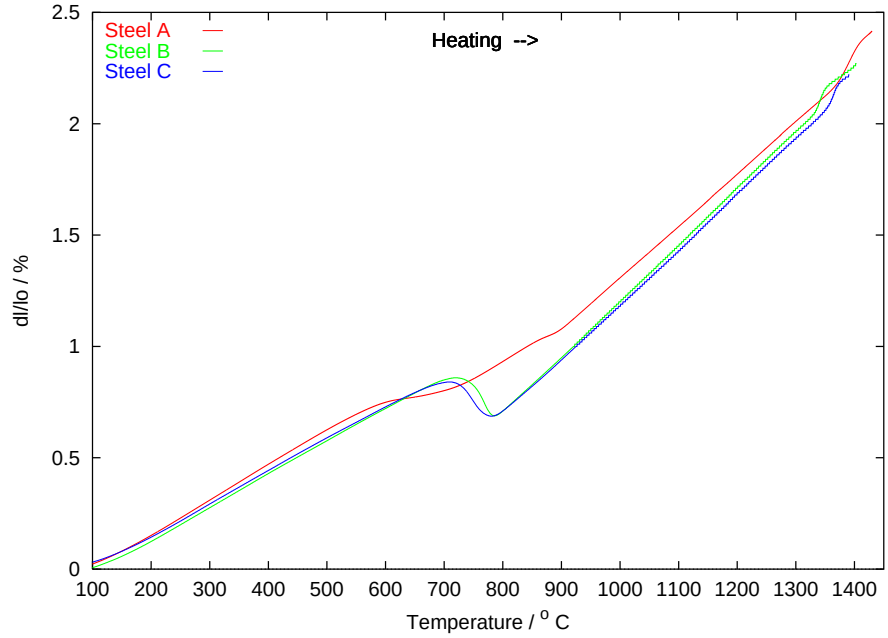

Figure 4.7: Heating part of the dilation curves obtained on steels A, B and C for a heating rate of 10 °C min^{-1}.

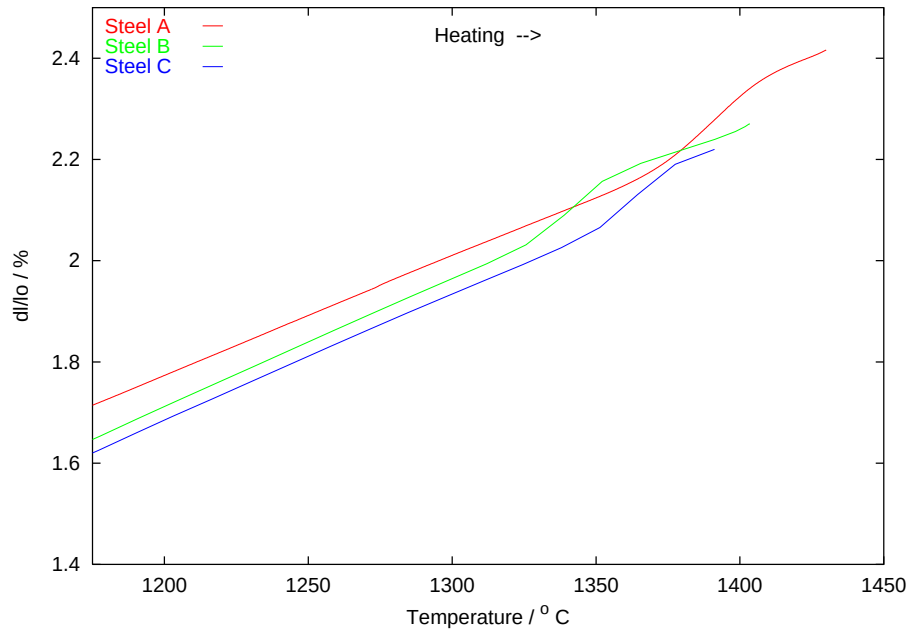

Figure 4.8: Magnified representation of the high temperature part of figure 4.7.

4.2.b Phase transformations on cooling

Figure 4.9 shows the high temperature cooling part of the three dilation curves plotted versus temperature. Under slow cooling condition all fully ferritised steels retransformed to austenite. The temperatures of the onset and completion of δ-ferrite dissolution on cooling, Ar_4 and Ar_5, which correspond to the change from the b.c.c. lattice to the f.c.c. lattice are reported in table 4.8.

Steel name	Ar_4	Ar_5	Ar_4-Ar_5
A	1388	1350	38
B	1265	1205	60
C	1285	1225	60

Table 4.8: Measured phase transformation temperatures and temperature intervals in (°C) of steels A, B and C using a cooling rate of 10 °C min^{-1}.

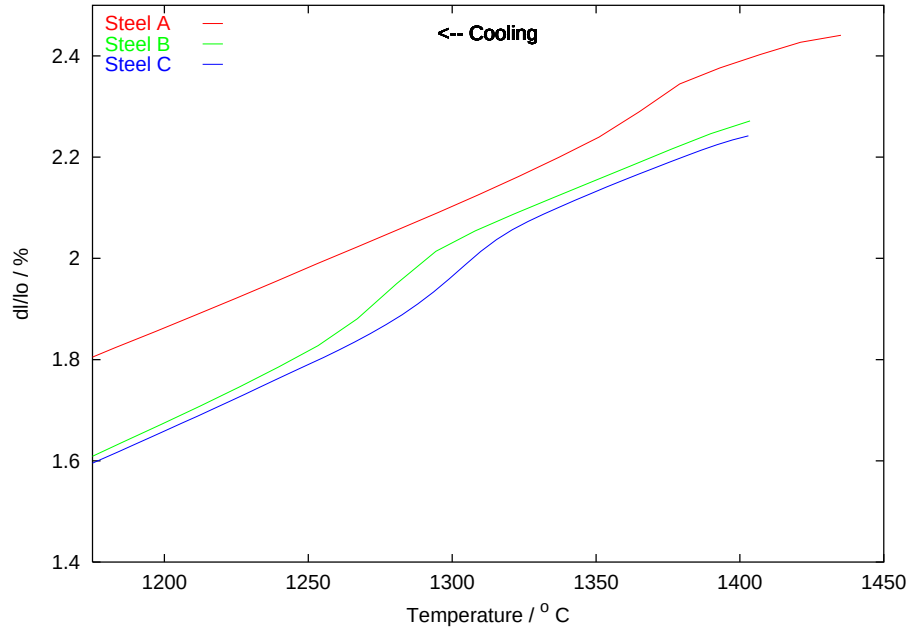

Figure 4.9: Cooling part of the dilation curves obtained on steel A, B and C for a cooling rate of 10 °C min^{-1}.

The reverse transformation temperatures of steel A were higher than those of steels B and C. It was also noted that steels B and C had similar Ar_4 temperatures and transformed to austenite over a longer temperature range (60 °C compared with 38 °C for steel A).

Finally the M_S and M_F temperatures of the three alloys (figure 4.10) are reported in table 4.9. As could be expected from the X-ray results, all M_F temperatures were above room temperature. Consistent with its relatively large alloying content, steel A, had the lowest M_S and M_F temperatures. Once again, molybdenum free, steels B and C, had similar phase transformation temperatures. A summary of all experimental phase transformation temperatures is presented in figure 4.11.

Steel name	$\mathbf{M_S}$	$\mathbf{M_F}$
A	205	105
B	410	230
C	420	250

Table 4.9: Measured M_S and M_F temperatures (in °C) of steels A, B and C using a cooling rate of 10 °C min^{-1}.

4.2.c Thermecmastor

The thermecmastor was also employed to attempt to determine the Ac_4 and Ac_5 temperatures in the 5 - 50 °C s^{-1} heating rate range. However due to unstability problems of the machine at elevated temperatures many experiments failed, or when the desired temperatures were reached the data were too noisy to allow the detection of the expansion associated with δ-ferrite formation. Therefore, this dilatometer was not suitable for our purpose.

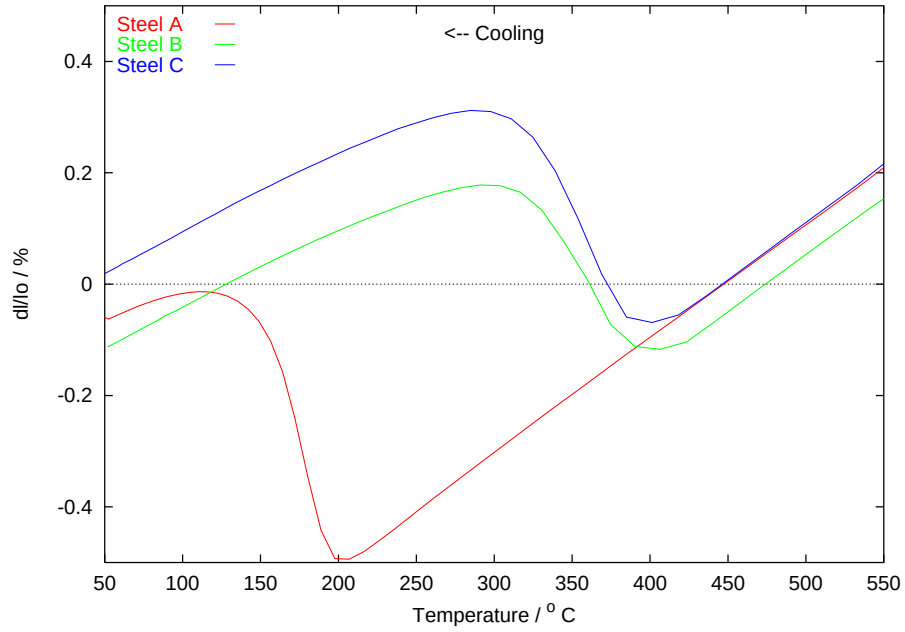

Figure 4.10: Low temperature cooling part of the dilation curves obtained on steels A, B and C for a cooling rate of 10 °C min^{-1}.

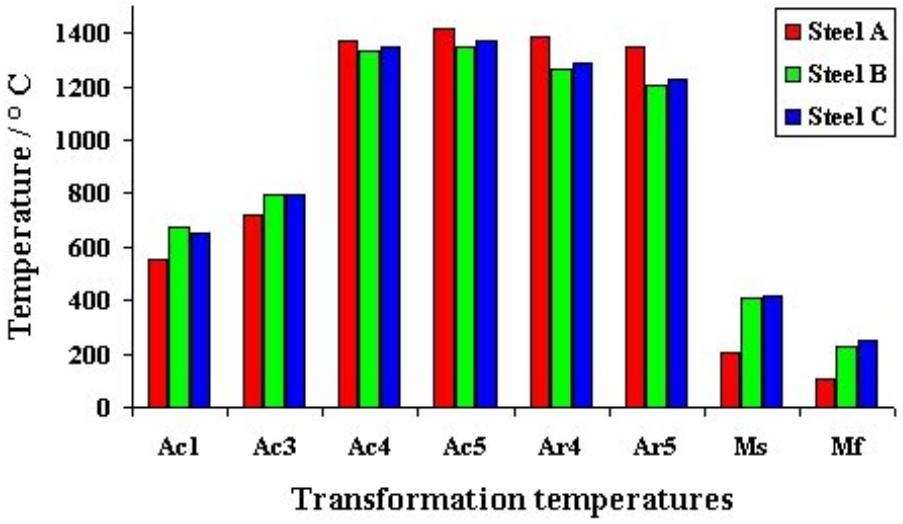

Figure 4.11: Summary of experimental phase transformation temperatures measured on steels A, B and C. Heating and cooling rate of 10 °C min^{-1}.

4.3 Thermodynamic predictions

Having measured the phase transformation temperatures of the three steels under condition close to equilibrium, it is now possible to assess the predictions of thermodynamic software such as MT-DATA (National Physical Laboratory) on the system of concern.

MT-DATA uses experimentally determined parameters to model thermodynamic variables. For this reason, the reliability of the calculations it performs depends on the parameters present in the databases. Mass conservation and a minimisation of Gibbs free energy allow calculations of the phase transformation temperatures, the volume fractions of phases present and their chemical compositions. As MT-DATA uses thermodynamics, equilibrium or paraequilibrium[1] are always assumed and no kinetic information is produced.

4.3.a Equilibrium calculations

Calculations of the phase transformation temperatures and phase mass fractions have been performed on the three steels over the temperature range 400 - 1600 °C at intervals of 25 °C using the *plus* and *sub-sgte* databases.

Simpler systems are more accurately predicted by MT-DATA hence only the elements in major quantities are taken into account in calculations. The latter were made without silicon since MT-DATA has been found to give silicon an excessively strong ferrite-forming tendency in the systems of concern. The most important elements and phases and the most common carbides and nitrides have been allowed and are listed in table 4.10.

[1]Carbon and nitrogen diffuse more rapidly than substitutional elements hence under rapid heating condition, the latter elements are unable to partition during the time scale related to the welding operation.

Alloy	Allowed elements	Allowed phases
A	Fe, C, Mn, Ni, Cr, Mo, Ti, N	$M_{23}C_6$, γ, δ, Fe_3C, M_7C_3, TiC, TiN, Liq
B	Fe, C, Mn, Ni, Cr, Cu, Ti, N	$M_{23}C_6$, γ, δ, Fe_3C, M_7C_3, TiC, TiN, Cu, Liq
C	Fe, C, Mn, Ni, Cr, Cu, Mo, Ti, N	$M_{23}C_6$, γ, δ, Fe_3C, M_7C_3, TiC, TiN, Cu, Liq

Table 4.10: List of elements and phases used for steels A, B and C in equilibrium calculations.

4.3.b Results

The mass fractions of the equilibrium phases of steels A, B and C are plotted against temperature in figures 4.12 to 4.14 and the equilibrium phase transformation temperatures are summarised in table 4.11.

Consistent with microstructural observations, all steels are predicted to have the capacity to become fully austenitic. The materials are also expected to undergo ferritisation at temperatures lower than 1300 °C and become entirely ferritic before melting starts ($\sim$ 1500 °C). On the other hand, it should be noted that Cu, $M_{23}C_6$, TiC and TiN were the only stable phases predicted by MT-DATA. Steel A was the only alloy predicted to contain austenite down to 400 °C, and to be free from $M_{23}C_6$.

The Ae_4-Ae_5 and Ae_5-solidus temperature ranges corresponding to the regions over which δ-ferrite forms and grows are listed in table 4.12. Steel A is predicted to possess the largest Ae_4-Ae_5 (159 °C) and the smallest Ae_5-solidus temperature interval (65 °C). On the other hand, steels B and C are predicted to have comparable Ae_4-Ae_5 and also Ae_5-solidus temperature range.

4.3.c Comparison with dilatometric measurements

Predicted versus measured Ac_3, Ac_4 and Ac_5 temperatures are reported in figure 4.15. As could be expected, predicted phase transformation temperatures were systematically lower than the measured ones. The Ae_3 temperatures were between 14 and 45 °C lower than the experimental values, but the Ae_5 temperatures were

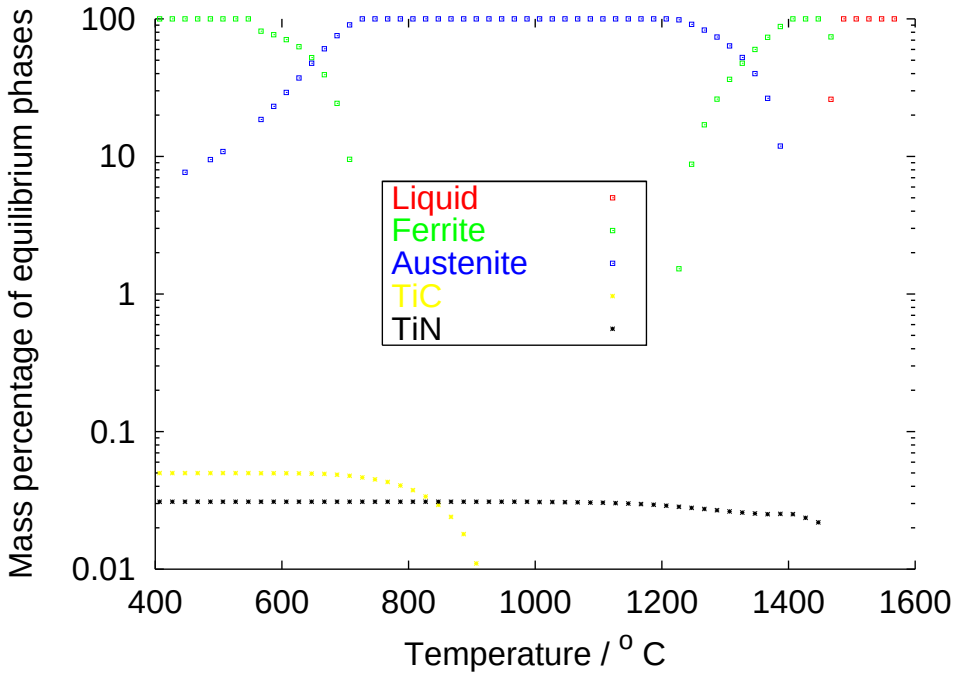

Figure 4.12: Results of MT-DATA equilibrium calculations performed on steel A.

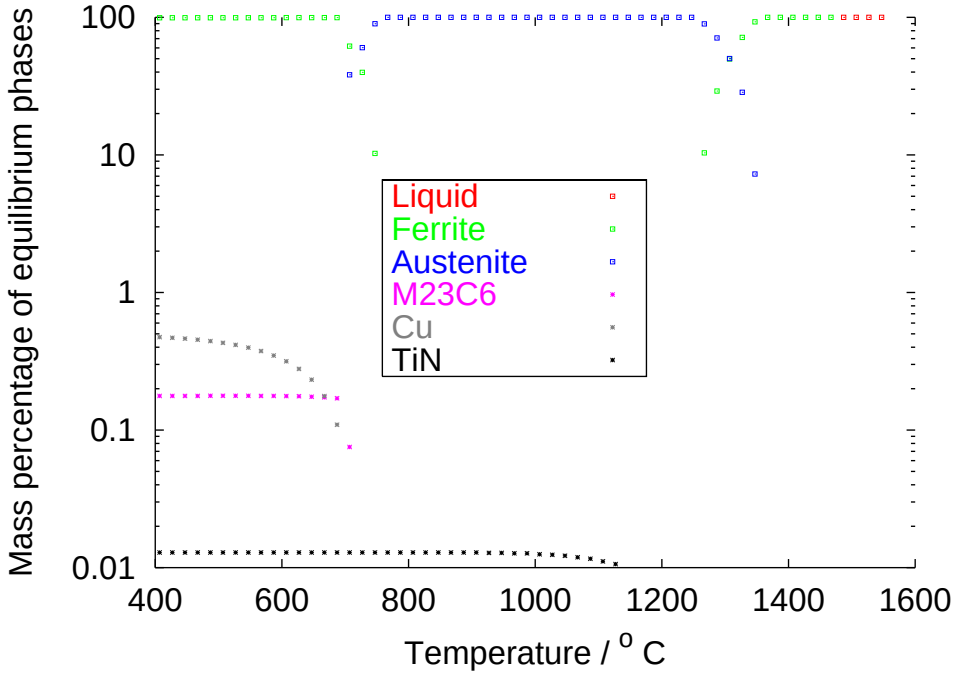

Figure 4.13: Results of MT-DATA equilibrium calculations performed on steel B.

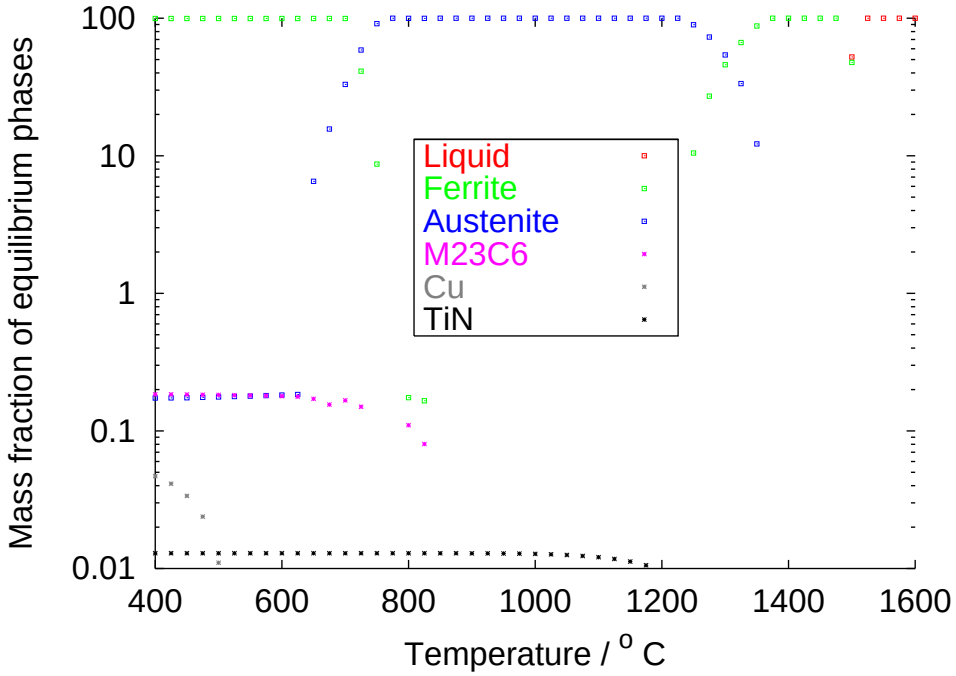

Figure 4.14: Results of MT-DATA equilibrium calculations performed on steel C.

Alloy	Ae_1 (5%)	Ae_3 (95%)	Ae_4 (5%)	Ae_5 (95%)	Solidus (5%)
A	$\prec$ 400	705	1237	1396	1461
B	692	750	1261	1350	1490
C	675	753	1242	1360	1492

Table 4.11: Equilibrium phase transformation temperatures (in °C) obtained after calculations performed on steels A, B and C. The Ae_1, Ae_4 and solidus temperatures have been obtained by taking the temperature at which 5 % of the growing phase have formed. Similarly, the Ae_3 and Ae_5 temperatures have been obtained by taking the temperature at which 95 % of the growing phase have formed.

Alloy	Ae_4 - Ae_5	Ae_5 - Solidus
A	159	65
B	89	140
C	118	132

Table 4.12: Equilibrium interval temperatures (in °C) between Ae_4-Ae_5 and Ae_5-solidus, deduced from table 4.11.

relatively well predicted by MT-DATA. However, poor agreement was found regarding the Ae_4 temperatures. The latter were between 70 to 135 °C lower than the actual temperatures. Although, there were significant differences between measured and predicted temperatures, steel A was successfully predicted to have the longest dual-phase field.

Unfortunately, the solidus temperatures could not be measured and consequently no comparison can be made for the Ae_5-solidus temperature range.

4.3.d Effects of Ni and Mo on phase diagrams

Nickel and molybdenum play a major role in the metallurgy of supermartensitic stainless steels, it is therefore interesting to study their effects on the extent of phase stability fields. Based on a simplified composition (0.01 C, 12.2 Cr, 0.5 Mn in wt%), two equilibrium pseudo-binary phase diagrams have been calculated using MT-DATA. The latter calculations were performed in the 0-10 wt% nickel range for 0 and 2 wt% molybdenum.

In the molybdenum free diagram (figure 4.16), the Ni concentration range over which the alloy has the capacity to become fully austenitic while keeping the ferritic solidification mode is large *i.e.* between 0.5 and $\sim$ 6 wt%. However, the addition of 2.5 wt% Mo significantly shortens this range and shifts it to higher nickel concentrations *i.e.* between 3.5 and $\sim$ 7.5 wt%. Therefore, consistent with Kondo *et al.* observations, the addition of molybdenum reduces the size of the fully austenitic domain [14].

As far as δ-ferrite is concerned, the austenite/δ-ferrite phase field is significantly

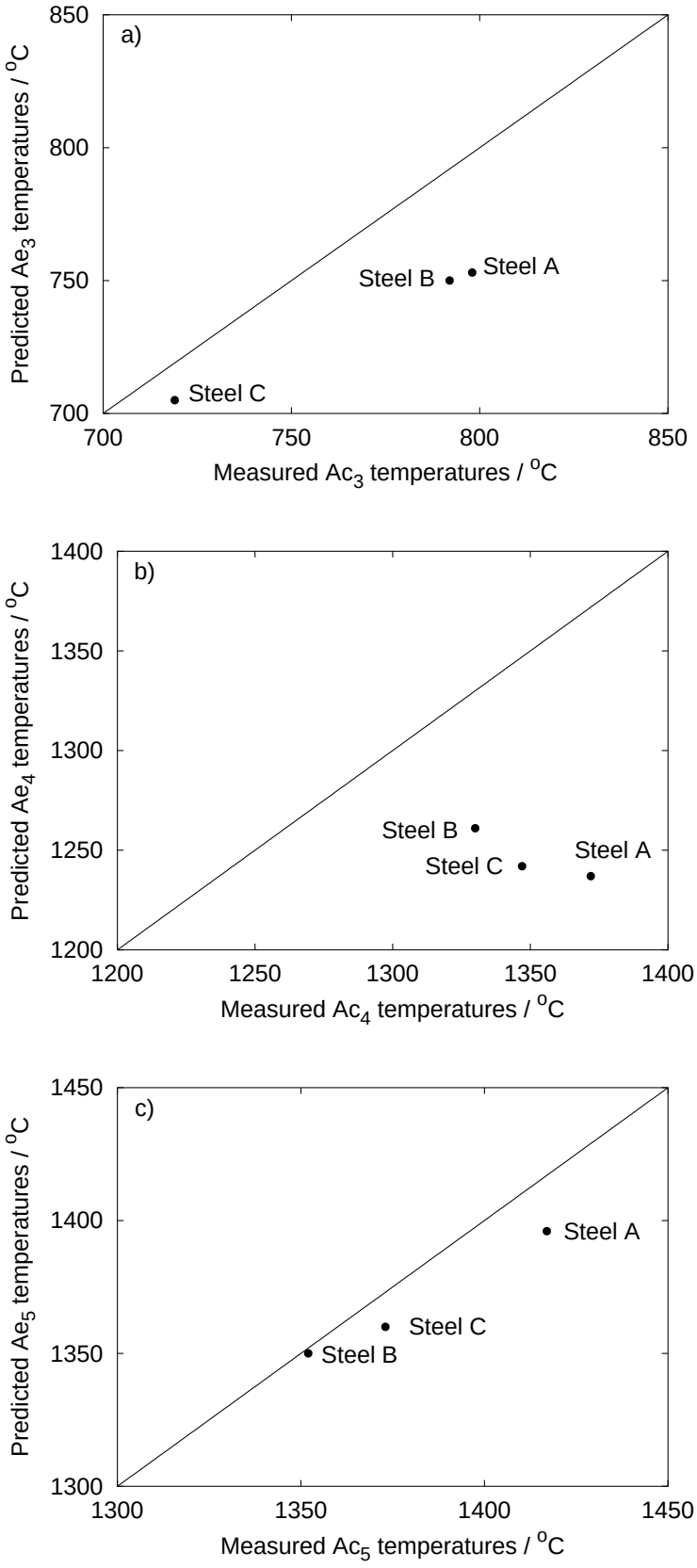

Figure 4.15: Comparison between MT-DATA predicted Ae_3, Ae_4 and Ae_5 temperatures and experimental temperatures measured by dilatometry.

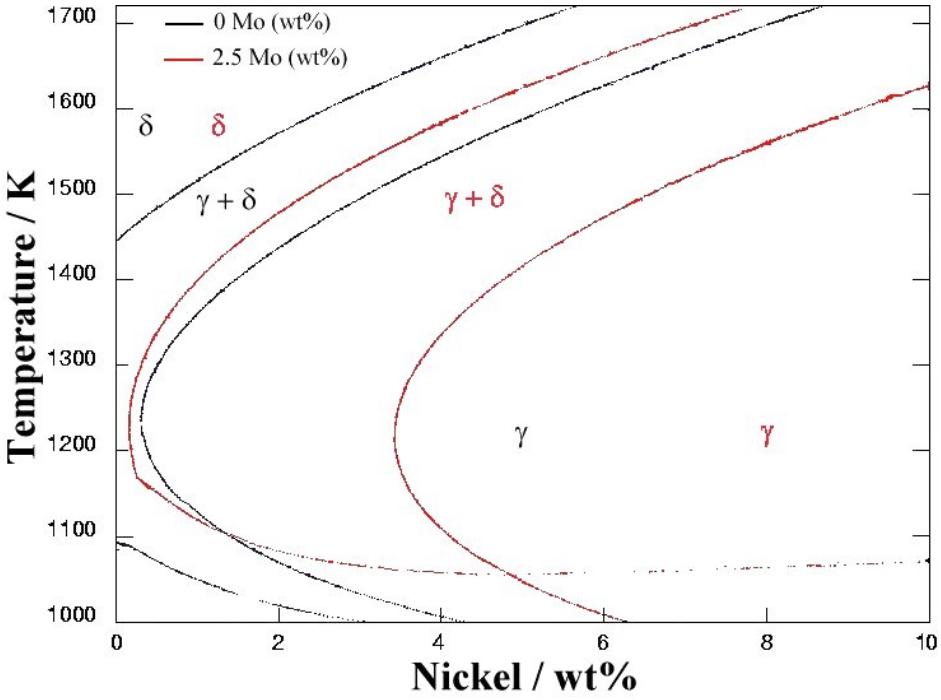

Figure 4.16: Calculated pseudo-binary phase diagram for a 0.01 C, 12.2 Cr, 0.5 Mn (wt%) with two different levels of molybdenum. Black curve corresponds to 0 Mo (wt%) and red curve 2.5 Mo (wt %). For clarity, the liquid + ferrite and liquid + ferrite + austenite fields have not been represented.

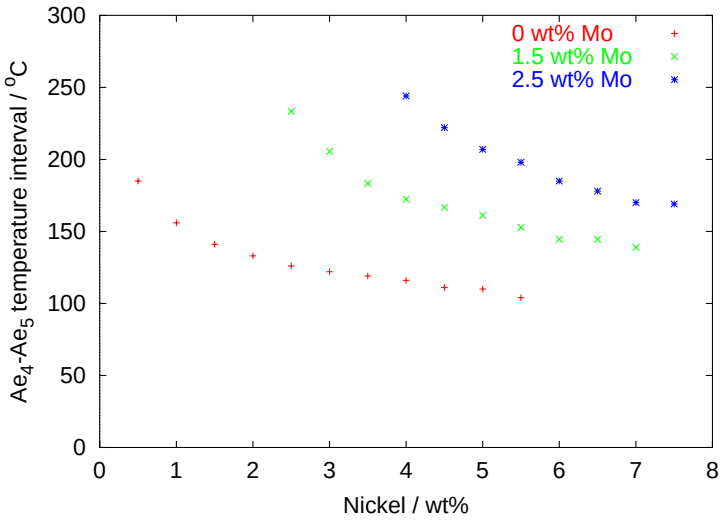

Figure 4.17: Equilibrium Ae_4-Ae_5 temperature intervals as a function of nickel and molybdenum concentrations. Calculations based on a simplified composition : 0.01 C, 12.2 Cr, 0.5 Mn (wt%).

enlarged by addition of molybdenum. For example a Mo free alloy with 4 wt% Ni is predicted to have an Ae_4-Ae_5 interval of 116 °C while the same temperature interval for a 2.5 wt% Mo alloys is 244 °C (figure 4.17). The enlarging effect of Mo on the dual-phase field could be noticed in the dilatometric tests. Indeed, steel A had its Ac_4-Ac_5 temperature interval twice as long as those of steels B and C, although the measured value did not exceed 45 °C.

Figure 4.18 shows the effect of nickel and molybdenum on the Ae_5-solidus temperature interval. The addition of nickel strongly reduces the extent of the fully ferritic range. Molybdenum, is however seen to expand this range, but its effect is less strongly marked compared with figure 4.17.

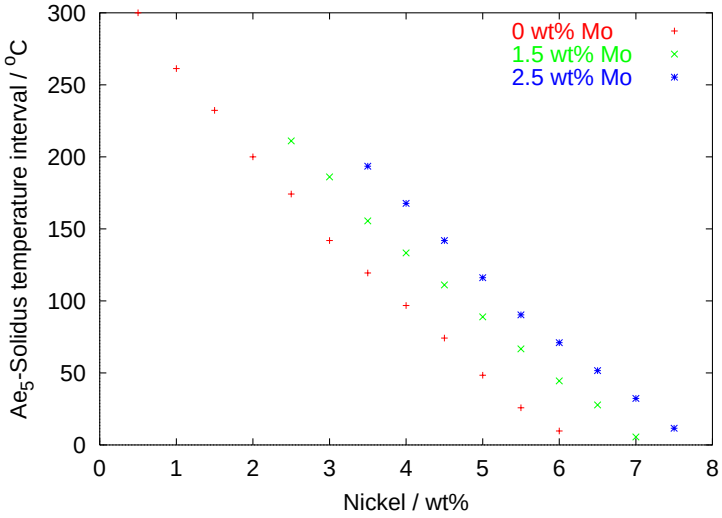

Figure 4.18: Calculated equilibrium Ae_5-solidus temperature intervals as a function of nickel and molybdenum concentrations. Calculations based on a simplified composition : 0.01 C, 12.2 Cr, 0.5 Mn (wt%).

Consequently, molybdenum free supermartensitic stainless steels, like steels B and C, tend to have short dual-phase field and long fully ferritic range, while the opposite applies to molybdenum containing alloys like steel A.

4.3.e Paraequilibrium calculations

Under the fast heating rates encountered during welding, substitutional elements might not have time to partition. Consequently, the concentration of substitutional

elements remain unchanged and the phase transformation temperatures and mass fractions are affected. Calculations under paraequilibrium conditions are therefore required. In practice, those calculations are made by specifying that the ratio of iron to substitutional atoms to be constant at all temperatures. Carbon and nitrogen, on the other hand, are allowed to redistribute.

In this part, the components and phases allowed for are listed in table 4.13. Under paraequilibrium condition, phases such as TiN, TiC or Cu cannot be allowed. However at elevated temperatures, TiN and TiC can be found to be stable under equilibrium condition. To account for the loss of carbon and nitrogen tied up in Ti(C,N) when these phases were predicted to be present under equilibrium condition, the stoichiometric amounts of C and N were removed from the bulk composition and then paraequilibrium calculations were performed.

Alloy	Allowed elements	Allowed phases
A	Fe, C, Mn, Ni, Cr, Mo, N	γ, δ-ferrite, Liq
B	Fe, C, Mn, Ni, Cr, Cu, N	γ, δ-ferrite, Liq
C	Fe, C, Mn, Ni, Cr, Cu, Mo, N	γ, δ-ferrite, Liq

Table 4.13: List of elements and phases used for steels A, B and C for paraequilibrium calculations.

4.3.f Results of paraequilibrium calculations

In the following, the temperature of the onset and completion of δ-ferrite formation under paraequilibrium conditions are referred to as Ap_4 and Ap_5. The Ap_4, Ap_5 and solidus temperatures are reported in table 4.14.

For each steel, δ-ferrite formation is predicted to start at about 1300 °C and the temperature range of ferrite formation is not predicted to exceed 30 °C. Steel A is predicted to possess the shortest Ap_4-Ap_5 and Ap_5-solidus temperature intervals (table 4.15).

Alloy	Ap_4 (5%)	Ap5 (95%)	solidus (5%)
A	1322	1323	1477
B	1302	1310	1500
C	1295	1322	1496

Table 4.14: Paraequilibrium phase transformation temperatures (in °C) obtained after calculation performed on steels A, B and C.

Alloy	Ap_4 - Ap_5	Ap_5 - solidus
A	1	154
B	8	190
C	27	174

Table 4.15: Paraequilibrium temperature ranges (in °C) between Ap_4-Ap_5 and Ap_5-solidus, deduced from table 4.14.

Although the predicted temperature ranges of δ-ferrite formation (Ap_4-Ap_5) were closer to those determined using dilatometry, the comparisons are not valid. This is because the dilatometric experiments were carried out under slow heating conditions (10 °C min^{-1}) and therefore partitioning of substitutional elements had time to occur at elevated temperatures, whereas under paraequilibrium condition redistribution of such solutes is forbidden.

4.3.g Comparison with equilibrium temperatures

A comparison between tables 4.11 and 4.14 indicates that the Ap_4 temperatures were between 27 and 58 °C higher than the equilibrium temperatures and the Ap_5 temperatures were between 40 and 73 °C lower than the corresponding Ae_5 temperatures. Also, under both conditions, the solidus temperatures were almost identical. As a result, under paraequilibrium conditions the temperature ranges of δ-ferrite formation were shorter, but the length of the fully ferritic domains were longer as shown on figure 4.19.

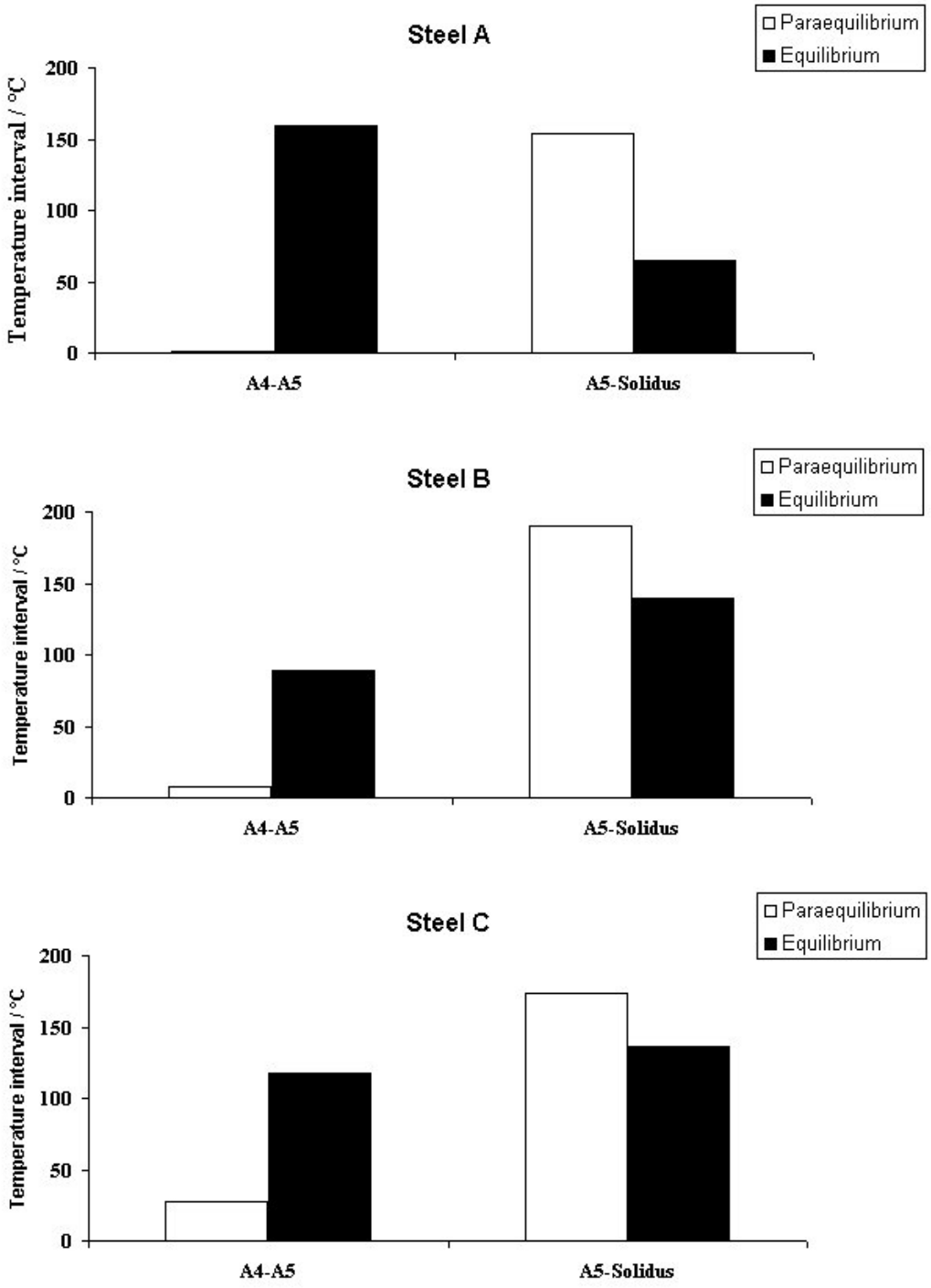

Figure 4.19: Comparison of the A_4-A_5 and A_5-solidus temperature intervals between equilibrium and paraequilibrium conditions for steels A, B and C.

4.4 Summary

In the three studied steels, austenite was only retained in the as-received microstructure of the richly alloyed steel. The presence of this phase was shown to be caused by a tempering treatment carried out in the intercritical temperature range. In the same alloy, the presence of titanium in concentration sufficient to bind all available carbon and nitrogen, was seen to limit martensite hardness change between the tempered and as-quenched conditions.

The dilatometric tests showed that δ-ferrite starts forming in supermartensitic stainless steels at temperatures above 1300 °C and the temperature range of formation does not exceed 50 °C. As a result, the HAZ region over which δ-ferrite forms can be expected to be narrow compared with the other HAZ regions.

MT-DATA correctly predicted all steels to have the capacity to become fully austenitic and completely ferritic before melting. However, the agreement between the equilibrium and experimental Ac_4 temperatures was particularly poor. The effects of nickel and molybdenum on equilibrium phase diagrams were also studied under equilibrium condition. Molybdenum restricts the nickel range over which the alloy can be made fully austenitic. It also strongly enlarges the Ae_4-Ae_5 temperature range but has a weaker effect on the fully ferritic range.

Finally, MT-DATA calculations performed under paraequilibrium conditions predicted shorter dual-phase fields but longer fully ferritic ranges compared with equilibrium predictions.

Chapter 5

Microstructure in high temperature heat-affected zone

Little work has been performed on the characterisation of the microstructure in the HAZ of welded supermartensitic stainless steels. In particular, the presence of δ-ferrite in the high temperature heat-affected zone[1] (HT-HAZ) has not been thoroughly investigated. The aim of the work presented in this chapter was therefore to provide a detailed study of the HT-HAZ microstructure, focussing on δ-ferrite location, morphology, volume fraction and to examine the effects that welding parameters have on its retention.

5.1 First series of single-pass welds

To examine the different HAZ regions and compare the high temperature HAZ microstructure developments between the three studied materials, a series of single-pass autogenous bead-on-plates have been produced.

5.1.a Experimental procedure

Plates of dimension 100×50×5 mm were machined out of the pipes and were taken so that the welds could be performed along the tube axis. To avoid reheating effects and to study how the heat input affects the microstructure, four autogenous

[1]The high temperature heat-affected zone refers to the HAZ regions next to the fusion line.

welds were produced using an automated T.I.G. (Tungsten Inert Gas) welding process and two heat inputs. To allow for direct microstructural comparison, steels A and B, and steels A and C were welded together as illustrated on figure 5.1.

The welding conditions are summarised in table 5.1. Argon was used as the shielding gas during the welding operation. After welding, a transverse section was taken approximately in the middle of each weld for optical examination. In the following, the welds produced with the higher heat input ($\sim$ 0.7 kJ mm^{-1}) are referred to as WAB1 and WAC1, and WAB2 and WAC2 for the lower energy welds ($\sim$ 0.3 kJ mm^{-1}).

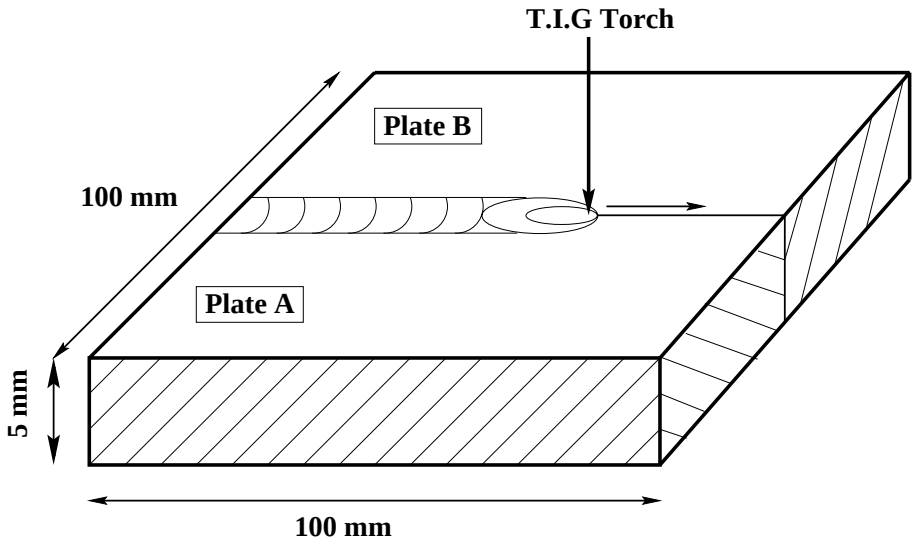

Figure 5.1: Schematic illustration of the welding configuration for plates A and B.

Condition	**Current (A)**	**Voltage (V)**	**Travel speed (mm s^{-1})**	**Arc efficiency** [22]	**Heat input (kJ mm^{-1})**
1	208	9.3	1.66	0.6	$\sim$ 0.7
2	101	9.2	1.66	0.6	$\sim$ 0.3

Table 5.1: Welding parameters for autogenous dissimilar welds produced.

5.1.b Results

The microstructures of weld WAB1 (side A and B) and WAC1 (side C) revealed with Villela's reagent and the electrolytic etchant are shown on figure 5.2. The microstructure of weld WAC1 side A is not shown because it is identical to that of WAB1 side A. The microstructures of welds performed with 0.3 kJ mm^{-1} (WAB2 and WAC2) are shown in figure 5.3.

The welds performed with the highest heat input showed the finger tip morphology, whereas welds carried out with the lower heat input showed hemispherical morphology. The microstructures of the HT-HAZ apparently consisted, from the fusion line of a coarse-grained and a two-phase (ferrite and martensite) region. The electrolytic etchant did not reveal martensite and thus proved very effective in showing ferrite in both the grain coarsened and dual-phase regions. However, the fusion lines and weld pools could not easily be observed. Specimens etched with Villela's reagent showed the martensite and outlined the fusion line so that the use of both etchants was complementary.

Contrarily to results presented by Enerhaug *et al.* the partially melted region could not be observed [53]. In fact in their work the partially melted region was most likely confused with the coarse-grained region. On the other hand, unlike steel HT9 (studied in chapter 2), supermartensitic stainless steels have the capacity to become fully ferritic before melting [63]. In this respect, it should be noted that MT-DATA calculations made under equilibrium and paraequilibrium conditions correctly predicted the existence of the fully ferritic domain (chapter 4).

5.1.c Coarse-grained heat-affected zone microstructure

The coarse-grained (CG) regions clearly had larger grain size than the dual-phase (DP) HAZs, thus indicating that the materials had been completely ferritised before cooling to room temperature.

In steel A, welds WAB1 and WAB2, the different morphologies of the austenite that had formed during cooling from δ-ferrite could clearly be observed (figure 5.4). In addition to allotriomorphic (localised at grain boundaries) and intragranular

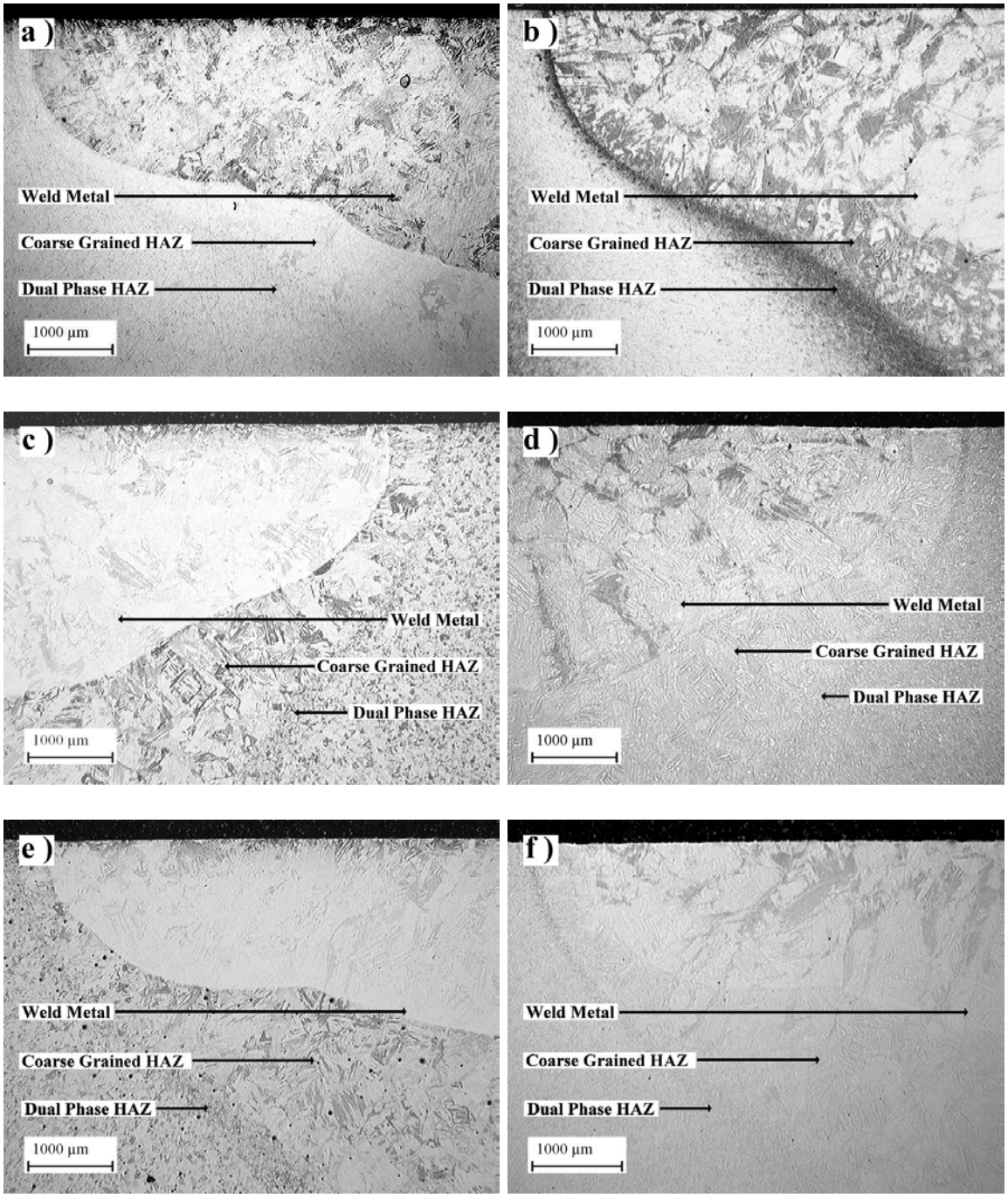

Figure 5.2: Optical micrographs of the same area of weld WAB1 side A ((a) and (b)). Optical micrographs of the same area of weld WAB1 side B ((c) and (d)). Optical micrographs of the same area of weld WAC1 side C ((e) and (f)). Villela's etchant was used for (a), (c) and (e). Electrolytic etchant was employed for (b), (d) and (f). Plate thickness 5 mm, heat input 0.7 kJ mm^{-1}.

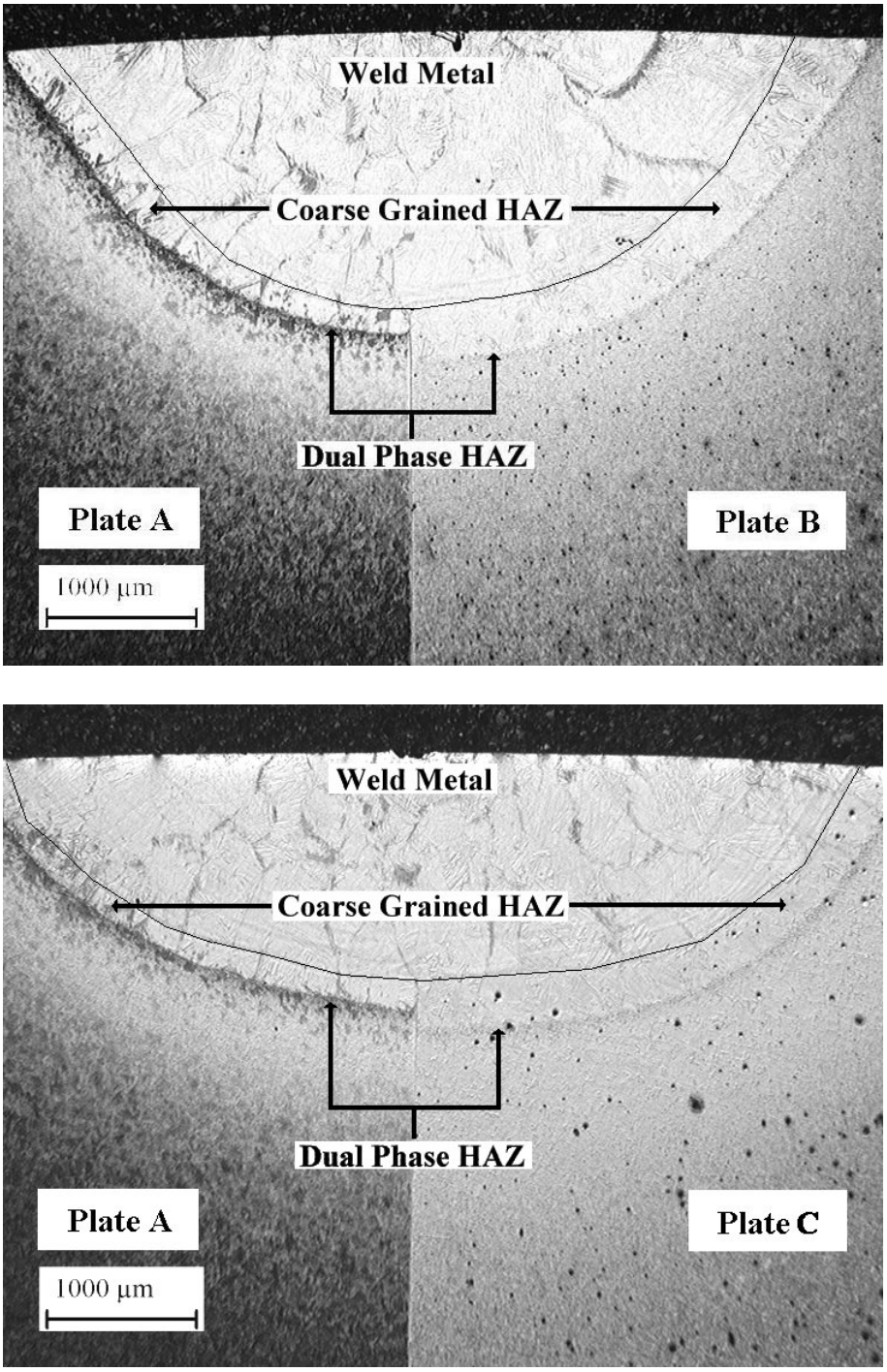

Figure 5.3: Optical micrographs of weld WAB2 and WAC2 electrolytically etched. The fusion line has been underlined and regions labelled. Plate thickness 5 mm, heat input 0.3 kJ mm^{-1}.

austenite, an unusual austenite morphology was found. A survey of the literature revealed this structure to be Widmanstätten austenite. Small amounts of "lathy" δ-ferrite, whose width was about 400 nm, could be found within former Widmanstätten austenite laths as seen on figure 5.5.

Mainly intragranular but also some Widmanstätten austenite could be found in coarse-grained HAZ of steels B and C (figures 5.6 and 5.7). Those steels apparently had a smaller volume fraction of Widmanstätten austenite compared with steel A. From these observations, it could be concluded that the reverse transformation from the fully ferritic region was virtually complete in all coarse-grained HAZ despite the presence of tiny δ-ferrite films between Widmanstätten austenite laths.

i Widmanstätten austenite

The Widmanstätten austenite structure is more common in austenitic stainless steels solidifying as δ-ferrite [65, 86]. Like Widmanstätten ferrite found in carbon steels, the appearance of Widmanstätten austenite is one of narrow wedges emanating either directly from a grain boundary, or from allotriomorphic ferrite (allotriomorphic austenite in the case of Widmanstätten austenite). In carbon steels, Widmanstätten ferrite forms on cooling from austenite in the temperature range $\sim$ 750-650 °C. The structure forms by a displacive mechanism in which the rate of transformation is controlled by the rate at which the carbon can diffuse to the side of the growing plate.

In austenitic stainless steels, the Widmanstätten austenite structure is believed to originate by reconstructive transformation [86, 87, 88]. In supermartensitic stainless steels, the morphology and coarseness of the Widmanstätten austenite (figure 5.5) provides evidence to support that it also forms through a reconstructive transformation mode. Indeed, displacive transformations in steels are accompanied by a shape deformation, which is an invariant-plane strain with a large shear component. To minimise the strain energy associated with the shape change, the transformation products adopt a morphology, which is a thin plate that tapers towards an ever decreasing thickness as the plate-edge is approached. In two-dimensional sections,

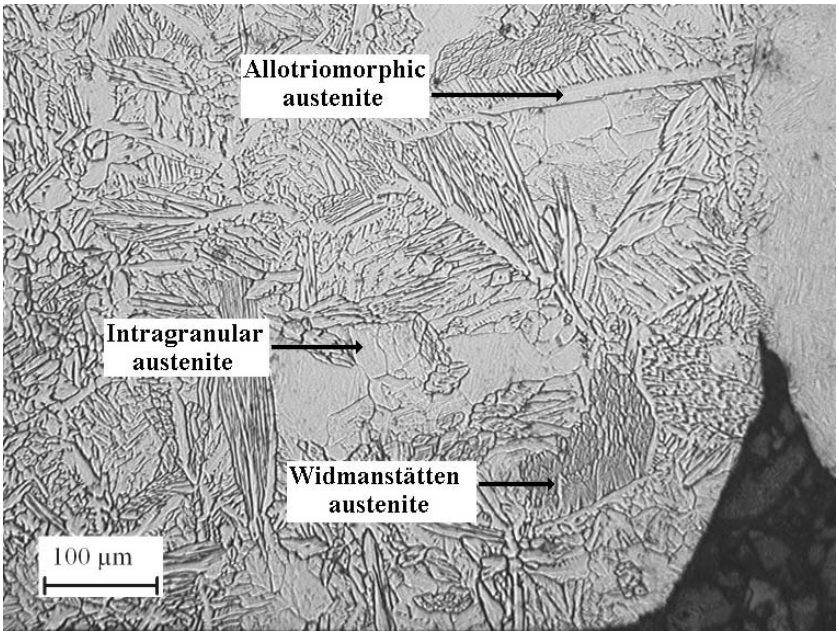

Figure 5.4: Details of the CG-HAZ of steel A in weld WAB1, as seen at the bottom of the plate (electrolytically etched). Plate thickness 5 mm, heat input 0.7 kJ mm^{-1}.

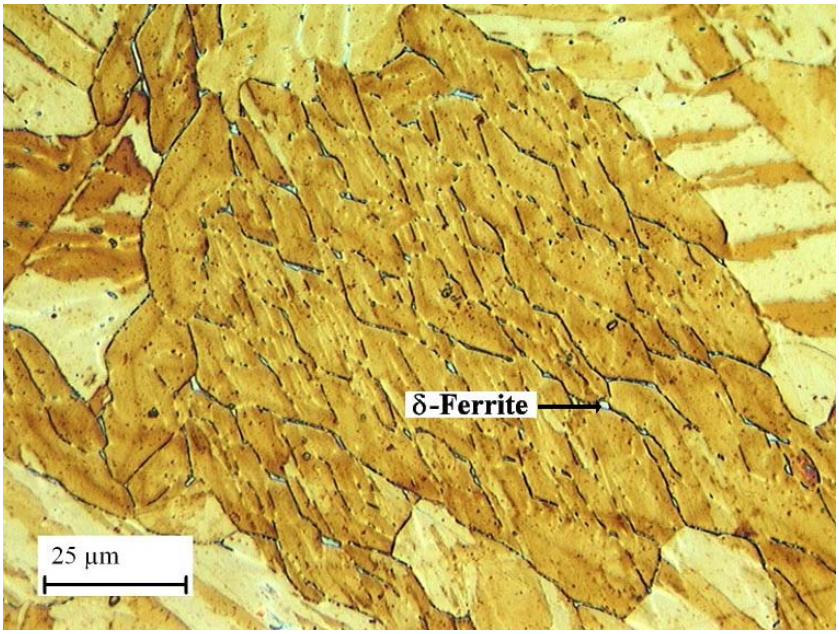

Figure 5.5: Ferrite (light blue color) trapped within the former Widmanstätten austenite in the CG-HAZ of weld WAB1 side A. Sample etched with color etchant. Plate thickness 5 mm, heat input 0.7 kJ mm^{-1}.

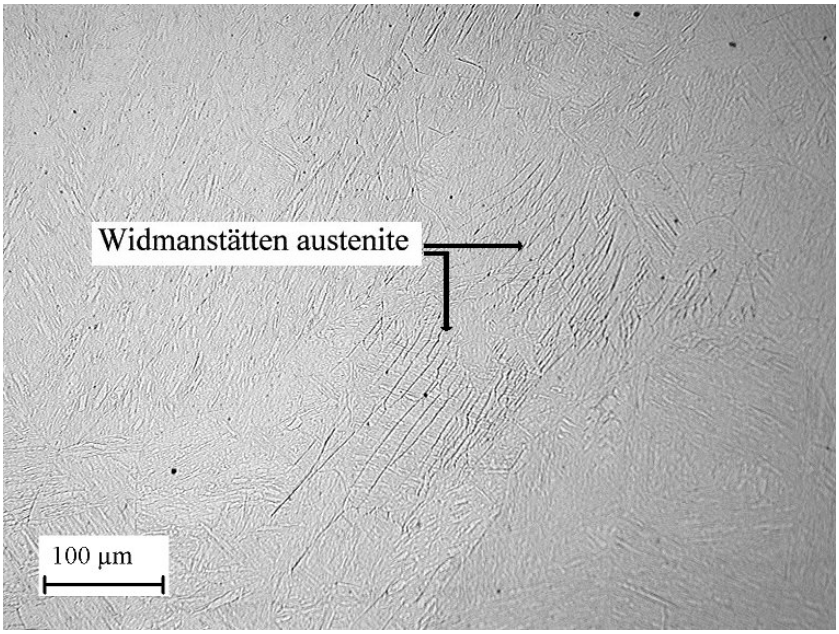

Figure 5.6: Widmanstätten austenite in the CG-HAZ of steel B in weld WAB1 (electrolytically etched). Plate thickness 5 mm, heat input 0.7 kJ mm^{-1}.

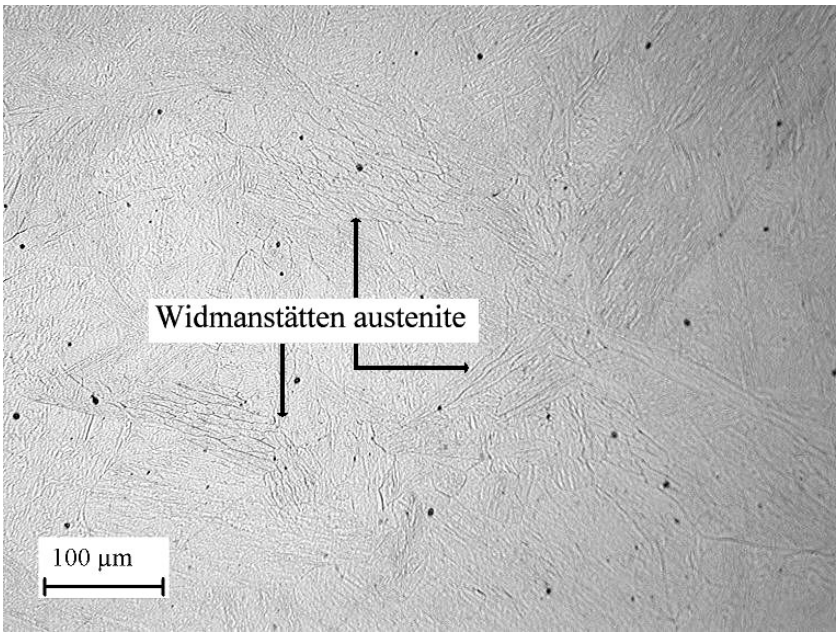

Figure 5.7: Widmanstätten austenite in the CG-HAZ of steel C in weld WAC1 (electrolytically etched). Plate thickness 5 mm, heat input 0.7 kJ mm^{-1}.

such a plate appears lenticular with sharply pointed ends. The rounded tips of the Widmanstätten austenite are therefore inconsistent with a displacive transformation mechanism.

ii Phase transformation sequence in coarse-grained HAZ

Figure 5.8, shows the expected microstructural changes occurring in the coarse-grained HAZ of supermartensitic stainless steels.

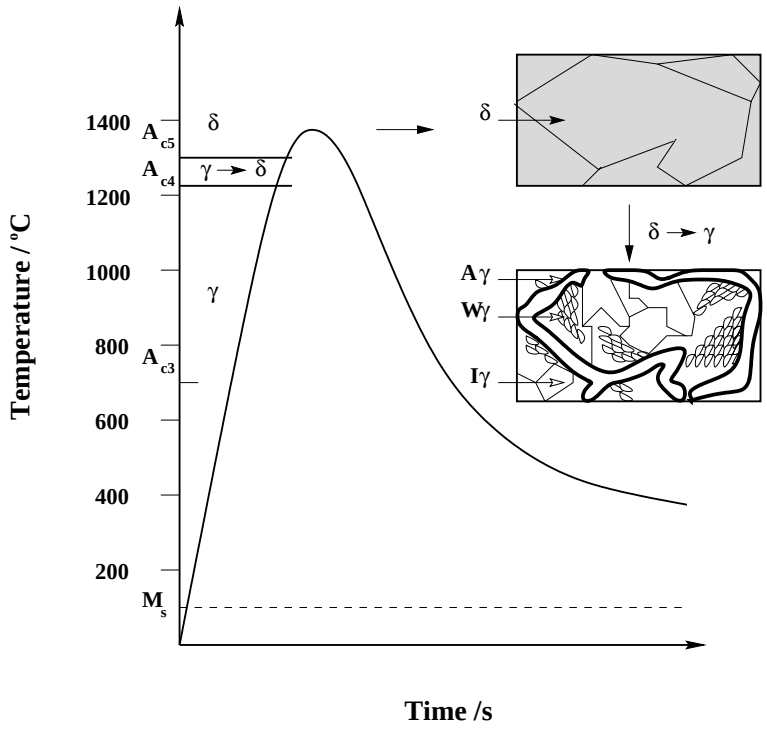

Figure 5.8: Schematic showing microstructure evolution in coarse-grained HAZ during welding. A_γ: allotriomorphic austenite, W_γ: Widmanstätten austenite, I_γ: intragranular austenite.

Upon heating, austenite starts to transform into δ-ferrite at the Ac_4 temperature, and the reaction is completed at the Ac_5 temperature. Once the δ-ferrite single-phase field has been reached, grain growth occurs. At high temperatures ($\geq$ 1300 °C), equilibrium establishes rapidly and therefore it is reasonable to assume that the ferrite had a homogeneous composition. Upon cooling δ-ferrite decomposed into allotriomorphic, intragranular and Widmanstätten austenite followed by austenite

transformation to martensite on cooling below M_S.

The difference in Widmanstätten austenite content between the three steels is probably due to the temperature at which Widmanstätten austenite forms from δ-ferrite since the dilatometric results (chapter 4) showed steel A to have its Ar_4 temperature about 100-120 °C higher than steels B and C.

5.1.d Dual-phase heat-affected zone microstructure

Micrographs of the δ-ferrite found in dual-phase HAZ of steels A, B and C for both heat inputs are reported in figure 5.9. According to its smaller grain size compared with the coarse-grained HAZ, the dual-phase region must have been partially ferritised before cooling. Unlike steels B and C, steel A showed two different δ-ferrite morphologies at the top and at the bottom surface of the plate of weld WAB1. At the cap of the dual-phase HAZ, δ-ferrite was present both at prior austenite grain boundaries and as parallel films within the grains (figures 5.10 and 5.9 (a)). At the root of the dual-phase HAZ, intragranular δ-ferrite was dissolved and only grain boundaries δ-ferrite remained (figure 5.9 (b)). The different morphologies can be attributed to a cooling rate difference between the top and bottom surface of the plate as indicated by the larger grain size of the coarse-grained region (figure 5.2 (b)). In fact as will be shown later, the cooling rate at the bottom of the plate was about 2.5 times slower than at the cap.

The ferrite content was also found to be different between the three alloys and dependent upon the heat input. For a given heat input, the volume percentage of δ-ferrite in dual-phase HAZ was apparently larger for steel A, however, quantification of δ-ferrite as a function of heat input is reported later in this chapter.

i Elemental partitioning

Tables 5.2 and 5.3 summarise the results of fifteen EDX microanalyses performed on the martensitic matrix and δ-ferrite in dual-phase HAZ of steels A, B and C.

Ferrite in steel A was significantly Cr and Mo enriched as well as Ni depleted compared to martensite. Similarly, δ-ferrite in steels B and C was enriched in Cr but depleted in Ni. This showed that despite the fast heating and cooling rates

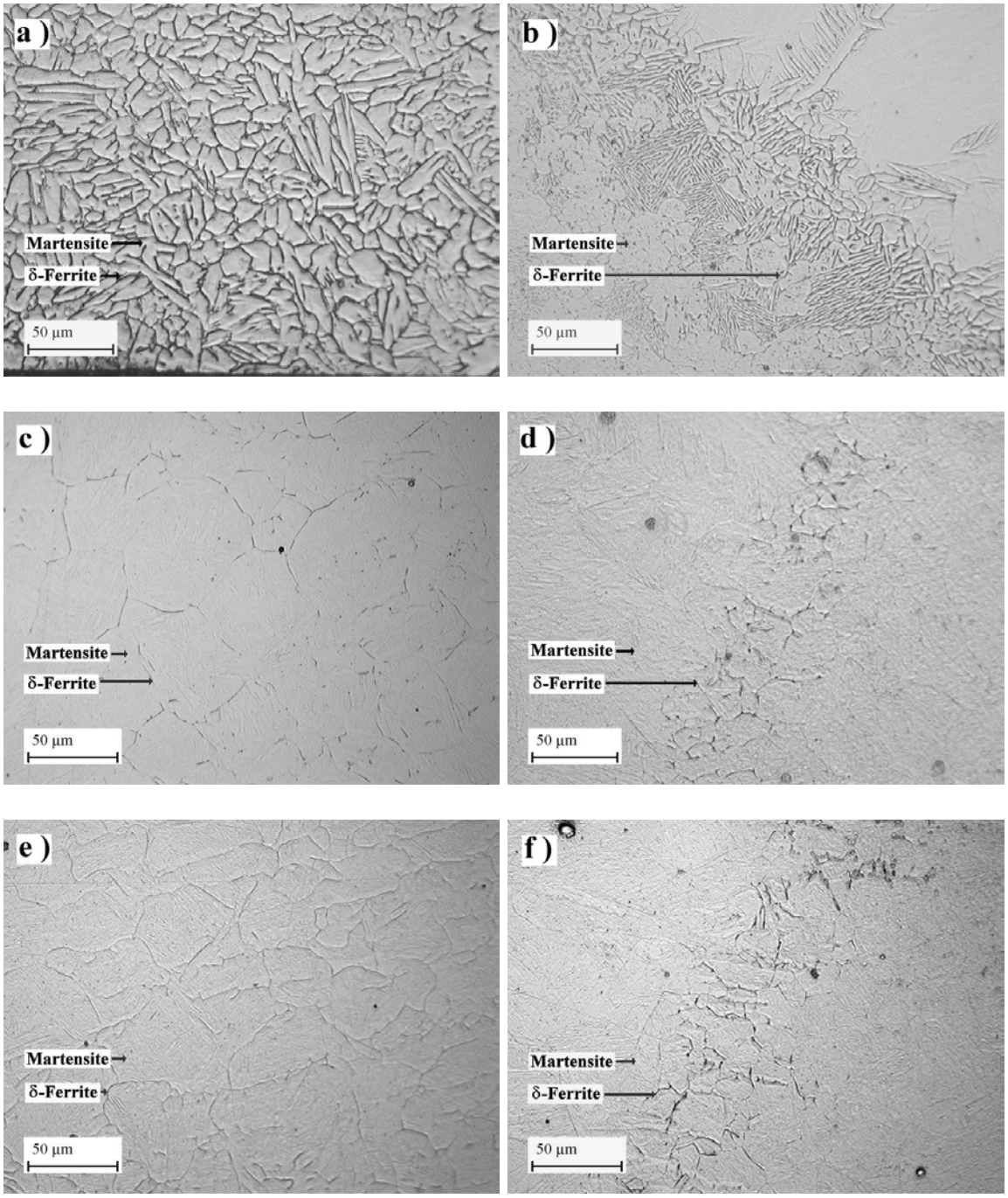

Figure 5.9: Optical micrographs of : weld WAB1 side A ((a) and (b)), weld WAB1 side B ((c) and (d)) and weld WAC1 side C ((d) and (e)). Villela's etchant was used for (a), (c) and (e). Electrolytic etchant was employed for (b), (d) and (e). Note the different DP-HAZ widths in (b), (d) and (f). Plate thickness 5 mm, heat input 0.3 kJ mm^{-1}.

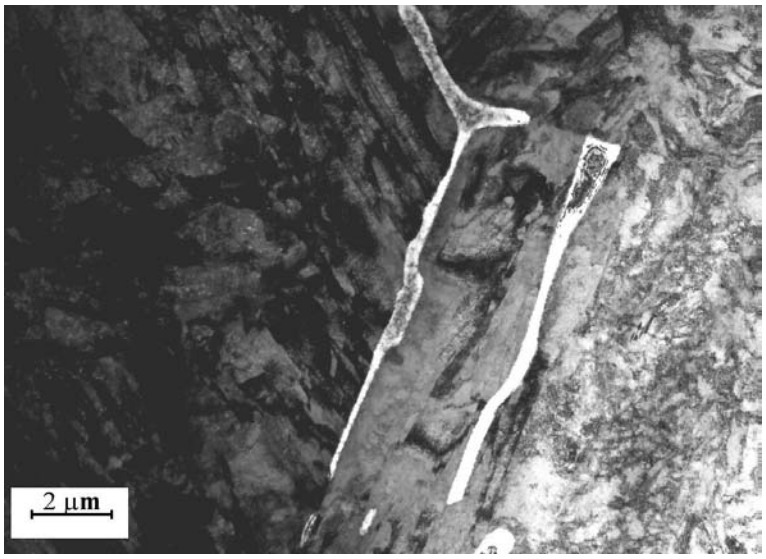

Figure 5.10: TEM micrograph showing grain boundary and intragranular δ-ferrite found in the dual-phase HAZ of weld WAB1 side A.

Phase	**Steel A**		
	Cr	**Ni**	**Mo**
δ-ferrite	13.5 ± 0.9	4.8 ± 1.0	2.6 ± 0.4
Matrix	11.7 ± 0.3	7.0 ± 0.4	1.7 ± 0.2

Table 5.2: EDX microanalysis (wt%) of ferrite and martensite in dual-phase of steel A (weld WAB1).

Phase	**Steel B**		**Steel C**	
	Cr	**Ni**	**Cr**	**Ni**
δ-ferrite	13.2 ± 0.7	0.8 ± 0.3	14.1 ± 0.8	2.1 ± 0.4
Matrix	10.6 ± 0.3	1.5 ± 0.2	12.1 ± 0.3	3.0 ± 0.2

Table 5.3: EDX microanalysis (wt%) of ferrite and martensite in dual-phase HAZ of steels B and C (weld WAB1 and WAC1).

experienced by the HAZ during welding, partitioning of substitutional elements had time to occur. An X-ray map taken in dual-phase HAZ of weld WAB1, side A, allowed direct observation of elemental distribution (figure 5.11).

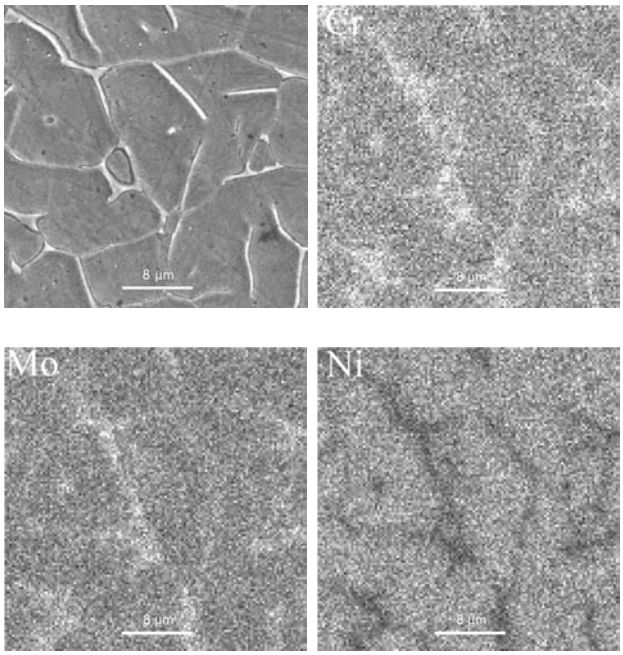

Figure 5.11: Secondary electron SEM image and X-ray mapping of Cr, Mo and Ni, in dual-phase HAZ of weld WAB1 side A. In each square the X-ray signal emitted by the element present in the square is acquired. The intensity (brightness) of the signal is a function of the element concentration at the location considered.

ii Microstructure evolution in dual-phase HAZ

In the dual-phase region, the microstructural development can be summarised as follows (figure 5.12). During heating, uncomplete growth of the δ-ferrite phase nucleated from prior austenite grain boundaries and intragranularly occurred in the Ac_4-Ac_5 temperature range. As EDX results showed, despite the fast heating and cooling rates experienced by the dual-phase HAZ, redistribution of substitutional elements and therefore also interstitial elements took place. The mechanism of ferrite formation is thus diffusional. Consequently, in the partially ferritised region, the extent of δ-ferrite dissolution is determined by the level of chromium and molybdenum enrichment of the δ-ferrite and the cooling rate. Fast cooling rates lead to the

retention of both types of ferrite, while slow cooling rates allow dissolution of the intragranular δ-ferrite.

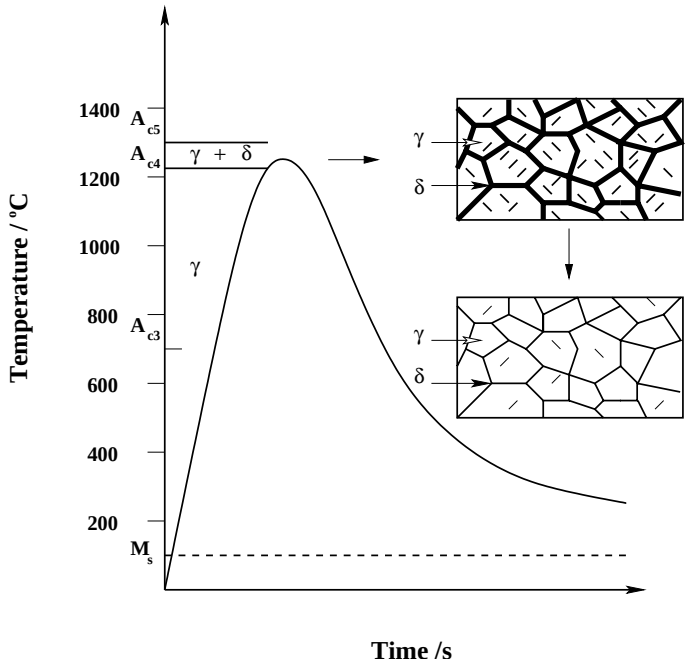

Figure 5.12: Schematic of the dual-phase HAZ microstructure evolution during welding.

iii Weld thermal cycle measurement

An attempt has been made to measure the cooling rate at the cap and at the root of the high temperature HAZ. The idea was to reproduce weld WAB1 and attach thermocouples as close as possible to the fusion line. Three holes of 0.5 mm diameter were consequently drilled in plate A at specific positions to accommodate R-type thermocouples of 0.25 mm diameter. Considering the small size of the high temperature HAZ, the main difficulty was to locate the thermocouples at the right place. Thermocouple T1 was located at the top of the plate and T2 and T3 at the bottom. The temperature was recorded using a data logger connected to a laptop.

Figure 5.13 shows the actual positions of the thermocouples after the experiment. Unfortunately during cutting the thermocouples moved or fell off the plate so that it was not possible to confirm their actual positions in the holes.

The temperature versus time plots are reported in figure 5.14. The times required to reach peak temperatures were surprisingly long *i.e.* about 9 s for each thermocouple. T1 and T2 reached almost the same peak temperature of about 1400 °C but T3 went only up to $\sim$ 1250 °C. The most interesting comparison was therefore between thermocouples 1 and 2. To determine the cooling rates, the cooling time between 1400 and 1200 °C (Δt_{14-12}) was chosen. The Δt_{14-12} was 1.7 s at the cap of the HAZ and 4.4 s at the bottom of the plate. Those times correspond to cooling rates of about 117 and 45 °C s^{-1} respectively. This shows that the cap of the HAZ cooled about 2.5 times faster than the bottom of the HAZ. It is the slower cooling rate of the bottom of the HAZ that allowed the intragranular δ-ferrite to dissolve.

5.2 Effect of cooling rate on δ-ferrite retention

The aim of this section was to study the effect of a wide range of cooling rates on the δ-ferrite retention in specimens quenched from the δ-ferrite single-phase field and the δ-ferrite plus austenite region. As microstructures were best revealed in steel A, only this steel has been selected for this part.

5.2.a Experimental procedure

Small coupons of dimension 10×15×3 mm were machined in steel A. Specimens were placed in a pre-heated furnace (at 1375 °C for the first test and then at 1350 °C) at the center of the bottom surface and were let in 5 minutes. Specimens were subsequently either water quenched, air cooled, or were left in the furnace switched off with the door open until the temperature reached about 700 °C and then water quenched. To get rid of the oxidation layer after heat-treatment, coupons were mounted and roughly ground to remove approximately 1 mm of matter. For optical examination specimens were finely ground, polished and electrolytically etched in sulfuric acid solution. The volume fractions of δ-ferrite were measured at a magnification of 100 using image analysis and the procedure described in chapter 3.

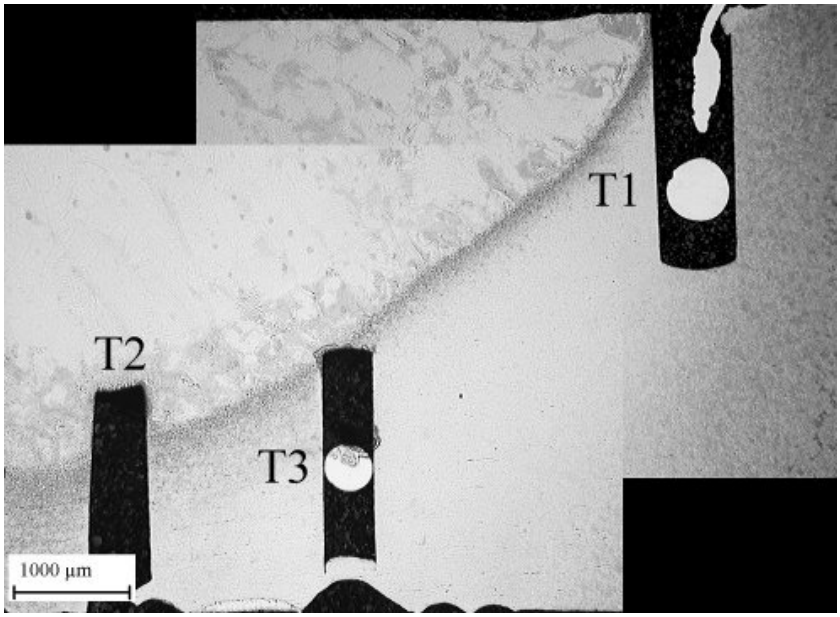

Figure 5.13: Macrograph showing the position of the three thermocouples in plate A. Plate thickness 5 mm, heat input 0.7 kJ mm^{-1}.

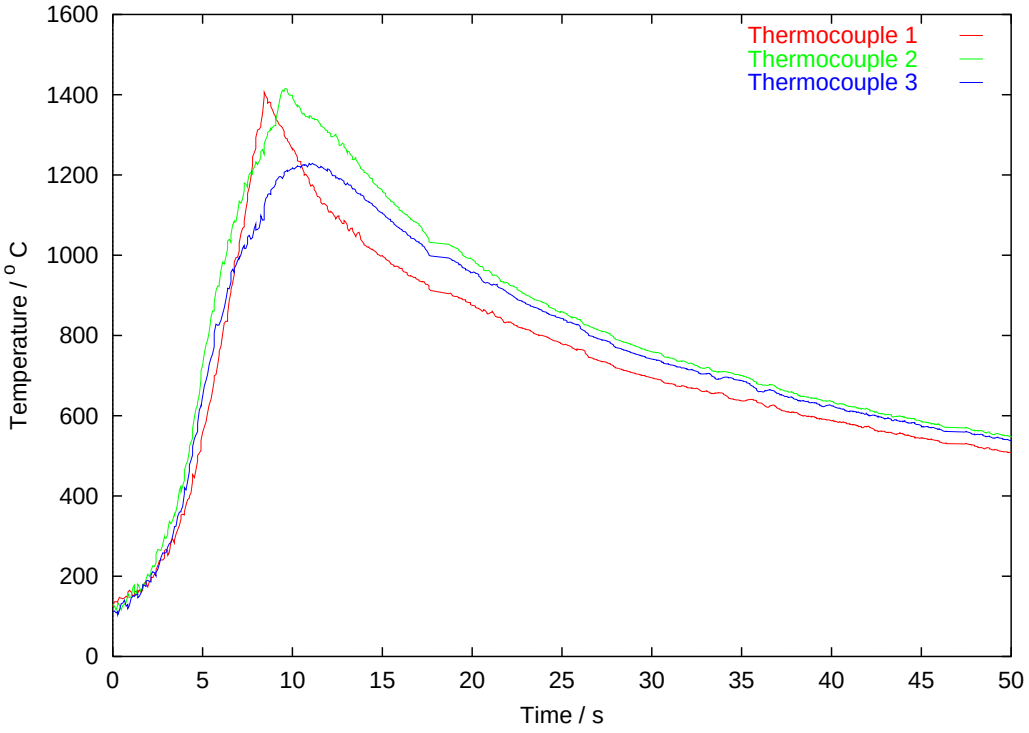

Figure 5.14: Thermal cycles measured at three different positions in HAZ of steel A.

5.2.b Results

Figure 5.15 shows the microstructures obtained after water quenching, air cooling and furnace cooling from 1375 °C. The specimen was clearly cooled from the δ-ferrite single-phase region as indicated by the large grain size. The volume fraction and coarseness of Widmansttäten austenite were seen to increase with decreasing cooling rate, as a result, increasingly thicker films of δ-ferrite remained trapped between Widmansttäten austenite subunits (figure 5.15 (b), (d) and (f)).

Figure 5.16 illustrates the microstructures obtained after cooling from 1350 °C. δ-ferrite was observed intragranularly and also at grain boundaries, the material was therefore quenched from the δ-ferrite + austenite phase field. Reducing the cooling rate clearly led to the retention of less ferrite.

The volume fraction of δ-ferrite measured for each heat-treatment and cooling method is plotted in figure 5.17. It can be seen that the quantity of retained δ-ferrite is dependent upon the cooling rate and heat-treatment temperature. When cooling occurs from the δ-ferrite single-phase field, fast cooling rates limit the formation of Widmansttäten austenite but not that of the allotriomorphic and intragranular austenite and consequently only small quantities of δ-ferrite are trapped. On the other hand, when cooling occurs from the δ-ferrite + austenite phase field, the faster the cooling rate the larger the δ-ferrite volume fraction. This is because solute redistribution is limited during fast cooling. Consequently in weld heat-affected zones fast cooling rates prevent δ-ferrite dissolution in dual-phase HAZ but limit its volume fraction in coarse-grained HAZ.

According to the dilatometric results of chapter 4, ferritisation should not have occurred at 1350 °C (*i.e.* Ac_4 was 1372 °C). However, inside the furnace chamber the temperature is not necessarily uniform and differences between the temperature set on the furnace and actual temperature are not surprising. It should also be mentioned that since the dilatometer used in chapter 4 did not allow the thermocouple to be attached to the specimen surface, a small error in the phase transformation temperatures can be expected. However considering the slow heating rate used in the dilatometric experiments, the extent of the error should be limited to few degrees.

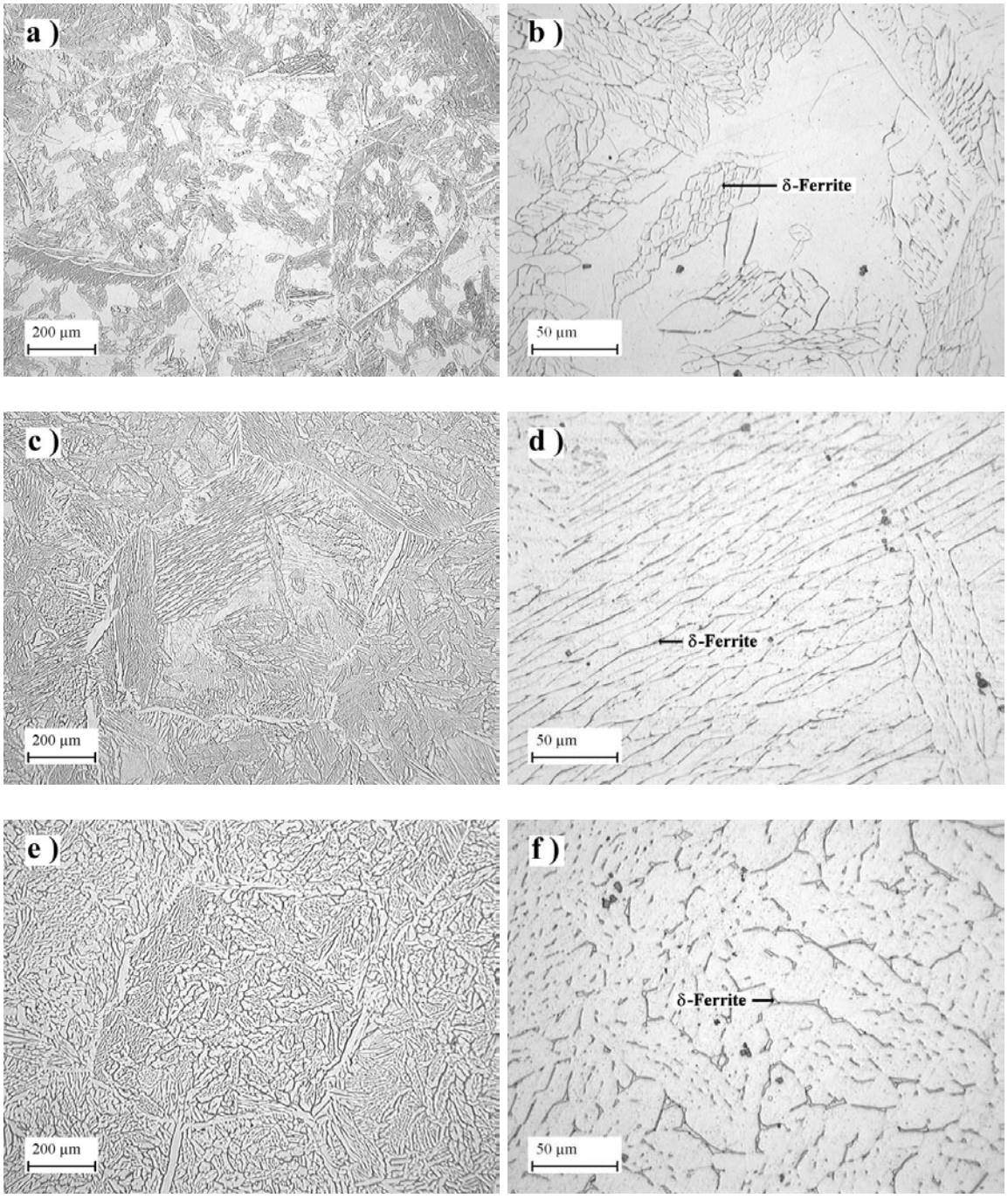

Figure 5.15: Optical micrographs illustrating the microstructures of steel A, obtained after isothermal transformation at 1375 °C for 5 minutes and water quenched ((a) and (b)), air cooled ((c) and (d)) and furnace cooled ((e) and (f)). Micrographs (b), (d) and (f) are magnified pictures of (a), (c) and (e) respectively. Electrolytically etched.

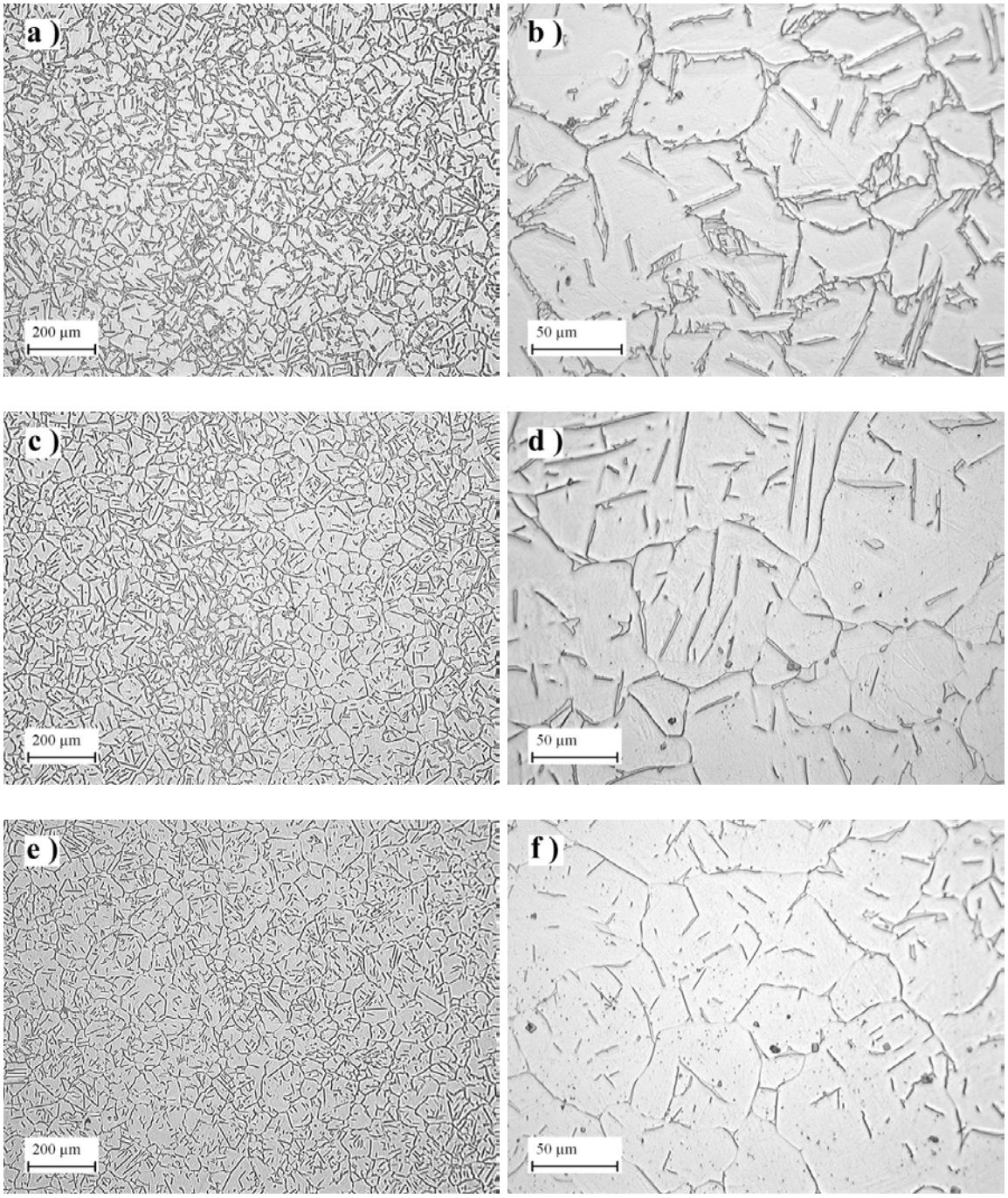

Figure 5.16: Optical micrographs illustrating the microstructures of steel A, obtained after isothermal transformation at 1350 °C for 5 minutes and water quenched ((a) and (b)), air cooled ((c) and (d)) and furnace cooled ((e) and (f)). Micrographs (b), (d) and (f) are magnified pictures of (a), (c) and (e) respectively. Electrolytically etched.

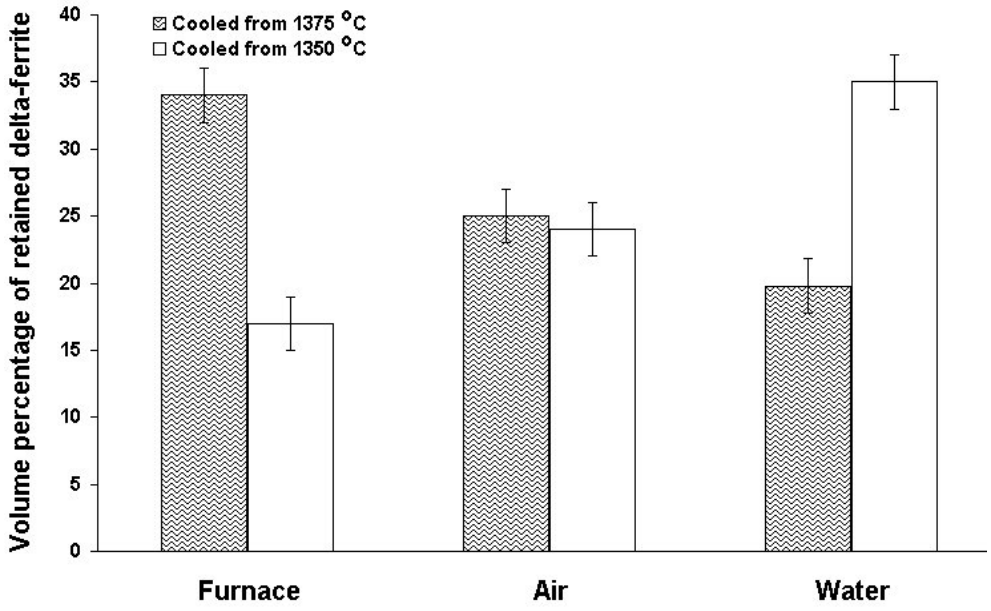

Figure 5.17: Volume fraction of retained δ-ferrite as a function of heat-treatment temperature and cooling mode.

5.3 Effect of heat input

There is no published information on the effect of heat input on δ-ferrite content in supermartensitic stainless steels. However, this information might be useful if the presence of δ-ferrite in HAZ is to be minimised. To quantify the effect of weld heat input a second series of bead-on-plates has been performed.

5.3.a Experimental Procedure

Three autogenous single-pass welds have been produced for each material using three heat inputs. Thicker plates of dimension (100×100×10 mm) have been machined to allow the use of a relatively high heat input and to keep the high temperature isotherms parallel to the weld pool (3 dimensional heat flow). Table 5.4 lists the welding parameters employed. The volume percentage of δ-ferrite in dual-phase HAZ was measured by image analysis according to the procedure described in chapter 3.

	Current (A)	Voltage (V)	Travel speed (mm s^{-1})	Heat input (kJ mm^{-1})
WX1.0	275	10.0	1.66	1.0
WX0.7	208	9.3	1.66	0.7
WX0.3	101	9.2	1.66	0.3

Table 5.4: Welding parameters for the three single-pass welds carried out on steels A, B and C. X is used to substitute A, B or C.

5.3.b Results

The microstructures of the welds performed on the three steels are reported in figures 5.18 to 5.20. As expected, the volume of the weld pool and the size of the HAZ increased with increasing heat input.

The volume percentages of retained δ-ferrite in dual-phase HAZ of the three steels are plotted as a function of heat input in figure 5.21. Ferrite presence never exceeded 15 % and had the tendency to decrease with increasing heat input. Consistent with the results of the observations made in the previous section, steel A contained larger amount of δ-ferrite in its dual-phase HAZ compared to steels B and C.

The volume fraction of δ-ferrite trapped in the coarse-grained regions could not be easily measured, because the distribution of Widmansttäten austenite was non uniform in those regions. However, being closer to the fusion line, the cooling rate of the coarse-grained HAZ is always faster than that of the dual-phase HAZ and therefore according to figure 5.15 less δ-ferrite is to be expected in this region.

5.4 Multipass welds

The work described in the previous sections established the effect of chemical composition and heat input on δ-ferrite retention in single-pass welds, but neglected reheating effects that occur during the deposition of subsequent passes. However,

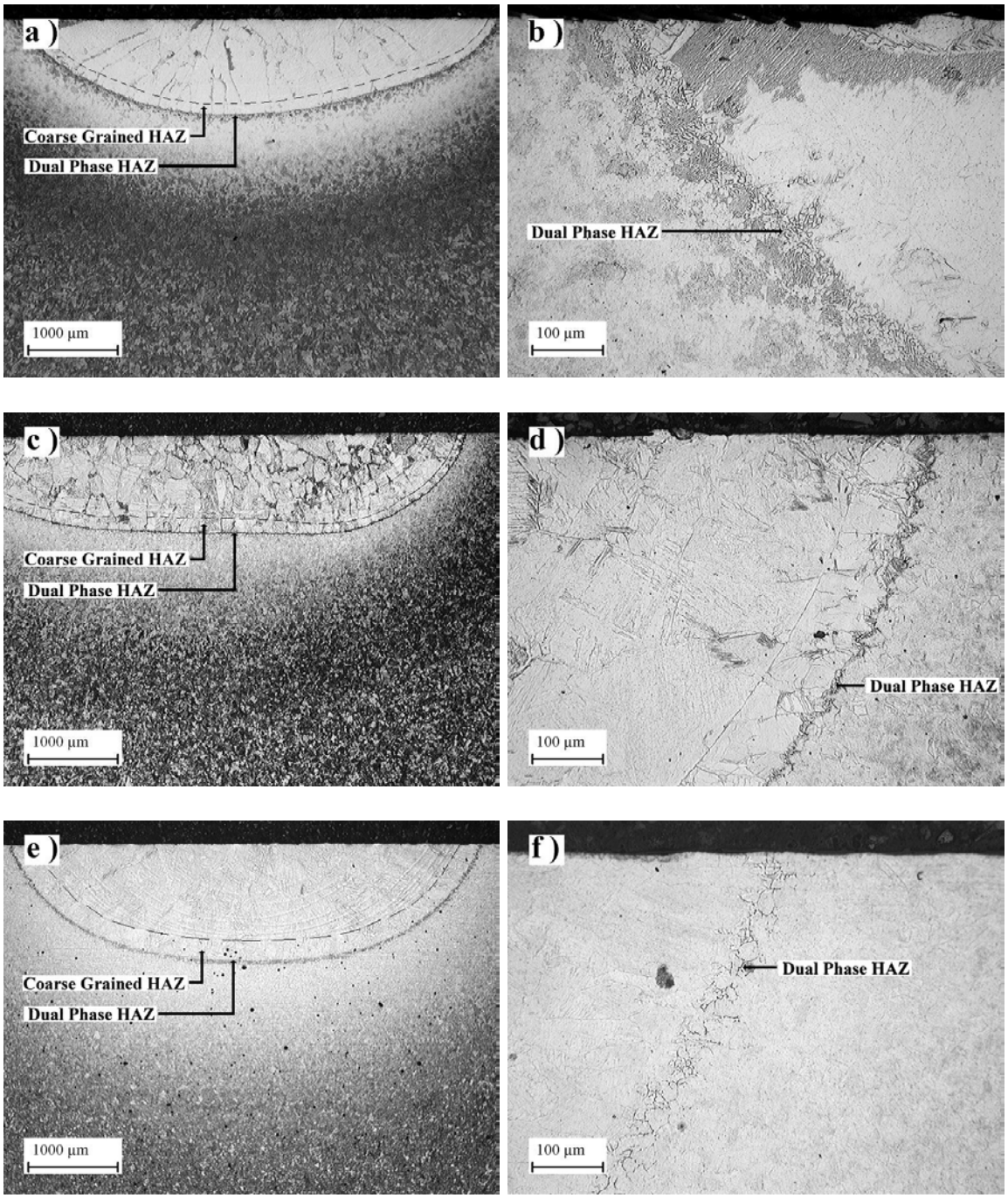

Figure 5.18: Optical micrographs of single-pass welds performed on steels A ((a) and (b)), B ((c) and (d)) and C ((e) and (f)) using a heat input of **0.3 kJ mm^{-1}** (electrolytically etched). Micrographs (b), (d) and (f) are magnified pictures of micrographs (a), (c) and (e) respectively. Plate thickness 10 mm.

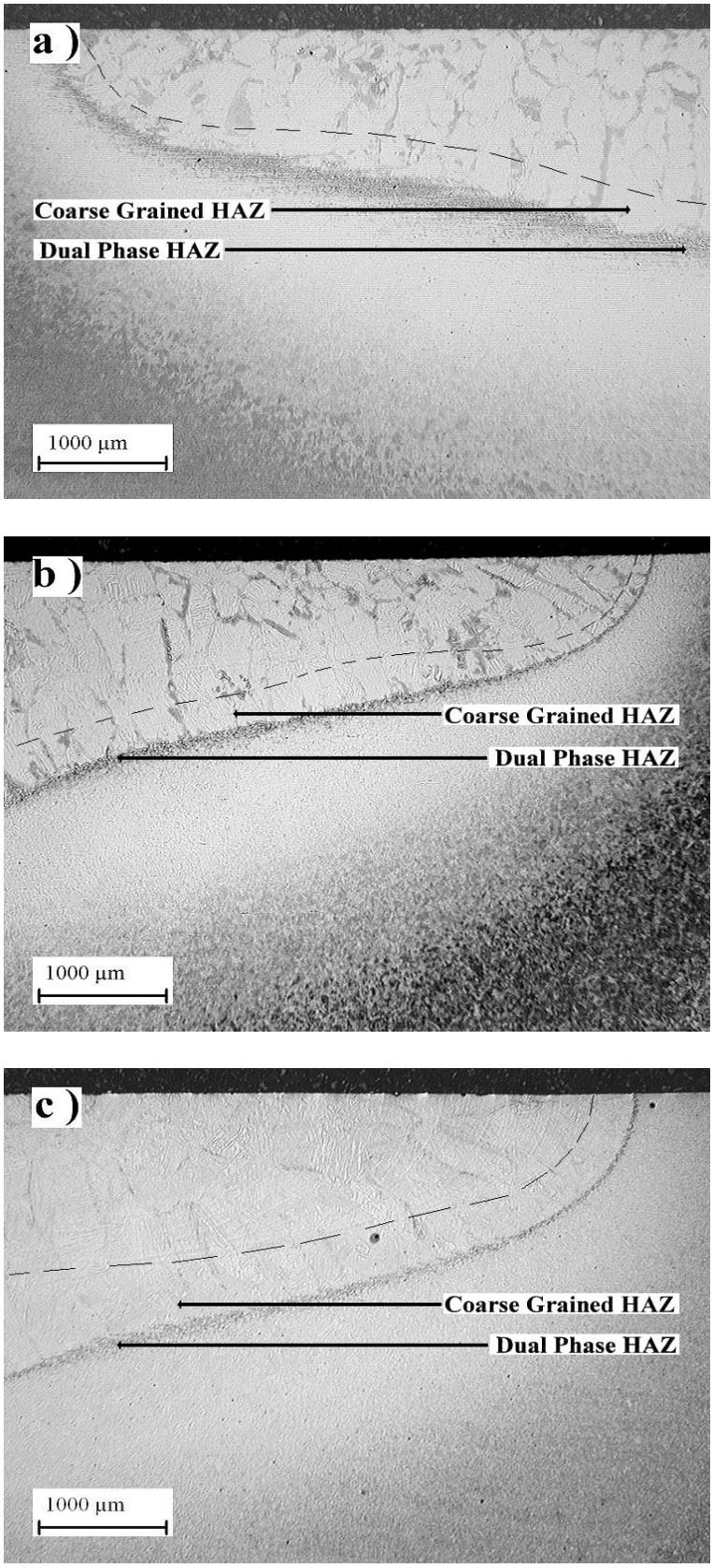

Figure 5.19: Optical micrographs of single-pass welds performed on steels A (a), B (b) and C (c) using a heat input of **0.7 kJ mm^{-1}** (electrolytically etched). Plate thickness 10 mm.

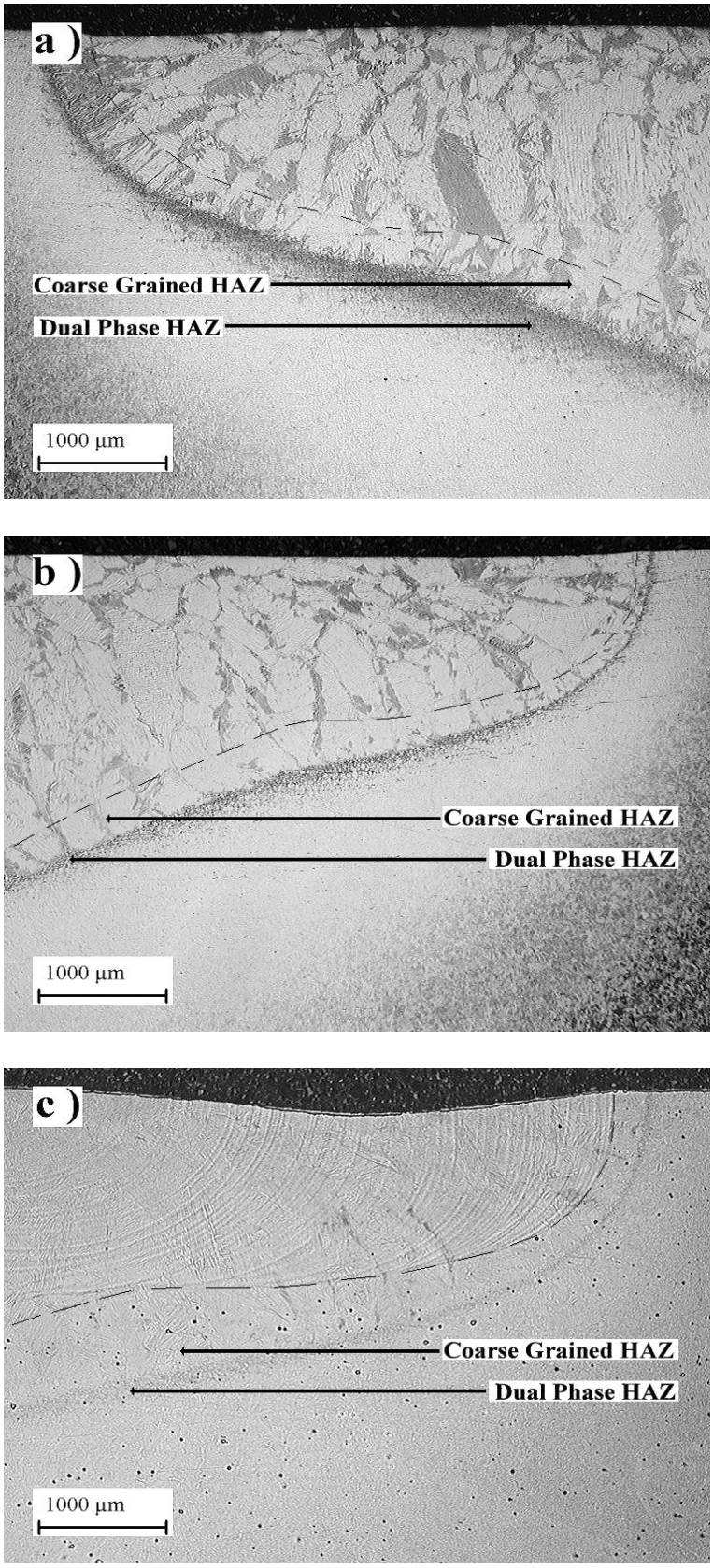

Figure 5.20: Optical micrographs of single-pass welds performed on steels A (a), B (b) and C (c) using a heat input of **1 kJ mm**$^{-1}$ (electrolytically etched). Plate thickness 10 mm.

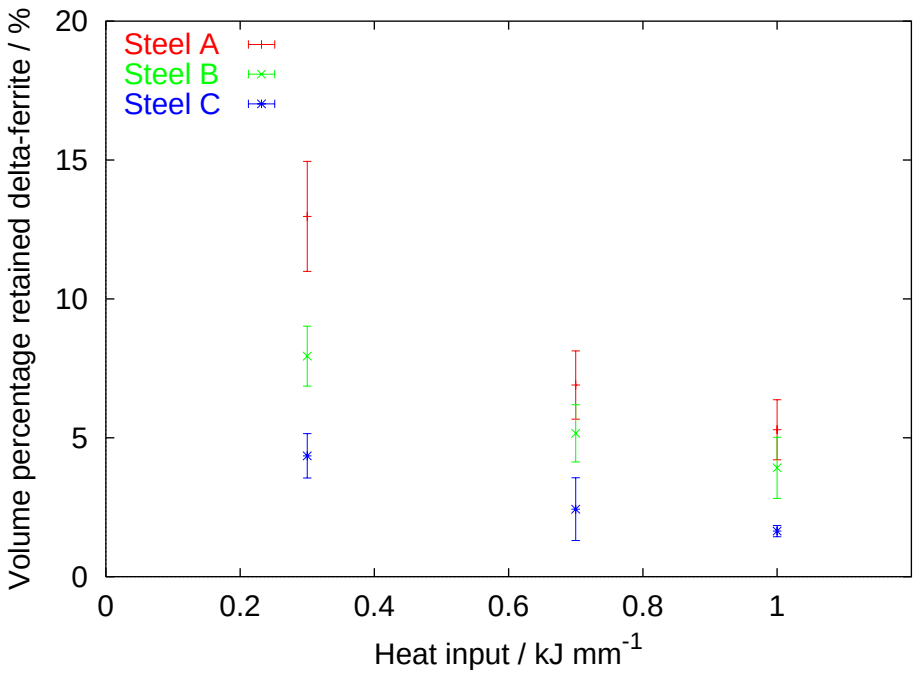

Figure 5.21: Volume fraction of retained δ-ferrite in dual-phase HAZ as a function of heat input for steels A, B and C. Plate thickness 10 mm.

actual welds are multipass and therefore the primary HAZ microstructure is subject to reheating. To check the effect of reheating on the high temperature HAZ microstructure, actual multipass welds have been observed.

The multipass welds studied were provided by TWI. They all had similar joint design *i.e.* 60° angle with no face root, and were welded using a duplex stainless steel filler wire (Zeron 100, table 5.5) employing up to 14 passes with an interpass temperature of 150 °C. Tables 5.6 to 5.8 summarise the welding parameters employed. The first two passes are usually deposited using a higher heat input due to heat loss through the gap between the workpieces.

5.4.a Observations

Details of the microstructure of multipass welds performed on steels A, B and C are reported in figures 5.22 to 5.27. The features of the high temperature HAZ were more difficult to observe in multipass welds due to various level of tempering.

	C	Si	Mn	Ni	Cr	Mo	Cu	W	N
Zeron 100	0.018	0.39	0.69	9.30	24.80	3.80	0.60	0.61	0.22

Table 5.5: Chemical composition of Zeron 100 in wt%.

Run number	Process	Filler size (mm)	Current (A)	Voltage (V)	Heat input (kJ mm^{-1})
1	TIG	2.4	60	9.0	1.10
2	TIG	2.4	88	9.5	1.24
3-4	MMA	2.5	62-66	22.1-23.9	0.44-0.70
5-7	MMA	3.2	82-96	22.2-24.3	0.70-1.06

Table 5.6: Welding parameters for multipass weld performed on steel A.

In each weld, attention was focussed to the cap and the root of the HAZ since it is those regions that are in contact with the external and internal environments.

No microstructure could be observed in the coarse-grained HAZ of the multipass weld performed on steel A (figure 5.22). The morphology and volume fraction of the δ-ferrite found in dual-phase HAZ were different at the cap of the weld HAZ compared to the root (figure 5.23). Similar to the observations made on the low heat input bead-on-plates on steel A, ferrite at the cap of the HT-HAZ was present at prior austenite grain boundaries and as intragranular films. Whilst at the HAZ root, δ-ferrite was only present at prior austenite grain boundaries.

The origin of the different ferrite morphologies is multiple. First a cooling rate difference it to be expected in HAZ between the cap and the root. Indeed due to the presence of a larger heat sink, the cap of the HAZ cools down faster than the root, and as seen before, this prevents the intragranular δ-ferrite from dissolving. In addition, due to the deposition of several layers, the HAZ root is reheated several times and this encourages the remaining ferrite to dissolve. Consequently, δ-ferrite

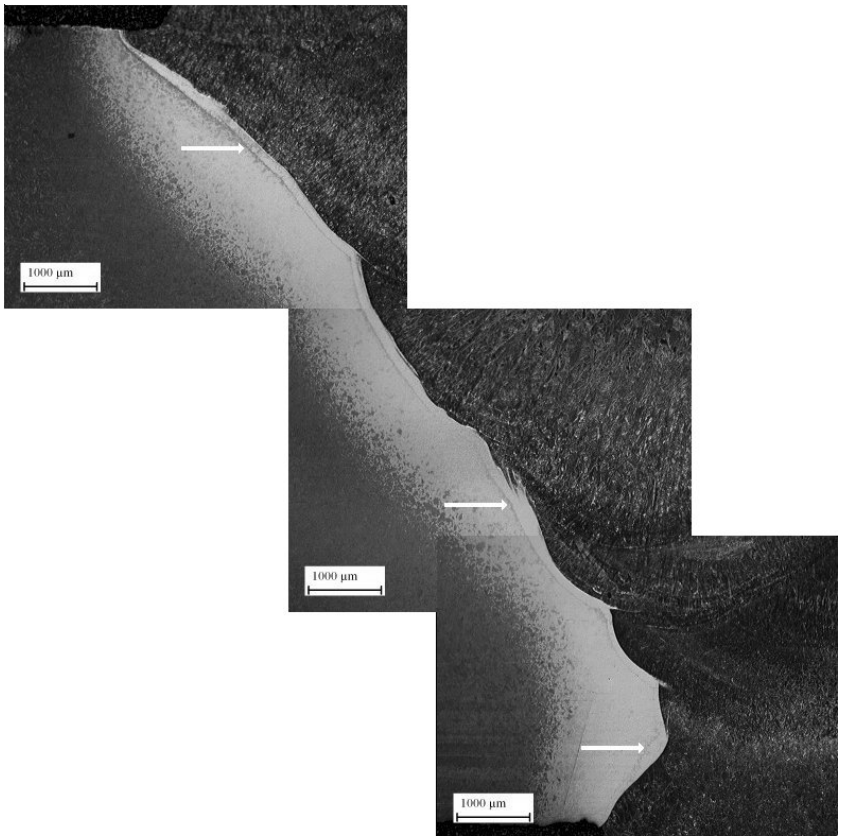

Figure 5.22: Optical macrograph showing continuous film of δ-ferrite (arrowed) in the high temperature heat-affected zone of the multipass weld performed on steel A (electrolytically etched). 7 passes were employed to complete the weld

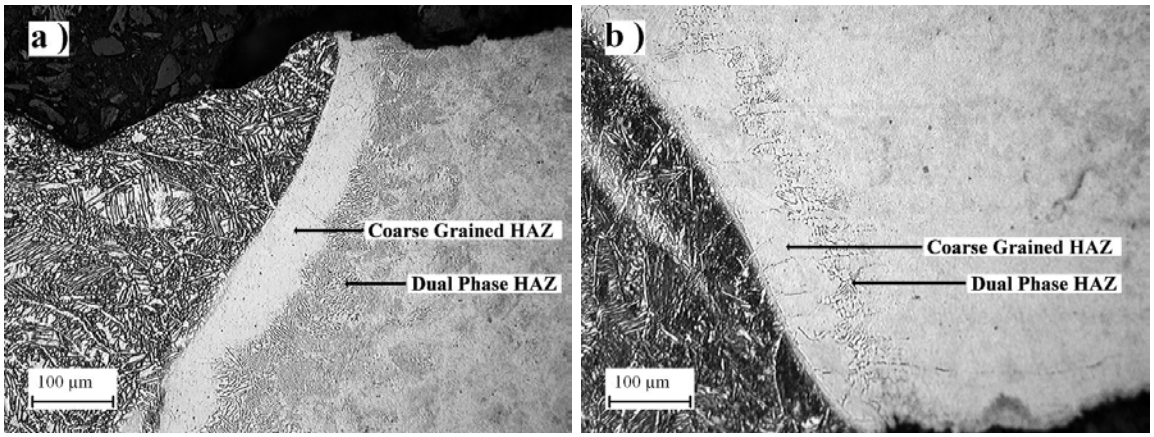

Figure 5.23: Optical photographs illustrating the different morphology of δ-ferrite in heat-affected zone (a) at the cap and (b) at the root (electrolytically etched).

Run number	Process	Filler size (mm)	Current (A)	Voltage (V)	Heat input (kJ mm^{-1})
1	TIG	2.4	80	10.0	1.36
2	TIG	2.4	110	11.0	1.43
3-11	MMA	2.5	69-77	22.0-26.4	0.57-1.23

Table 5.7: Welding parameters for multipass weld performed on steel B.

Run number	Process	Filler size (mm)	Current (A)	Voltage (V)	Heat input (kJ mm^{-1})
1	TIG	2.4	95	9.8	1.48
2	TIG	2.4	122	10.5	1.50
3-14	MMA	3.2	86-91	23.1-25.9	0.59-1.50

Table 5.8: Welding parameters for multipass weld performed on steel C.

distribution in the whole dual-phase HAZ is far from homogenous and quantification is therefore difficult. However, based on the results of the previous section, the volume fraction of δ-ferrite at the cap of the HAZ can be estimated to be of the order of 10 to 15 %.

Ferrite in dual-phase HAZ of steels B and C could not be revealed using the electrolytic etchant, instead, Villela's reagent was employed (figure 5.24 and 5.26). The coarse-grained HAZs at the cap of steels B and C were clearly larger than that of steel A, and showed the presence of some Widmansttäten austenite. Also, consistent with the results obtained on the bead-on-plates, steels B and C showed little or no evidence of δ-ferrite retention in dual-phase HAZ. Contrarily to steel A, grain refinement was observed at the root of the HAZ of steels B and C. The latter difference might be explained by the larger number of passes employed to perform those welds.

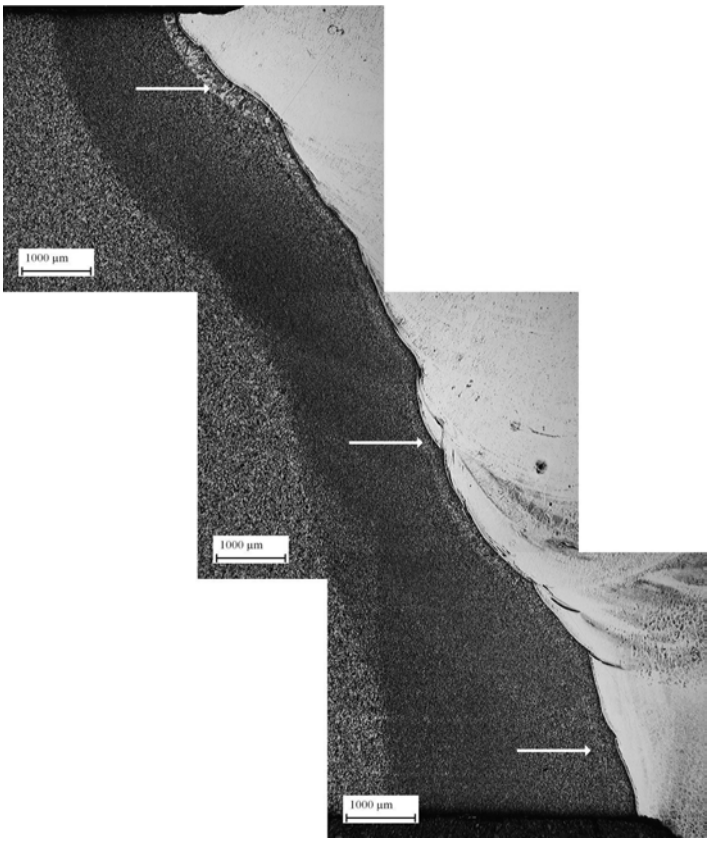

Figure 5.24: Optical macrograph showing the high temperature heat-affected zone (arrowed) of the multipass weld performed on steel B (etched with Villela's reagent). 11 passes were employed to complete the weld.

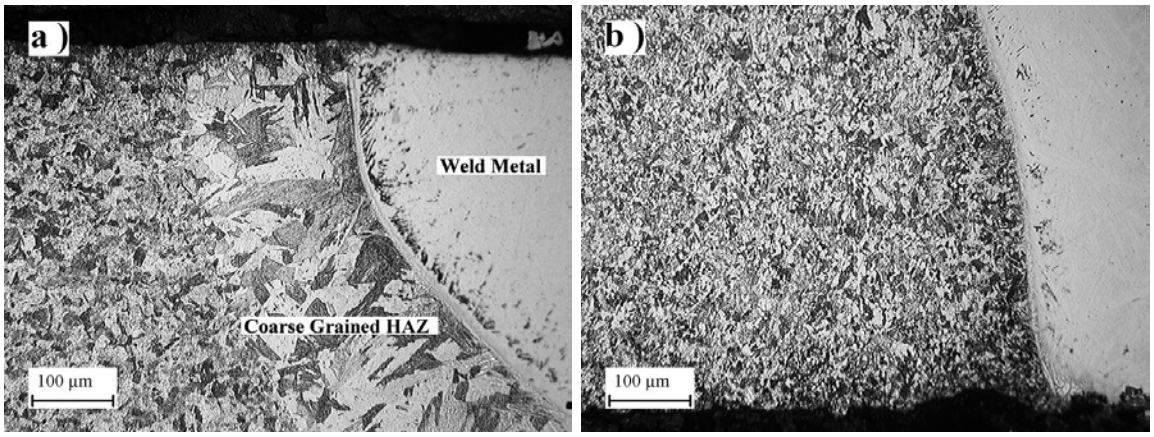

Figure 5.25: Close-up of (a) the cap of the HT-HAZ and (b) the root of the HT-HAZ (etched with Villela's reagent).

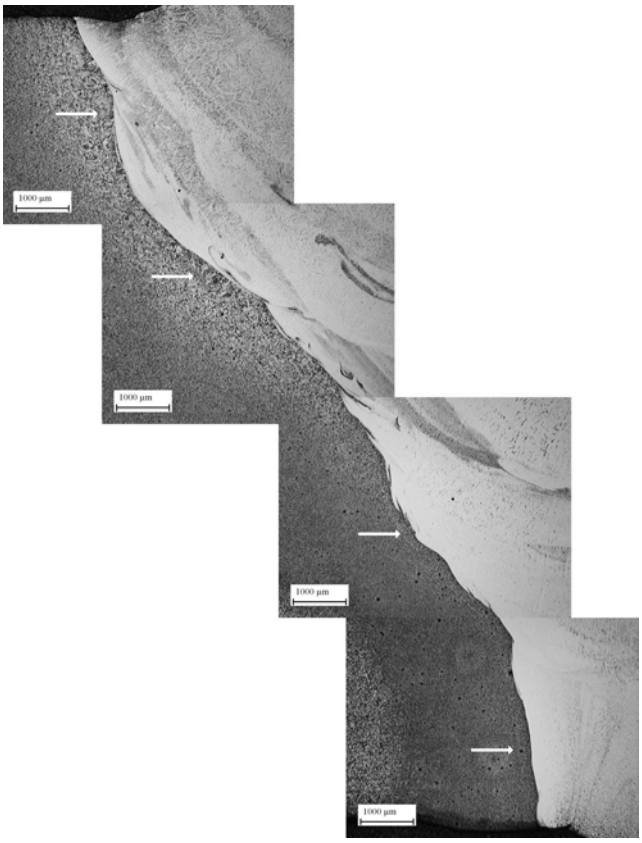

Figure 5.26: Optical macrograph showing the high temperature heat-affected zone (arrowed) of the multipass weld performed on steel C (etched with Villela's reagent). 14 passes were employed to complete the weld.

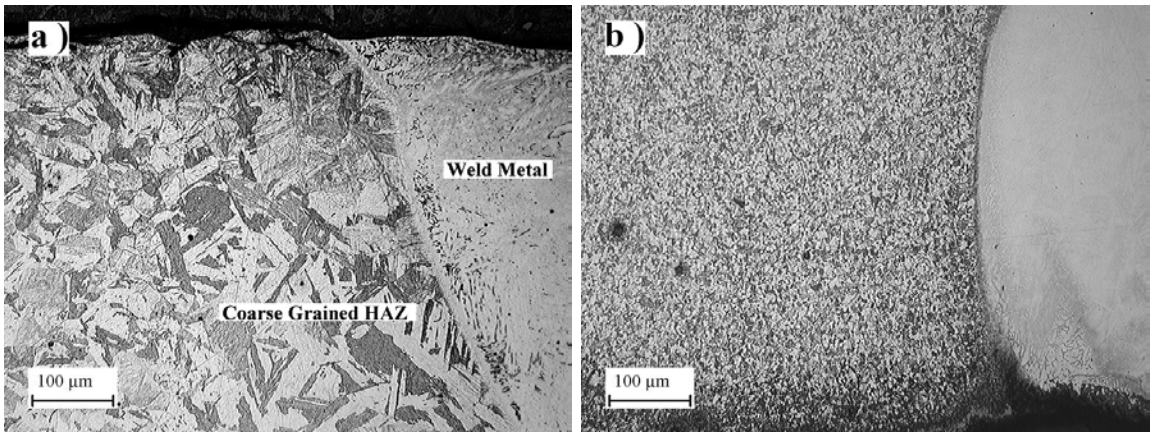

Figure 5.27: Close-up of (a) the cap of the HT-HAZ and (b) the root of the HT-HAZ (etched with Villela's reagent).

5.4.b Remarks

Compared with the high temperature HAZ of the semi-ferritic stainless steel showed in figure 2.7, supermartensitic stainless steels retain significantly less δ-ferrite and possess a more complex microstructure. Consequently, establishing the effect of δ-ferrite on the properties is more difficult. However, since steels similar to steel A are more likely to retain detectable amount of δ-ferrite in HAZ, it is advisable to use those materials to establish the effect of δ-ferrite on impact and corrosion resistance properties. On the other hand, assuming δ-ferrite to be undesirable, attention should be drawn to the top surface of the weld HAZ, since the previous section revealed δ-ferrite to be mainly concentrated at the cap of the HAZ.

The effect of the nature of the filler wire on δ-ferrite retention has not been investigated. Nevertheless considering that the dual-phase HAZ is usually located at around 100 μm from the fusion line, the migration of carbon or nitrogen from or towards the weld metal is unlikely.

5.5 Summary and conclusions

The use of autogenous bead-on-plates has permitted the identification of the different high temperature HAZ regions and sequence of phase transformations. The high temperature HAZ consists of a coarse-grained and a narrow dual-phase HAZ. Thorough examination of the microstructure revealed the presence of small amounts of δ-ferrite in both regions. In coarse-grained HAZ, δ-ferrite was retained as thin films between Widmanstätten austenite laths. On the other hand, δ-ferrite was found at prior austenite grain boundaries and also within the austenite grains in dual-phase HAZ. Strong partitioning of ferrite stabilising elements into δ-ferrite and fast cooling rates explained its retention.

Using small heat-treated specimens and different cooling methods, it could be demonstrated that fast cooling rates favour ferrite retention in specimens cooled from the austenite plus δ-ferrite region but minimise its presence in specimens cooled from the fully ferritic field.

On the other hand, the volume fraction of δ-ferrite retained in dual-phase HAZ

was quantified as a function of heat input. Larger heat inputs led to wider dual-phase HAZ regions and lower δ-ferrite volume fractions. In all experiments, the most corrosion resistant alloy (containing molybdenum) retained larger quantities of δ-ferrite, and had a higher tendency to form Widmanstätten austenite when cooled from the fully ferritic phase field.

Actual weldments, performed using arc welding techniques, show a non-uniform distribution of δ-ferrite in dual-phase HAZ. Due to reheating effects δ-ferrite formed during the deposition of the first layer, tend to dissolve and consequently δ-ferrite is mainly located at the cap of the weld HAZ. This is, however, mainly noticeable on molybdenum containing alloys.

Chapter 6

Predicting δ-ferrite retention and dual-phase HAZ width

As described in chapter 5, examination of single-pass bead-on-plate weld deposits, revealed that the richly alloyed supermartensitic steel was more prone to ferrite retention and possessed a larger dual-phase HAZ than any of the other alloys studied. Since the presence of δ-ferrite might be harmful to the properties, it would be interesting to be able to predict the susceptibility to δ-ferrite retention and to be able to estimate the extent of the region where it proliferates.

6.1 Assessment of existing methods of ferrite prediction

6.1.a Ferrite factor and Balmforth diagram

The chemical compositions of the three steels listed in table 6.1 have been used to calculate their ferrite factor (FF, equation 6.1 in wt%) and locate their position on the recently developed Balmforth diagram (chapter 2).

$$FF = \mathrm{Cr} + 6\mathrm{Si} + 8\mathrm{Ti} + 4\mathrm{Mo} + 2\mathrm{Al} + 4\mathrm{Nb} - 2\mathrm{Mn} - 4\mathrm{Ni} - 40(\mathrm{C} + \mathrm{N}) \qquad (6.1)$$

Steel A had the lowest ferrite factor (-3.04) followed by steel C (0.68) and B (2.94). This order suggests that steel B should retain the largest amount of ferrite,

but as figure 2.9 shows, FF values below 5 lead to relatively small amounts of retained δ-ferrite, typically less than 10 %. Experimentally, although the volume fractions of HAZ retained δ-ferrite are of the same order of magnitude, steel A contained more ferrite than the other alloys. Consequently, it is concluded that the ferrite factor is not very helpful for making comparisons.

Steel name	C	Si	Mn	Ni	Cr	Mo	Cu	Ti	N
A	0.01	0.26	0.46	6.46	12.20	2.48	0.03	0.09	0.0070
B	0.01	0.18	1.14	1.55	10.90	$\leq$ 0.01	0.49	0.01	0.0060
C	0.01	0.19	0.24	3.12	12.50	0.02	0.06	0.01	0.0120

Table 6.1: Chemical composition of steels A, B and C in wt%.

On the other hand, the Balmforth diagram (figure 6.1) predicts steels B and C to retain similar levels of ferrite (about 20 %), but less than steel A (50 %). In fact, the larger volume percentage predicted for steel A is mainly due to the presence of molybdenum. The coefficient 2 attributed to molybdenum significantly affects the value of the Cr_{eq} and consequently raises the expected level of retained ferrite. On the other hand, the low levels of C and N in supermartensitic steels means that the Ni_{eq} virtually equals the nickel concentration. Considering that Mo and Ni are the elements whose concentrations vary the most in supermartensitic steels, it is the balance between those elements that strongly influences ferrite retention.

Although the absolute levels of ferrite retention do not match with the experimental values of chapter 5, Balmforth diagram correctly predicts that steel A has the highest tendency to retain ferrite.

6.1.b MAP-neural-ferrite-number

There exist more advanced methods for estimating δ-ferrite retention in welds. The methods based on empirical modelling such as neural networks[1] can be very useful when complex interactions between solutes are expected to affect the retained

[1]An introduction to neural networks is given in chapter 8.

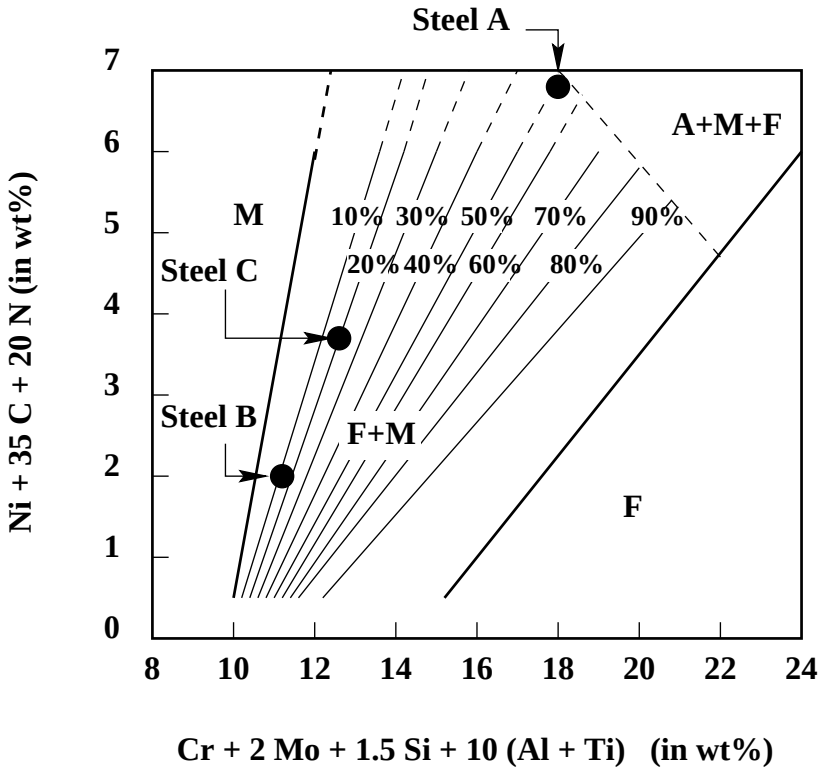

Figure 6.1: Balmforth diagram and the position of steels A, B and C [43].

ferrite content. Some models designed to predict the ferrite number (FN [2] as opposed to ferrite percentage FP) of austenitic weld metals have recently been developed.

Because magnetic methods offer a convenient way of measuring the ferrite content in an austenitic matrix, a large number of data of the kind essential to empirical modelling can be produced. As mentioned in chapter 2, such magnetic methods cannot be employed for martensitic steels because ferrite and martensite are both ferromagnetic. However, neural networks are in principle capable of making extrapolations for compositions that are not covered in the data range used to create them, assuming that relationships are recognised and that each predictions is accompanied by an estimate of uncertainty.

Although the main interest here is on heat-affected zones and not weld metals,

[2]It is possible to relate FN to FP by relationships such as $FN = 1.7 \times FP$ as introduced in chapter 2

the aim of the following calculations is to compare the capacity of an alloy to retain δ-ferrite regardless of its location within the weld.

The recent neural network model proposed by Murugananth *et al.*, MAP-NEURAL-FERRITE-NUMBER[3] was chosen to conduct calculations [80]. The model uses chemical composition as the input and was trained on a database containing 925 experimental data. The composition range of the elements considered in the analysis is reported in table 6.2.

Input element	Minimum	Maximum	Mean	Standard deviation
C	0.00	0.20	0.04	0.02
Mn	0.35	12.67	1.85	1.73
Si	0.03	6.46	0.53	0.34
Cr	1.05	32.00	20.47	2.70
Ni	4.61	33.50	11.26	2.60
Mo	0.01	10.70	1.48	1.55
N	0.01	2.13	0.08	0.10
Nb	0.01	0.88	0.04	0.09
Ti	0.01	0.54	0.03	0.04
Cu	0.02	6.18	0.15	0.41
V	0.04	0.27	0.06	0.02
Co	0.01	0.69	0.05	0.04
Fe	45.60	72.51	63.98	4.21
FN	0.00	117.00	12.63	18.40

Table 6.2: Input variables used in the model. Composition in wt% [80].

[3]www.msm.cam.ac.uk/map/neural/programs/ferrite-number.html

To check the capacity of the neural network model to make predictions on supermartensitic stainless steels, the effect of the major solute elements on the FN has been investigated using steel A as a base composition. The results of these predictions are reported in figure 6.2 for the austenite stabilising elements and figure 6.3 for the ferrite stabilising elements.

The neural network model identified clear trends for the effects of nickel, chromium, molybdenum and titanium on the ferrite number. Consistent with the nature of each of these elements the FN values were predicted to decrease with Ni and to increase with the addition of Cr, Mo and Ti.

i Effects of Cr, Ni and Mo

Contour plots have been drawn to visualise the effects of Cr, Ni and Mo on the predicted ferrite number. The calculations were performed on a Cr-Ni-Mo ternary alloy with Cr and Ni concentrations varying between 9-14 wt% and 0-8 wt% respectively, and with two different levels of molybdenum (0 and 2 wt%).

Most of the FN values do not exceed 10 in the molybdenum-free diagram (figure 6.4). However consistent with Balmforth diagram, a sensible FN increase is felt for high chromium and low nickel containing alloys, the maximum value being about 40. On the other hand, at 2 wt% molybdenum (figure 6.5), the FN values are significantly higher than in the previous case. Also, similar to the molybdenum-free diagram the effect of molybdenum on ferrite retention is more strongly felt at low Ni concentrations. Finally in both cases, the errors become larger as the nickel concentration is reduced. The latter was to be expected since the database did not contain experimental data on low nickel containing steels.

ii Application to steels A, B and C

Figure 6.6 (a) shows the predicted FN values for steels A, B and C. Due to the size of the error bars it cannot be concluded that steel A is more likely to retain δ-ferrite than steels B and C. However the maximum predicted levels were typically 20 FN (equivalent to about 12 %) and were consistent with those measured in chapter 5.

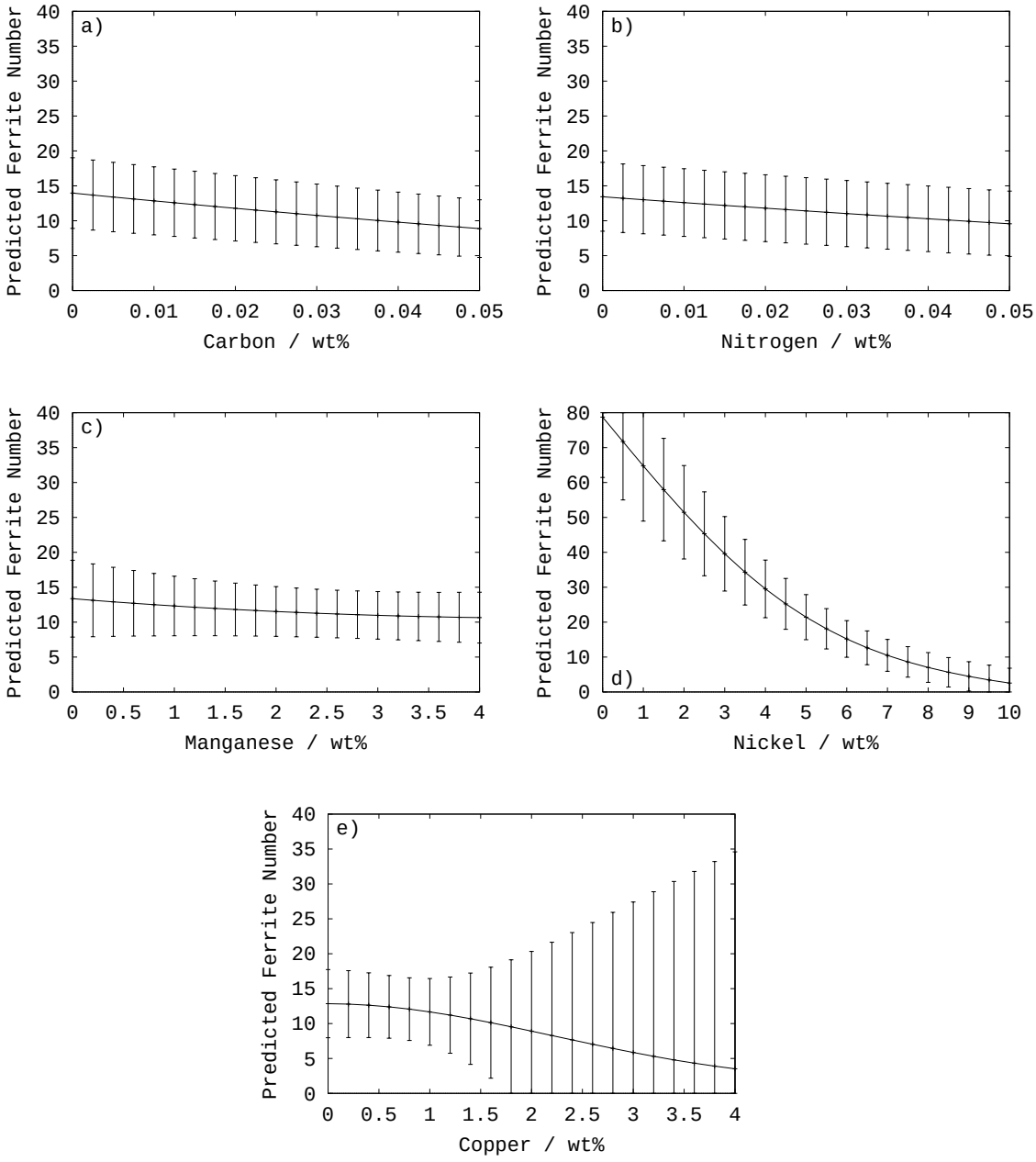

Figure 6.2: Predictions of ferrite number (FN) as a function of chemical composition for austenite stabilising elements (base composition steel A : 0.01 C, 0.46 Mn, 0.26 Si, 12.2 Cr, 6.46 Ni, 2.48 Mo, 0.007 N, 0.09 Ti wt%). The calculations were done using a published neural network model [80].

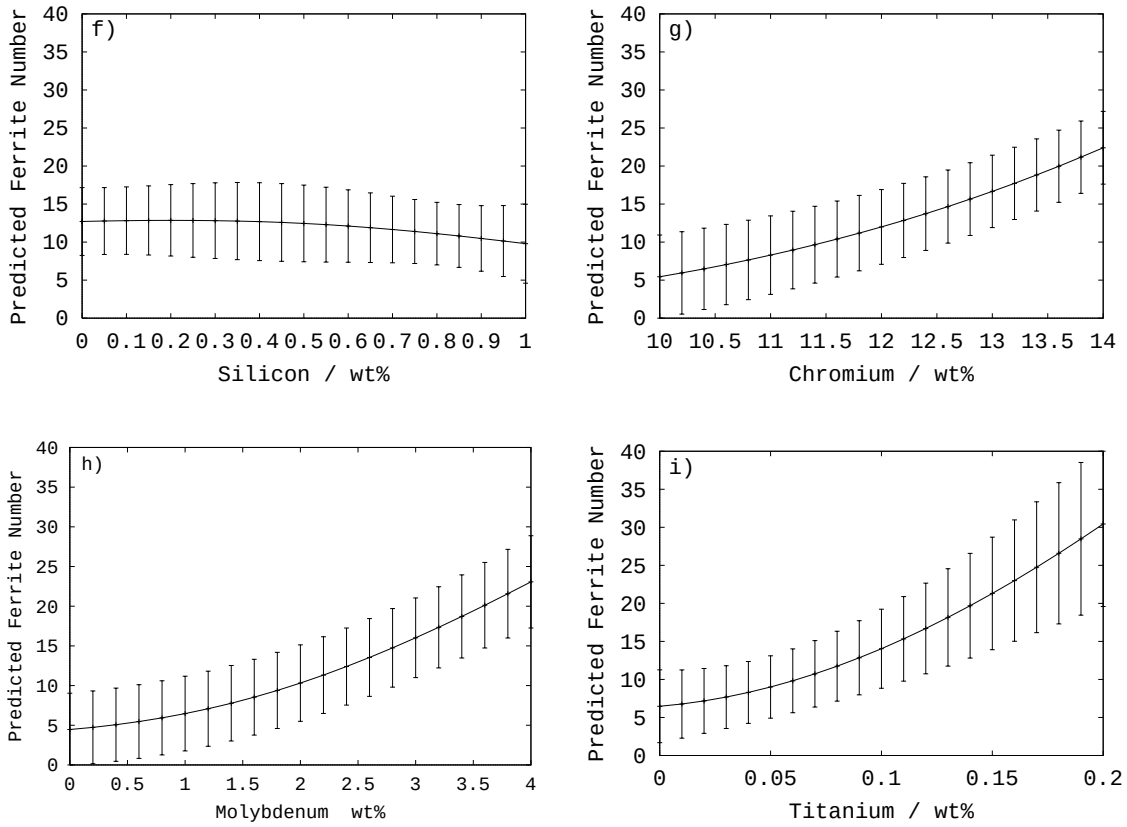

Figure 6.3: Predictions of ferrite number (FN) as a function of chemical composition for ferrite stabilising elements (base composition steel A : 0.01 C, 0.46 Mn, 0.26 Si, 12.2 Cr, 6.46 Ni, 2.48 Mo, 0.007 N, 0.09 Ti wt%). The calculations were done using a published neural network model [80].

The evolution of FN as a function of nickel concentration was also investigated for each steel (figure 6.6 (b) and (c)). The level of nickel required to suppress δ-ferrite retention was significantly greater for steel A ($\geq$ 10 wt%) than for steels B and C. This showed that although the presence of Mo must be balanced by the appropriate amount of Ni to allow the steel to become fully austenitic at elevated temperature (6.5 wt% in the case of steel A), the nickel concentration required to suppress δ-ferrite retention might be larger. It should however be noted that the addition of an extra 4 wt% Ni to steel A would strongly depress the M_S temperature and possibly change the solidification mode and hence would not necessarily lead to a completely martensitic alloys after cooling to room temperature.

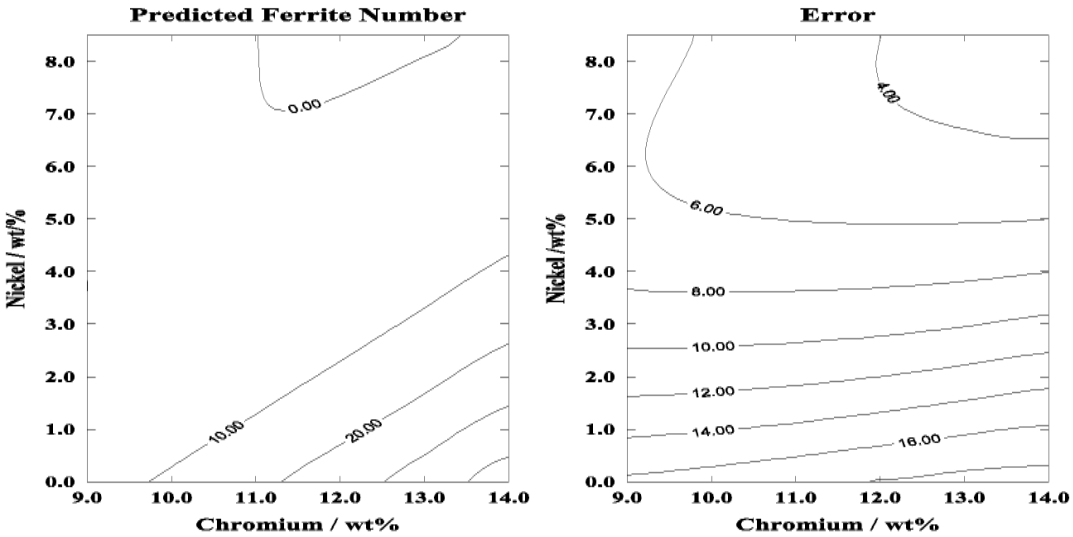

Figure 6.4: Contour plots showing predicted FN and associated errors as a function of Cr and Ni concentration for a ternary alloy with 0 wt% Mo.

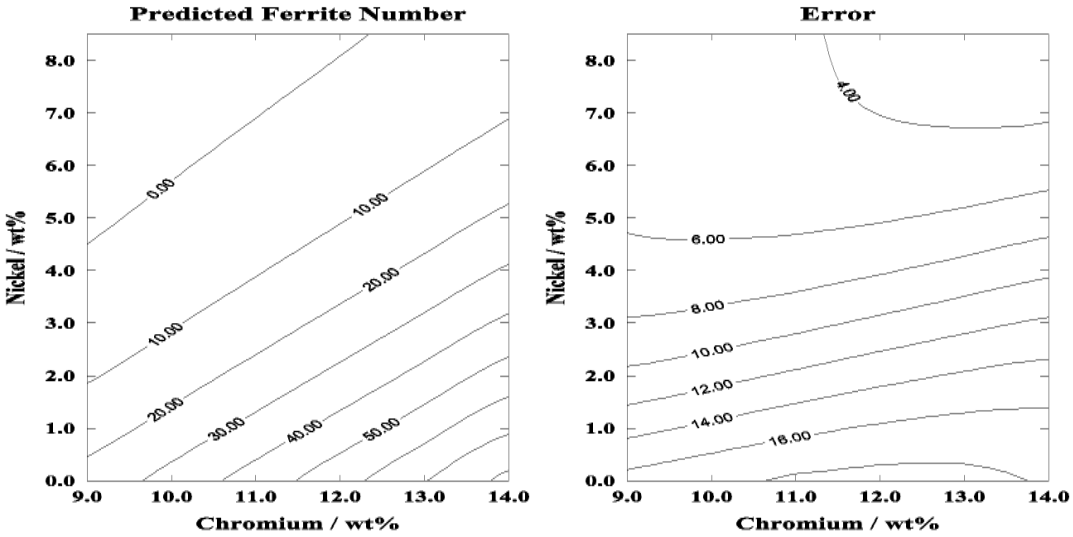

Figure 6.5: Contour plots showing predicted FN and associated errors as a function of Cr and Ni concentration for a ternary alloy with 2 wt% Mo.

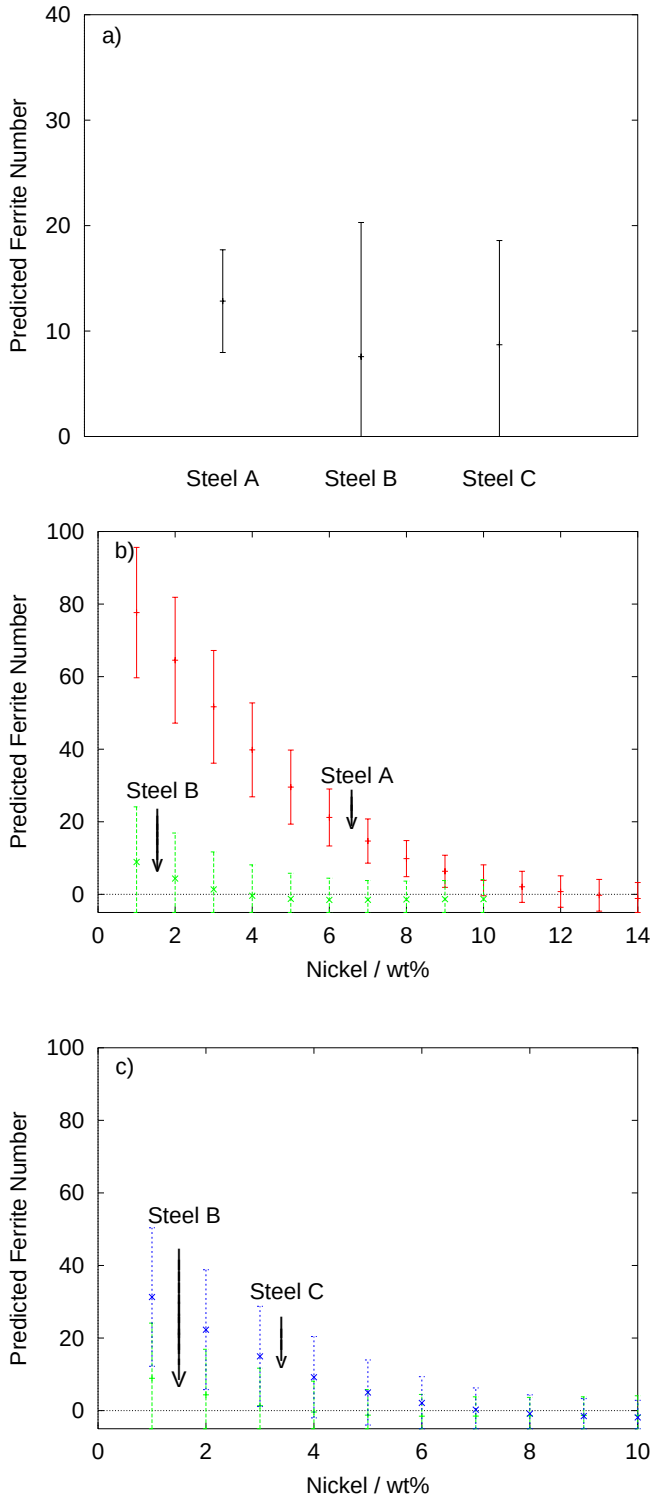

Figure 6.6: Predicted ferrite number for steels A, B and C (a). Effect of nickel on FN in steels A and B (b) and B and C (c). The arrows indicate the nickel content and corresponding predicted FN positions of steels A, B and C.

6.2 Dual-phase HAZ width

The aim of the work presented in this section was to compare the extent of the dual-phase HAZs of the welds performed in chapter 5 with values estimated using Rosenthal's heat-flow equations.

6.2.a Experimental data

The nine welds performed on the 10 mm thick plates of steels A, B and C in chapter 4 have been chosen for providing experimental data. The widths of all dual-phase HAZs have been measured according to the procedure described in chapter 3, and the results are plotted as a function of the employed heat input in figure 6.7.

As expected, the extent of the dual-phase regions were small (maximum value of about 150 μm) and increased with increasing heat input. For any given heat input, steel A had the largest range of δ-ferrite formation followed by steels C and B respectively.

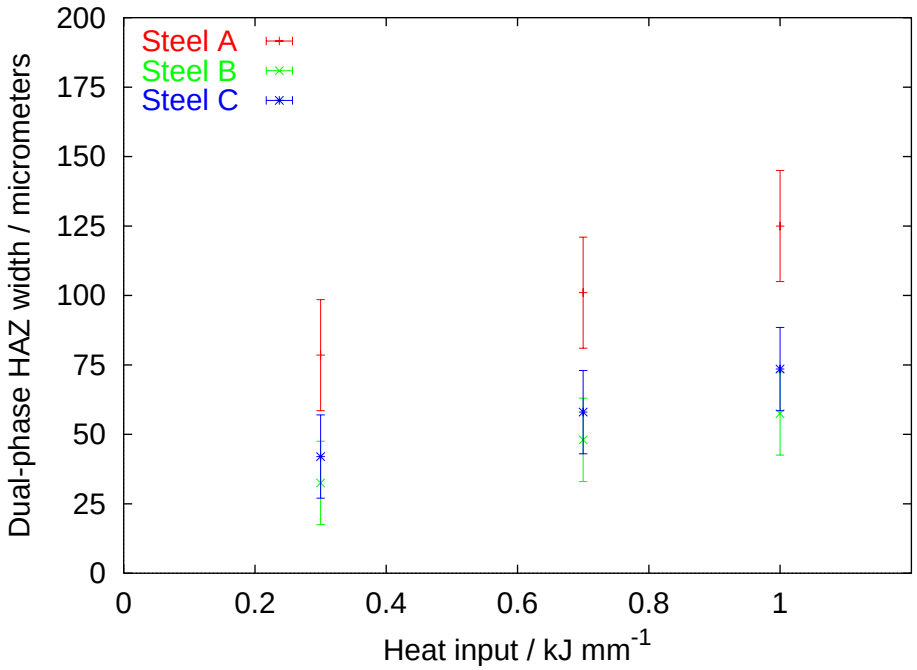

Figure 6.7: Measured widths of the dual-phase heat-affected zones as a function of heat input for steels A, B and C. Plate thickness 10 mm.

6.2.b Weld thermal cycle prediction

During welding the temperature profile in HAZ can be estimated by using Rosenthal's equations [22]. There are well known assumptions associated with this analytical method but experience has shown that they can be a useful approximation. In arc welding processes, the flow of heat from the source depends on the thickness of the plate. For thick plates, the arc is assimilated to a point source of constant power moving along the surface of an isotropic semi-infinite body, at initial temperature T_0, limited in one direction by a plane that is impermeable to heat. The thermal cycle experienced by the heat-affected zones (assuming instantaneous application of heat) at a certain fixed position from the heat source as defined by a radial distance r gives [49] :

$$T = T_0 + \frac{\frac{q}{v}}{2\pi\lambda t} \exp\left(-\frac{r^2}{4at}\right) \tag{6.2}$$

T_0 is the temperature prior to welding or the pre-heat temperature in K,
q is the arc power (J s^{-1}),
v is the arc velocity (m s^{-1}),
t is the time expressed in second,
r is the radial distance from the weld centre line (m),
a is the thermal diffusivity (m^2 s^{-1}) and is defined as follows :

$$a = \frac{\lambda}{\rho c} \tag{6.3}$$

where λ is the thermal conductivity in J s^{-1} m^{-1} K^{-1} and ρc specific heat per unit volume in J m^{-3} K^{-1}.

Equation 6.2 gives a reasonable description of the thermal cycle as experienced by the heat-affected base metal and is to be applied only at temperatures outside the fusion zone. The peak temperature at a given distance in HAZ is then obtained using the following equation:

$$T_p = T_0 + \frac{2}{\pi \mathrm{e}} \frac{\frac{q}{v}}{\rho c r^2} \tag{6.4}$$

where e= 2.718.

It should be noted that the latter equation does not depend upon thermal conductivity.

6.2.c Application

The equilibrium and paraequilibrium phase transformation temperatures determined in chapter 4 (summarised in table 6.3) were used together with the expression of the peak temperature distribution (equation 6.4) to determine the extent of the dual-phase HAZ for a given heat input. To allow for more precise comparisons with experimental data, calculations were only performed for a level of heat input of 0.3 kJ mm^{-1}, for which the high temperature isotherms were found to be almost semi-circular (figure 5.18). The value of ρc was taken to be 4.60 10^6 J m^{-3} K^{-1} according to reference [89].

	Ap_4 (5%)	Ap_5 (95%)	Ae_4 (5%)	Ae_5 (95%)
Steel A	1322	1323	1237	1396
Steel B	1302	1310	1261	1350
Steel C	1295	1322	1242	1360

Table 6.3: Reminder of equilibrium and paraequilibrium phase transformation temperatures (in °C) calculated in chapter 4.

The results are presented in figure 6.8. The dual-phase HAZ widths calculated using the paraequilibrium temperatures were, considering the error bars, in relatively good agreement with the measured values except for steel A, where the Ap_4-Ap_5 temperature interval is only 1 °C. On the other hand, the dual-phase HAZ widths calculated using the equilibrium temperatures overestimated the actual width by a factor varying between 3 and 4.

For steels B and C, the satisfactory agreement between actual and calculated

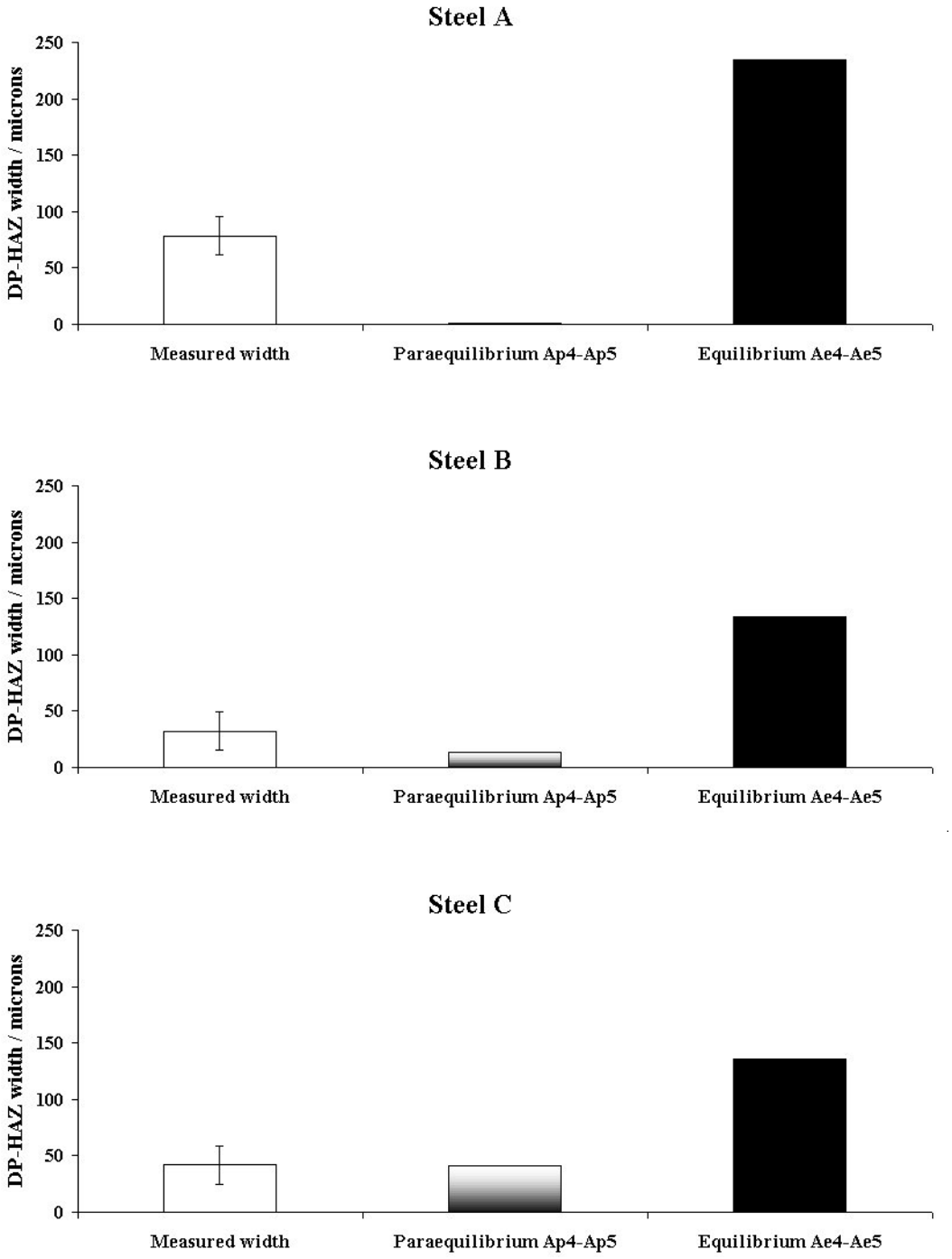

Figure 6.8: Comparisons between measured and calculated widths of the dual-phase HAZ of steels A, B and C for a heat input of 0.3 kJ mm^{-1}.

widths using paraequilibrium temperatures suggests that ferritisation is governed by carbon and nitrogen diffusion. It should however be kept in mind that partitioning was observed between δ-ferrite and austenite and therefore the transformation is certainly governed by an intermediate state.

As far as equilibrium temperatures are concerned, the poor agreement with experimental values might be explained by the fact that kinetics have been neglected. Indeed under rapid heating condition the ferritisation reaction might start at a higher temperature, but the completion of the transformation is also likely to be delayed. However, the dilatometric tests carried out under slow heating conditions in chapter 4 clearly showed MT-DATA systematic underestimation of the Ae_4 temperature. MT-DATA unsatisfactory predictions are related to the relatively large number of elements allowed in the calculations (often 8 or 9), and the lack of experimental thermodynamic data relevant to supermartensitic stainless steels.

It is therefore clear that neither paraequilibrium nor equilibrium conditions are satisfactory to predict the width of the dual-phase HAZ of supermartensitic stainless steels. Consequently improvement of MT-DATA databases are required to solve the problem.

6.3 Summary

While the ferrite factor equation did not provide a useful means for making comparisons between different supermartensitic alloys, the diagram proposed by Balmforth correctly predicted the higher capacity of steel A to retain δ-ferrite. Besides the expressions of the Cr_{eq} and Ni_{eq} indicated that Ni and Mo play a major role on the extent of δ-ferrite retention.

According to the neural network results, it is difficult to balance the ferrite stabilising effect of molybdenum by only adding the minimum amount of nickel required to obtain a fully austenitic steel at high temperature. Unfortunately, due to the size of the error bars the predictions made using the neural network model did not show steel A's larger capacity to retain ferrite. Consequently, only Balmforth diagram seems suitable for supermartensitic stainless steels.

Due to a lack of accurate thermodynamic data on the systems of concern, it was not possible to predict the extent of the HAZ region where δ-ferrite is mainly concentrated.

Chapter 7

Effect of HAZ δ-ferrite on Charpy impact toughness

Supermartensitic stainless steel components in the oil and gas industry usually operate at temperatures of the order of 100 °C. However, during the rapid closure of a well-head in an emergency, the loss of pressure can result in a rapid decrease of temperature to about -40 °C. In this case, good low temperature impact toughness of the welded joint is necessary. The work presented in this chapter had the aim of determining whether δ-ferrite found in dual-phase heat-affected zones of supermartensitic stainless steels significantly affects the impact properties.

7.1 Introduction

It is well established that coarse δ-ferrite grains reduce the Charpy impact toughness of low carbon semi-ferritic and martensitic stainless steels [57, 58, 59]. However, in supermartensitic stainless steel heat-affected zones (HAZ) there is as yet no evidence to support the notion that δ-ferrite is a threat to impact properties.

In the heat-affected zones of supermartensitic alloys, δ-ferrite is present mainly in the dual-phase region of the high temperature HAZ. As this region is narrow, typically 50 to 100 μm wide, sampling in isolation is impossible even using sub-size specimens. To avoid this problem, attempts have been made to reproduce on a larger scale, the microstructure of the dual-phase HAZ using a furnace and a weld HAZ simulator.

Since steel A (table 7.1) was particularly prone to δ-ferrite retention in HAZ (chapter 5) the work presented in this chapter focuses on this material.

	C	Si	Mn	Ni	Cr	Mo	Cu	Ti	N
Steel A	0.01	0.26	0.46	6.46	12.2	2.48	0.03	0.09	0.0070

Table 7.1: Chemical composition of steel A in wt%.

7.2 Furnace heat-treated specimens

7.2.a Microstructures required

To compare the effect of δ-ferrite on impact properties, a fully martensitic and a ferritic-martensitic microstructures were required.

A furnace heat-treatment at a temperature of 1100 °C for 15 minutes was chosen to generate the fully martensitic microstructure. On the other hand, following results presented in chapter 4, the temperature of 1350 °C was chosen to produce the mixed ferrite-martensite microstructure. However, due to the relatively slow heating rate of the furnace, a difference in prior austenite grain size between the two microstructures was expected. To remedy, that problem, another fully martensitic microstructure (consisting of martensite and dissolved δ-ferrite) was also studied. The latter microstructure was produced using a supercritical annealing treatment. The heat-treatment which allowed dissolution of most of the δ-ferrite without changing the austenite grain size was carried out at 1100 °C for an hour.

Besides, Charpy impact tests were also carried out on the material in its as-received condition. In this case the microstructure consisted of tempered martensite with about 13 % retained austenite (chapter 4).

7.2.b Procedure

Specimens of 12 mm square section and 60 mm long were machined from the pipe of steel A in the longitudinal direction as shown in figure 7.1. The samples were then placed in a pre-heated furnace at the center of the bottom surface and were let in for 15 minutes before water quenching.

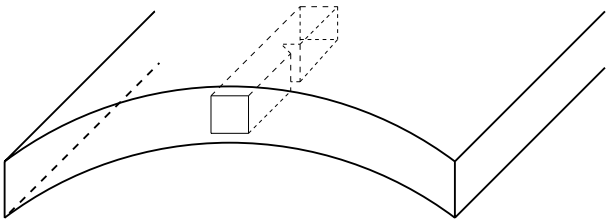

Figure 7.1: Orientation of the Charpy specimen within the pipe.

After optical verification of the desired microstructures, specimens were machined to the standard dimension of 10 mm square section × 55 mm with a 2 mm deep V-notch positioned through-thickness. Charpy impact tests were finally carried out between 20 and -200 °C to reveal the ductile brittle transition and ten specimens were used to generate each curve.

A hyperbolic tangent function was chosen to fit the transition curves :

$$\text{Impact energy (J)} = A_0 + B_0 \tanh\left(\frac{T - T_0}{C_0}\right) \tag{7.1}$$

Where A_0, B_0, C_0 and T_0 are fitting constants and T is the temperature in °C. This representation of the transition curve facilitates comparison and the determination of the ductile to brittle transition temperature (DBTT). The latter was taken as the temperature coresponding to half the height of the transition curve.

7.2.c Characterisation of heat-treated specimens

To facilitate the interpretation of the results, heat-treated specimens were characterised before impact-testing in terms of phase presence, volume fraction, hardness and grain size.

i Microstructure

Figure 7.2 shows the microstructures of the fully martensitic, martensitic/ferritic and annealed martensitic/ferritic specimens observed on the actual-size Charpy specimens. Typical cuboid Ti(C,N) precipitates were the only observed non-metallic particles. The latter were up to 10 μm long and occurred in random dispersion or as small distinct clusters. There were no obvious differences in volume fractions and distribution of those particles between the different microstructures.

In the martensitic/ferritic microstructure, δ-ferrite was located both at grain boundaries and within the grains and its volume percentage measured by image analysis was 14 % ± 2 %. This figure was comparable to the results obtained in chapter 4.

Annealing of the mixed microstructure led to a reduction of the δ-ferrite content to 2 % ± 0.5 % and spheroidisation of the remaining ferrite. The dissolution of δ-ferrite took a long time despite the relatively elevated annealing temperature. This is because significant partitioning of substitutional solutes occurred at elevated temperature (chapter 4) and back diffusion takes time even at 1100 °C.

ii Hardness and grain size

The hardness and grain size measured on the heat-treated materials are reported in table 7.2. There was little hardness change between the different microstructures even in the presence of δ-ferrite up to 14 %. As hardness is proportional to tensile strength, all specimens could be assumed to have a similar strength [4].

There was a small difference in grain size between the various microstructures. In fact, the prior austenite grain size of the specimens heat-treated at 1350 °C was about 20 μm larger than the one heat-treated at 1100 °C. Due to the grain boundary pinning effect of δ-ferrite there was no grain size difference between the martensitic/ferritic and annealed martensitic/ferritic microstructures.

iii Retained austenite

The presence of retained austenite in the furnace heat-treated specimens has been checked using X-ray diffraction. No austenite could be detected in any of the specimens (figure 7.3).

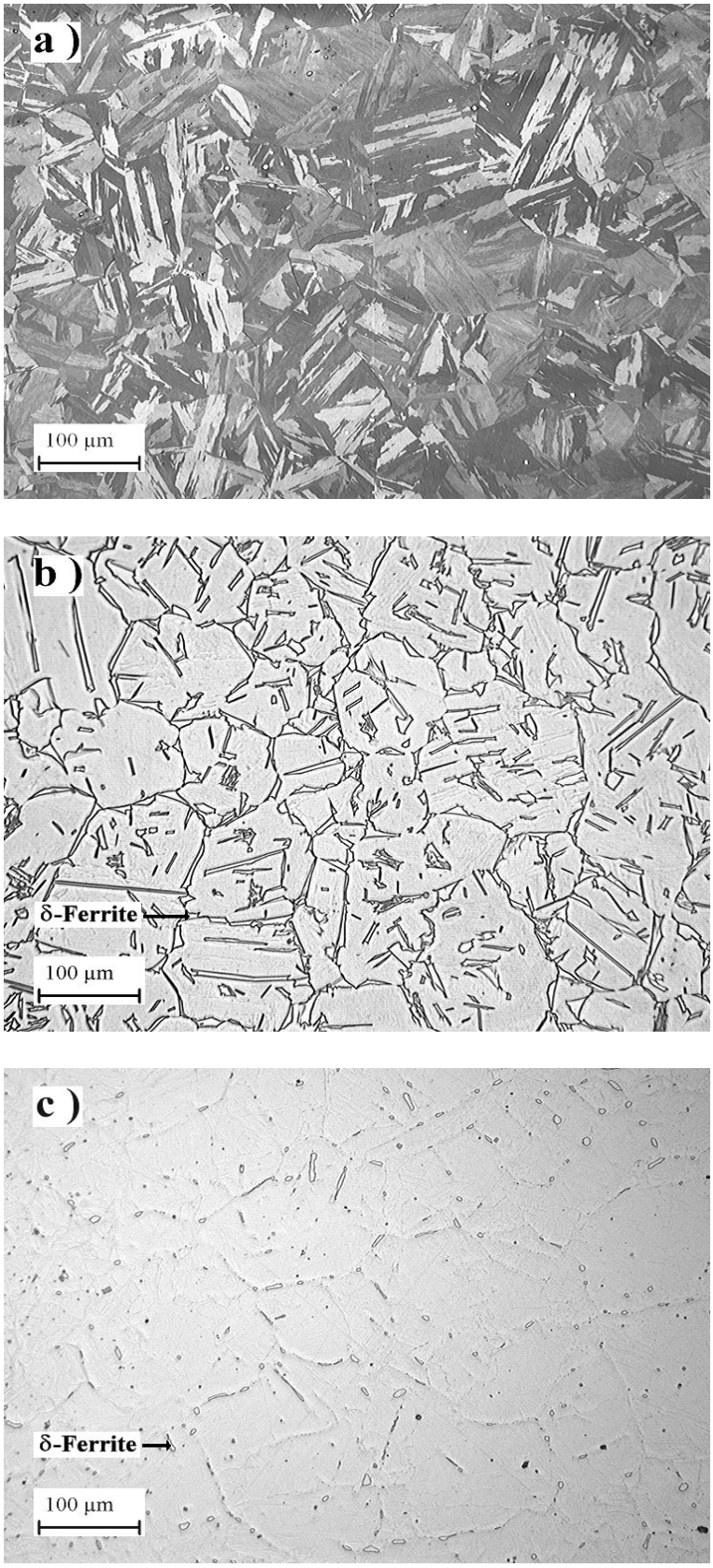

Figure 7.2: Microstructures obtained after isothermal treatment at (a) 1100 °C and (b) 1350 °C for 15 minutes and water quenched. (c) Microstructure obtained after treatment at 1350 °C for 15 minutes and water quenched followed by annealing at 1100 °C for 60 min and water quenched.

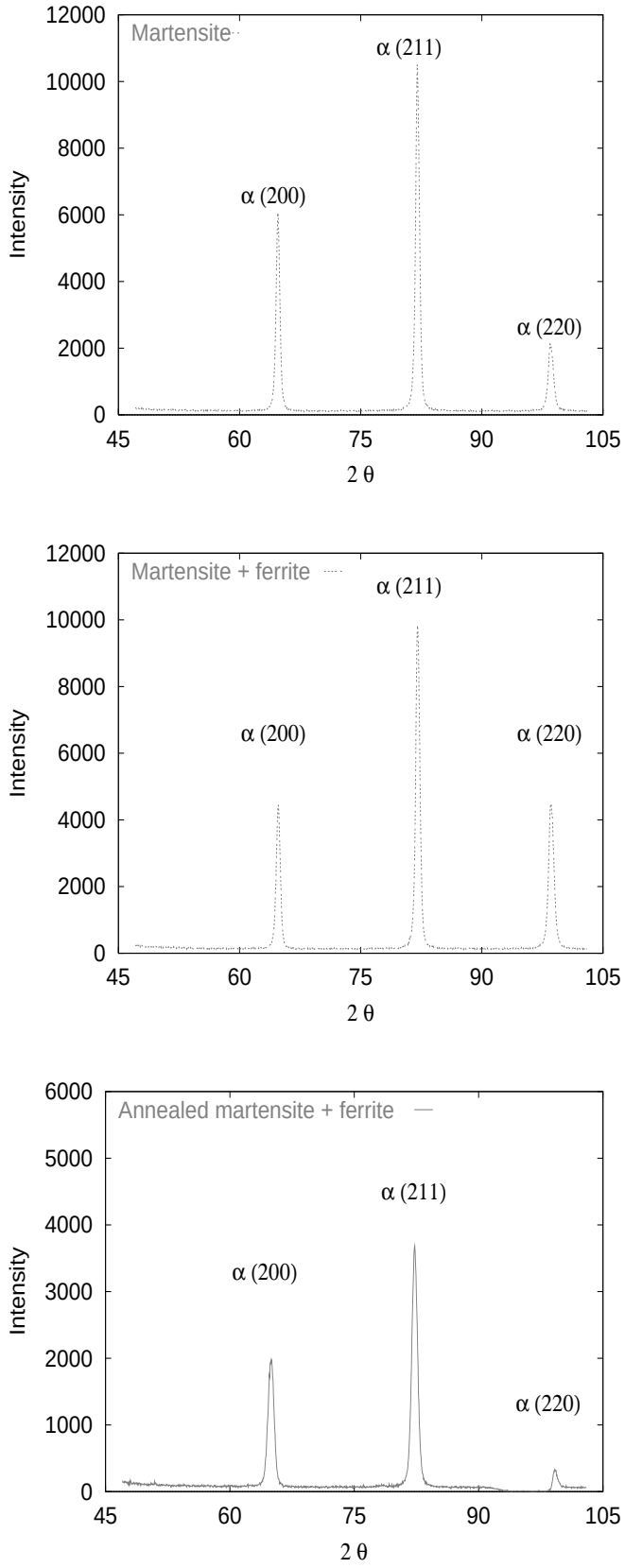

Figure 7.3: X-ray diffraction patterns of the fully martensitic, martensitic/ferritic and annealed ferritic/martensitic microstructures.

Microstructure	Hardness	Grain size / μm
Tempered martensite + retained austenite	296 ± 3	25 ± 4
Martensite	317 ± 8	60 ± 9
Martensite + δ-ferrite	311 ± 8	80 ± 12
Annealed Martensite + δ-ferrite	304 ± 7	80 ± 12

Table 7.2: Macro-hardness (HV_{10kg}) and grain size of the studied microstructures.

7.2.d Results of Charpy impact tests

Table 7.3 summarises the measured ductile to brittle transition temperatures (DBTT) for each tested microstructure.

Microstructure	DBTT (°C)
Tempered martensite + retained austenite	-98
Martensite	-98
Martensite + ferrite	-46
Annealed martensite + ferrite	-86

Table 7.3: Ductile to brittle transition temperatures obtained for each studied microstructure.

Figure 7.4 shows the impact transition curves obtained from the as-received, fully martensitic and martensitic/ferritic microstructures. The fitted transition curves of the as-received and fully martensitic microstructures were similar. Their DBTT were also identical and far below 0 °C. However, the as-received microstructure had slightly higher failure energies at low temperatures. This is because austenite that remains stable down to -196 °C (chapter 4) tends to transform to martensite during impact and thus absorbs some energy and raise the toughness as proposed by Bilmes *et al.* [42]. At room temperature there was more scatter in the energy required to

break the specimens but there was apparently no significant difference between the two microstructures.

Similarly, there was no difference between the high temperature failure energies of the fully martensitic and martensitic/ferritic microstructures (figure 7.4). However, a significant shift in ductile to brittle transition temperature was observed. In fact, the DBTT of the martensitic/ferritic microstructure was raised by about 52 °C to about -46 °C. The origin of this increase could not be attributed directly to the presence of δ-ferrite since there was a 20 μm difference in prior austenite grain size between the two microstructures.

The observation of the transition curves of the martensitic/ferritic and annealed martensitic/ferritic microstructures of identical grain size removed this uncertainty (figure 7.5). In fact the microstructure containing a reduced amount of δ-ferrite had significantly better DBTT (-86 °C compared to -46 °C). This consequently showed that for a given prior austenite grain size the presence of δ-ferrite significantly affects the transition temperature.

Figure 7.6 compares the transition curves of the annealed martensitic/ferritic (grain size 80 μm) with the tempered microstructure (grain size 25 μm). Annealing clearly improved the notch toughness to a level comparable to that of the as-received condition. This indicated that the effect of the prior austenite grain size in the 25 - 80 μm range on the ductile to brittle transition temperature was not significant.

7.2.e Fractography

Observation of the fracture surfaces in the SEM revealed a variety of fracture modes. In particular, ductile rupture, cleavage and quasi-cleavage could be identified. Mc Donald *et al.* summarise these fracture modes as follows [90, 91] :

1. Ductile rupture. Dimples resulting from microvoid formation and coalescence, are characteristic of ductile rupture. Microvoids are generally initiated at inclusions which can sometimes be observed within the dimples.

2. Cleavage. Stepped facets are caused by fracture through regions of different crystallographic orientation. Cleavage occurs by rapid propagation of a

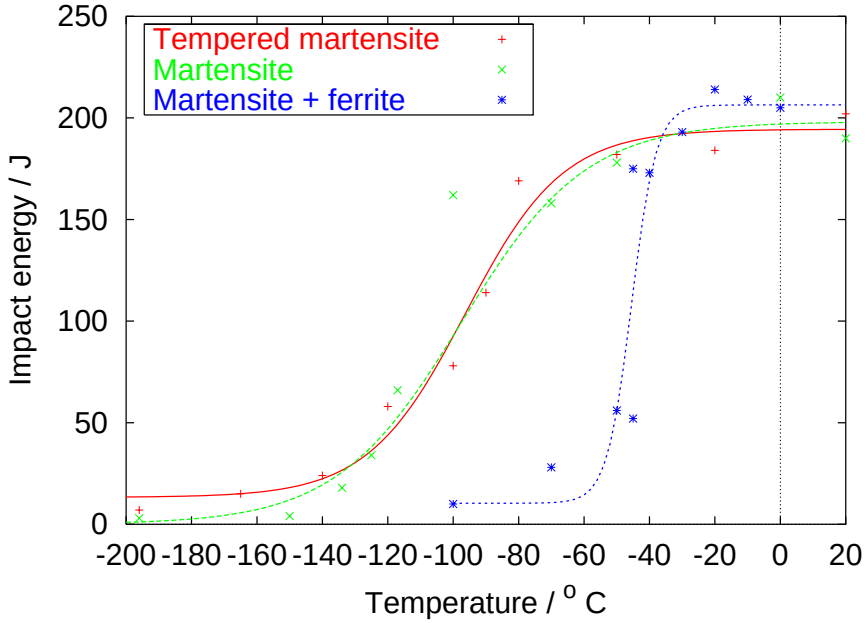

Figure 7.4: Charpy impact energy curves obtained on the tempered martensite + retained austenite (as-received condition), fully martensitic and martensitic/ferritic microstructures.

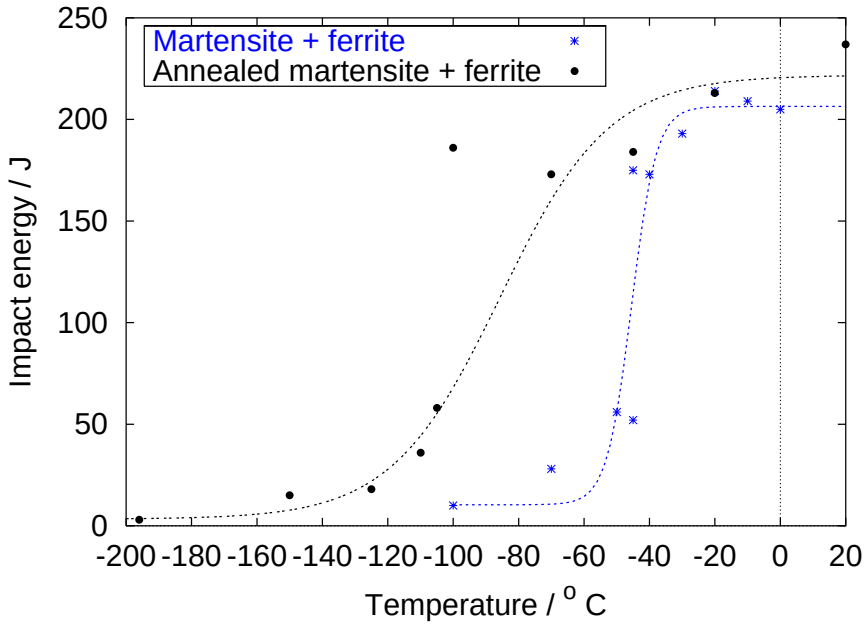

Figure 7.5: Charpy impact energy curves obtained on the martensitic/ferritic and annealed martensitic/ferritic microstructures. Note that both microstructures have identical prior austenite grain size of 80 μm.

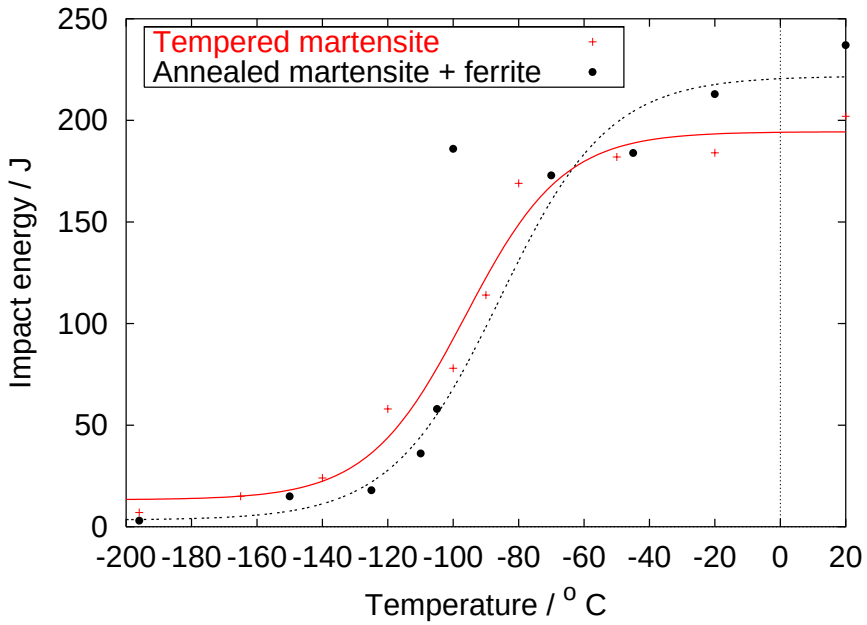

Figure 7.6: Comparison of the Charpy impact energy curves between the as-received and annealed martensitic/ferritic microstructures.

crack along crystallographic planes, and may be initiated by inclusion/matrix decohesion. This is a very low energy-absorbing mode of fracture.

3. Quasi-cleavage. A less well-defined fracture mode, known as quasi-cleavage, is associated with tear ridges which represent limited plastic deformation separating cleavage facets. Unlike pure cleavage, energy is absorbed as a result of the limited plastic deformation.

Examples of ductile rupture obtained from the fully martensitic and martensitic/ferritic microstructures tested at 0 °C are shown in figure 7.7. Most particles associated with initiation were cracked. These particles were easily identified as titanium carbo-nitride by EDX and also due to their typical cuboid shape.

Specimens tested at low temperatures fractured in a transgranular manner (figure 7.8). This indicated that the presence of grain boundaries δ-ferrite did not embrittle the latter. In general, the cleavage facet sizes appeared similar but the martensitic/ferritic microstructure showed more secondary cracks.

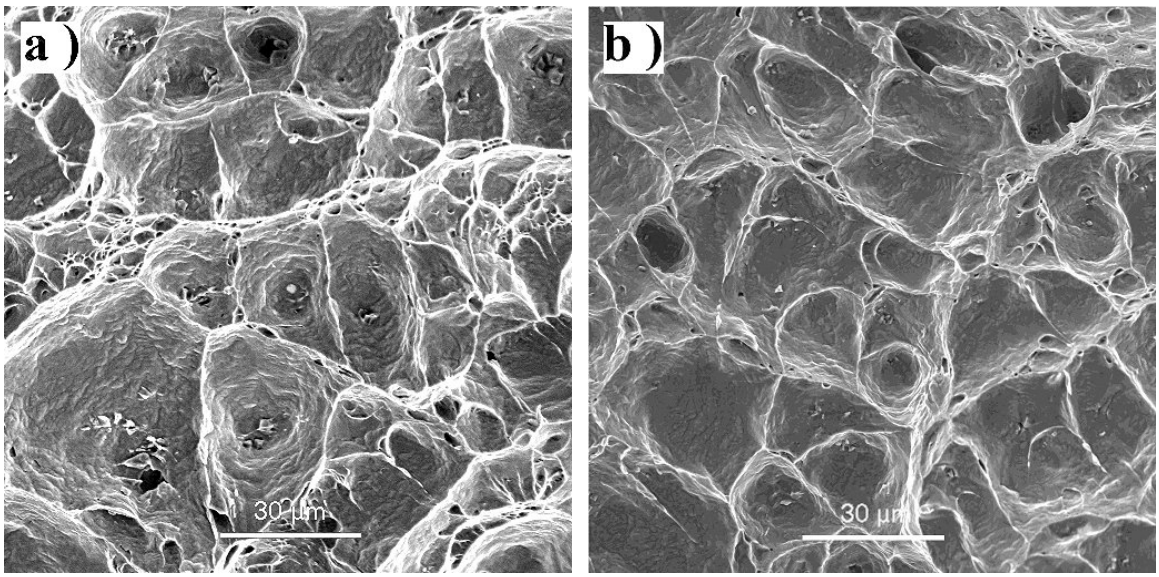

Figure 7.7: Dimpled fracture surfaces of the fully martensitic (a), and martensitic/ferritic (b) microstructures tested at 0 °C.

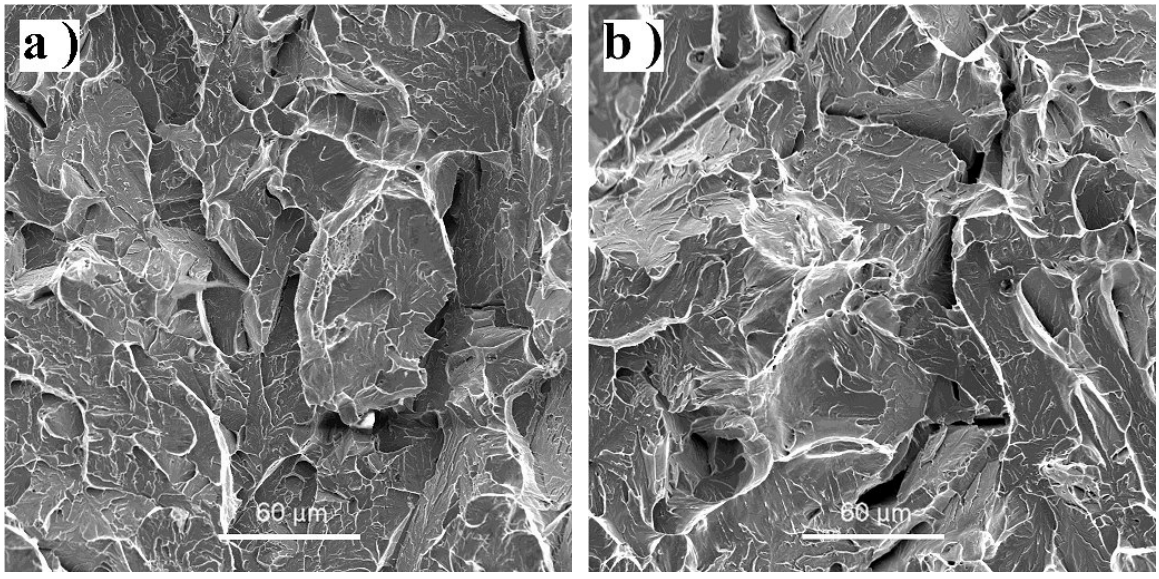

Figure 7.8: Fracture surfaces of the fully martensitic (a) and martensitic/ferritic (b) microstructures tested at -150 and -100 °C respectively.

Titanium carbo-nitride particles were often seen to initiate cracks in all studied microstructures. River markings on the cleavage facets of the specimens showed evidence of both cleavage (figure 7.9) and quasi-cleavage fracture (figure 7.10) initiated by Ti(C,N) inclusions. The capacity of these particles to reduce toughness is well known. Brittle fracture induced by the cleavage of TiN inclusions has recently been investigated by Fairchild *et al.* [92, 93]. TiN particles are well bonded to the matrix and thus allow high stresses in a notch tip plastic zone to act on inclusions without debonding the interface. Once an inclusion cleaves, the strong bond allows for transfer of the crack into the martensitic matrix.

In addition to the SEM observation, cross sections perpendicular to the fracture surfaces, as shown in figure 7.11, have been observed to reveal the fracture path.

Figures 7.12 and 7.13 show example of such cross sections for specimens of the martensitic/ferritic and annealed martensitic/ferritic microstructures that failed by cleavage. In the martensitic/ferritic specimens, secondary intragranular cracks propagated through martensite and δ-ferrite stringers, while shorter cracks were seen to initiate both in martensite and at the δ-ferrite martensite interface in the annealed microstructure. In the latter case, cracks could not easily link up when δ-ferrite was more dispersed and possessed a spheroidised morphology, thus explaining the better impact properties.

7.3 Gleeble simulated HAZ

The furnace heat-treated specimens allowed the impact properties of the martensitic/ferritic microstructure to be studied. To investigate the effect of δ-ferrite on HAZ toughness in a situation closer to actual welds, a Gleeble HAZ simulator (described in chapter 3) has been used.

7.3.a Procedure

Ten specimens of dimension 11×11×100 mm were sent to Corus Swinden Technology Centre for HAZ simulation. The operation was performed at the maximum temperature that the equipment could achieved *i.e.* 1350 °C, using a fast cooling

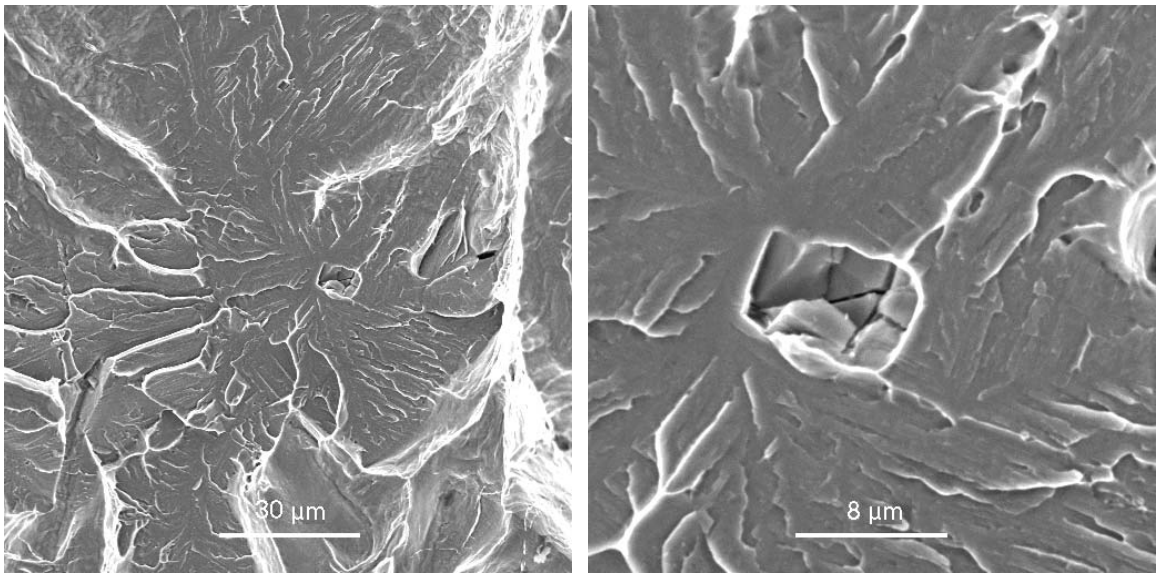

Figure 7.9: Fracture surfaces of the ferritic/martensitic microstructure tested at -100 °C showing Ti(C,N) initiated cleavage.

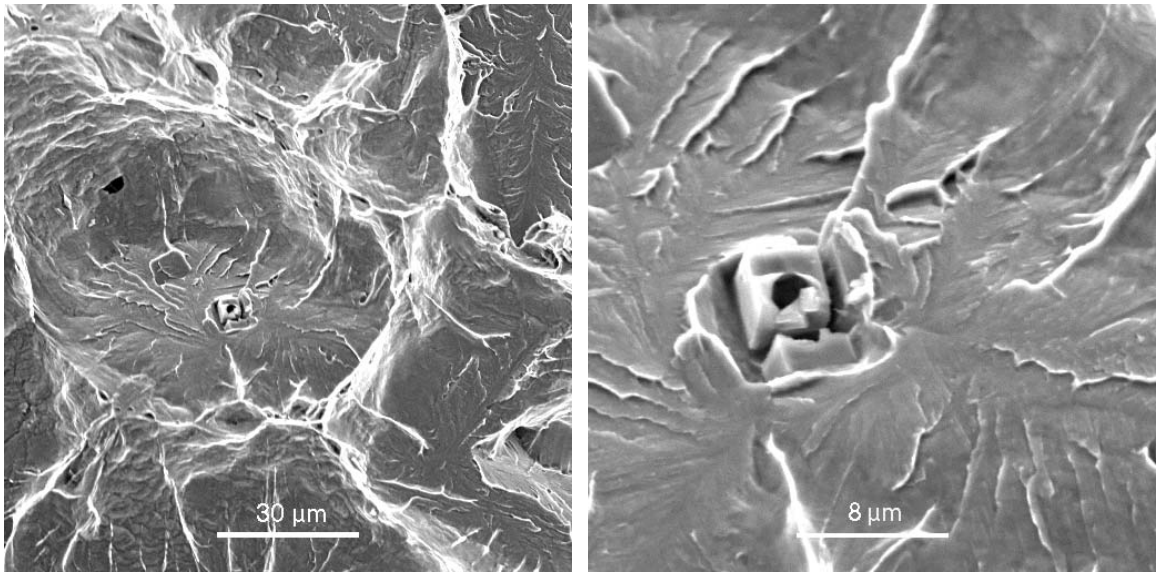

Figure 7.10: Fracture surfaces of the ferritic/martensitic microstructure tested at -100 °C showing Ti(C,N) initiated quasi-cleavage.

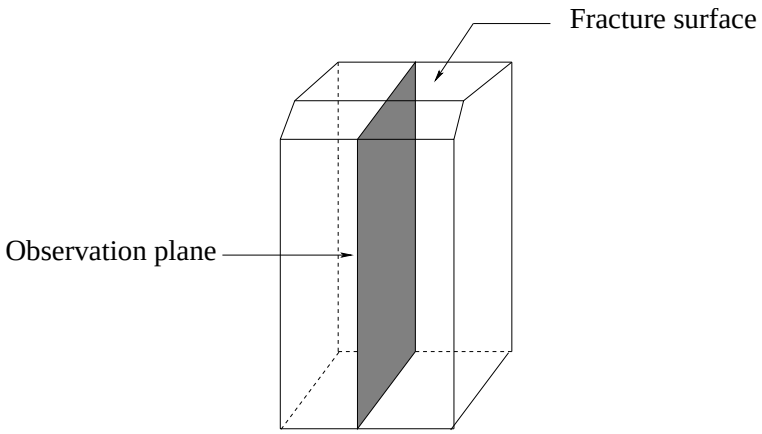

Figure 7.11: Location of transverse section in the Charpy specimens.

rate (cooling time between 800-500 °C of 10 s). After simulation, all specimens were polished and etched to reveal the microstructure and to decide the notch location for the final machining to standard size Charpy specimens.

7.3.b Microstructure

The typical microstructure of the simulated specimens is shown in figure 7.14 (a). The central part of the specimens showed three high temperature HAZ regions and therefore indicated the existence of a peak temperature gradient in the middle of the specimens. The coarse grained region, figure 7.14 (b), had semi-circular shape and depth of 2.5 mm. The martensite + δ-ferrite region, figure 7.14 (c), surrounded the previous region and in turn was surrounded by the prior fully austenitic area.

The simulated specimens showed a range of grain size. The coarse-grained and dual-phase regions had prior δ-ferrite grain size of about 160 μm and 30 μm, respectively. Similar to the microstructure observed in the dual-phase HAZ of the low heat input single-pass welds of chapter 5, δ-ferrite was present at grain boundaries and as films within the prior austenite grains. It could be noted that the width of the dual-phase region was significantly larger compared to actual weld HAZs. In addition, the volume percentage of δ-ferrite measured by image analysis at a magnification of 200 was also larger than that of single-pass weld HAZs *i.e.* 40 % $\pm$ 5 %.

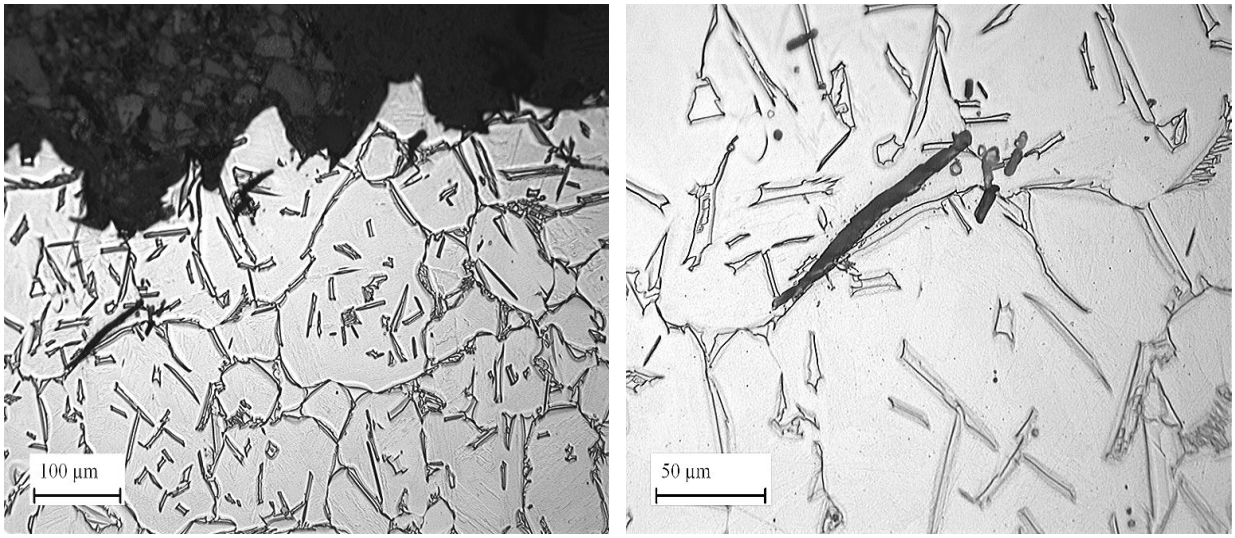

Figure 7.12: Cross section of the fracture surface of the martensitic/ferritic microstructure tested at -100 °C. Electrolytically etched to reveal δ-ferrite.

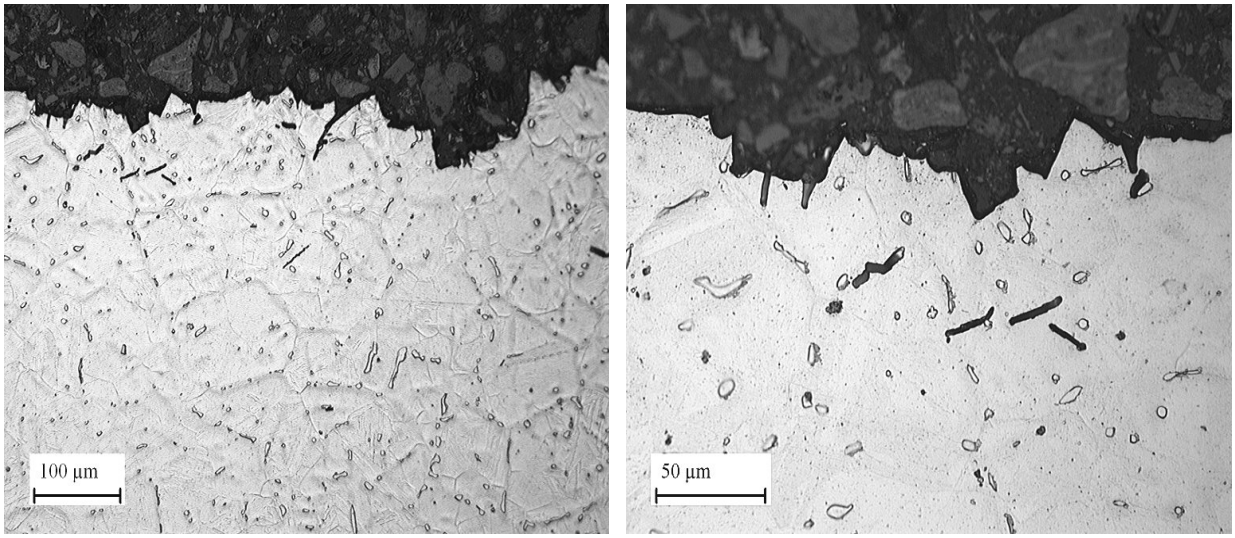

Figure 7.13: Cross section of the fracture surface of the annealed martensitic/ferritic microstructure tested at -150 °C. Electrolytically etched to reveal δ-ferrite.

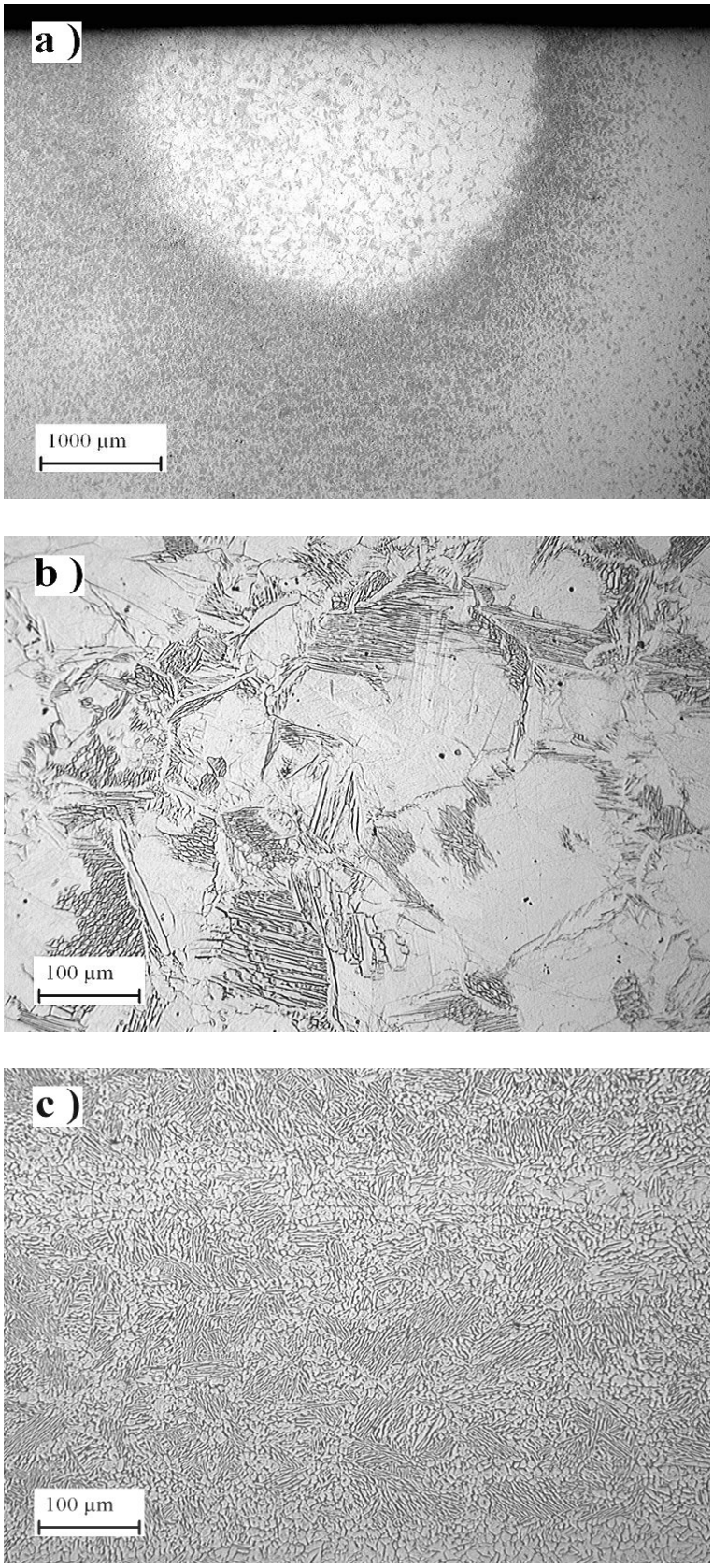

Figure 7.14: Microstructure of Gleeble simulated specimens. (a) Low magnification of the central region, (b) close-up of the coarse-grained region and (c) close-up of the dual-phase region. All specimens were electrolytically etched to reveal δ-ferrite.

7.3.c Results

The transition curve obtained on the Gleeble simulated specimens is presented on figure 7.15. For comparison the transition curves of the as-received and martensitic/ferritic microstructures have been reported. The Gleeble specimens had the lowest upper shelf energy of the three curves. The latter was probably due to the combined action of large grain size and presence of δ-ferrite in the tested microstructure. More importantly, the simulated HAZ had a ductile to brittle transition temperature comparable to that of the as-received material (-94 °C and -98 °C respectively) although like the ferritic/martensitic microstructure the transition occurred over a shorter temperature range. The behaviour of the Gleeble simulated specimens at low temperatures was therefore significantly better than the ferritic/martensitic microstructure studied in the first part.

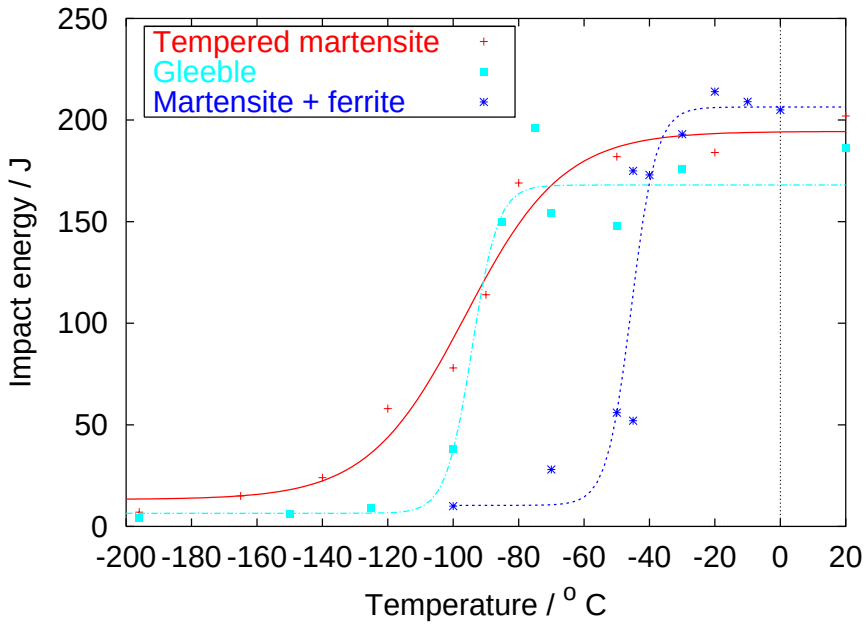

Figure 7.15: Charpy impact energy curves obtained using the Gleeble and comparison with real weld HAZ.

7.3.d Fractography

All specimens tested at temperatures above -100 °C showed ductile failure mode while those broken at temperatures below -100 °C showed completely brittle behaviour. Interestingly the Gleeble specimen tested at -100 °C showed two fracture modes (figure 7.16). Observation of a cross section revealed the coarse-grained region to fail by cleavage whilst the dual-phase region showed evidence of ductility below the transition temperature (figure 7.17). The ductility of the dual-phase HAZ indicates that the DBTT of this region is lower than -100 °C. These results provide evidence to support that the presence of δ-ferrite in dual-phase HAZ up to 40 % does not significantly affect the impact properties of the whole high temperature HAZ. Clearly the specimen transition temperature was strongly influenced by the grain size of the coarse-grained HAZ.

7.4 Summary

Part I of the study revealed that for a similar strength, particle volume-fraction and distribution, and a given prior austenite grain size, the ductile to brittle transition temperature was very sensitive to the volume fraction of δ-ferrite stringers in the microstructure. On the other hand, the effect of prior austenite grain size in the 25 - 80 μm range on the transition temperature was small. It was therefore clear that the presence of δ-ferrite up to 14 % had a greater influence on toughness than austenite grain size variation in the 25 - 80 μm range.

On the other hand, the tests carried out on the Gleeble simulated specimens revealed that the dual-phase HAZ does not play a major role in determining the DBTT even when δ-ferrite is present up to 40 %. This is apparently because the small grain size of the dual-phase region offers suitable obstacles to cracks propagation. With a prior δ-ferrite grain size of 160 μm, the coarse-grained region strongly influences the impact properties of the high temperature HAZ but the transition-temperature was raised by only few degrees compared with the as-received microstructure. As multipass welding contributes to the reduction of δ-ferrite content in HAZ the effect

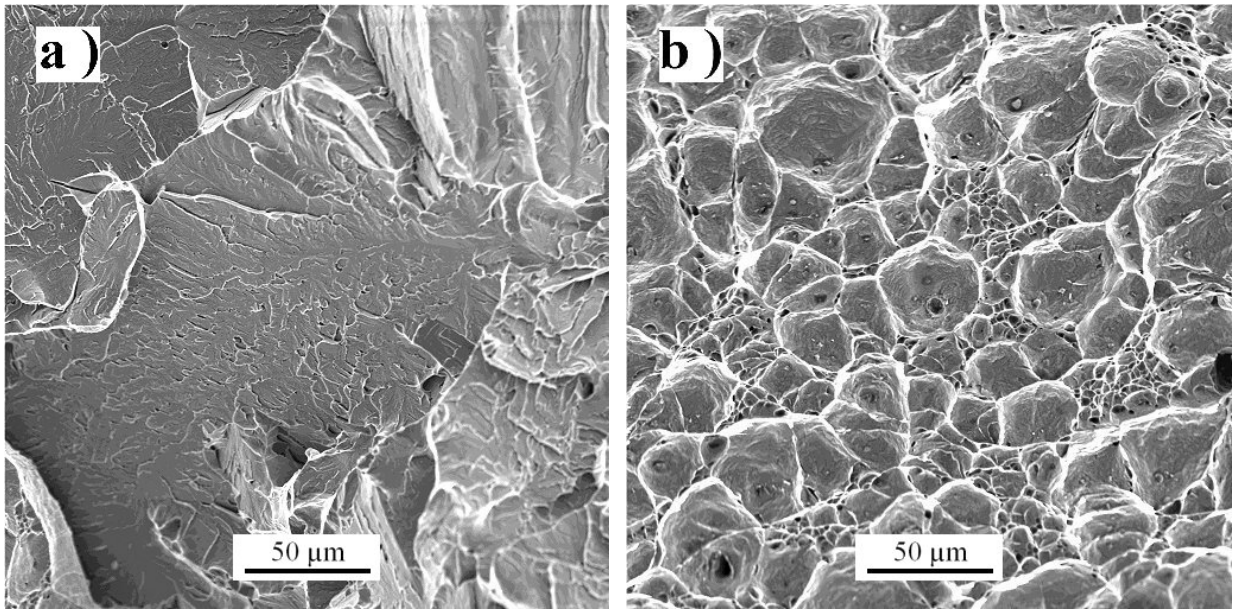

Figure 7.16: Fracture surfaces of the coarse-grained (a) and dual-phase region (b) of the Gleeble simulated specimen tested at -100 °C.

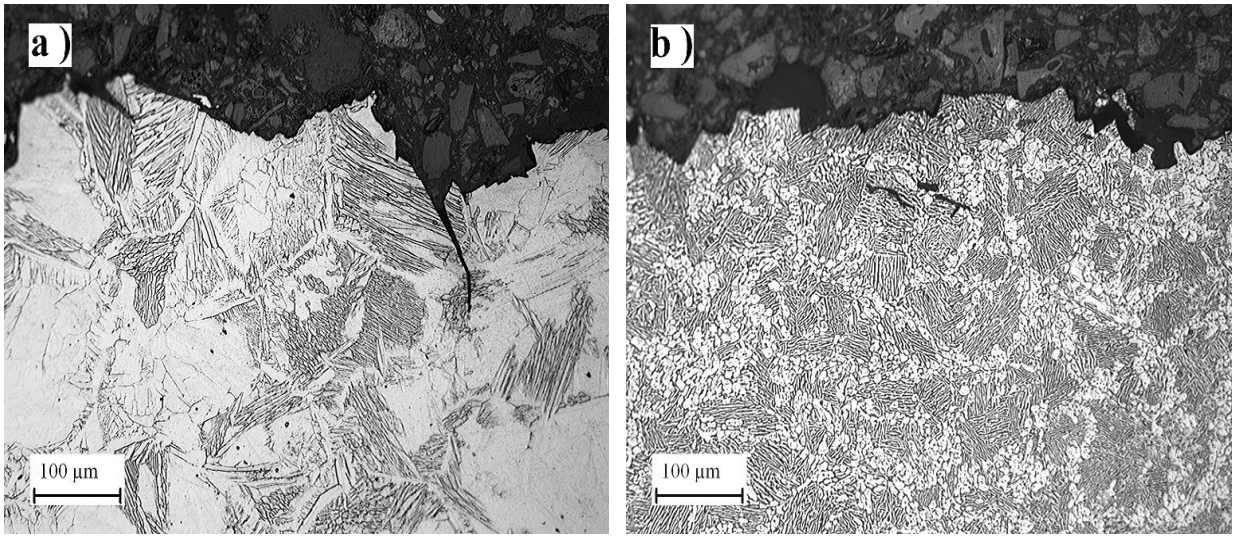

Figure 7.17: Cross section of the fracture surface showed in figure 7.16. Coarse-grained (a) and dual-phase region (b). This cross section was taken perpendicular to the examination plane shown in figure 7.11.

of this phase on the transition temperature of actual welds should be even smaller.

It should be noted that no attempts have been made to evaluate the effect of Widmanstätten austenite in coarse-grained region on the impact properties. However, due to its morphology and coarseness, Widmanstätten austenite might be detrimental. As fast cooling rates minimise its volume fraction (chapter 4) it could be advised to weld supermartensitic stainless steels using low heat inputs to generate fast cooling rates and minimise grain growth.

The results presented in this work have been obtained on a highly alloyed titanium-stabilised supermartensitic stainless steel. Medium and lean alloys are less prone to δ-ferrite formation in dual-phase HAZ but might have larger coarse-grained HAZ and harder martensite for a given C and N content (chapter 4). In this case the high temperature HAZ impact properties are likely to be governed by the coarse-grained HAZ grain size and the potential presence of Ti(C,N) particles.

Chapter 8

Neural network model for estimating the Ac_1 temperature

8.1 Introduction

Although efforts are being devoted to avoid the need for post-weld heat-treatments (PWHT) in supermartensitic stainless steels, this operation is still often employed to reduce martensite hardness and thus improve the heat-affected zone sulfide stress-corrosion cracking resistance. The tempering operation should be carried out few degrees below the steel Ac_1 temperature in order to avoid the formation of austenite which may subsequently transform into untempered martensite on cooling to room temperature.

In practice, when an estimation of the Ac_1 temperature is required empirical formulae are often employed [38]. However, such relationships often neglect potential interactions between elements and do not have a mechanism to indicate the uncertainties of extrapolation.

A more general method of regression analysis involves neural networks within a Bayesian framework. Gavard *et al.* employed neural networks to model Ac_1 and Ac_3 temperatures of a wide range of steels as a function of their chemical composition and of the heating rate used to measure the temperatures [94]. Using this approach, it was possible to satisfactorily predict phase transformation temperatures and reproduce known metallurgical trends, although Ac_1 temperatures were harder to model than Ac_3. This is because of the lack of good data and also the

neglect of the initial microstructure as an input to the model.

While the number of experimental Ac_1 data can easily be increased, the microstructure is rarely reported in the published literature. Because of the latter, predicting the Ac_1 temperature of a weld HAZ is difficult but as a first step it is still interesting to improve the original neural network model and thus obtain better guidance than with linear regression equations.

8.2 Introduction to neural network

A neural network is a powerful non-linear regression tool which when implemented within a Bayesian framework allows the calculation of error bars representing the uncertainty in the fitting parameters. To explain how a neural network works it is interesting to first introduce conventional regression analysis.

8.2.a Regression analysis

In conventional regression analysis the data are best-fitted to a specified relationship which is usually linear. The result is an equation in which each of the input x_i is multiplied by a weight w_i; the sum of all such products and a constant θ then gives an estimate of the output :

$$y = \sum_i w_i x_i + \theta \tag{8.1}$$

Equation 8.2 is an example of such linear regression used to estimate the Ac_1 temperature of low carbon 13 wt% Cr steels as a function of chemical composition (in wt%) [38].

$$Ac_1(^\circ\mathrm{C}) = -1500(\mathrm{C}+\mathrm{N}) - 50\mathrm{Ni} - 25\mathrm{Mn} + 25\mathrm{Si} + 25\mathrm{Mo} + 20\mathrm{Cr} + 650 \tag{8.2}$$

8.2.b Neural networks

In neural network analysis, an expression similar to that of a linear regression (*i.e.* $\sum_i w_i\, x_i + \theta$) forms the argument of, in the present work, a hyperbolic tangent function and gives the output of a so-called *hidden unit*. The output of a hidden unit is therefore a non-linear function of the inputs and the hyperbolic tangent function is chosen because of its flexibility. To capture more complex relationships, neural networks are often composed of several hidden units and each of them possesses its own set of adjustable weigths and constant as :

$$h_j = \tanh\left(\sum_i w_{ij}^{(2)}\, x_i + \theta_j^{(2)}\right) \tag{8.3}$$

The output y of the neural network model is then simply obtained by a linear combination of the output of each hidden unit and by adding another constant $\theta^{(1)}$ as :

$$y = \sum_j w_{ij}^{(1)}\, h_j + \theta^{(1)} \tag{8.4}$$

Figure 8.1 illustrates the structure of a three layers neural network consisting of the inputs, the hidden units and the output. The existence of the hidden layer allows the model to identify interaction between variables. Notice that the complexity of the model is related to the number of hidden units. The weights and constants used in the hidden units are adjusted during the training of the model. The latter operation is made using an algorithm which implements a learning method based on Bayesian statistics.

8.2.c Bayesian method

In regression analysis, the most probable values of the weigths are used for a given model. This method results in an overall error obtained by comparing the predictions against experimental values, with no indication of the uncertainty as a function of position in the input space.

MacKay has developed a useful treatment of neural networks using Bayesian statistics that recognises that there are many functions which can be fitted or extrapolated into uncertain regions of the input space, without compromising the fit

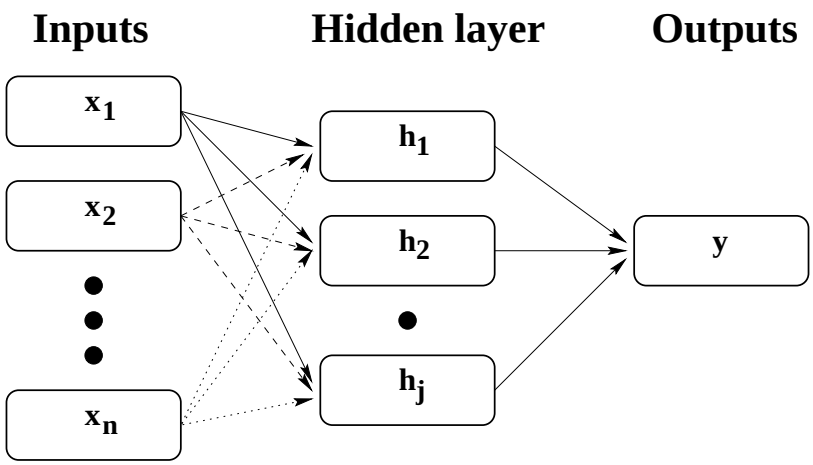

Figure 8.1: Schematic illustration of the input, hidden and output layers of a neural network model of n inputs and j hidden units. Each arrow represents a weight.

in adjacent regions which are rich in accurate data [95]. Instead of calculating the best set of weights, the algorithm infers a probability distribution for the weights from the data presented. When making predictions, the variety of model solutions corresponding to different possible set of weights are averaged using the probability of these sets of weights, a process called *marginalising*. It results that it is possible to quantify the uncertainty of fitting. If the inferred distribution is sharply peaked in the weight space, the most probable set will give by far the largest contribution to the prediction and alternative solutions will have little importance. Consequently, the prediction will be associated with a small uncertainty. If on the contrary, the data are such that different sets of weights are equally probable, alternatives will contribute in similar proportions and the error bars will be large. This is typically the case in regions of the input space where data are scarce or exceptionally noisy as illustrated in figure 8.2.

8.3 Analysis

8.3.a The variables

The dataset employed in this work is from earlier work by Gavard *et al.* compiled from published literature to include some 788 experiments [94]. In addition to the

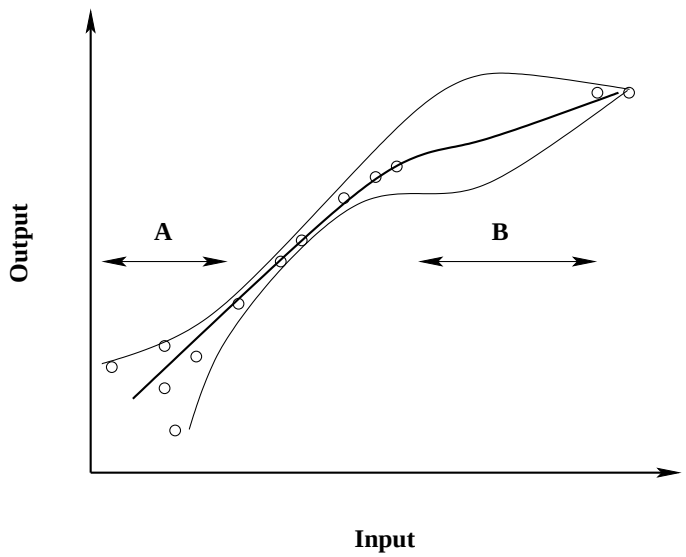

Figure 8.2: Schematic illustration of the uncertainty in defining a fitting function in regions where data are sparce (B) or where they are noisy (A). The thinner lines represent error bounds due to uncertainties in determining the weigths [96].

heating rate, the original input variables consisted of the elements C, Si, Mn, Cu, Ni, Cr, Mo, Nb, V, W and Co together with the trace elements S, P, Ti, Al, B, As, Sn, Zr, N and O. A Gaussian process analysis by Bailer-Jones *et al.* revealed that the dataset could be reduced to the 11 major elements without significantly affecting the accuracy of the predictions [97]. Following these results, the set of inputs for the present work (table 8.1) included the chemical composition of the first 11 elements (in wt%), the heating rate (°C s^{-1}) and measured Ac_1 temperatures (°C). It is emphasised that unlike linear regression analysis, the ranges stated in table 8.1 cannot be used to define the range of applicability of the neural network model. This is because the inputs are in general expected to interact.

A total of 88 sets of experimental data were added to the original database including data generated during this project and some collected from published literature on 9 - 13 wt% Cr steels [35, 59, 72, 98, 99, 100]. The experimental Ac_1 temperatures that have been added to the original database have been measured on steels as-received microstructures (*i.e.* tempered martensite and possibly retained austenite). The final database contained 876 experiments and a total of 113 data

were from 9 - 13 wt% Cr steels. A visual impression of the spread of the data is shown in figure 8.3.

Input element	Minimum	Maximum	Mean	Std. deviation
C	0.0	0.96	0.28	0.17
Si	0.0	2.83	0.39	0.45
Mn	0.0	3.06	0.81	0.39
Cu	0.0	2.01	0.05	0.14
Ni	0.0	9.12	1.08	1.61
Cr	0.0	17.97	2.03	3.54
Mo	0.0	4.80	0.35	0.43
Nb	0.0	0.52	0.00	0.04
V	0.0	2.45	0.06	0.13
W	0.0	8.59	0.08	0.49
Co	0.0	4.07	0.06	0.40
Heating rate	0.01	100.0	2.37	8.36
Ac_1	520.0	921.0	729.6	57.4

Table 8.1: Input variables used to develop the new model. Composition in wt%, heating rate in °C s^{-1} and Ac_1 in °C.

8.3.b Normalisation

All the variables were normalised within a range ± 0.5 as follows :

$$x_N = \frac{(x - x_{min})}{(x_{max} - x_{min})} - 0.5 \tag{8.5}$$

where x_N is the normalised value of x, which has the minimum and maximum values given by x_{min} and x_{max}, respectively. The normalisation operation facilitates the subsequent comparison of the relative significance of the variables.

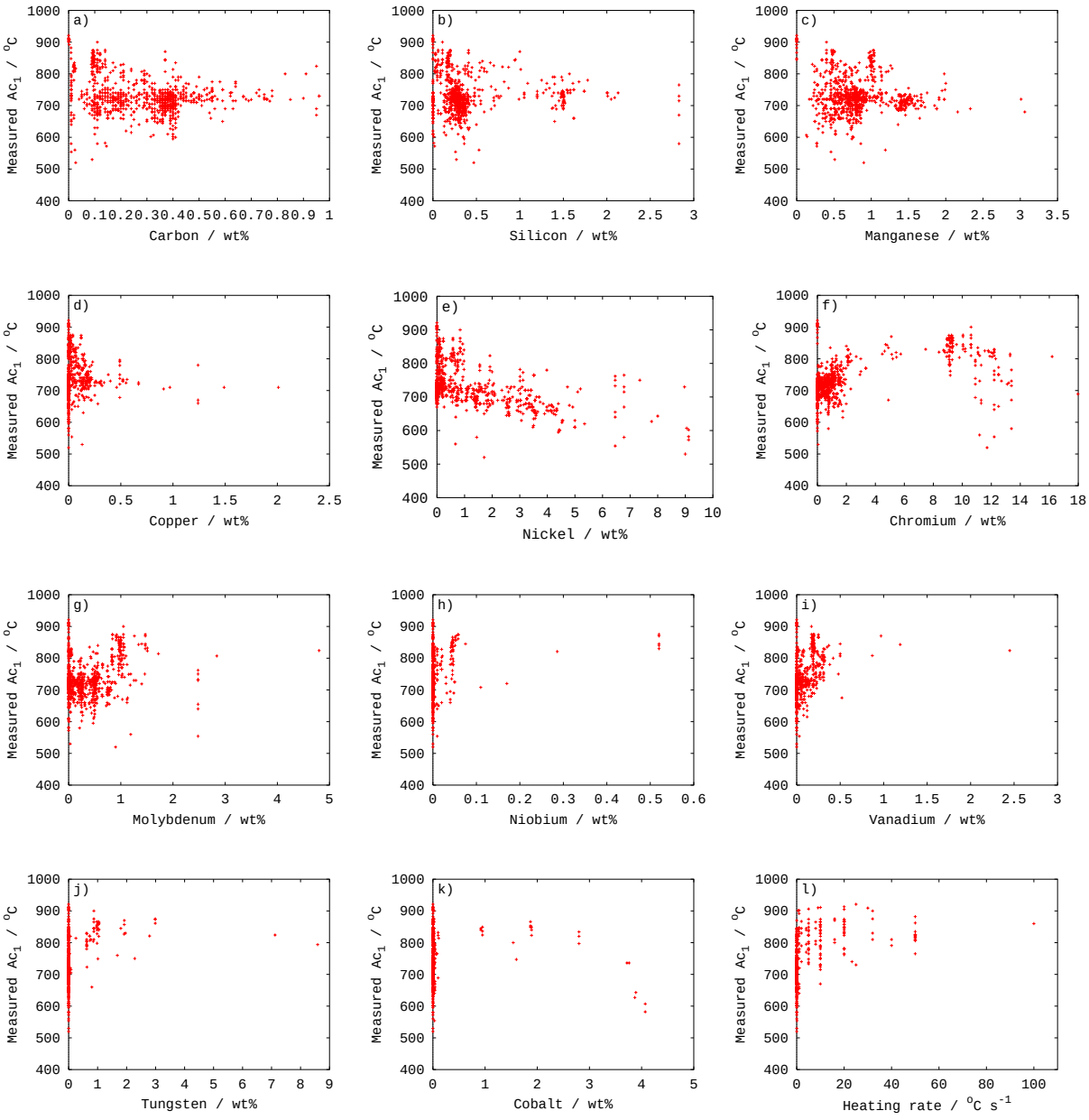

Figure 8.3: The database values of each variable versus the Ac_1 temperature.

8.3.c Overfitting

Because of the great flexibility of the functions used in the neural network, there is a possibility of *overfitting* data. This can occur when the generated models become too complex for predicting a simple trend (figure 8.4). To avoid overfitting two solutions are implemented. The first is contained in the algorithm due to MacKay : complexity parameters α and β (see equation 8.6) are inferred from the data and allow automatic control of the model complexity. The second consists of equally dividing the experimental database into a *training* and a *test* dataset. The training set is used to create a large number of models with different number of hidden units (1 to 22) and different sets of initial weights (6 in this case). The test data set is used to see how the trained models generalise on unseen data. The error on the testing set decreases at first, as the fitting improves, but increases again when overfitting occur (figure 8.5 (b)).

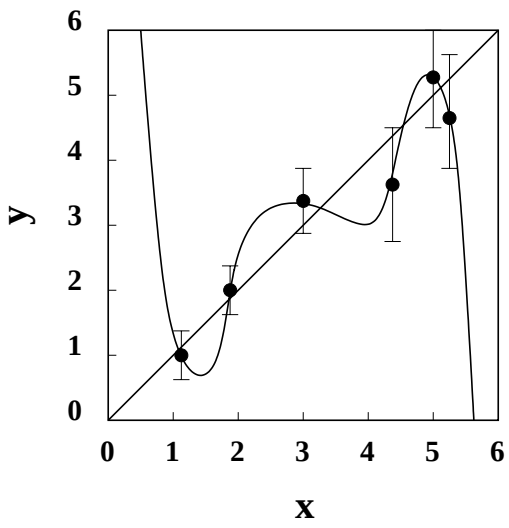

Figure 8.4: A complicated model may overfit the data. In this case, a linear relationship is all that is justified by the noise in the data.

8.3.d Training and testing of models

The training of a model involves the derivation of the weights which minimise an objective function, typically :

$$\begin{aligned} M(\mathbf{w}) &= \beta E_D + \alpha E_W \\ E_D &= \frac{1}{2}\sum_m \left(t^{(m)} - y^{(m)}\right)^2 \\ E_W &= \frac{1}{2}\sum_m w_m^2 \end{aligned} \tag{8.6}$$

where $\mathbf{w}$ is a vector describing the set of weights, E_D is the overall error, and E_W the regulariser, used to force the network to use small weights. α and β are control parameters which influence the complexity of the model. $t^{(m)}$ is the target in the database for the set of inputs $x^{(m)}$, while $y^{(m)}$ is the corresponding predicted output.

The perceived noise level during training tends to decrease as the model becomes more complex figure 8.5 (a). The models are then tested on the unseen test data and are subsequently ranked using either the test error (TE) as in figure 8.5 (b), or the log predictive error (LPE) (figure 8.5 (c)). The TE and LPE are calculated as :

$$\text{TE} \propto \sum_m \frac{1}{2}\left(t^{(m)} - y^{(m)}\right)^2 \tag{8.7}$$

$$\text{LPE} = \sum_m \left[\frac{1}{2}\left(t^{(m)} - y^{(m)}\right)^2 / {\sigma_y^{(m)}}^2 + \log\left(\sqrt{2\pi}\ \sigma_y^{(m)}\right)\right] \tag{8.8}$$

where $\sigma_y^{(m)}$ $(= \frac{1}{\beta^{1/2}})$ is related to the uncertainty of fitting for the set of inputs $x^{(m)}$.

As predictions with error bars are preferred to simple scalar predictions, it is more judicious to compare models in term of their predictive performance as measured by the LPE. Under the LPE, as contrasted with the TE, the penalty of making a wild prediction is much less if that wild prediction is accompanied by appropriately large error bars [101]. The best models should have high LPE values. Figure 8.5 (e) and (f) show normalised predicted values versus experimental values for the best model possessing five hidden units.

8.3.e Committee

Combining the output of several models, by building a committee often makes optimum predictions. The predictions, $\bar{y}$, of a committee is the average of the prediction of its members, and the associated error bar is calculated as :

$$\begin{aligned} \bar{y} &= \frac{1}{L}\sum_{l} y^{(l)} \\ \sigma^2 &= \frac{1}{L}\sum_{l} \sigma_y^{(l)2} + \frac{1}{L}\sum_{l} \left(y^{(l)} - \bar{y}\right)^2 \end{aligned} \tag{8.9}$$

Where L is the number of networks in the committee. It should be noted that equation 8.9 considers the prediction for a given, single set of inputs and that the exponent (l) refers to the model used to make prediction.

The optimum size of a committee is determined by including an increasing number of models in the committee and by comparing their performance on the testing set. A plot of the test error of the committee versus its size L gives a minimum error when the committee contains more than one model as shown on figure 8.5 (d). The committee with two models possessing five hidden units each was found to have an optimum membership with the smallest combined test error.

After selection, the models in the committee are retrained (weights adjusted) on the entire database without changing the complexity of each model. The committee of models is generally referred to as the "neural network model". The predictions of the latter on the complete database show few outliers as illustrated in figure 8.7.

Because the algorithm used to train the model includes an automatic relevance determination, variables that are found not to influence the output are assigned small weights. This therefore helps identify the most important variables in the analysis. Figure 8.8 illustrates the significance of each of the input variables in the two best models, as perceived by the neural network, in influencing the Ac_1 temperature. The magnitude of the significance reflects the extent to which a particular input explains the variation of the output. As expected, the nickel and chromium content

as well as the heating rate feature prominently, on the other hand, niobium, cobalt and tungsten are not seen to be influencial.

8.4 Application of the model

The neural network can capture interactions between the inputs because the functions involved are non-linear. The nature of these interactions is implicit in the values of the weights, but the weights are not always easy to interpret. For example, there may exist more than just a pairwise interaction, in which case the problem becomes difficult to perceive from an examination of the weights. A better method is to actually use the network to make predictions and to see how these interactions depend on various combinations of inputs.

8.4.a Effect of chemical composition and heating rate

The effects of element additions on Ac_1 have been examined on steel C, a medium alloyed supermartensitic steel of the following chemical composition : 0.01 C, 0.19 Si, 0.24 Mn, 0.06 Cu, 3.12 Ni, 12.5 Cr, 0.02 Mo, 0.009 Nb, 0.03 V, 0.04 Co wt%. For these predictions calculations were made at a heating rate of 1 °C s^{-1} which was close to the database mean heating rate and were made on the maximum range of data present in the database.

It is emphasised that Ti and N are not taken into account in this analysis, but as these elements combine to form very stable TiN particles the error associated with their neglection is expected to be small. However, if Ti is present in quantities greater than 4×N (stoichiometric ratio in wt%) then the appropriate amount of carbon should be removed to allow TiC to form. Conversely, if nitrogen is in excess it will combined with nitride forming elements such as Cr, Mo and V but considering that the excess will be smaller than 0.01 wt% (in supermartensitic stainless steels), its effect on Ac_1 is probably negligible.

Figures 8.9 and 8.10 presents the results of all calculations. Some predictions

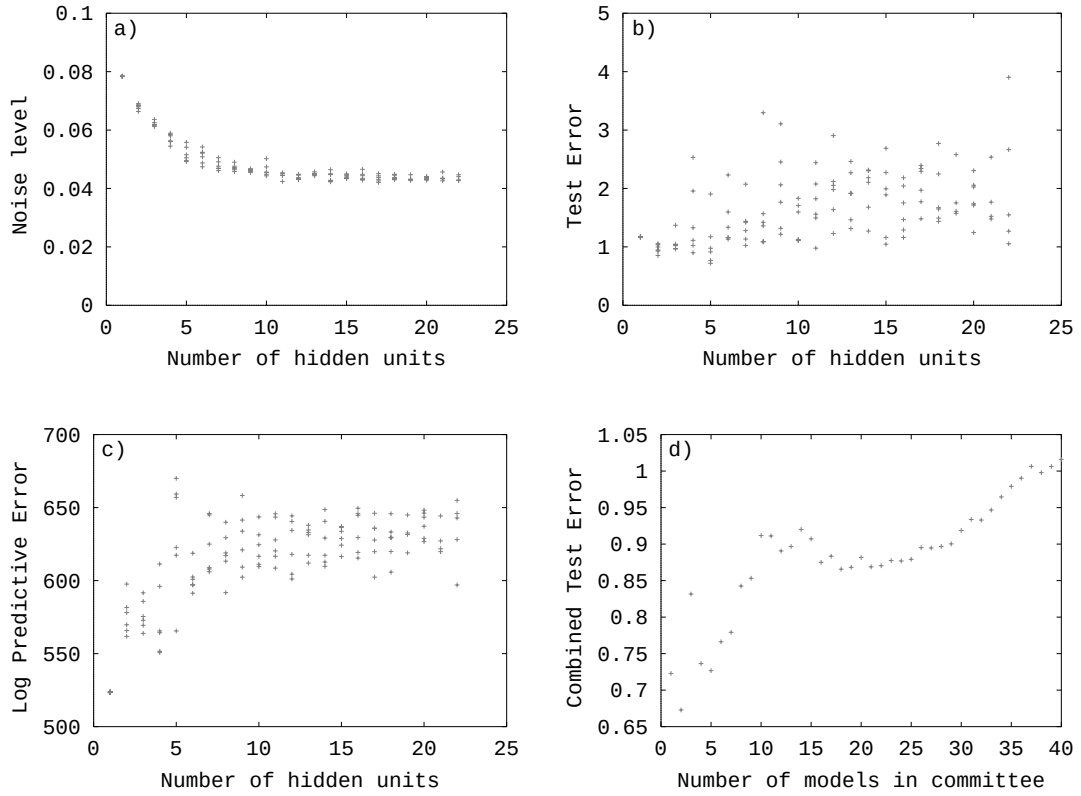

Figure 8.5: The perceived noise level (a), the test error (b), the log predictive error (c) of the models with increasing number of hidden units, the combined test error (d) for an increasing number of models in committee.

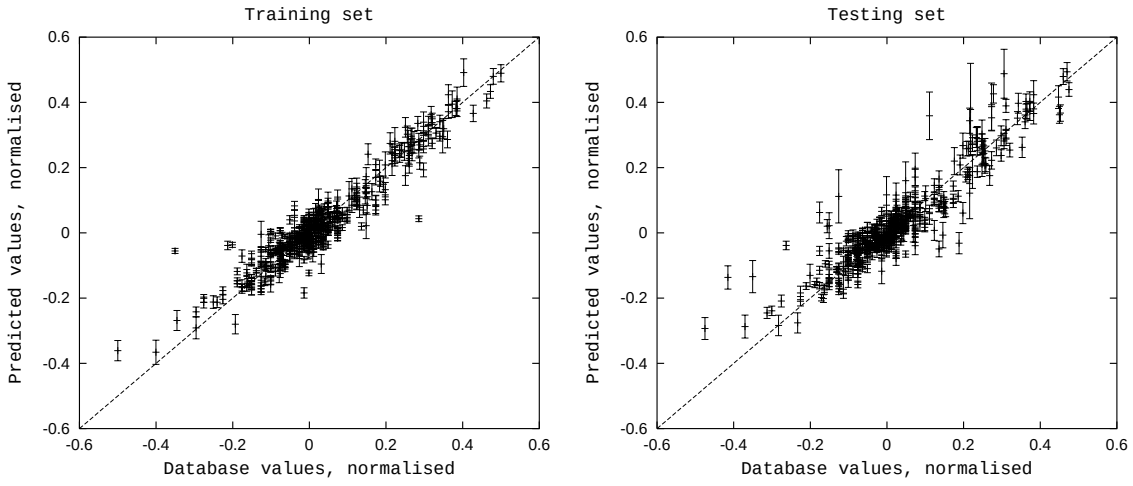

Figure 8.6: Plots of the predicted Ac_1 temperature against experimental values (normalised) for the training and testing of the best model. The plotted error bars correspond to the fitting uncertainties.

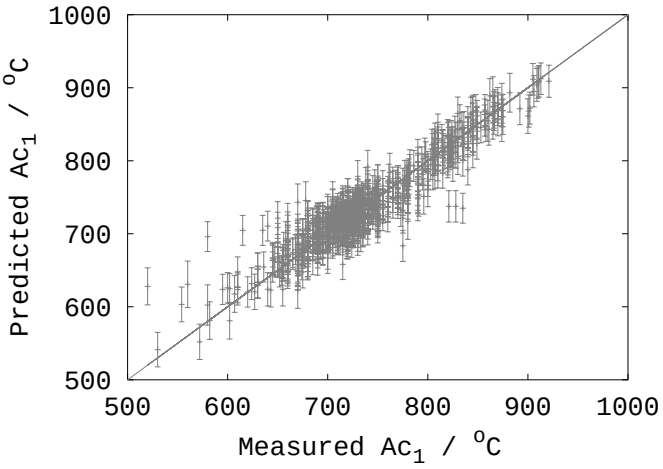

Figure 8.7: Predicted against measured Ac_1 temperatures performed on the complete database using the optimum committee. The plotted error bars correspond to $\pm$ 1 σ as defined in equation 8.9.

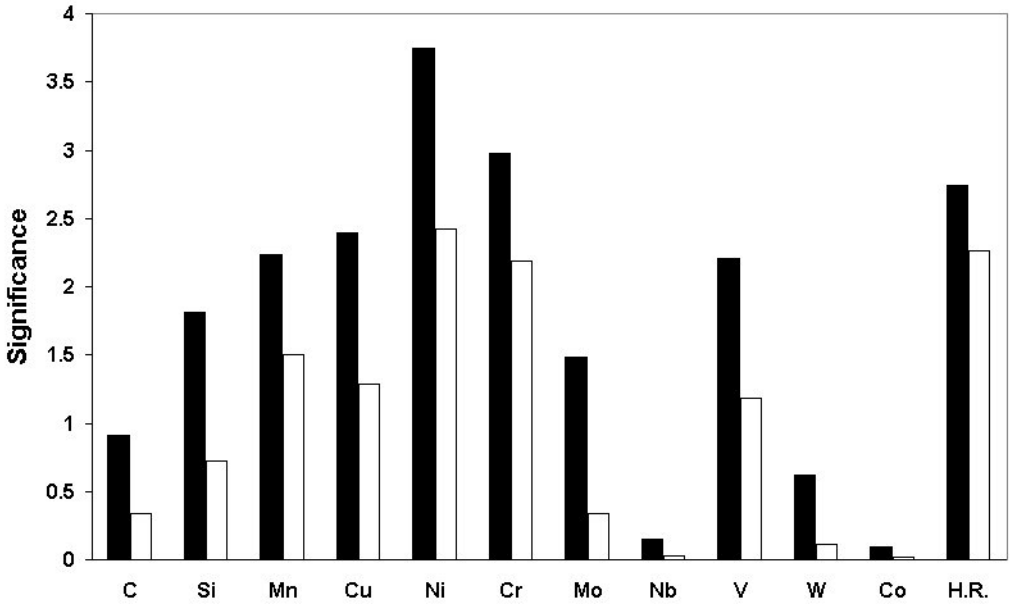

Figure 8.8: Perceived significance of input parameters in the best two models for each input variable. H.R. stands for heating rate.

showed clear trends in the evolution of Ac_1 as a function of the input data considered. This was namely the case for manganese and nickel (figure 8.9 (c) and (e)). Those solutes are both well-known austenite stabilising elements, and consistent with the model predictions, their addition decrease Ac_1.

No clear trends could be observed on the remaining elements. However, the model provides predictions with error bars that are dependent upon the input space region and this represents a significant improvement compared with traditional linear regression equations. For example, there is little information in the database for vanadium in concentration greater than 0.5 wt% (figure 8.10 (i)) and the model recognises this by yielding increasingly large error bars. On the other hand, examination of the model inferred significance (figure 8.8) reveals that Nb, W and Co have little influence on Ac_1 and thus could be removed in a future analysis.

The evolution of Ac_1 as a function of heating rate is reported in figure 8.11. A clear increase of Ac_1 temperature is identified by the model at heating rates up to ~ 20 °C s^{-1}. The initial temperature increase is explained by the diffusive nature of the transformation. In fact, the number of successful atomic jumps per unit of time of substitutional elements across the martensite/austenite interface is reduced at faster heating rates so that the transformation starts at a higher temperature. The model successfully recognised the effect of heating rate on Ac_1 temperature while linear regression equations usually disregard this effect.

8.4.b Application to steel T91

To show the performance of the new model on martensitic stainless steels, comparison has been made using steel T91 (table 8.2), an alloy studied in Gavard *et al.* work [94]. It should be noted that the data from this alloy were not included in the database.

As can be seen from figure 8.12, the new neural network model shows small error bars and good agreement with the experimental data except at 20 °C s^{-1}. However it should be noted that no experimental error bars were provided but assuming those to be $\pm$ 10 °C, all predictions become satisfactory.

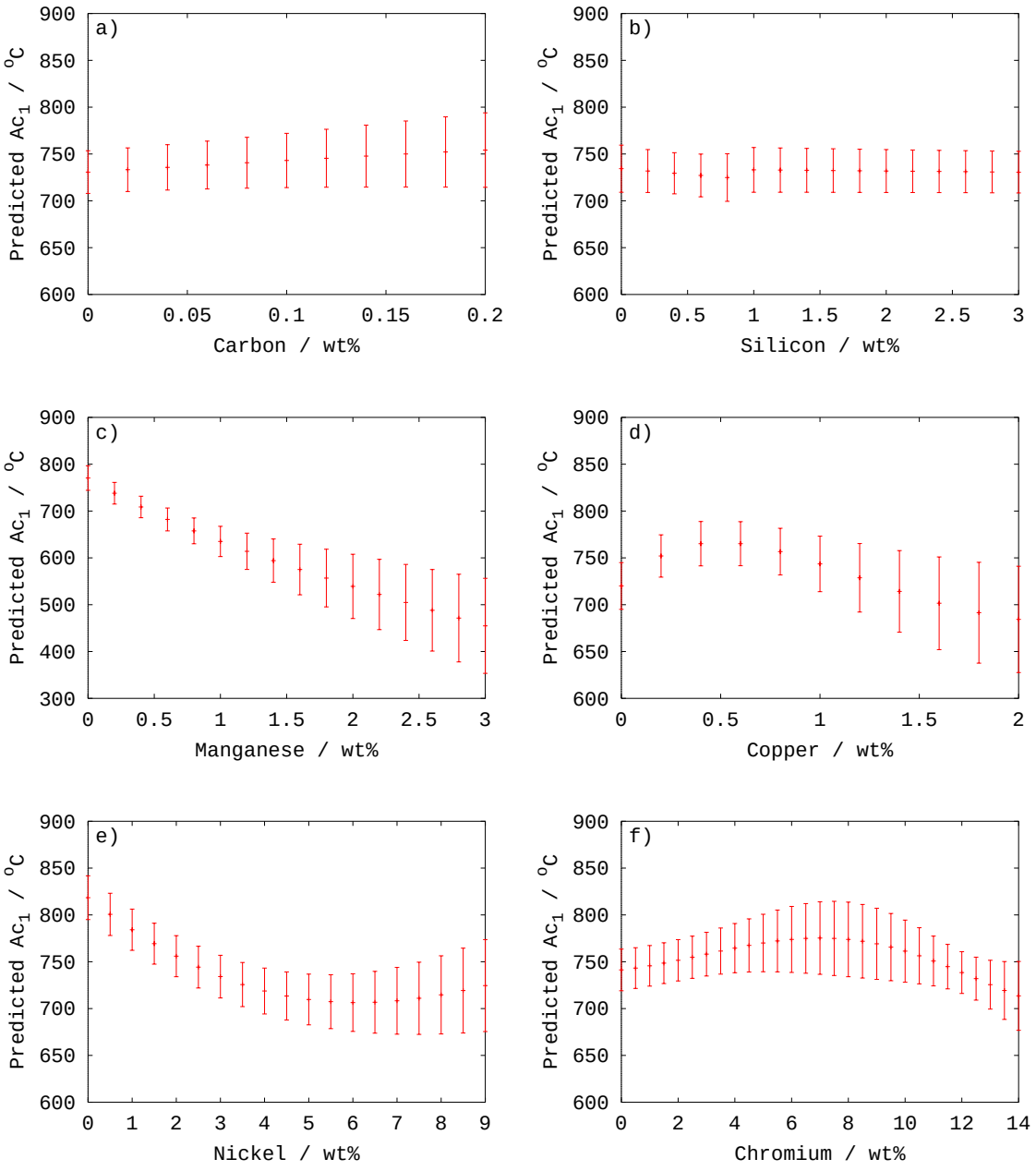

Figure 8.9: Predicted variation in Ac_1 temperature as a function of chemical composition for C, Si, Mn, Cu, Ni and Cr. Prediction made on steel C : 0.01 C, 0.19 Si, 0.24 Mn, 0.06 Cu, 3.12 Ni, 12.5 Cr, 0.02 Mo, 0.009 Nb, 0.03 V, 0.04 Co wt%. The neural network error bars correspond to $\pm$ 1 σ as defined in equation 8.9.

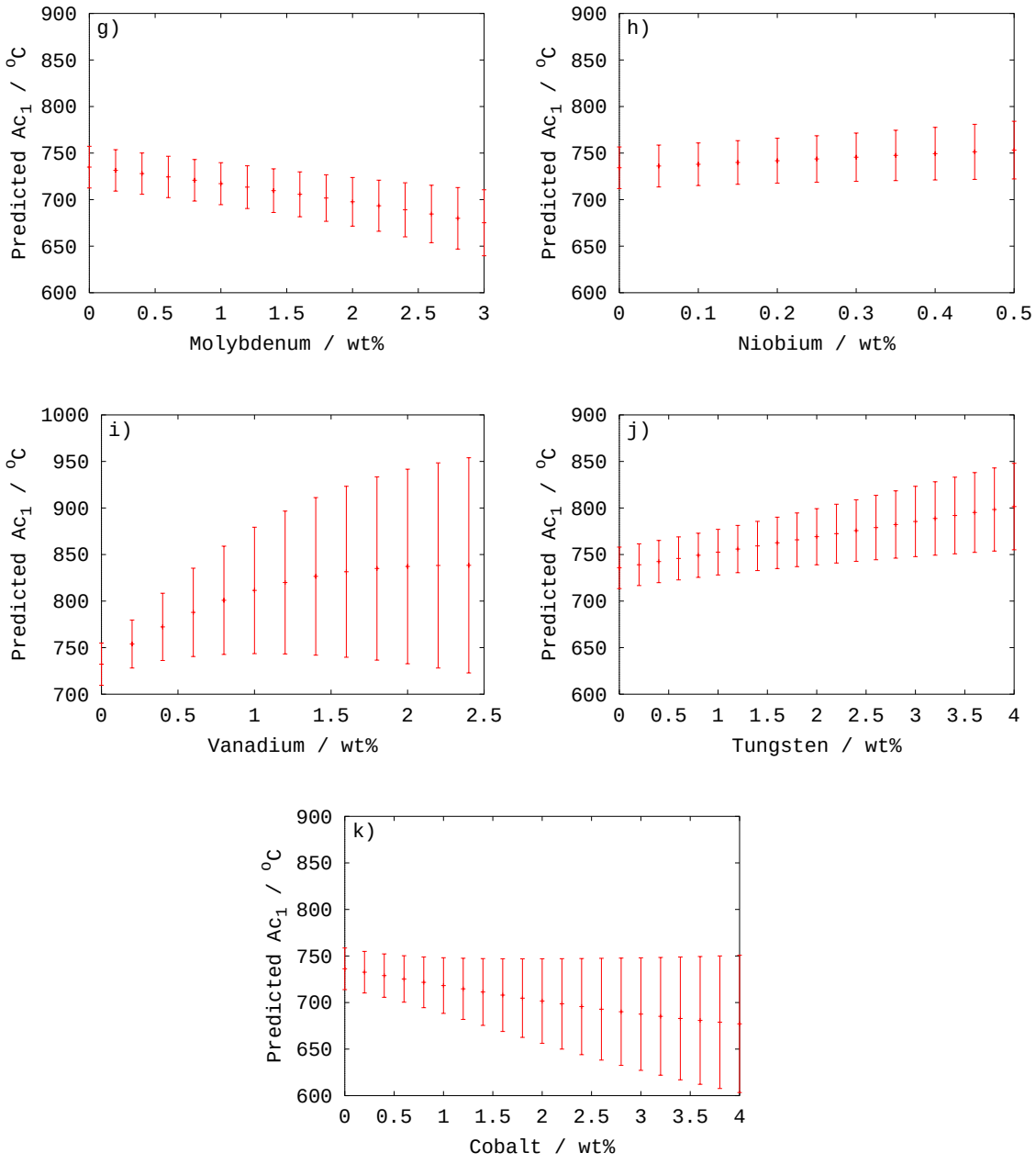

Figure 8.10: Predicted variation in Ac_1 temperature as a function of chemical composition for Mo, Nb, V, W and Co. Prediction made on steel C : 0.01 C, 0.19 Si, 0.24 Mn, 0.06 Cu, 3.12 Ni, 12.5 Cr, 0.02 Mo, 0.009 Nb, 0.03 V, 0.04 Co wt%. The neural network error bars correspond to $\pm$ 1 σ as defined in equation 8.9.

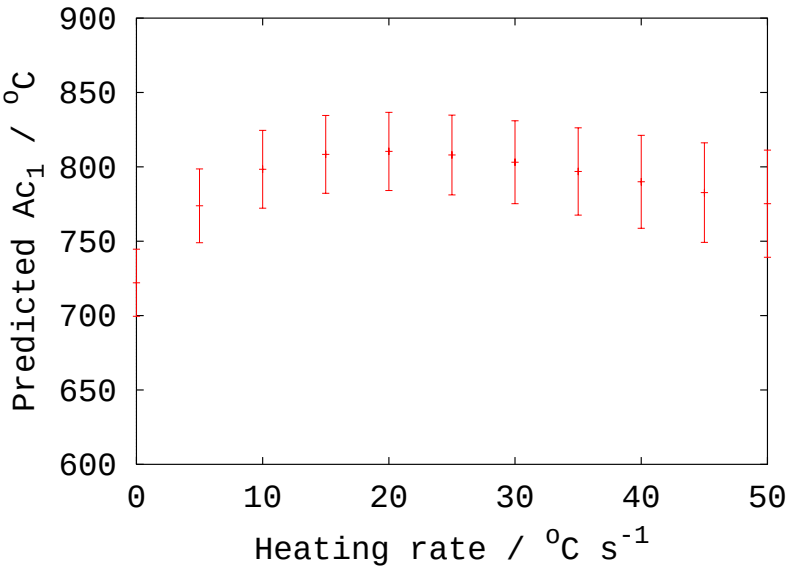

Figure 8.11: Effect of heating rate on Ac_1 temperature for a medium alloyed supermartensitic stainless steel of compositions (wt%): 0.01 C, 0.19 Si, 0.24 Mn, 0.06 Cu, 3.12 Ni, 12.5 Cr, 0.02 Mo, 0.009 Nb, 0.03 V, 0 W, 0.04 Co.

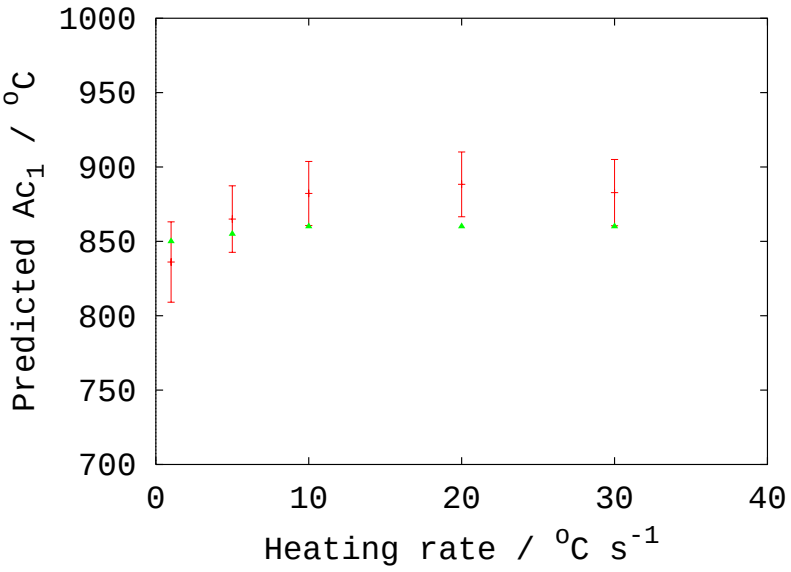

Figure 8.12: Predicted and experimental Ac_1 temperatures as a function of heating rate for steel T91.

Material	C	Si	Mn	Cr	Mo	Ni	N	Nb	V
T91	0.105	0.43	0.37	8.20	0.97	0.13	0.051	0.075	0.2

Table 8.2: Chemical composition of steel T91. Compositions in wt % [94].

8.4.c Application to supermartensitic steels

A range of supermartensitic stainless steels has been chosen to make prediction over their Ac_1 temperatures. The selection of alloys (table 8.3) is ranked as increasing (Cr+Mo)/Ni ratio to separate high (small ratio) and low alloy steels. Steels A, B and C that have been studied in the previous chapters are included in the list: (Cr+Mo)/Ni ratio of 2.27, 7.04 and 4.01 respectively.

Figure 8.13 (a) shows the results of all predicted Ac_1 temperatures for a heating rate of 1 °C s^{-1}. As expected steels possessing a (Cr+Mo)/Ni ratio between 2 and 3 (high nickel alloys) had lower Ac_1 temperatures compared with leaner alloys. According to these predictions, tempering at the common temperature of 650 °C would lead to partial reaustenitisation in high alloy steels but it would not be so at a heating rate of 10 °C s^{-1}(figure 8.13 (b)). Faster heating rates allow therefore the use of higher tempering temperatures and as a consequence of atoms higher mobility, shorter tempering time. This illustrates the importance of taking heating rate into account when tempering those steels.

8.4.d Effect of the microstructure and discussion

In practice, the HAZ regions that need tempering are those that have been completely reaustenitised during welding. However, the additional experimental Ac_1 temperatures have been obtained on steels in their as-received conditions. It is therefore interesting to estimate the effect of the initial microstructure on Ac_1 in supermartensitic stainless steels.

To investigate the effect of the microstructure on Ac_1, a dilatometric test using two cycles has been performed. The retained austenite-free as-received microstruc-

$\frac{Cr+Mo}{Ni}$	C	Si	Mn	Cu	Ni	Cr	Mo	Nb	V	Co	Ti	N
2.27	0.01	0.26	0.46	0.03	6.46	12.2	2.48	0.01	0.03	0.03	0.09	0.007
2.30	0.009	0.20	0.43	0.03	6.40	12.2	2.51	0.009	0.03	0.03	0.12	0.005
2.47	0.012	0.18	0.27	0.03	5.90	12.4	2.19	0.009	0.03	0.01	0.024	0.012
2.70	0.017	0.20	1.77	0.51	4.87	11.7	1.39	0.005	0.02	0.0	0.007	0.011
2.71	0.013	0.12	0.54	0.04	5.10	11.8	2.03	0.009	0.04	0.06	0.004	0.009
2.80	0.013	0.16	0.65	0.03	5.10	13.5	0.78	0.009	0.04	0.03	0.088	0.006
2.93	0.021	0.17	1.79	0.47	4.40	11.5	1.39	0.009	0.02	0.03	0.008	0.012
3.12	0.02	0.30	0.46	1.24	3.98	11.3	1.12	0.04	0.06	0.04	0.02	0.008
3.52	0.02	0.22	0.39	0.01	3.91	12.8	0.97	0.009	0.02	0.03	0.009	0.051
4.01	0.01	0.19	0.24	0.06	3.12	12.5	0.02	0.009	0.03	0.04	0.01	0.012
4.23	0.011	0.19	0.30	0.08	2.91	12.3	0.02	0.009	0.04	0.02	0.013	0.009
4.34	0.011	0.10	1.77	0.48	2.45	10.6	0.06	0.006	0.02	0.0	0.006	0.006
4.67	0.011	0.11	1.83	0.50	2.26	10.5	0.06	0.009	0.02	0.01	0.004	0.006
7.04	0.01	0.18	1.14	0.49	1.55	10.9	≤ 0.01	0.009	0.05	0.04	0.01	0.006

Table 8.3: Chemical composition of steels used to make predictions ranked as increasing (Cr+Mo)/Ni ratio. All compositions in wt% [30, 102, 8].

ture of steel B was heated up to 1000 °C using a heating rate of 1 °C s^{-1} and was held at temperature for 10 minutes before cooling (cycle 1). A second cycle on the same specimen allowed the measurement of the Ac_1 temperature of fresh martensite (cycle 2).

As figure 8.14 (a) shows there is no significant differences between the two cycles *i.e.* Ac_1 is about 730 °C. This result indicates that Ac_1 is not greatly affected by the level of tempering of the microstructure when retained austenite is absent. The model prediction for steel B at a heating rate of 1 °C s^{-1} is in good agreement with the experimental values *i.e.* 751 ± 24 °C.

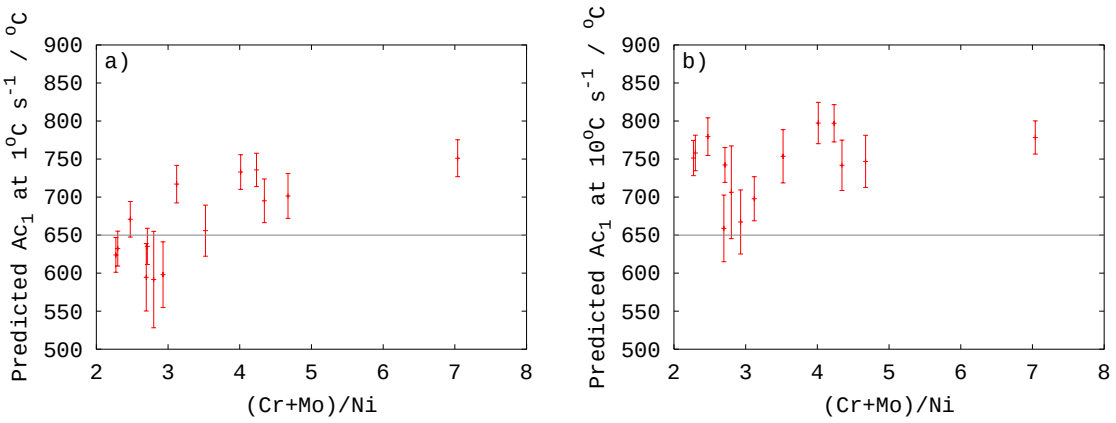

Figure 8.13: Steels predicted Ac_1 temperatures versus (Cr+Mo)/Ni ratio for heating rates of 1 °C s^{-1} (a), and 10 °C s^{-1} (b).

On the other hand, steel A contained 13 % retained austenite in its as-received microstructure (chapter 4). To determine the extent of the effect of austenite presence on Ac_1 another dilatometric experiment similar to the one reported before has been conducted.

Figure 8.14 (b) shows an increase of 125 °C in the Ac_1 temperature between the two cycles with 610 °C and 735 °C, respectively. This difference originates from the fact that when present, austenite precludes the need for nucleation during heating and thus significantly lowers the temperature of the onset of the transformation. The model prediction for the same heating rate is 624 ± 23 °C. The latter result clearly shows that the neural network model underestimates the critical temperature of the quenched microstructure of high alloy supermartensitic stainless steels. The presence of retained austenite plays therefore an important role and represents a source of error in the model.

Nevertheless, the model can be used as a guide to estimate the post-weld heat-treatment temperature in lean and medium alloyed supermartensitic welds. It should also be remembered that in the case of multipass welds the situation is further complicated by reheating effects and those have been neglected in this work.

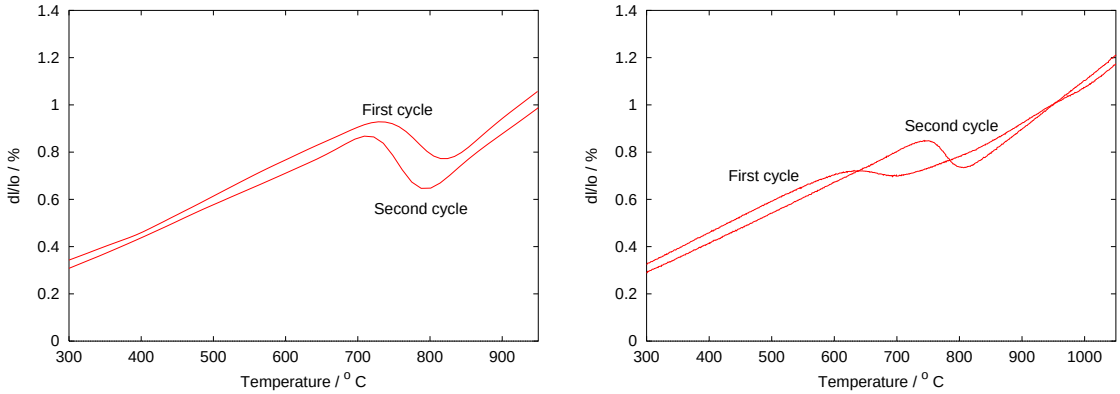

Figure 8.14: Dilation curves of the two cycles performed on steels B (a) and A (b). Heating rate of 1 °C s^{-1} and maximum temperature of 1000 °C.

8.5 Summary

A new neural network model for predicting Ac_1 as a function of chemistry and heating rate has been developed focussing on martensitic stainless steels. Although few metallurgical trends were identified, the model represents a significant improvement compared with linear regression equations. The model can be used to estimate the PWHT temperature of lean and medium supermartensitic stainless steels and is available freely on the world wide web at *http://www.msm.cam.ac.uk/map/steel /programs/ac1new.html*.

Future analysis should consider the level of retained austenite in the starting microstructure as an input parameter.

Although not explored in this work, the new model can also be employed to make predictions on low alloy steels since most of the data in the original database have been obtained on those steels [94].

Chapter 9

Summary and future work

The work presented in this thesis was concerned with the evolution of microstructure in the high temperature HAZ of three recently designed supermartensitic stainless steels, with particular attention to austenite and the often neglected δ-ferrite phase which is potentially detrimental to the properties.

Dilatometry was employed to measure the phase transformation temperatures of the different alloys and thus helped identify the different regions of the heat-affected zone. In each steel, the temperature ranges of δ-ferrite formation were short and thus explained the small size of the dual-phase HAZ in the experimental welds. On the other hand, MT-DATA successfully predicted the steels to have the capacity to become fully austenitic and fully ferritic before reaching the melting temperature. A comparison between the actual and equilibrium predicted temperatures revealed a systematic underestimation of the Ae_4 temperatures. Finally, a comparison of the predicted temperature ranges of δ-ferrite formation and growth obtained using both equilibrium and paraequilibrium conditions revealed contradicting trends.

Detailed examination of a series of autogenous bead-on-plates revealed the presence of δ-ferrite films in dual-phase and coarse-grained HAZ regions and showed the greater tendency of the most corrosion resistant alloy to retain δ-ferrite. The effect of cooling rates on δ-ferrite volume fraction was studied on furnace heat-treated coupons. This revealed that while fast cooling rates favour δ-ferrite retention in partially ferritised specimens, the opposite applies to specimens cooled from tem-

peratures above Ac_5. On the other hand, it was possible to correlate the δ-ferrite volume fraction in dual-phase HAZ with the employed heat input. The volume percentage of δ-ferrite in dual-phase HAZ decreased with heat input and never exceeded 15 %. Furthermore, observations of actual multipass welds showed a non-uniform distribution of δ-ferrite between the root and the cap of the HAZ. In fact reheating effects contributed to δ-ferrite dissolution at the root of the HAZ.

The methods available to estimate the tendency of the steel to retain δ-ferrite have been compared. The Balmforth diagram was found suitable to make comparisons between different supermartensitic alloys. The expressions of the Cr_{eq} and Ni_{eq} indicated that the balance between molybdenum and nickel plays a major role on δ-ferrite retention. In fact, predictions made using a published neural network model indicate that it is difficult to balance the ferrite stabilising effect of molybdenum by only adding the minimum amount of nickel required to obtain a fully austenitic steel at high temperature. Finally, based on the predicted phase transformation temperatures and Rosenthal's equations, an attempt has been made to predict the extent of the dual-phase HAZ. Unfortunately, due to the lack of accurate thermodynamic data the agreement with experiments was poor. Improvement of the thermodynamic databases is therefore required.

Heat-treated specimens allowed the effects of δ-ferrite on Charpy impact toughness to be investigated in the alloy most prone to ferrite retention. The results showed that even relatively large amount of δ-ferrite in dual-phase HAZ have little effect on the ductile to brittle transition temperature. Testing of Gleeble simulated HAZ confirmed the weak influence of δ-ferrite on the behaviour of the whole HAZ. In fact, the impact toughness of the coarse-grained HAZ was found to be a more serious issue because of the large grain size that can be observed in this area. However, the problem might be more acute for lean supermartensitic stainless steels since MT-DATA predicted those alloys to possess larger coarse-grained HAZ.

Finally, a neural network model has been proposed to predict the Ac_1 temperature of steels and in particular martensitic stainless steels as a function of chemical composition and the employed heating rate. Predictions made with this model have

been shown to be able to reproduce correctly known metallurgical trends and to be superior to conventional extrapolation methods. Experimentally, the Ac_1 temperatures were seen to be significantly affected by the presence of retained austenite in the tested microstructure. This represents a potential source of error in the neural network model and consequently future analysis should take the retained austenite volume fraction into account in the input variables. Nevertheless, the neural network model can be used as a guide to estimate the post-weld heat-treatment temperature of single-pass welds in martensitic stainless steels and also carbon steels.

The effect of the presence of HAZ δ-ferrite on corrosion resistance was not investigated in this work. However, work is being performed on the topic at TWI. So far it has not been clearly demonstrated that δ-ferrite presence is responsible for crack initiations.

APPENDIX ONE

MAP_STEEL_AC1TEMP

This appendix presents the model described in chapter 8 and associated documentation following the MAP format, http://www.msm.cam.ac.uk/map/mapmain.html.

1 Provenance of Source Code

Dominique Carrouge
Phase Transformations and Complex Properties Group,
Department of Materials Science and Metallurgy,
University of Cambridge,
Cambridge, CB2 3QZ U.K.

The neural network program was produced by:
David MacKay,
Cavendish Laboratory,
University of Cambridge,
Madingley Road,
Cambridge, CB3 0HE, U.K.

Added to MAP: September 2002.

2 Purpose

A program for the prediction of the Ac_1 temperatures of steels, including martensitic stainless steels, as a function of chemical composition and heating rate.

3 Specification

Language: C
Product Form: Source Code (Unix version only)
Operating System: Tested on Solaris, Linux and PC.

4 Description

MAP_STEEL_AC_1TEMP contains the programs which enable the user to estimate the Ac_1 temperature of steels, including martensitic stainless steels, as a function of chemical composition and heating rate. It makes use of a neural network program called *generate44*, which was developed by David MacKay and is part of the *bigback5* program. A total of eighty three experimental data relevant to 9-13 wt% Cr steels were added to the original database from Gavard *et al.* work [1] and the updated database "database_ac1_martensitic.txt" is provided. Following a Gaussian process analysis by Bailer-Jones *et al.* [2], the elements considered to affect the Ac_1 temperature in this neural network model are : C, Si, Mn, Cu, Ni, Cr, Mo, Nb, V, W and Co. The model presented here combines the output of two different models which had five hidden units and different initial weights. The programs automatically calculate the result of each model and average those results to produce a prediction of the Ac_1 temperature and an error estimate.

A Linux/Unix and a PC version of the program are provided. To make predictions with the PC version alter the *test.dat* file and double click on *model.exe*. The results are in the file *Model_RESULT.dat*. In the Linux/Unix version, the source code is accompanied by a program to install the program, which should run on most versions of UNIX. Once uncompressed, and once the 'install' program runs, the directory contains :

MINMAX
A text file containing the minimum and maximum limits of each input and output variable. This file is used to normalise and unnormalise the input and output data.

test.dat
The input file that needs to be edited to make predictions. The variables should be entered in line, separated by a single space and in the following order : C, Si, Mn, Cu, Ni, Cr, Mo, Nb, V, W, Co and Heating rate.

model.gen
This is a UNIX shell file containing the commands required to run the model. It can be executed by typing 'sh model.gen' at the command prompt. This shell file normalises the input data, executes the neural network program, unnormalises the results and combine them to produce the final *committee* result.

.normalise
Hidden executable file, to normalise the input data.

.generate44
Hidden executable file, for the neural network program. It reads the normalised input file and also uses a configuration file *spec.t* generated by *.generate_spec* and the weight files, located in the subdirectory *c*.

.generate_spec
Hidden executable file, generates the configuration file read by *.generate44*.

.gencom
Hidden executable file, combines the output of the different models in a *committee* result.

.treatout
Unnormalise the results.

SUBDIRECTORY c

_w*f
The weight files of the different models.

***.lu**
Files containing information for calculating the size of the error bars for the different models.

_c*
Files containing information about the perceived significance value [3] for each model.

_R*
Files containing information about the noise, test error and log predictive error [3] for each model.

SUBDIRECTORY d

outran.x
A normalised output file which was created during the building of the model. It is accessed by *.generate44*.

SUBDIRECTORY outprdt

out1, out2, *etc.*
The normalised output files for each model.

com.dat
The normalised output file containing the committee results. It is generated by *.gencom*.

5 References

1. L. Gavard, H. K. D. H. Bhadeshia, D. J. C. MacKay and S. Suzuki, *Bayesian Neural Network Model for Austenite Formation in Steels*, Materials Science and Technology 12:453-463, 1996.

2. C. A. L. Bailer-Jones, H. K. D. H. Bhadeshia and D. J. C. MacKay, *Gaussian Process Modelling of Austenite Formation in Steel*, Materials Science and Technology 15:287-294, 1999.

3. D. J. C. MacKay, *Probable Networks and Plausible Predictions - A Review of Practical Bayesian Methods For Supervised Neural Networks*, 1995, Web site : http://wol.ra.phy.cam.ac.uk/mackay/BayesNets.html.

6 Input parameters

As mentioned before, the input variables are C, Si, Mn, Cu, Ni, Cr, Mo, Nb, V, W, Co and Heating rate. The maximum and minimum values for each variable are given in the file MINMAX.

7 Output parameters

The output is written in the file *result* in the Linux/Unix version and in *Model_RESULT.dat* for the PC version. This file contains the predicted Ac_1 temperatures (in °C), the error bar value, the predicted value - the error and the predicted value + the error.

Program data

See sample file test.dat

Program results

See sample file result.txt

Keywords

Neural networks, Ac_1 temperature, heating rate, martensitic stainless steels, carbon steels.

Bibliography

[1] A. G. Haynes. Some Factors Governing the Metallurgy and Weldability of 13 % Cr and Newer Cr-Ni Martensitic Stainless Steels. In *Supermartensitic Stainless Steels '99'*, pages 25–32, Belgium, 1999.

[2] P. E. Biagiotti and J. S. Reichman. Justifying the Use of 13Cr Steels For Corrosive CO_2 Operations. In *CORROSION 1995, paper 81*, NACE International, 1995.

[3] J. Charles. How to Specify CRA's Cost Effectively. In *Stainless Steel World 2002*, pages 13–27, Houston USA, 2002.

[4] D. William and Jr. Callister. *Materials Science and Engineering an Introduction*. John Wiley and Sons, Inc, New York, USA, 1999.

[5] L. M. Smith and M. Celant. Martensitic Stainless Steel Flowlines, Do They Pay. In *Supermartensitic Stainless Steels '99'*, pages 66–73, Belgium, 1999.

[6] J. R. Davis. Selection of Wrought Martensitic Stainless Steels. *ASM, Metals Handbook*, 6:432–442, 1971.

[7] M. Ueda, H. Amaya, K. Kondo, K. Ogawa, and T. Mori. Corrosion Resistance of Weldable Super 13Cr Stainless Steel in H_2S Containing CO_2 Environments. In *CORROSION 1996, paper 58*, NACE International, 1996.

[8] E. Deleu, A. Dhooge, and Dufrane J. J. Weldability and Hot Deformability of Different Supermartensitic Stainless Steel Grades by Weld Simulation testing. In *Supermartensitic Stainless Steels '99'*, pages 232–240, Belgium, 1999.

[9] C. Dillon. Compositional Effects in Corrosion of Stainless Steels in Chemical Environments. *Corrosion*, 16:433t–440t, 1960.

[10] E. Folkhard. *Welding Metallurgy of Stainless Steels*. Springer-Verlag, Wien, New York, 1988.

[11] R. Castro and J. J. De cadeney. *Welding Metallurgy of Stainless and Heat-Resisting Steels*. Cambridge University Press, Cambridge, 1974.

[12] K. Bungardt, E. Kunze, and E. Horn. Untersuchungenüber den Aufbau des Systems Eisen-Chrom-Kohlenstoff. *Arch. eisenhüttenwes*, 29:193–203, 1958.

[13] M. Kimura, Y. Miyata, Y. Yasuyoshi, T. Takaaki, and N. Yoshifumi. Corrosion Resistance of High Strength Modified 13Cr Steel. In *CORROSION 1997, paper 22*, NACE International, 1997.

[14] K. kondo, M. Ueda, K. Ogawa, H. Amaya, H. Hirata, and H. Takabe. Alloy Design of Super 13 Cr Martensitic Stainless Steel (Development of Super 13 Cr Martensitic Stainless Steel for Line Pipe-1). In *Supermartensitic Stainless Steels '99'*, pages 11–18, Belgium, 1999.

[15] H. Asahi, T. Muraki, H. Inoue, and H. Tamehiro. High Chromium Martensitic Stainless Linepipes. *Pipeline Technology ASME 1996*, V:223–230, 1996.

[16] H. Asahi, T. Hara, A. Kawakami, and A. Takahashi. Development of Sour Resistant Modified 13Cr OCTG. In *CORROSION 1995, paper 79*, NACE International, 1995.

[17] T. G. Gooch. Welding Martensitic Stainless Steels. *Welding Institute Research Bulletin*, 18:343–349, 1977.

[18] Sumitomo Metal Industries Ltd. European Patent Specification : Martensitic Stainless Steels for Use in Oil Wells. *Bulletin 1997/30*, 1997. Patent number EP 0 565 117 B1.

[19] Y. Miyata, M. Kimura, T. Koseki, T. Toyooka, and F. Murase. Martensitic Stainless Steel Seamless Linepipe With Superior Weldability and CO_2 Corrosion resistance. In *CORROSION 1997, paper 19*, NACE International, 1997.

[20] A. Miyasaka and H. Ogawa. Influence of Metallurgical Factors on Corrosion Behaviors of Modified 13 %Cr Martensitic Stainless Steels. In *CORROSION 1990, paper 67*, NACE International, 1990.

[21] J. Pleva and S. Nordin. Properties of Different MMA Welds on Modified Type 329 Ferritic-Austenitic Stainless Steel. In *Duplex Stainless Steels '82'*, pages 603–629, St. Louis, 1982.

[22] Ø. Grong. *Metallurgical Modelling of Welding*. The Institute of Materials, London, 1994.

[23] Standard MR0175. Sulphide Stress Cracking Resistant Metallic Materials for Oilfield Equipment. *Nace International*, 2001.

[24] P. P. Koistinen and R. E. Marburger. A General Equation Prescribing The Extent of The Austenite-Martensite Transformation in Pure Iron-Carbon Alloys and Plain Carbon Steels. *Acta Metallurgica*, 7:59–60, 1959.

[25] Honeycombe, R. W. K. and Bhadeshia, H. K. D. H. *Steels Microstructures and Properties*. Edward Arnold, London, 1995.

[26] T. Maki, K. Tsuzaki, and I. Tamura. The Morphology of Microstructure Composed of Lath Martensites in Steels. *ISIJ*, 20:207–214, 1980.

[27] K. Takano, M. Sakakibara, T. Matsui, and S. Takaki. Effects of Alloying Elements and Microstructure on Corrosion Resistance and Hardness of Martensitic Stainless Steels. *Tetsu to Hagane*, 86:123–130, 2000.

[28] J. J. Dufrane. Metallurgical Basis for the Development of Weldable Martensitic Stainless Steels. In *Supermartensitic Stainless Steels '99'*, pages 19–24, Belgium, 1999.

[29] J. A. Ribenolt and W. J. Harris. Effect of Alloying Elements on Notch Toughness of Pearlitic Steels. *Transactions of the american society for metals*, 43:1175–1201, 1951.

[30] P. Woollin. The Weldability of Improved Martensitic Stainless Steels. Technical Report 5673/9A/98, Welding Institute Internal Report, 1998.

[31] J. K. Solberg, E. V. Ladanova, G. Rorvik, and P. E. Kvaale. Post Weld Heat Treatment Response of Coarse Grained Heat Affected Zone in a Supermartensitic Stainless Steel. In *Supermartensitic Stainless Steels '99'*, pages 56–63, Belgium, 1999.

[32] K. Nose and H. Asahi. Effect of Microstructure on Corrosion Resistance of a Martensitic Stainless Linepipe. In *CORROSION 2000, paper 145*, NACE International, 2000.

[33] M. Kimura, Y. Miyata, and T Toyooka. Effect of Retained austenite on Corrosion Performance for Modified 13% Cr Steel Pipe. In *CORROSION 2000, paper 137*, NACE International, 2000.

[34] C. Leymonie, M. C. Ottmann, R. Risacher, and G. Thauvin. Contribution a l'etude des Transformations Structurales des Aciers a 13%Cr - 4%Ni. *Revue de Metallurgie*, 12:815–826, 1979.

[35] L. Dong-Seok, L. Yong-Deuk, J. Joong-Hwan, and C. Chong-Sool. Amount of Retained Austenite at Room Temperature After Reverse Transformation of Martensite to Austenite in an Fe-13%Cr-7%Ni-3%Si Martensitic Stainless Steel. *Scripta materialia*, 45:767–772, 2001.

[36] I. Varga, E. Kuzmann, and A. Vertes. Kinetics of α-γ Phase Transition of Fe-12Cr-4Ni Alloy Aged Between 500-650 °C. *Hyperfine Interactions*, 112:169–173, 1998.

[37] I. Varga, E. Kuzmann, M. Kaldor, and A. Vertes. Mössbauer Study of the Kientic Behavior of Anomalous Austenite Formation in Fe-12Cr-4Ni Steel. *J. Radioanal. Nucl. Chem.*, 165:115–126, 1992.

[38] T. G. Gooch, P. Woollin, and A. G. Haynes. Welding Metallurgy of Low Carbon 13 %Cr Martensitic Steels. In *Supermartensitic Stainless Steels '99'*, pages 188–195, Belgium, 1999.

[39] A. Kulmburg, F. Korntheuer, O. Gründler, and K. Hutterer. Umwandlungsund Ausscheidungsverhalten von Weichmartensitischen und Hochfesten Korrosionsbeständigen Stählen. *Berg. u. hüttenm. Mh.*, 126:104–108, 1981.

[40] C. Leymonie, M. C. Lecocq, and M. C. Ottmann. Relations entre la Structure et les Proprietes Mecaniques de Deux Aciers a 16%Cr - 4%Ni. *Traitement thermiques*, 165:57–62, 1982.

[41] H. J Niederau. Entwicklungsstand Nichtrostender Weichmartensitischer Chrom-Nickel-Stähle unter besonderer Berücksichtigung des Stahles X 5 CRNi13 4. *Stahl u. Eisen*, 98:385–392, 1978.

[42] P. D. Bilmes, M. Solari, and C. L. Llorente. Characteristics and Effects of Austenite Resulting From Tempering of 13Cr-Ni-Mo Martensitic Steel Weld Metals. *Materials Characterisation*, 46:285–296, 2001.

[43] M. C. Balmforth and J. C. Lippold. A Preliminary Ferritic-Martensitic Stainless Steels Constitution Diagram. *Welding Journal*, 77:1s–7s, 1998.

[44] J. C. M. Farrar and A. W. Marshall. Super Martensitic Stainless Steels - Overview and Weldability. *IIW-IX-H-423-98*, pages 1–16, 1998.

[45] S. Hashizume. A new 15 %Cr Martensitic Stainless Steel Developed for OCTG. In *CORROSION 1991, paper 28*, NACE International, 1991.

[46] Y. Ishizawa, T. Shimada, and M. Tanimura. Effect of Microstructure on the Sulphide-Stress Corrosion Cracking Resistance of AISI 410 and 420 Steels. In *NACE International, paper 124*, Houston, Texas, 1982.

[47] T. Hara and H. Asahi. Effect of δ-Ferrite on Sulphide Stress Cracking in a Low Carbon 13 mass % Chromium Steel. *ISIJ International*, 40:1134–1141, 2000.

[48] TWI web site. www.twi.co.uk.

[49] K. Easterling. *Introduction to the Physical Metallurgy of Welding*. Butterworth & Co Ltd, 1983.

[50] D. P. Smith, D. J. Carney, L. W. Eastwood, and C. E. Sims. *Gases in Metals*. American Society for Metals, Cleveland, Ohio USA, 1953.

[51] A. W. Marshall and J. C. M. Farrar. Welding of Ferritic and Martensitic 11-14% Cr Steels . *Welding in the world*, 45:32–55, 2001.

[52] J. F. Lancaster. *Metallurgy of Welding, fourth edition.* Allen and Unwin Ltd, 40 Museum street, London WC1A 1LU, UK, 1987.

[53] J. Enerhaug, Ø. Grong, and U. M Steinsmo. Factors Affecting Initiation of Pitting Corrosion in Super Martensitic Stainless Steel Weldments. *Science and Technology of welding and Joining*, 6:330–338, 2001.

[54] L. Coudreuse, M. Verneau, and J. J. Dufrane. Sulphide Stress Cracking Resistance of Weldable Super-Martensitic Stainless Steels. In *Supermartensitic Stainless Steels '99'*, pages 299–306, Belgium, 1999.

[55] G. Rørvik, P. E. Kvaale, and O. M. Akselsen. Sources and Levels of Hydrogen in TIG Welding of 13% Cr Martensitic Stainless steels. In *Supermartensitic Stainless Steels '99'*, pages 196–203, Belgium, 1999.

[56] P. Woollin and D. Carrouge. Heat Affected Zone Microstructures in Supermartensitic Stainless Steels. In *Supermartensitic Stainless Steels 2002*, Belgium, 2002. Paper 027.

[57] T. G. Gooch and B. J. Ginn. Heat Affected Zone Toughness of MMA Welded 12 %Cr Martensitic-ferritic Steel. Technical Report 373, Welding Institute Members Report, 1988.

[58] C. Grobler. *Weldability Studies on 12 % and 14 % Chromium Steels.* PhD thesis, University of Pretoria, 1987.

[59] J. J. J. Zaayman and G. T. Van Rooyen. The Toughness of the Heat Affected Zone of Welds in 11.5 per cent Chromium Steels. In *Proceedings of the 1st International Chromium Steels and Alloys Congress, Volume 2, SAIMM*, pages 137–142, Cape town, Johannesburg, 1992.

[60] L. Karlsson, S. Rigdal, A. Dhooge, E. Deleu, M. Goldschmitz, and J. Van den Broek. Degassing Response of Supermartensitic Weld Metals. Technical Report IIW-IX-H-514-2001, International Institute of Welding, 2001.

[61] N. Petch. *Fracture*. John Wiley & son, New York, USA, 1959.

[62] J. F. Knott. *Fundamentals of Fracture Mechanics*. Butterworths, London, UK, 1988.

[63] R. Fenn and M.F. Jordan. Microstructure of Weld Heat-Affected Zone of 12Cr-Mo Steel. *Metals Technology*, 9:327–337, 1982.

[64] H. Hoffmeister and R. Mundt. Untersuchungen zum Einfluß des Kohlenstoffs und des Stickstoffs auf die δ-γ Umwandlung ferritisch-austenitischer Chrom-Nickel- Stäle. *Arch. eisenhüttenwes*, 52:159–164, 1981.

[65] J. Singh, G. R. Purdy, and G. C. Weatherly. Microstructural and Microchemical Aspect of The Solid State Decomposition of Delta-ferrite in Austenitic Stainless Steels. *Metallurgical Transactions*, 16A:1363–1369, 1985.

[66] H. Hemmer. *A Process Model for Electron Beam Welding of Duplex stainless steels*. PhD thesis, Norges teknisk-naturvitenskapelige universitet, 1999.

[67] W. T. Delong. Ferrite in Austenitic Stainless Steels Weld Metal. *Welding Journal*, 53:273s–286s, 1974.

[68] C. G. Long and W. T. Delong. The Ferrite Content of Austenitic Stainless Steel Weld Metal. *Welding Journal*, 52:281s–297s, 1973.

[69] D. J. Kotecki. Welding Parameter Effects on Open-Arc Stainless Steel Weld Metal Ferrite. *Welding Journal*, 57:109s–117s, 1978.

[70] D. J. Kotecki. Extension of the WRC Ferrite Number System. *Welding Journal*, 61:352s–361s, 1982.

[71] R. H. Kaltenhauser. Improving the engineering properties of ferritic stainless steels. *Metals Engineering Quaterly*, 11:41–47, 1971.

[72] J. Hewitt. High-Chromium Controlled-Hardenability Steels. In *Proceedings of the 1st International Chromium Steels and Alloys Congress, Cape Town. Volume 2. Johannesburg, SAIMM*, pages 71–88, 1992.

[73] T. G. Gooch. Corrosion Behaviour of Welded Stainless Steels. *Welding Journal*, 75:135s–154s, 1996.

[74] A. L. Schaeffler. Constitution diagram for stainless steel weld metal. *Metal Progress*, 56:680–680B, 1949.

[75] M. C. Balmforth and J. C. Lippold. A New Ferritic-Martensitic Stainless Steels Constitution Diagram. *Welding Journal*, 79:339s–345s, 2000.

[76] T. A. Siewert, C. N. McCowan, and D. L. Olson. Ferrite Number Prediction to 100 FN in Stainless Steels Weld Metal. *Welding Journal*, 67:289s–298s, 1988.

[77] D. J. Kotecki and T. A. Siewert. WRC-1992 Constitution Diagram for Stainless Steels Weld Metals : a Modification of the WRC-1988 Diagram. *Welding Journal*, 71:171s–178s, 1992.

[78] J. M. Vitek, Y. S Iskander, and E. M. Oblow. Improved Ferrite Number Prediction in Stainless Steel Arc Welds Using Artificial Neural Networks - Part 1 : Neural Network Development. *Welding Journal*, 79:33s–40s, 2000.

[79] J. M. Vitek, Y. S. Iskander, and E. M. Oblow. Improved Ferrite Number Prediction in Stainless Steel Arc Welds Using Artificial Neural Networks - Part 2 : Neural Network Results. *Welding Journal*, 79:41s–50s, 2000.

[80] M. Vasudevan, M. Murugananth, and A. K. Bhaduri. Application of Bayesian Neural Network For Modelling and Prediction of Ferrite Number in Austenitic Stainless Steel Welds. *Mathematical Modelling of Weld Phenomena*, 6:1079–1099, 2002.

[81] P. Woollin. Metallurgical Examination of Martensitic Stainless Steel Weldments. Technical Report 620886/1/95, Welding Institute Internal Report, 1995.

[82] E. Beraha and B. Shpigler. *Color Metallography*. American Society for Metals, 1977.

[83] B. D. Cullity. *Elements of X-ray Diffraction*. Addison-Wesley, 1978.

[84] BS EN 10045-1. Charpy Impact Test on Metallic Materials. Part 1: Test Method. *British Standard*, 1990.

[85] R.D. Campbell and D.W. Walsh. Weldability Testing. *ASM, Metals Handbook*, 6:603–613, 1971.

[86] G. L. Leone and H. W. Kerr. The Ferrite to Austenite Transformation in Stainless Steels. *Weld. J. res. suppl.*, 61:13s–22s, 1982.

[87] J. C. Lippold and W. F. Savage. Solidification of Austenitic Stainless Steels Weldments Part I- a Proposed Mechanism. *Weld. J. res. suppl.*, 58:362s–374s, 1979.

[88] G. Blanc and R. Tricot. Solidification, Segregation et Homogeneisation des Aciers Inoxydables Austenitique Contenant de la Ferrite Delta. *Mem. Sci. Rev. Met.*, 58:735–753, 1979.

[89] NKK Weldable 13 %Cr Seamless Line Pipe Material. Technical report, NKK Japan, 1999.

[90] R. D. Knutsen and R. Hutchings. Occurence of Non-metallic Inclusions in 3CR12 Steel and Their Effect on Impact Toughness . *Materials Science and Technology*, 4:127–135, 1988.

[91] M. M. McDonald and Ludwigson D. C. Fractographic Examination in the Scanning Electon Microscope as a Tool in Evaluating Through-Thickness Tension Test Results. *Journal of Testing and Evaluation*, 11:165–173, 1983.

[92] D. P. Fairchild, D. G. Howden, and W. A. T. Clark. The Mechanism of Brittle Fracture in a Microalloyed Steel : Part I. Inclusion-Induced Cleavage. *Metallurgical and Materials Transactions A*, 31A:641–652, 2000.

[93] D. P. Fairchild, D. G. Howden, and W. A. T. Clark. The Mechanism of Brittle Fracture in a Microalloyed Steel : Part II. Mechanistic Modelling. *Metallurgical and Materials Transactions A*, 31A:653–667, 2000.

[94] L. Gavard, H. K. D. H. Bhadeshia, D. J. C. MacKay, and S. Suzuki. Bayesian Neural Network Model for Austenite Formation in Steels. *Materials Science and Technology*, 12:453–463, 1996.

[95] D. J. C. MacKay. Probable Networks and Plausible Predictions - A Review of Practical Bayesian Methods For Supervised Neural Networks. *http://wol.ra.phy.cam.ac.uk/mackay/BayesNets.html*, 1995.

[96] H. K. D. H. Bhadeshia. Neural Network in Materials Science. *ISIJ International*, 39:966–979, 1999.

[97] C. A. L. Bailer-Jones, H. K. D. H. Bhadeshia, and D. J. C. MacKay. Gaussian Process Modelling of Austenite Formation in Steel. *Materials Science and Technology*, 15:287–294, 1999.

[98] C. Downs and H. K. D. H. Bhadeshia. Unpublished work. 2001.

[99] A. Ball, Y. Chauhan, and G. B. Schaffer. Microstructure Phase Equilibria and Transformations in Corrosion Resistant Dual Phase Steel Designated 3CR12. *Materials Science and Technology*, 3:189–196, 1987.

[100] A. Alamo, J. C. Brachet, A. Castaing, F. Lepointtevin, and F. Barcelo. Physical Metallurgy of FeCrWTaV Low Activation Martensitic Steels. Effect of Chemical Composition. *Journal of Nuclear Metallurgy*, 258-263:1228–1235, 1998.

[101] D. J. C. MacKay. Bayesian Non-Linear Modelling Neural Networks. *http://wol.ra.phy.cam.ac.uk/mackay/BayesNets.html*, 1996.

[102] P. Woollin. Optimising The Properties of Weldments in Weldable Martensitic and Supermartensitic Stainless Steel. Technical Report 12097/5/01, Welding Institute Internal Report, 2001.